https://journals.vsu.ru/kcmf/about

ISSN 1606-867X
eISSN 2687-0711

Конденсированные среды и межфазные границы

РЕЦЕНЗИРУЕМЫЙ НАУЧНЫЙ ЖУРНАЛ

Condensed Matter and Interphases

PEER-REVIEWED SCIENTIFIC JOURNAL

Том / Vol. 28, № / No. 1
2026

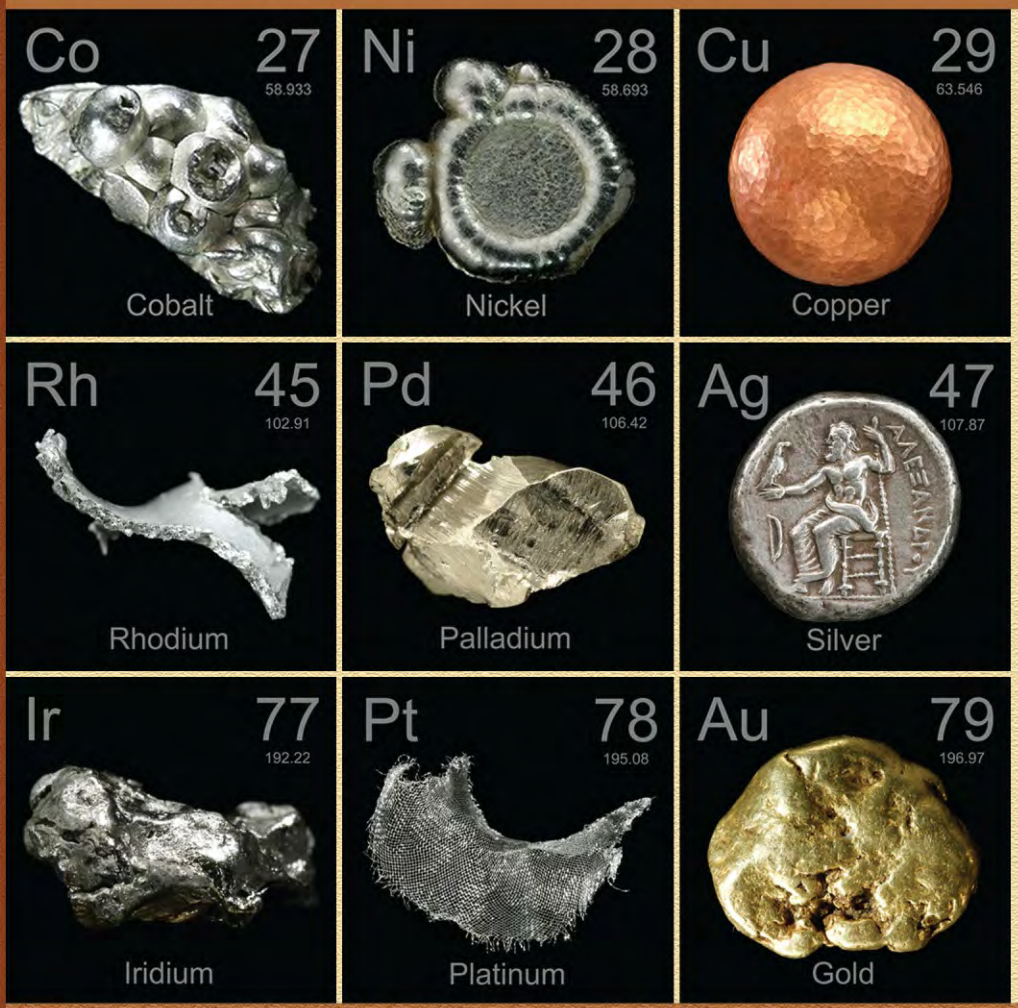

Condensed Matter and Interphases
Kondensirovannye sredy i mezhfaznye granitsy

Peer-reviewed scientific journal
Published since January 1999
Periodicity: Quarterly
Volume 28, No. 1, 2026

Full-text version is available in the Russian language on the website: https://journals.vsu.ru/kcmf

Condensed Matter and Interphases (Kondensirovannye Sredy i Mezhfaznye Granitsy) publishes articles in Russian and English dedicated to key issues of condensed matter and physicochemical processes at interfaces and in volumes.

The mission of the journal is to provide open access to the results of original research (theoretical and experimental) at the intersection of contemporary condensed matter physics and chemistry, material science and nanoindustry, solid state chemistry, inorganic chemistry, and physical chemistry, and to share scientific data in the **following sections**: atomic, electron, and cluster structure of solids, liquids, and interphase boundaries; phase equilibria and defect formation processes; structure and physical and chemical properties of interphases; laser thermochemistry and photostimulated processes on solid surfaces; physics and chemistry of surface, thin films and heterostructures; kinetics and mechanism of formation of film structures; electrophysical processes in interphase boundaries; chemistry of surface phenomena in sorbents; devices and new research methods.

The journal accepts for publication: reviews, original articles, short communications by leading Russian scientists, foreign researchers, lecturers, postgraduate and undergraduate students.

FOUNDER AND PUBLISHER:
Voronezh State University

The journal is registered by the Russian Federal Service for Supervision of Communications, Information Technology and Mass Media, Certificate of Registration ПИ № ФС77-78771 date 20.07.2020

The journal is included in the List of peer reviewed scientific journals published by the Higher Attestation Commission in which major research results from the dissertations of Candidates of Sciences (PhD) and Doctor of Science (DSc) degrees are to be published. Scientific specialties of dissertations and their respective branches of science are as follows: 1.4.1. – Inorganic Chemistry (Chemical sciences); 1.4.4. – Physical Chemistry (Chemical sciences); 1.4.6. – Electrochemistry (Chemical sciences); 1.4.15. – Solid State Chemistry (Chemical sciences); 1.3.8. – Condensed Matter Physics (Physical sciences).

The journal is indexed and archived in: Russian Scientific Index Citations, Scopus, Chemical Abstract, EBSCO, DOAJ, CrossRef

Editorial Board and Publisher Office:
1 Universitetskaya pl., Voronezh 394018
Phone: +7 (432) 2208445
https://journals.vsu.ru/kcmf
E-mail: kcmf@main.vsu.ru

ISSN 1606-867X (Print)
ISSN 2687-0711 (Online)
Конденсированные среды и межфазные границы / Condensed Matter and Interphases. 2026, 28(1)

CONTENTS

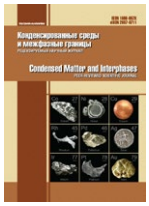

ISSN 1606-867X (Print)
ISSN 2687-0711 (Online)
Condensed Matter and Interphases
Kondensirovannye Sredy i Mezhfaznye Granitsy
https://journals.vsu.ru/kcmf/

Original articles

Research article
https://doi.org/10.17308/kcmf.2026.28/13554

Tunable magnetic, dielectric, and optical properties of cobalt ferrite/PVA nanocomposites: Effect of nanoparticle calcination temperature

Noor A. Saeed[1], Wafaa A. Hussain[1], Mukhlis M. Ismail[1], Mudatheer M. Al-Slivani[2]✉

[1]Department of Applied Physics, College of Applied Science, University of Technology, Baghdad, Iraq

[2]Al-Furqan University, College of Education for Pure Sciences, Department of Physics, Mosul, Iraq

Abstract

Objectives: This study investigates the magnetic and dielectric properties of nanocomposites composed of cobalt ferrite ($CoFe_2O_4$) nanoparticles embedded in a polyvinyl alcohol (PVA) matrix.

Experimental: $CoFe_2O_4$ nanoparticles were synthesized via a sol-gel auto-combustion method and subsequently calcined at 600 and 900 °C. X-ray diffraction results indicated that increasing the calcination temperature from 600 to 900 °C led to an increase in crystallite size from 23.3 nm to 48.5 nm. This was accompanied by an enhancement in saturation magnetization (*M*s) from 68.7 emu/g to 81.3 emu/g and a decrease in coercivity (*H*c) from 1150 to 860 Oe.

Conclusions: Most importantly, the PVA/$CoFe_2O_4$ composites exhibited enhanced dielectric properties compared to pure PVA. At 100 Hz, the dielectric constant (ε′) of the composite increased from approximately 18 (for PVA/CF600) to 42 (for PVA/CF900), values significantly higher than that of pure PVA, which was approximately 9. This enhancement highlights a synergistic effect between the ferrite nanoparticles and the polymer matrix, opening possibilities for designing composites with tunable dielectric responses for applications such as embedded capacitors and electromagnetic wave absorption devices.

Keyword: Cobalt ferrite, Nanocomposites, Polyvinyl alcohol (PVA), Magnetic properties, Dielectric constant, Optical band gap, Sol-gel

For citation: Saeed N. A., Hussain W. A., Ismail M. M., Al-Slivani M. M. Tunable magnetic, dielectric, and optical properties of cobalt ferrite/PVA nanocomposites: Effect of nanoparticle calcination temperature. *Condensed Matter and Interphases*. 2026;28(1): 3–14. https://doi.org/10.17308/kcmf.2026.28/13554

✉ Mudatheer M. Al-Slivani, e-mail: mudatheeralslivani@gmail.com

1. Introduction

Polymeric magnetic nanocomposites are of great scientific and technological interest since they can incorporate the inherent physical and chemical strength of organic polymers and gain the magnetic properties that are peculiar to nanoparticles [1–3]. These materials have benefits compared to traditional composites such as superior mechanical, thermal, and electrical characteristics and controllable magnetic action. Their versatility allows them to be used in a wide range of industries including water purification, medicine, dentistry, energy storage, environmental remediation, and delivering drugs [4–11]. Nanocomposites offer a promising field of study in the development of complex useful materials because particular design opportunities are offered through the incorporation of the magnetic nanoparticles in polymer matrices. Spinel ferrite nanocrystalline structures have received a lot of attention as they exhibit unique physical and chemical characteristics due to their surface effects and quantum confinement [12–17].

Cobalt ferrite ($CoFe_2O_4$) has been identified to be versatile and finds various uses including magnetic biosensing systems, drug delivery, and magnetic resonance imaging, alongside other magnetic ferrites. These nanoparticles can also be incorporated with polymers in nanocomposites with the magnetic particles being embedded in a non-magnetic matrix to make a soft ferrite system. This incorporation adds functional attributes to the material, and the material can be used in advanced biomedical and electronic gadgets [18]. The process of calcification of nanoparticles is effective in affecting the magnetic properties, particularly for those containing iron oxide, cobalt, nickel, and their compounds because of its explicit influence on the size and distribution of the nanoparticles by taking into account the changes that take place during the steps of nucleation and growth [19].

Magnetic characteristics are greatly affected by the size of the nanoparticles and changes in size distribution by modifying some of the parameters, including the coercivity (H_c), remanent magnetization (M_r), and saturation magnetization (M_s). Moreover, the surface and interface properties of the nanoparticles might be changed during the calcification process which in turn alters the magnetic behavior of the nanoparticles in addition to the above-mentioned processes; the surface oxidation, surface reconstruction, spin disorder, and magnetic coupling processes taking place on the surface of nanoparticles are all related to the calcification process, which is closely related them [20]. The calcification process is also accompanied by phase transitions and alterations in the crystalline structure of magnetic nanoparticles as is found with the phase transition of iron oxide maghemite or hematite into maghemite or hematite, respectively, in the presence of heat [21].

Nanoparticles grow in a directed manner during the calcification process resulting in different magnetic properties with the magnetic moments existing along the crystallographic directions. Conversely, conditioning creates defects and disturbances on the magnetic properties. E.g., lattice vacancies, dislocations, grain boundaries, which are created during the calcination process influence the magnetic field structure, the rotational process and the magnetic relaxation process of the magnetic nanoparticle. The calcification process influences the thermal stability and coercive strength and also promotes crystallization and granular development. The calcification process is regarded as an essential and significant action in enhancing the characterization of magnetic nanoparticles to be used in numerous applications like magnetic recording, magnetic sensors, and biomedical imaging among others because it is attained by enhancing the magnetic parameters [22–34].

PVA cobalt ferrite composites have already been prepared and investigated. As an example, Rashidi et al., 2016 [35] prepared the composite by mechanical alloying, which resulted in magnetic properties according to milling time. On the same note, Garcias-Cerda et al. (2007) [36] also made composite films and showed the reliance of their characteristics on the concentration of ferrite. The current work is characterized by the emphasis it placed on the pre-calcination temperature of the ferrite nanoparticles on the ultimate characteristics of the composite, a factor that has not been fully elaborated in the previous works. We show that the temperature of calcification can

be employed as an accurate means of modulating the dielectric constant of the composite.

This research is important as it provides valuable insights into how calcination temperature affects the magnetic and dielectric properties of cobalt ferrite nanoparticles embedded in a polyvinyl alcohol matrix. Understanding these effects is crucial for improving the performance of nanomaterials in a variety of applications, including sensors, magnetic storage, and biomedical devices. The study helps us to better understand how to optimize the properties of these nanocomposites, offering potential solutions for advanced technological and medical uses.

2. Experimental

Using an aqueous solution of cobalt nitrate and iron nitrate, with citric acid as a fuel, an ammonia solution was added until a pH of 7 was attained in the sol–gel auto combustion process. The mixture of metal nitrates and fuel (often in a molar ratio of 1:2:3). This mixture was heated to 80 °C on a magnetic stirrer while being continuously stirred to generate a viscous gel. After two hours of heating at 150 °C the gel undergoes self-propagating combustion that enabling the formation of ferrites. The resulting loose powder was thoroughly crushed and then calcined at 600 and 900 °C.

PVA granules (20 g) was added slowly to 100 ml of distilled room temperature water while stirring to prevent clumping. For complete dissolution, the solution put on a heated plate of magnetic stirrer at temperature 60 to 80 °C. The solution was held at this temperature for approximately five to seven hours to ensure full solubilization, by which point it turned transparent.

X-ray diffraction (XRD) was used to analyze the crystalline structure of the prepared powders using a Shimadzu XRD-6000 diffractometer with a voltage of 40 kV and a current of 30 mA, with Cu$K\alpha$ (1.5406 Å) radiation. The scan was carried out in the 2θ (20–80)° range. A JEOL JSM-6390LV Scanning Electron Microscope (SEM) was used to find out the morphology and the particle size. The Brunauer–Emmett–Teller (BET) method of surface area determination was used on a Quantachrome NOVA 2200e surface area analyzer to determine the specific surface area of the powders. Measurement of magnetic properties at room temperature was done with a Lake Shore 7404 Vibrating Sample Magnetometer (VSM). The dielectric characteristics of the PVA/$CoFe_2O_4$ composites were measured at a frequency of 100 Hz to 5 MHz on Agilent 4284A Precision LCR meter.

The experimental conditions were carefully selected based on established chemical principles and previous studies to ensure the synthesis of high-quality nanoparticles. The pH was adjusted to 7 to ensure the complete precipitation of metal ions and the formation of a homogeneous gel, which is optimal for the hydrolysis and condensation reactions in the sol-gel method. The 1:2:3 molar ratio of Co/Fe/fuel was chosen to provide a sufficient amount of fuel (citric acid) for a complete auto-combustion process, promoting the formation of the pure spinel phase while minimizing secondary phases. The calcination temperatures of 600 and 900 °C were selected to study the effect of the structural evolution from a nanocrystalline phase (at 600 °C) to a more well-defined crystalline structure (at 900°C) on the final properties of the nanocomposite.

A deliberate two-step methodology was employed to fundamentally understand the relationship between the nanoparticle filler and the final composite material. First, the standalone cobalt ferrite ($CoFe_2O_4$) powder was characterized (via XRD, SEM, BET) to establish its intrinsic properties (crystallite size, morphology, surface area) and their dependence on calcination temperature. These baseline properties are critical as they govern the subsequent behavior of the nanoparticles. Second, these well-characterized nanoparticles were embedded into the polyvinyl alcohol (PVA) matrix to investigate the composite's properties. The role of PVA is not passive but critical to the measurements. For the magnetic characterization (VSM), the PVA matrix acts as a separator, preventing nanoparticle agglomeration. This allows for the measurement of the magnetic response of largely isolated particles, thus providing a more accurate reflection of the size-dependent effects. For the optical measurements (UV-Vis), the measured band gap is a property of the composite system as a whole, arising from the electronic interactions between the ferrite filler and the polymer matrix.

Therefore, PVA is not merely a transparent medium but an active component that influences the final optical properties of the system.

3. Results and discussions

Fig. 1 shows the XRD results of the cobalt ferrite nanoparticles as-dried particles obtained at different temperatures (room temperature, 600, and 900 °C). XRD verified that the synthesized as-prepared and calcined $CoFe_2O_4$ were their crystal structure face-centered cubic (FCC) and phase identification with JCPDS card no. 22-1086 as shown in Fig. 1. The XRD analysis indicates that the result mostly indexed to $CoFe_2O_4$ with the miller indices of the reflection planes of (220), (311), (222), (400), (422), and (511). This pattern was also validated by previously studies [25, 26].

In comparison to the pure ferrite sample, the XRD peaks are wider, and this is correlated with the size of the nanocrystallite. As demonstrated in Fig. 1, calcination was carried out to eliminate secondary phases and remove internal stress that accompanying with the preparation of nanocobalt ferrite. When cobalt ferrite is calcined, the highest peak associated with the (311) plane which exhibits a higher diffraction angle increases with calcination as shown in Fig. 1. Also, Fig. 1 clearly illustrates shift of the highest peak (311) towards to higher 2θ angles, which suggests that there is a change in lattice constant with rising calcined temperature. When the calcined temperature reaches 600 °C, the peaks in the XRD pattern for $CoFe_2O_4$ become sharper, and their FWHM (full width at half maximum) decreases, indicating an increase in crystallite size. Based on the Williamson Hall (W-H) plot [27–29] (Fig. 2), the crystallite size and strain of the prepared $CoFe_2O_4$ are 44 nm and 0.00133 respectively. As seen in Fig. 2, it is observed that the crystallite size and strain also changes with the calcined temperature.

The crystallite size increased from 44 nm at room temperature to 56.68 and 73.1 nm at 600, and 900 °C as shown in Table 1. The growth of crystal size is attributed to the calcination process. This growth causes internal strains within the material. Due to differences in thermal expansion rates and grain boundaries, the characteristics of cobalt ferrite changed as the calcination temperature increased. The resulting lattice constants (*a*) of all powders are displayed in Table 1. It is evident that as the calcined temperature increased, the lattice constant increased. Thermal expansion of the crystal lattice resulted from increasing temperature, causing an increasing in the lattice constant. The X-ray density (ρ_x) results are illustrated in same Table. A slight decrease in X-ray density value is indicated with increasing temperatures. This result may be attributed to changes in crystal size

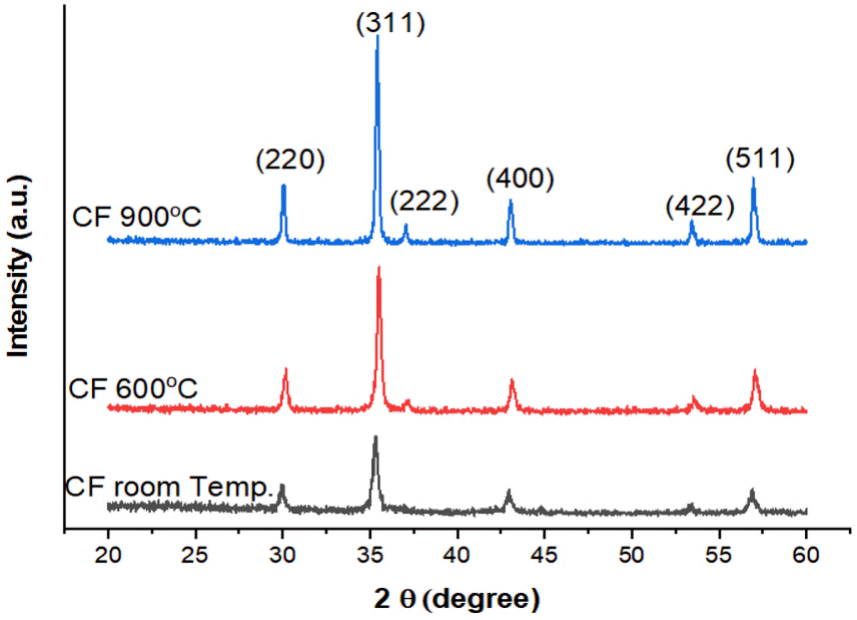

Fig. 1. XRD of CF (a) at room temperature, calcined at 600 and 900 °C

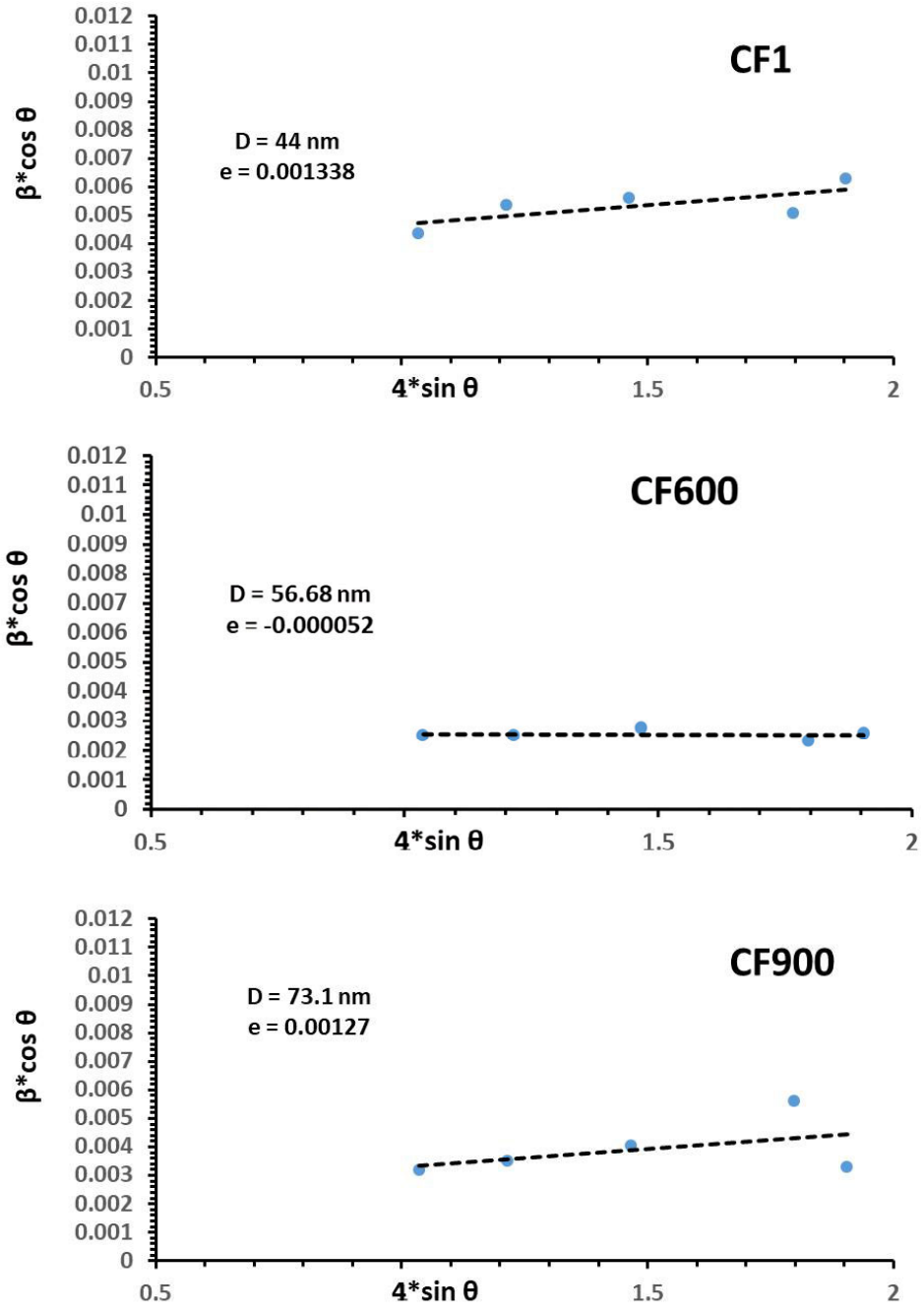

Fig. 2. W-H plot of CF at room temperature, calcined at 600 and 900 °C

and lattice parameters. Surface area per unit mass is called specific surface area (*S*) and its results are also listed in Table 1. The specific surface area values of room temperature and calcined powders have been reported to range between 26.1–15.6 (m^2/gm) as the calcined temperature increases.

This reduction is attributed to crystal size growth and particle agglomeration. In addition, the calculated values of hopping lengths for A-site (L_A) and B-site (L_B) are listed in Table (1). The hopping lengths of A-site and B-site are influenced by temperature. L_A and L_B were increased due to an expanding lattice parameter because of thermal expansion in which greater spacing between ions. The results of ionic radii (r_A) and (r_B) depending on oxygen positional parameter μ (= 0.0375 nm) and its radius of 0.135 nm are given in Table 1. Increasing

Table 1. Crystallite size *D*, strain, lattice constants (*a*), X-ray density (ρ_X), Specific area (*S*), the hopping lengths for A-site (L_A) and B-site (L_B), packing factor (*p*), and the tetrahedral (r_A) ionic radii and octahedral ionic radii (r_B)

Samples	CF1	CF600	CF900
Crystallite size *D* (nm)	44.001	56.681	73.123
Strain	0.001338	−0.00005	0.00127
Lattice constant *a* (Å)	8.374	8.404	8.420
X-ray density ρ_x (g/cm^3)	5.306	5.268	5.219
Specific area (*S*) (m^2/gm)	26.125	19.914	15.615
L_A (Å)	3.646	3.626	3.634
L_B (Å)	2.977	2.961	2.967
r_A (Å)	0.463	0.467	0.473
r_B (Å)	0.743	0.748	0.755
packing factor *(p)*	17.421	22.413	28.912

the calcination temperature of cobalt ferrite ($CoFe_2O_4$) leads to a larger ionic radius due to the expansion of the lattice. The packing factor (*P*) is a measure of how efficiently atoms are arranged in a crystal structure. The value of packing factor increases with higher calcination temperature due to enhanced crystallinity and particle growth as shown in Table 1. This growth leads to improve bulk density and higher packing factor, which is attributed to the heating of nanoparticles. The angle and the distance between atoms was determined with the help of the analysis using the HighScore Expert software. Also, the same program produced the Texture Coefficients and they were calculated using the following relationship provided in Equation [30, 31]:

$$d_{hkl} = 1/\sqrt{((h^2/a^2)+(k^2/b^2)+(l^2/c^2))}. \quad (1)$$

Where I_0 is the identified phase's XRD peak intensity, the peak intensities for all XRD are I_1, I_2, ... I_n.

FESEM images of CF nanoparticles annealed at various temperatures are displayed in Fig. 3. Images taken at room temperature showed that the fine particles were clumped together and had a spherical form. Due to the significant volume of gases released during combustion, pores or cavities were visible in the photographs of every sample. The porous network shown in Fig. 3 is a confirmed finding that is closely related to those powders prepared by combustion. As seen in Fig. 3, the nanoferrite particle size increased with the calcined temperature. At 900 °C, it is about 57.32 % (= 900/1570) of $CoFe_2O_4$ melting point (1570 °C), it is seen that the particle developed from separated single nanoparticles to compact nanoparticle granules. The micrometric aggregation shown in Fig. 3 can be explained by the occurrence of interaction between magnetic particles, especially at high temperatures, which could be primarily responsible for the occurrence of agglomerations [32–33]. Therefore, these nanoparticles exploit the thermal energy resulting from the calcination process to agglomerate, which results in the formation of larger granular particles. Fig. 4 displays the UV spectra of the PVA and PVA/CF composite. PVA's absorbance spectrum exhibits a distinctive peak at 200 nm that is related to the remaining acetate groups [34]. With a minor band position variation, the CF embedded PVA solutions exhibit every band seen in neat PVA and CF. As a result, the UV-vis spectra revealed relatively little absorbance in the visible wavelength range and primarily in the UV region. Using the Tauc plot as shown in Fig. 5, the energy gap for the PVA was found to be 3.87 eV, whereas it dropped to 3.1 eV for the PVA/CF composite where the cobalt nanoferrite was calcinated at 600 °C. As the degree of calcification of the ferrite increased, the energy gap began to increase, reaching 3.33 eV at 900 °C as shown in Fig. 6. Increasing the degree of calcination can cause significant changes in the crystal structure.

At low degrees of calcination, the degree of agglomeration in the nanoparticles is high, with crystallization being incomplete (as shown in Fig. 1 (XRD)), which leads to limiting the role and effectiveness of these nanoparticles. These obstacles can be overcome by increasing the degree of calcination, which in turn leads

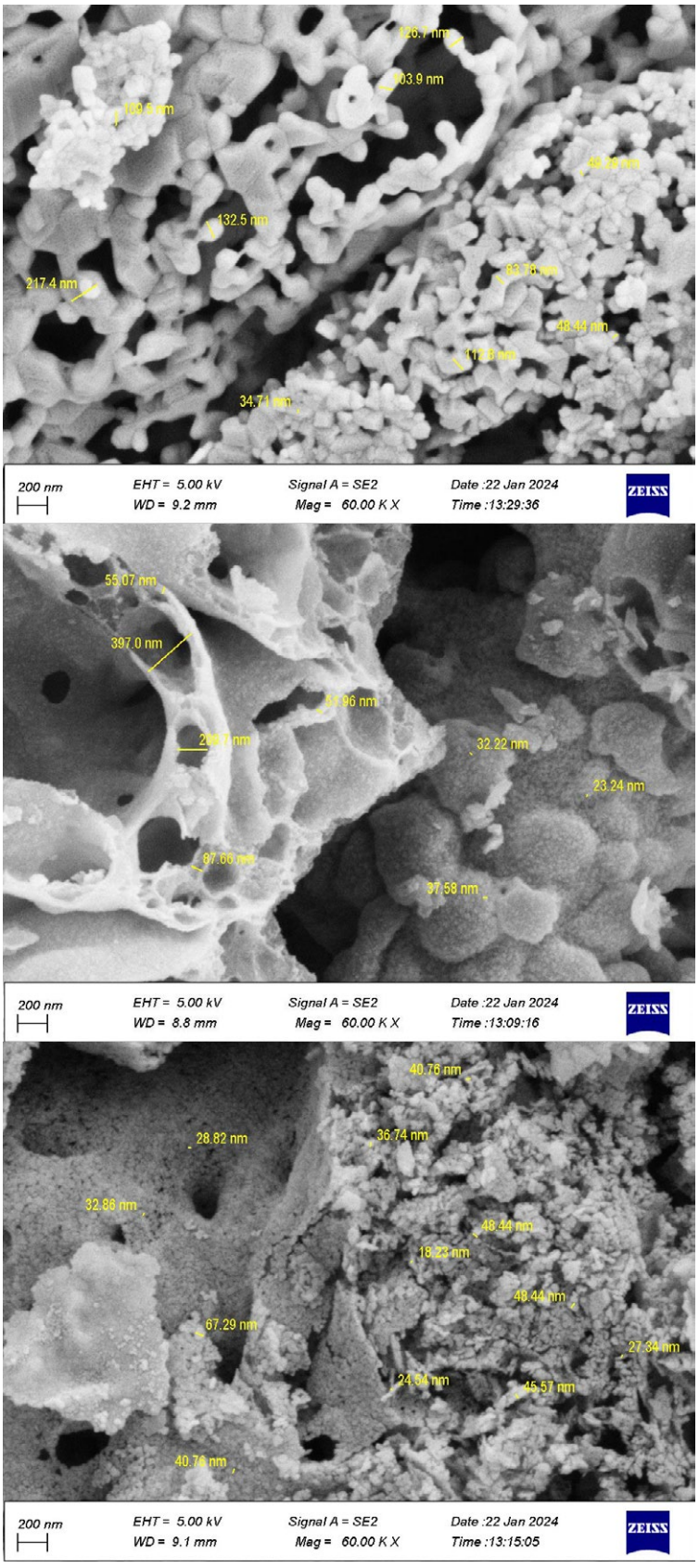

Fig. 3. Field Emission Scanning electron microscopy (FESEM) of CF at room temperature, calcined at 600 and 900 °C

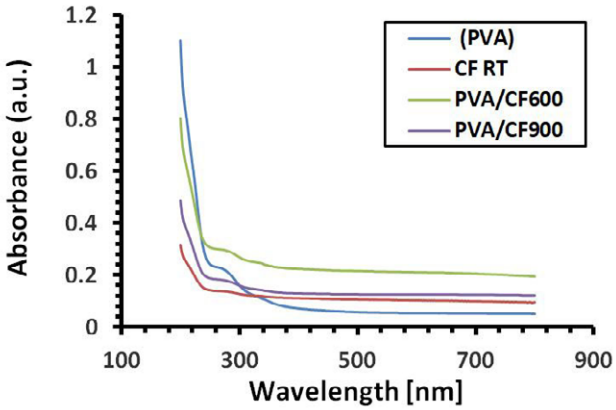

Fig. 4. UV-Vis spectra of PVA and PVA/CF composites

to an increase in the energy gap due to the phenomenon of quantum confinement. On the other hand, increasing calcination can affect the surface chemistry, as it leads to the removal of contaminants and surface defects such as oxygen vacancies, thus increasing the energy gap. Hysteresis loops (*M*-*H* curves) for PVA/CF composites are displayed in Fig. 6. The loops show saturation at 10000 Oe applied field. While the H_c values were noticeably high, the M_s and M_r values are low, most likely due to the influence of the small particle size. As the calcination temperature of cobalt ferrite increased, the saturation and

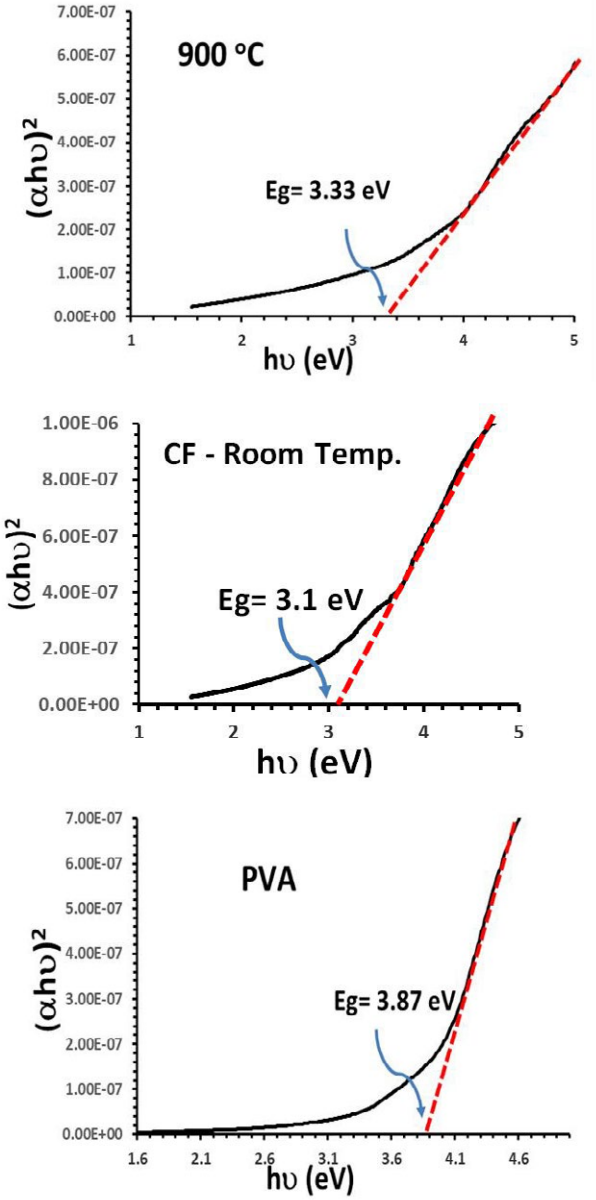

Fig. 5. Tauc plot of PVA and PVA/CF composites

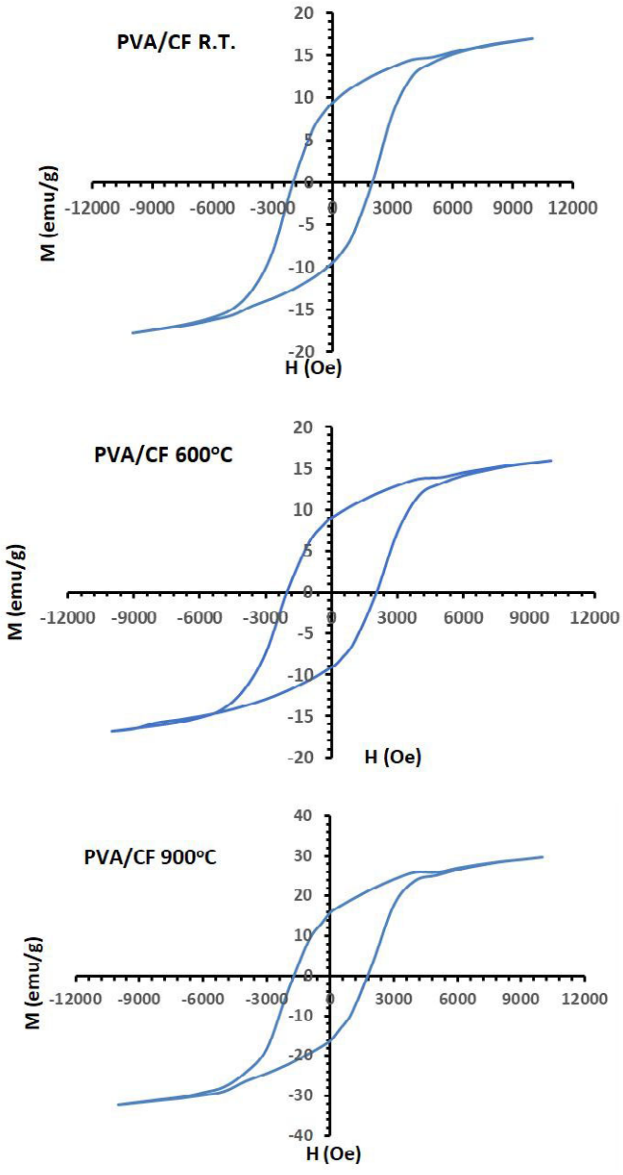

Fig. 6. *M*-*H* loop of PVA/CF composites

remnant magnetizations increased, while the coercivity decreased, as shown in Fig. 6. Calcination improves the crystallinity and intermolecular interaction of ferrites, where the crystallized materials mean a more efficient alignment of magnetic moments within the crystalline lattice, leading to higher magnetization. Also, calcination can reduce structural defects such as vacancies, dislocations, and grain boundaries in the CF that disrupt the alignment of magnetic moments.

The calcination of CF at high temperatures resulted in minimized defects. Together, these factors provide calcined ferrite materials with their improved magnetic characteristics and increased magnetization. The reduction of internal stresses, enhanced crystallinity, reduced structural defects, and composition optimization brought about by the calcination process are responsible for the overall decrease in coercivity seen with calcined CF. The effect of calcination temperature on the dielectric constant (ε) and dielectric loss of CF is shown in Fig. 7 and 8. The Fig. 7 shows the decrease of ε with increasing frequency and it increase with increasing degree of ferrite calcination. The Fig. 7 also shows that the dielectric constant of the PVA/CF600 composite appeared higher than that of the pure PVA, and its value increased more when the degree of calcination of the ferrite increased to 900 °C (PVA/CF900).

Table 2 summarizes the key magnetic parameters derived from the hysteresis loops for all samples. As indicated in the table, the saturation magnetization (M_s) exhibits a clear increase with rising calcination temperature, from 55.3 emu/g for the as-prepared sample (PVA/CFRT) to 81.3 emu/g for the sample treated at 900 °C (PVA/CF900). This enhancement is attributed to the improved crystallinity and growth of the nanoparticles. In contrast, the coercivity (H_c) decreases from 1350 to 860 Oe. This reduction is a typical behavior for ferrite nanoparticles as they grow larger and transition from a single-domain to a multi-domain magnetic structure.

The inhomogeneous microstructure and the superexchange connections are attributed to the dielectric behavior. The ascent and descent of the dielectric constant are significantly influenced by the grain boundaries. Furthermore, it was shown that the grain boundaries are more effective at lower frequencies. The grain effect in dielectric medium prevails at low frequency because the grain boundaries are low conductivity, while

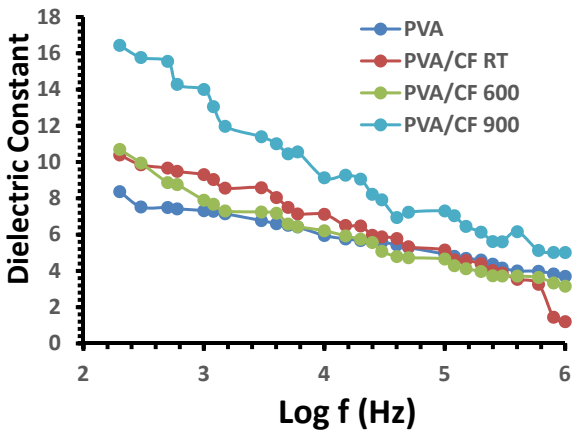

Fig. 7. Dielectric constant of PVA and PVA/CF composites

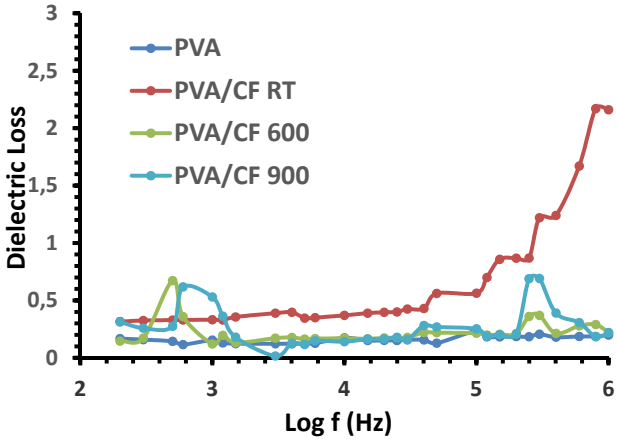

Fig. 8. Dielectric constant of PVA and PVA/CF composites

Table 2. Magnetic parameters of the PVA/$CoFe_2O_4$ nanocomposite samples

Sample	Saturation Magnetization (M_s) (emu/g)	Coercivity (H_c) (Oe)	Remanence (M_r) (emu/g)
PVA/CFRT	55.3	1350	23.4
PVA/CF600	68.7	1150	28.5
PVA/CF900	81.3	860	22.1

the grains are conductive. Because of the charge carriers, polarization becomes much slower in the high-frequency region when an AC field is applied. The reason for this result is that the particle suffers changes from separated single particles to compact nanoparticle granules. As frequency increases, dielectric loss decreases as seen in Fig. 8, where the interface that separates conductive from insulating nature plays a significant role. This is shown by the fact that PVA/CF nanocomposites exhibit a higher dielectric loss than the PVA, which could be attributed to the micro-mechanical stress, and effect of surface depolarization domain wall. The low conductivity and dielectric loss in pure PVA is due to the amorphous nature of the surface, which can be avoided by charge transfer from the ligand to the metal added in the PVA chain, which leads to increased packing density and probabilistic, which supports dielectric behavior.

The observed increase in the dielectric constant of the composite with higher ferrite calcination temperature is a highly desirable property for numerous technological applications. Materials with a high dielectric constant are required for the fabrication of embedded capacitors in electronic devices, as they allow for storing more energy in a smaller volume. They also play a critical role in microwave absorption and electromagnetic interference (EMI) shielding applications, where the material's ability to store electrical energy contributes to the dissipation of unwanted electromagnetic wave energy. The ability to tune the band gap of the composite opens doors for applications in optoelectronics. For instance, a material with a tunable band gap could be used in photosensors or in photocatalysis, where the band gap value determines the wavelength of light the material can efficiently absorb and interact with. The increase in the band gap we observed could enhance the material's stability under high electric fields and reduce leakage currents in electronic devices.

4. Conclusion

The investigation into the magnetic and dielectric properties of cobalt ferrite ($CoFe_2O_4$) nanoparticles embedded in a polyvinyl alcohol (PVA) matrix under varying calcination temperatures has demonstrated the significant influence of thermal treatment on the material's properties. The study showed that increasing calcination temperature from room temperature to 900 °C enhances the crystallinity and magnetic characteristics of the nanocomposite. The crystallite size increased, and structural defects were minimized, leading to improved magnetization and reduced coercivity. Notably, the dielectric constant and loss also exhibited a temperature-dependent enhancement, with higher calcination temperatures contributing to superior material performance. These findings underline the critical role of the calcination process in optimizing the magnetic and dielectric behavior of PVA/$CoFe_2O_4$ composites for potential applications in areas such as energy storage, biomedical imaging, and magnetic sensors. Furthermore, the study highlights the synergistic effect between the polymer matrix and magnetic nanoparticles, offering an insight into the design of advanced nanocomposites with tunable properties. Thus, the research opens avenues for further exploration into the tailoring of magnetic and dielectric properties in nanocomposite systems for specialized applications.

Author contributions

Noor A. Saeed and Mudatheer M. Al-Slivani conceived the study and designed the experiments. Wafaa A. Hussain performed the synthesis and characterization. Mukhlis M. Ismail analyzed the data. All authors wrote and reviewed the manuscript.

References

1. Romero-Fierro D., Bustamante-Torres M., Bravo-Plascencia F., Magaña H., Bucio E. Polymer-magnetic semiconductor nanocomposites for industrial electronic applications. *Polymers*. 2022;14(12): 2467. https://doi.org/10.3390/polym14122467

2. Shivamurthy S., Yashas R., Shahmoradi B., Wantala K., Shivaraju H. P. Potentiality of polymer nanocomposites for sustainable environmental applications: a review of recent advances. *Polymer*. 2021;233: 124184. https://doi.org/10.1016/j.polymer.2021.124184

3. Popova V., Dmitrienko E., Chubarov A. Magnetic nanocomposites and imprinted polymers for biomedical applications of nucleic acids. *Magnetochemistry*. 2023;9(1): 12. https://doi.org/10.3390/magnetochemistry9010012

4. Ziedan W., Hussain W. A., Ismail M. M. Porous adsorbent based on kaolin and nanomagnetic cobalt ferrite for effective removal of Pb(II) from wastewater. *Journal of Superconductivity and Novel Magnetism*. 2024;37: 587–596. https://doi.org/10.1007/s10948-024-06700-1

5. Hussain W. A., Al-Mosawe E. H. A., Ismail M. M., Alwan L. H. Porous biphasic calcium phosphate for biomedical application. *Journal of Biomimetics, Biomaterials and Biomedical Engineering*. 2021;49: 101–110. https://doi.org/10.4028/www.scientific.net/jbbbe.49.101

6. Hashim F. S., Ismail M. M., Hussain W. A. Tri-calcium phosphate (nanoparticles/nanofibers)/PVA for bone tissue engineering. *Acta Physica Polonica A*. 2021;140(4): 337–343. https://doi.org/10.12693/aphyspola.140.337

7. Assim F., Al-Mosawe E. H. A., Hussain W. A. Studying the physical and biological characteristics of denture base resin PMMA reinforced with ZrO_2 and TiO_2 nanoparticles. *Karbala International Journal of Modern Science*. 2022;8(4): 503–513. https://doi.org/10.33640/2405-609x.3268

8. Ismail M. M., Hussain W. A., Hashim F. S. Bio-application of poly (vinyl alcohol)/biphasic calcium phosphate scaffold as bone tissue replacement. *Current Materials Science*. 2022;15(3): 271–279. https://doi.org/10.2174/2666145415666220330110601

9. Taher S. Y., Hussain W. A. The effect of acidic treatment of carbon fiber on denture mechanical properties. *Journal of Physics: Conference Series*. 2021;1879(3): 032082. https://doi.org/10.1088/1742-6596/1879/3/032082

10. Hussain W. A., Ismail M. M., Taher S. Incorporation of treated woven carbon fiber to methacrylate resin for heat-cured acrylic denture composite. *Journal of Biomimetics, Biomaterials and Biomedical Engineering*. 2022;56: 153–164. https://doi.org/10.4028/p-627g18

11. Hussain W. A., Jawad S. M. H. A., Hannon S. A Effect of carbon fibre layer with alumina and tri calcium phosphate on mechanical properties of denture base. *International Journal of Nano and Biomaterials*. 2021;10(1): 22–33. https://doi.org/10.1504/ijnbm.2021.114691

12. Saha M., Mukherjee S., Bera P., Seikh Md. M., Gayen A. Structural, optical, dielectric, and magnetic properties of spinel MFe_2O_4 (M = Co and Zn) nanoparticles synthesized by CTAB-assisted hydrothermal method. Ceramics *International*. 2022;48(23): 35719–35732. https://doi.org/10.1016/j.ceramint.2022.07.058

13. Salih S. J., Mahmood W. M. Review on magnetic spinel ferrite (MFe_2O_4) nanoparticles: from synthesis to application. *Heliyon*. 2023;9(12): e16601. https://doi.org/10.1016/j.heliyon.2023.e16601

14. Ravinder D., Hashim M., Upadhyay A., … Khalilullah A. Structural, elastic and magnetic properties of Co-Mg nanoferrites. *Solid State Communications*. 2022;342: 114629. https://doi.org/10.1016/j.ssc.2021.114629

15. Ismail M. M., Jaber N. A. Structural analysis and magnetic properties of lithium-doped Ni-Zn ferrite nanoparticles. *Journal of Superconductivity and Novel Magnetism*. 2018;31(6): 1917–1923. https://doi.org/10.1007/s10948-017-4428-3

16. Ismail M. M., Jaber N. A. Structural and elastic properties of nickel–zinc ferrite nano-particles doped with lithium. *Journal of the Brazilian Society of Mechanical Sciences and Engineering*. 2018:40(5): 250. https://doi.org/10.1007/s40430-018-1164-y

17. Rafeeq S. N., Ismail M. M., Sulaiman J. M. A. (2017). Magnetic and dielectric properties of $CoFe_2O_4$ and $Co_xZn_{1-x}Fe_2O_4$ nanoparticles synthesized using sol-gel method. *Journal of Magnetics*. 2017;22(3): 406–413. https://doi.org/10.4283/jmag.2017.22.3.406

18. Farzaneh S., Hosseinzadeh S., Samanipour R., Hatamie S., Ranjbari J., Khojasteh A. Fabrication and characterization of cobalt ferrite magnetic hydrogel combined with static magnetic field as a potential bio-composite for bone tissue engineering. *Journal of Drug Delivery Science and Technology*. 2021;64: 102525. https://doi.org/10.1016/j.jddst.2021.102525

19. Basak M., Rahman Md. L., Ahmed Md. F., Biswas B., Sharmin N. Calcination effect on structural, morphological and magnetic properties of nano-sized $CoFe_2O_4$ developed by a simple co-precipitation technique. *Materials Chemistry and Physics*. 2021;264: 124442. https://doi.org/10.1016/j.matchemphys.2021.124442

20. Mahdi S. H., Jassim W. H., Hamad I. A., Jasima K. A. Epoxy/silicone rubber blends for voltage insulators and capacitors applications. *Energy Procedia*. 2017;119: 501–506. https://doi.org/10.1016/j.egypro.2017.07.059

21. Aleabi S. H., Watan A. W., Salman E. M.-T., Jasim K. A., Shaban A. H., AlSaadi T. M. The study effect of weight fraction on thermal and electrical conductivity for unsaturated polyester composite alone and hybrid. *AIP Conference Proceedings*. 2018;1968(1): 020019. https://doi.org/10.1063/1.5039178

22. Hu P., Chang T., Chen W.-J., … Volinsky A. A. Temperature effects on magnetic properties of Fe_3O_4 nanoparticles synthesized by the sol-gel explosion-assisted method. *Journal of Alloys and Compounds*. 2019;773: 605–611. https://doi.org/10.1016/j.jallcom.2018.09.238

23. Purnama B., Wijayanta A. T., Suharyana. Effect of calcination temperature on structural and magnetic properties in cobalt ferrite nano particles. *Journal of King Saud University – Science*. 2019;31(4): 956–960. https://doi.org/10.1016/j.jksus.2018.07.019

24. Akbarzadeh A., Samiei M., Davaran S. Magnetic nanoparticles: preparation, physical properties, and applications in biomedicine. *Nanoscale Research Letters*. 2012;7(1): 144. https://doi.org/10.1186/1556-276x-7-144

25. Hashim M., Ahmed A., Ali S. A., … Ravinder D. Structural, optical, elastic and magnetic properties of Ce and Dy doped cobalt ferrites. *Journal of Alloys and Compounds*. 2020;834: 155089. https://doi.org/10.1016/j.jallcom.2020.155089

26. Hashim M., Boda N., Ahmed A., … Nasir M. Influence of samarium doping on structural, elastic, magnetic, dielectric, and electrical properties of nanocrystalline cobalt ferrite. *Applied Physics A*. 2021;127(7): 526. https://doi.org/10.1007/s00339-021-04686-4

27. Ismail M. M., Jaber N. A. Effect of Li doping on the microstructure and some physical properties of Ni-Zn ferrite nanoparticles. *Surface Review and Letters*. 2018;25(03): 1850076. https://doi.org/10.1142/s0218625x18500762

28. Salman O. N., Agool I. R., Ismail M. M. Preparation of the scattering layer based on TiO_2 nanotube and their dye sensitized solar cell applications. *Applied Physics A*. 2017;123(6). https://doi.org/10.1007/s00339-017-1012-4

29. Ismail M. M., Shaker S. S., Kamil R. A. Influence of pulse laser energy on structural and magnetic properties of $CoFe_2O_4$ and $CoLa_{0.01}Fe_{1.99}O_4$ thin films. *ECS Journal of Solid State Science and Technology*. 2023;12(3): 033005. https://doi.org/10.1149/2162-8777/acc136

30. Al-Slivani M. M., Hammod M. A., Abed M. A. Partial substitution effect of silver on the structural and electrical

properties of high temperature superconductor ($Bi_{2-x}Ag$–$Ba_2Ca_2Cu_3O_{10+\delta}$). *Ochrona Przed Korozja*. 2025;68(1): 15–20. https://doi.org/10.15199/40.2025.3.2

31. Al-Slivani M. M., Hammod M. A., Abed M. A. Double partial substitution effect of silver (Ag) and strontium (Sr) on the structural and electrical properties of high temperature $Bi_{2-x}Ag_xBa_{2-y}Sr_yCa_2Cu_3O_{10+\delta}$ superconductor. *Functional Materials*. 2025;32(1): 42–49. https://doi.org/10.15407/fm32.01.42

32. Priyadharsini P., Pradeep A., Chandrasekaran G. Novel combustion route of synthesis and characterization of nanocrystalline mixed ferrites of Ni–Zn. *Journal of Magnetism and Magnetic Materials*. 2009;321(12): 1898–1903. https://doi.org/10.1016/j.jmmm.2008.12.005

33. To Loan N. T., Hien Lan N. T., Thuy Hang N. T., … Van Tran T. $CoFe_2O_4$ nanomaterials: effect of annealing temperature on characterization, magnetic, photocatalytic, and photo-fenton properties. *Processes*. 2019;7(12): 885. https://doi.org/10.3390/pr7120885

34. Guirguis O. W., Moselhey M. T. H. Optical study of poly(vinyl alcohol)/hydroxypropyl methylcellulose blends. *Journal of Materials Science*. 2011;46(17): 5775–5789. https://doi.org/10.1007/s10853-011-5533-5

35. Rashidi S., Ataie A. Structural and magnetic characteristics of PVA/$CoFe_2O_4$ nano-composites prepared via mechanical alloying method. *Materials Research Bulletin*. 2016;80: 321–328. https://doi.org/10.1016/j.materresbull.2016.04.021

36. García-Cerda L. A., Escareño-Castro M. U., Salazar-Zertuche M. Preparation and characterization of polyvinyl alcohol–cobalt ferrite nanocomposites. *Journal of Non-Crystalline Solids*. 2007;353(8–10): 808–810. https://doi.org/10.1016/j.jnoncrysol.2006.12.046

Information about the authors

Noor A. Saeed, M.Sc., Assistant Lecturer, Researcher, Department of Applied Physics, College of Applied Science, University of Technology (Baghdad, Iraq).
https://orcid.org/0009-0001-0488-7230
as.22.57@grad.uotechnology.edu.iq

Wafaa A. Hussain, PhD, Professor, Department of Applied Physics, College of Applied Science, University of Technology (Baghdad, Iraq).
https://orcid.org/0000-0002-0994-9381
100067@uotechnology.edu.iq

Mukhlis M. Ismail, PhD, Professor, Department of Applied Physics, College of Applied Science, University of Technology (Baghdad, Iraq).
https://orcid.org/0000-0002-7834-4191
mmismail009@gmail.com

Mudatheer M. Al-Slivani, M.Sc., Assistant Lecturer, Department of Physics, College of Education for Pure Sciences, Al-Furqan University (Mosul, Iraq).
https://orcid.org/0009-0004-5231-7461
mudatheeralslivani@gmail.com

Received September 2, 2025; approved after reviewing December 4, 2025; accepted for publication January 15, 2026; published online April 01, 2026.

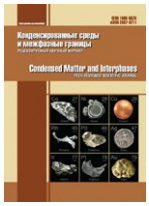

ISSN 1606-867X (Print)
ISSN 2687-0711 (Online)
Condensed Matter and Interphases
Kondensirovannye Sredy i Mezhfaznye Granitsy
https://journals.vsu.ru/kcmf/

Original articles

Research article
https://doi.org/10.17308/kcmf.2026.28/13555

On the formation of the Ag_2Si metastable phase in an Ag-Si film obtained by ion-beam sputtering

K. A. Barkov[1]✉, V. V. Babakov[1], G. P. Potudansky[1], S. A. Ivkov[1], Ya. A. Peshkov[1], I. V. Polshin[1], E. S. Kersnovsky[1], S. Y. Khydyrova[2], K. M. Moiseev[2], I. E. Zanin[1], A. K. Pelagina[1], N. S. Buylov[1], Tran Van Tu[3], A. E. Nikonov[4], A. V. Sitnikov[4]

[1]*Voronezh State University,*
1 Universitetskaya pl., Voronezh 394018, Russian Federation

[2]*Bauman Moscow State Technical University,*
2nd Baumanskaya st., 5, p. 1, Moscow 105005, Russian Federation

[3]*University of Medicine and Pharmacy at Ho Chi Minh city,*
217 Hong Bang Street, Wars 11, District 5, HCMC, Viet Nam

[4]*Voronezh State Technical University,*
84 20 let Oktyabrya st., Voronezh 394006, Russian Federation

Abstract

Objectives: Nanocomposite films based on Ag-Si compounds have application in many areas of science and technology. However, their manufacturing process can be accompanied by the formation of silicides and metastable phases. In this connection, the task of developing methods for their identification arises. In this work, we attempted to solve this task using X-ray diffraction, ultra-soft X-ray emission spectroscopy, and theoretical calculations of the electron density of states for an $Ag_{55}Si_{45}$ film obtained by ion-beam sputtering of a composite target.

Experimental: As a result of comprehensive studies, a nanogranular structure of the film was revealed, with an average silver particle size of ~15 nm, separated by a matrix based on phases of amorphous silicon *a*-Si, SiO_2, and suboxide $SiO_{1.3}$, as well as a silver silicide phase. A comparison of the experimental Si $L_{2,3}$ X-ray emission spectrum of the $Ag_{55}Si_{45}$ film with theoretically calculated spectra of the $AgSi_3$, Ag_2Si, and Ag_3Si phases shows the best agreement with the spectrum of the Ag_2Si phase. Moreover, the Ag_2Si phase was detected in the works of other authors.

Conclusions: Thus, based on X-ray diffraction, X-ray emission spectroscopy, and theoretical calculations of the electronic density of states, it has been established that a metastable Ag_2Si phase is formed in the $Ag_{55}Si_{45}$ film produced by ion-beam sputtering.

Keywords: Metastable Ag-Si-based phases, $AgSi_3$, Ag_2Si, Ag_3Si, silver silicides, ion-beam sputtering, Ultra-soft X-ray emission spectroscopy (USXES), Electronic density of states (DOS)

Funding: This work was funded by the Russian Science Foundation, under grant number 23-79-10294, https://rscf.ru/project/23-79-10294/

Acknowledgments: The research results were partially obtained using the equipment of the Voronezh State University's Center for Collective Use. URL: http://ckp.vsu.ru

For citation: Barkov K. A., Babakov V. V., Potudansky G. P., Ivkov S. A., Peshkov Ya. A., Polshin I. V., Kersnovsky E. S., Khydyrova S. Y., Moiseev K. M., Zanin I. E., Pelagina A. K., Buylov N. S., Tran Van Tu, Nikonov A. E., Sitnikov A. V On the formation of the Ag_2Si metastable phase in an Ag-Si film obtained by ion-beam sputtering. *Condensed Matter and Interphases*. 2026;(1): 15–27. https://doi.org/10.17308/kcmf.2026.28/13555

✉ Konstantin A. Barkov, e-mail: barkov@phys.vsu.ru

Для цитирования: Барков К. А., Бабаков В. В., Потуданский Г. П., Ивков С. А., Пешков Я. А., Польшин И. В., Керсновский Е. С., Хыдырова С. Ю., Моисеев К. М., Занин И. Е., Пелагина А. К., Буйлов Н. С., Tran Van Tu, Никонов А. Е., Ситников А. В. О формировании метастабильной фазы Ag_2Si в пленке Ag-Si, полученной ионно-лучевым распылением. *Конденсированные среды и межфазные границы*. 2026;(1): 15–27. https://doi.org/10.17308/kcmf.2026.28/13555

Introduction

Ag-Si nanocomposite films are currently used in the fabrication of SERS substrates (Surface-enhanced Raman spectroscopy) [1–6], plasmonic reflectors [7, 8], anodes for lithium-ion batteries [9, 10], memristor structures [11–21], as well as electrical synapses for neuromorphic systems [22–24]. At the same time, the phase diagram of the Ag-Si system is of the eutectic type, which should lead to the formation of silver and silicon particles [25]. However, during the formation of nanostructured *Me*-Si films by methods characterized by the high energy of sputtered particles, the formation of metastable compounds [26, 27] and solid solutions, such as Ag_2Si [28–30], is possible. Furthermore, databases also contain information about theoretically calculated phases of silver silicide $AgSi_3$ and Ag_5Si [31, 32], as well as data on the formation of compounds with an unknown crystal structure in works [33, 34]. Based on this, it becomes necessary to investigate the possibility of forming metastable phases of silver silicides in Ag-Si films. Therefore, this work employs the method of ultra-soft X-ray emission spectroscopy to identify the phases of silver silicide in an $Ag_{55}Si_{45}$ film obtained by ion-beam sputtering.

2. Methods

2.1. Method of obtaining Ag-Si film by ion-beam sputtering

An $Ag_{55}Si_{45}$ film with a thickness of about 1 μm was deposited on a Si (100) substrate of KDB-12 grade by ion-beam sputtering of a composite target made of pure Ag (99.99 %) and silicon pieces of Si (KDB-12). To form a film with the required atomic composition – $Ag_{55}Si_{45}$, silicon pieces 10 mm wide were placed on the surface of a silver plate with an 18 mm gap. Deposition was carried out in a vacuum chamber (residual pressure 10^{-6} Torr). The methodology for obtaining Ag-Si films by ion-beam sputtering is described in more detail in our previous work [35].

2.2. Research methods for structure and phase composition

The elemental composition of the film was determined by energy-dispersive spectroscopy (EDS) on a JEOL JSM-6380LV scanning electron microscope (SEM) equipped with an INCA Energy 250 microanalysis system at a primary electron energy of 5 keV. This energy value was chosen to perform elemental analysis exclusively within the film volume. SEM imaging was performed at an accelerating voltage of 20 kV.

An analysis of the formation of crystalline phases in the $Ag_{55}Si_{45}$ sample was carried out by X-ray diffraction on a PANalytical Empyrean B.V. diffractometer with Cu$K\alpha_{1,2}$ radiation $\lambda = 1.542$ Å.

The phase composition of the $Ag_{55}Si_{45}$ film was determined using a unique technique of ultra-soft X-ray emission spectroscopy (USXES), implemented on an RSM-500 spectrometer. The USXES method provides information on the distribution of Si 3*s* states in the valence band based on the Si $L_{2,3}$ X-ray emission spectrum [36, 37]. As a result of the simulation of the experimental spectra, the USXES method allows for the identification of the presence of crystalline and amorphous silicon phases, as well as silicides and silicon oxides in the surface layers from 10 to 120 nm [38].

2.3. The method for calculating the electron density of states in the valence band

The calculations of the electron density of states and the Si $L_{2,3}$ X-ray emission spectra for the $AgSi_3$, Ag_2Si, and Ag_3Si phases were carried out within the framework of density functional theory using the linearized augmented plane wave (LAPW) method. In this work, the calculations were performed using the PBE-GGA generalized gradient approximation for the exchange-correlation energy in the Wien2k software package [39]. The crystal potential was constructed as a full potential, accounting for anisotropy, which allows the LAPW method to calculate compounds with directional covalent bonds, such as silicon-based compounds.

3. Results and discussion

3.1. Analysis of the elemental and phase composition of the Ag-Si film

Analysis of the elemental composition of the $Ag_{55}Si_{45}$ film by energy-dispersive spectroscopy confirms the Ag:Si = 55:45 ratio. As a result of ion-beam sputtering of a composite target based on Ag and Si under the specified conditions, the formed surface of the $Ag_{55}Si_{45}$ film has a continuous and homogeneous structure with uniform graininess and a characteristic grain size of 50–200 nm, as seen on the SEM image of the surface in Fig. 1a. The film thickness is ~0.8 μm (Fig. 1b). The nanogranular structure of the pure silver film is explained by the specifics of the ion-beam sputtering technology, during which nanoclusters of the target material several nanometers in size are predominantly sputtered from the target; these nanoclusters possess sufficiently high energy upon reaching the substrate and can form metastable phases. Therefore, X-ray structural and X-ray spectral studies were conducted to analyze the presence of metastable compounds in the formed $Ag_{55}Si_{45}$ film.

Fig. 2a shows the X-ray diffraction patterns of the ion-beam $Ag_{55}Si_{45}$ film, pure Ag, polycrystalline silicon (poly-Si), and the silver silicide phases $AgSi_3$, Ag_2Si, and Ag_3Si. The diffraction patterns of the $AgSi_3$, Ag_2Si, and Ag_3Si phases were theoretically calculated using the Vesta program [40], based on the unit cells published in the Springer Materials [41] and Materials Explorer [31, 32] databases. The X-ray diffraction pattern of the $Ag_{55}Si_{45}$ film shows diffraction peaks at 2θ = 37.98° and 64.35°, corresponding to the interplanar spacings d = 2.367 and 1.448 Å. These reflections are associated with the Ag (111) and Ag (220) crystallographic planes, respectively [ICDD (International Centre for Diffraction Data), PDF-2 Database, Card No. 00-004-0783]. The Ag diffraction peaks in the $Ag_{55}Si_{45}$ film are significantly broadened (FWHM Ag (111) = 0.66 2θ deg.) compared to the corresponding peaks in the pure silver reference (FWHM Ag (111) = 0.12 2θ deg.), indicating a small silver crystallite size, which, according to the Debye-Scherrer method [42], is ~15 nm. However, in the angular region of 39–40°, the Ag (111) reflection has a shoulder. Moreover, the decomposition of the Ag (111) reflection into the Cu$K\alpha_1$,α_2 doublet lines by Lorentz functions indeed reveals an additional reflection with an interplanar spacing of 2.314 Å (top inset in Fig. 2). The most intense reflections from the $AgSi_3$, Ag_2Si, and Ag_3Si phase diffractograms are located in this angular region (Fig. 2). Furthermore, the Ag (200) reflection in the $Ag_{55}Si_{45}$ film is broadened more strongly compared to the Ag (111) and Ag (220) reflections, which is clearly seen from the $\beta \times \cos\theta$ vs. $\sin\theta$ dependence (bottom inset in Fig. 2) constructed using the Williamson-Hall method [43]. (The diffractogram of the $Ag_{55}Si_{45}$ sample, recorded over a larger angular range, is shown in Fig. S1 in the supplementary materials file). The large half-width of the Ag (200) reflection in the $Ag_{55}Si_{45}$ film may be due to the contribution of reflections from the $AgSi_3$

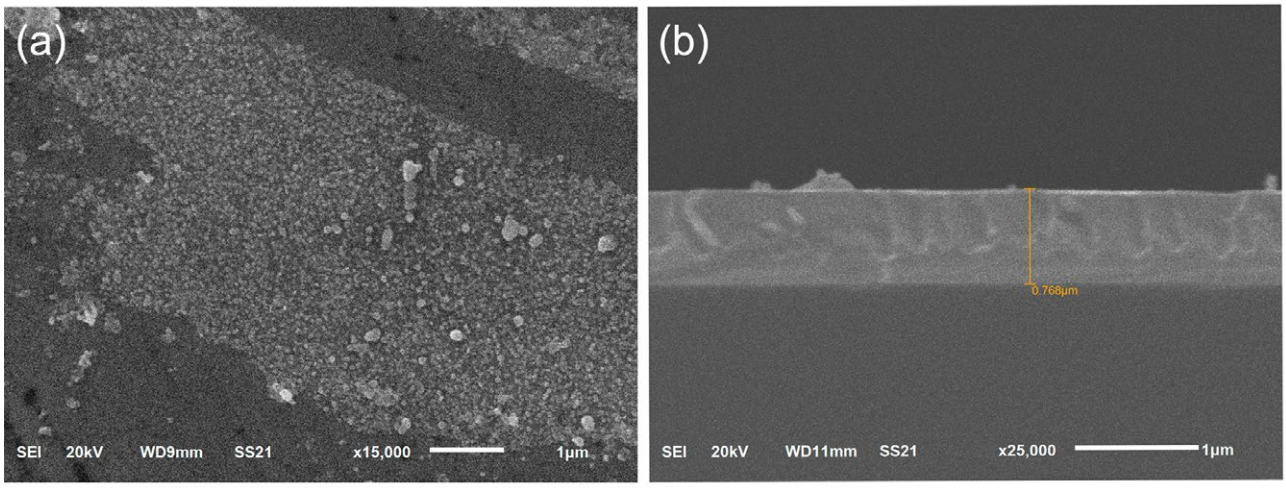

Fig. 1. SEM micrographs of the surface (a) and fracture (b) of the $Ag_{55}Si_{45}$ ion-beam deposited film

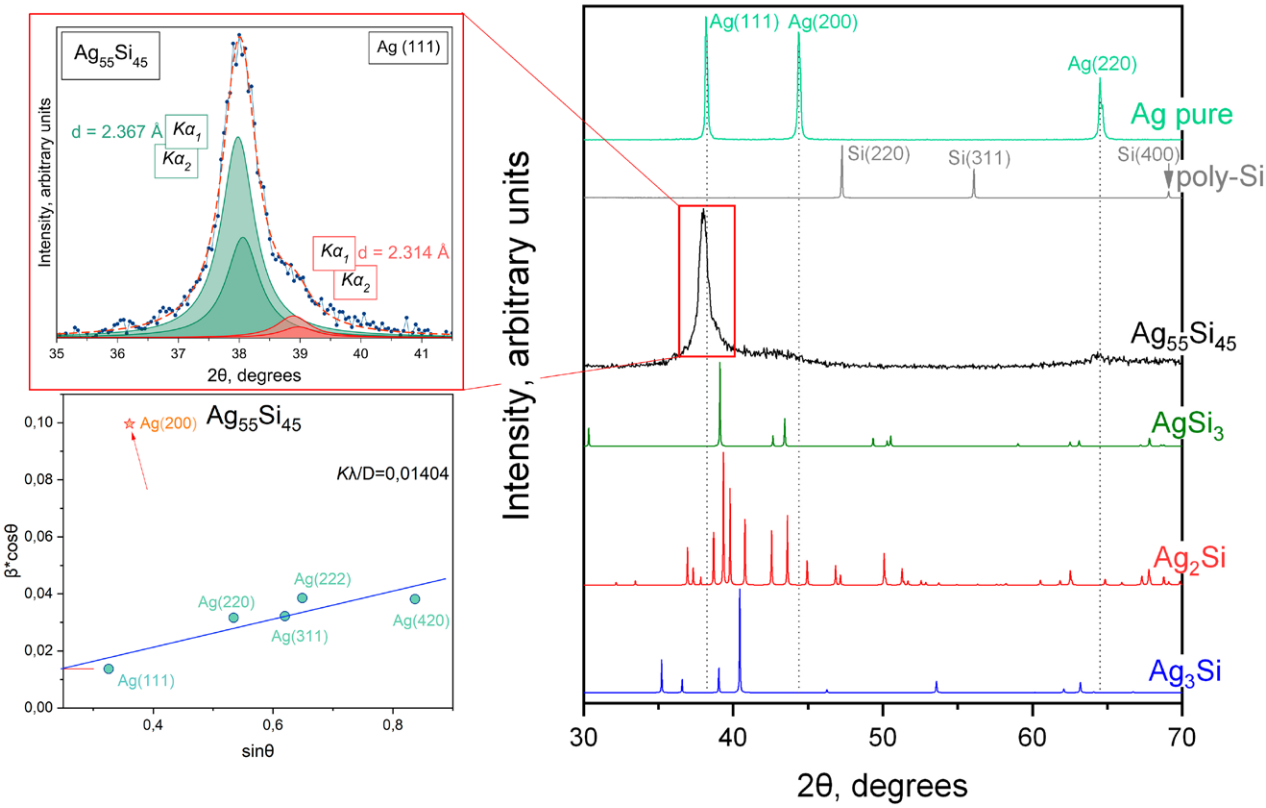

Fig. 2. X-ray diffractograms of the $Ag_{55}Si_{45}$ film, reference standards of pure silver (Ag) and polycrystalline silicon (poly-Si), as well as silver silicides $AgSi_3$, Ag_2Si, and Ag_3Si [31, 41, 32]. The top inset shows the X-ray diffractogram in the region of the Ag (111) reflection. The bottom inset presents the calculation of crystallite size and lattice microstrain using the Williamson–Hall method

and Ag_2Si phases located in the angular region of 43–44°. Moreover, for the $Ag_{55}Si_{45}$ sample, the Williamson-Hall method, based on the universal deformation model (UDM) [43], reveals the presence of a microstrain of the crystal lattice of ~ 1.2 %, while the size of the Ag nanocrystals is ~ 11 nm, which is in good agreement with the Debye–Scherrer method.

The combination of such factors as the overestimated value of the full width at half maximum for the Ag (200) reflex, as well as the asymmetry of the Ag (111) diffraction reflex, with the detection of an additional reflex with an interplanar spacing value of 2.314 Å, may indicate the formation of $AgSi_3$, Ag_2Si, and Ag_3Si phases in the $Ag_{55}Si_{45}$ film, whose most intense reflexes are located in the region of the considered Ag (111) and Ag (200) reflexes (Fig. 2). However, according to X-ray diffraction data, it is almost impossible to attribute the noted features to any specific silver silicide phase ($AgSi_3$, Ag_2Si, or Ag_3Si). Therefore, for the unambiguous identification of the silver silicide phase formed in the $Ag_{55}Si_{45}$ film, X-ray emission Si $L_{2,3}$-spectra will be obtained. However, due to the lack of published X-ray emission Si $L_{2,3}$-spectra for the $AgSi_3$, Ag_2Si, and Ag_3Si phases, theoretical calculations of the electronic density of states and X-ray spectra will be performed.

3.2. Calculation of the electron density of states in the valence band of metastable compounds $AgSi_3$, Ag_2Si, and Ag_3Si

To calculate the electronic density of states (DOS) for the $AgSi_3$ phase, a tetragonal unit cell (Fig. 3a) with the space group symmetry (*I4/mmm*, 139) and lattice parameters $a = b = 4.16$ Å, $c = 7.38$ Å, $\alpha = \beta = \gamma = 90°$ was used. The structural data and atomic coordinates (Table TS1) for the $AgSi_3$ phase (*I4/mmm*, 139) were taken from the Materials Explorer database [31]. In $AgSi_3$, silver atoms are located at the vertices of the tetragonal unit cell, and silicon atoms occupy

two nonequivalent positions, $Si^{(1)}$ and $Si^{(2)}$, with different distances to the nearest silver atom of 2.78 and 2.94 Å, respectively. The DOS of the $AgSi_3$ phase is mainly determined by the density of silver *d*-states, which are highly localized and have a maximum at ~ 5.5 eV below E_F, as well as by the silicon *s*- and *p*-states (Fig. 3b). The DOS of the silicon atoms $Si^{(1)}$ and $Si^{(2)}$ in $AgSi_3$ is almost identical (Fig. 3c, e), with the highest density of *s*-states concentrated in the region of 6–13 eV below E_F, and *p*-states in the region of 0–6 eV below E_F with a maximum at -6 eV. Such a DOS is characteristic of higher transition metal silicides [44-46]. The difference in the partial DOS of the *s*- and *p*-states of the $Si^{(1)}$ and $Si^{(2)}$ atoms (Fig. 3d) is due to the difference in the local atomic environment. Fig. 3f shows the X-ray emission spectrum of the $AgSi_3$ phase calculated by us, which was compared with the obtained experimental spectrum of the $Ag_{55}Si_{45}$ film.

The orthorhombic unit cell (Fig. 4a) with the space group (*Cmcm*, 63) and lattice parameters $a = 5.56$ Å, $b = 9.16$ Å, $c = 8.49$ Å, $\alpha = \beta = \gamma = 90°$ was used for the calculation of the DOS for the Ag_2Si

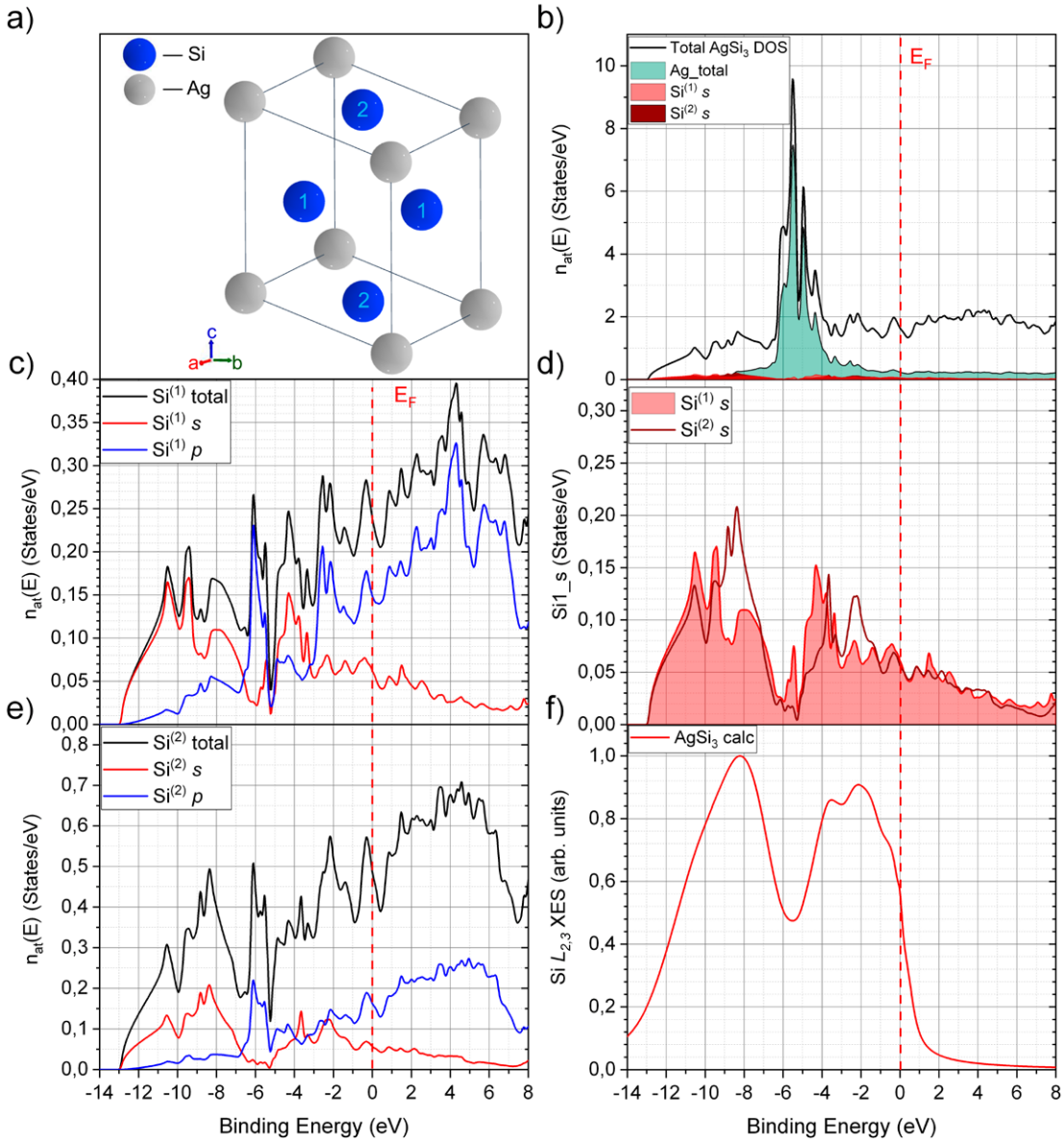

Fig. 3. Unit cell (a), partial and total densities of states for $Si^{(n)}$ atoms (c, d, e). Total DOS for Ag and $AgSi_3$, as well as s-states for $Si^{(n)}$ atoms (b). Calculated X-ray emission Si $L_{2,3}$-spectrum of the $AgSi_3$ phase (*I4/mmm*, 139) (f)

phase. The structural data and atomic coordinates (Table TS2) for the Ag_2Si phase (*Cmcm*, 63) were taken from the Springer Materials database [41]. In this unit cell, Ag atoms occupy three non-equivalent positions: $Ag^{(1)}$ and $Ag^{(3)}$ atoms are located the farthest from the silicon atoms (3.09 and 3.06 Å, respectively); $Ag^{(2)}$ atoms are located the closest to the Si atoms at a distance of 3.01 Å. The total and partial DOS were calculated for each $Ag^{(n)}$ atom in the Ag_2Si compound (Fig. 4b, d, f). The DOS of each $Ag^{(n)}$ atom is mainly formed by *d*-states and contains four maxima: *A* (*E* ~ -2.8 eV), *B* (*E* ~ -3.5 eV), *C* (*E* ~ - 4.5 eV) and *D* (*E* ~ -5.7 eV). At the same time, for all $Ag^{(n)}$ atoms, a deviation in the intensity ratio and a shift of ~ 1 eV towards low *E* values of the DOS maxima are observed compared to bulk FCC Ag (Fig. S2). These changes in the DOS of the $Ag^{(n)}$ atoms result from hybridization with each other (for example, in the case of $Ag^{(3)}$ atoms, mainly with $Ag^{(2)}$ atoms), as well as with silicon atoms, as can be seen from the DOS of the $Ag^{(2)}$ atoms, where peak *B* becomes the main one due to the hybridization of Ag *d* and Si *s*-states (Fig. 4d). The result of this hybridization is noticeably reflected in the partial DOS of Si *s*-states, where an intense peak appears

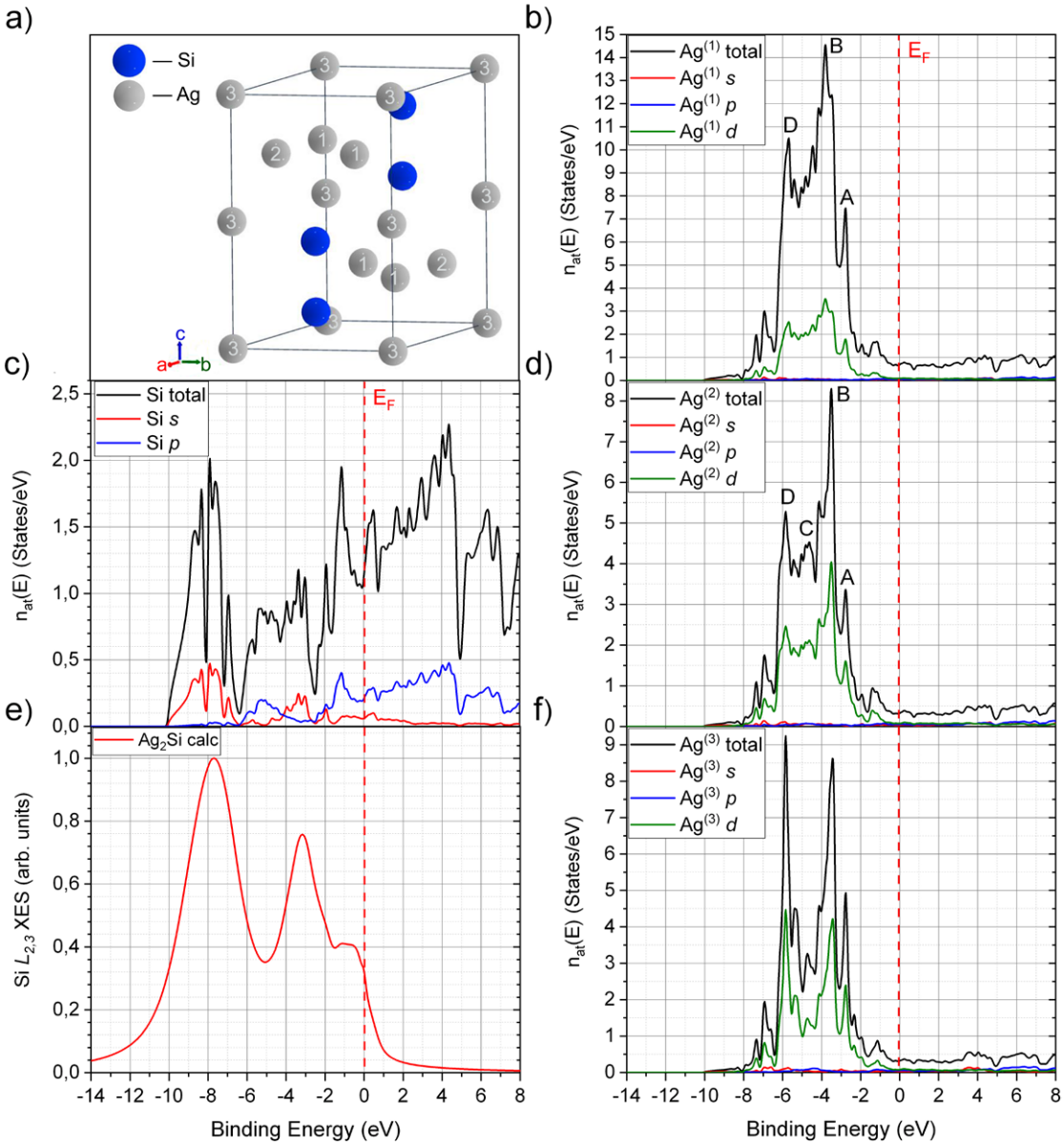

Fig. 4. Unit cell (a), partial and total DOS for $Ag^{(n)}$ atoms (b, d, f), Si atoms (c), and the calculated X-ray emission Si $L_{2,3}$-spectrum of the Ag_2Si phase (*Cmcm*, 63) (e)

at -3 eV (Fig. 4c). The presence of this peak is also observed in the calculated X-ray Si $L_{2,3}$ emission spectrum of the Ag_2Si phase (Fig. 4f).

For the calculation of the DOS for the Ag_3Si phase, a hexagonal unit cell (Fig. 5a) with the space group symmetry (*P*-6*m*2, 187) and lattice parameters $a = b = 2.94$ Å, $c = 9.22$ Å, $\alpha = \beta = 90°$, $\gamma = 120°$ was used. The structural data and atomic coordinates (Table TS3) for the Ag_3Si phase (*P*-6*m*2, 187) were taken from the Materials Explorer database [32]. In the unit cell of the Ag_3Si phase, silver atoms occupy two non-equivalent positions, $Ag^{(1)}$ and $Ag^{(2)}$ (Fig. 5a). The DOS of both $Ag^{(1)}$ and $Ag^{(2)}$ atoms is localized in the region of 2–8 eV below E_F (Fig. 5c, e) and defines the total density of states of the Ag_3Si phase. However, due to the close proximity of $Ag^{(1)}$ atoms to silicon atoms (2.77 Å), their partial DOS differs most significantly from that of bulk silver with an FCC structure (Fig. 5c and Fig. S2) and has a main maximum at -3 eV. At the same time, the $Ag^{(2)}$ atoms in the Ag_3Si phase are located in the same layer and are surrounded by silver atoms, which results in a DOS character close to that of

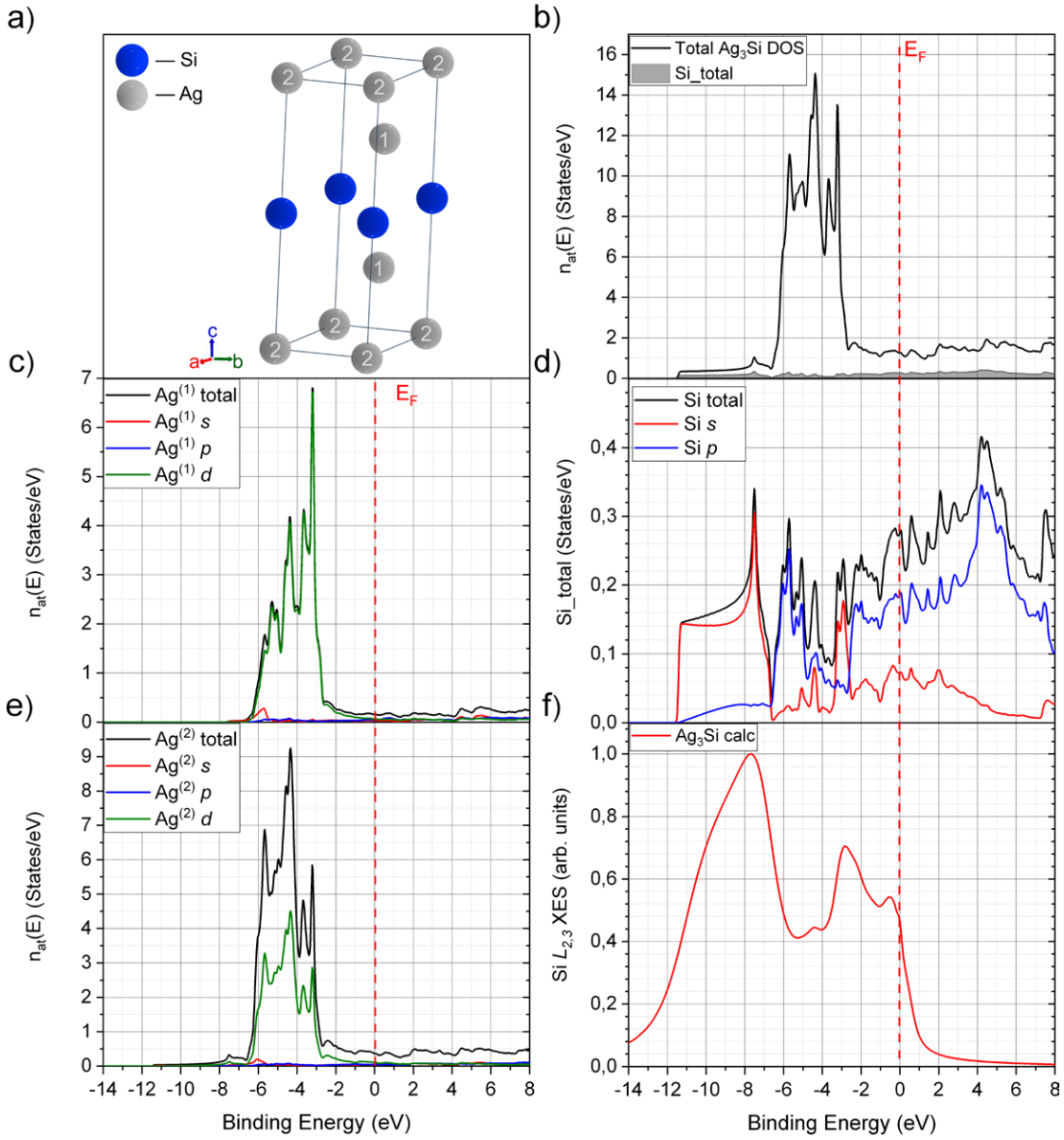

Fig. 5. Unit cell (a), partial and total DOS for $Ag^{(n)}$ atoms (c, e) and Si atoms (d). Total density of states for Ag_3Si and Si (b), calculated X-ray emission Si $L_{2,3}$-spectrum of the Ag_3Si phase (*P*-6*m*2, 187) (f)

bulk Ag (Fig. 5e). The Si *3p* DOS is concentrated in the region from 0 to –8 eV and has a maximum at -6 eV (Fig. 5d). The density of *s*-states of Si atoms in Ag_3Si is mostly concentrated in the range of 6–12 eV below E_F with a maximum at ~ -7.5 eV (Fig. 5d). Furthermore, the *s*-states have an additional maximum at ~ –3–3.5 eV, caused by hybridization with *d*-states, which is clearly manifested in the calculated X-ray Si $L_{2,3}$ emission spectrum (Fig. 5f).

Thus, using the linearized augmented plane wave method, the Si $L_{2,3}$ X-ray emission spectra for the $AgSi_3$, Ag_2Si and Ag_3Si phases were theoretically calculated, reflecting the partial density of electronic *s*-states. The spectra of all silver silicides have two distinct intensity maxima at ~ 7–8 eV (the main maximum) and at ~ 2–3 eV below E_F. The presence of the low-energy maximum is due to the result of hybridization of Si *s* and Ag *d*-states. To compare the calculated Si $L_{2,3}$ X-ray emission spectra with the experimental ones obtained by the USXES method, their energy scales were aligned taking into account the Si *2p* level binding energy of 99.9 eV [47].

3.3. Identification of silver silicides in Ag-Si film by USXES

Fig. 6a presents the ultrasoft X-ray emission Si $L_{2,3}$-spectra of the $Ag_{55}Si_{45}$ film obtained at an analysis depth of 60 nm (black dots). To identify the formation of the silver silicide phase in the $Ag_{55}Si_{45}$ film, computer simulation of the X-ray emission Si $L_{2,3}$-spectrum was performed based on reference spectra. The theoretically calculated spectra of silver silicides $AgSi_3$, Ag_2Si, and Ag_3Si, as well as the spectra of amorphous silicon *a*-Si, dioxide SiO_2, and suboxide $SiO_{1.3}$ of silicon (Fig. 6b) were used as reference spectra, the presence of which in Ag-Si films is possible according to previous studies [35]. The simulation of the X-ray emission Si $L_{2,3}$-spectrum of the $Ag_{55}Si_{45}$ film was performed three times, using only one spectrum of silver silicide $AgSi_3$, Ag_2Si, or Ag_3Si, as well as the spectra of the *a*-Si, SiO_2 and $SiO_{1.3}$ phases in the ratio that best describes the experimental spectrum according to the method [38]. Simulated spectra obtained using the $AgSi_3$, Ag_2Si, and Ag_3Si standards are presented in Fig. 6a as green, red, and blue lines, respectively, and the simulation

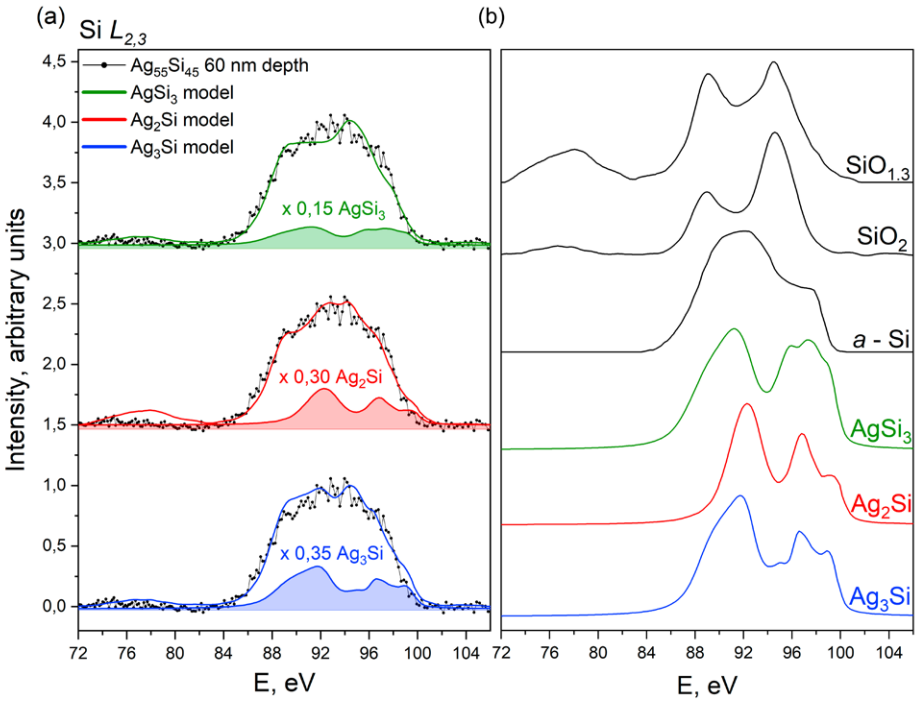

Fig. 6. X-ray emission Si $L_{2,3}$-spectra of the $Ag_{55}Si_{45}$ film obtained at an analysis depth of 60 nm, as well as spectra obtained through computer modeling (a). Spectra of reference standards: silicon suboxide ($SiO_{1.3}$), silicon dioxide (SiO_2), amorphous silicon (*a*-Si), and theoretically calculated spectra of silver silicides ($AgSi_3$, Ag_2Si, and Ag_3Si). The experimental spectrum is represented by dots, the model – by solid lines of various colors (b)

results are given in Table 1. It can be seen from Fig. 6a that the simulation using the $AgSi_3$ spectrum (green curve) fails to describe the experimental spectrum of the $Ag_{55}Si_{45}$ film in the region of the main maximum (89–93 eV), as well as near the top of the valence band (96–98 eV). At the same time, this simulation variant reveals about 15 % of the $AgSi_3$ phase in the $Ag_{55}Si_{45}$ film (Table 1). At the same time, the simulated spectrum using the Ag_2Si standard allows to describe all the features of the experimental spectrum (Fig. 6a, red curve) and reveals about 30 % of the Ag_2Si phase in the $Ag_{55}Si_{45}$ film (Table 1). Using the reference spectrum of the Ag_3Si phase for simulation also reveals a fairly high content of this silver silicide (35 %); however, the simulated spectrum has a higher intensity in the region of 89–92 eV relative to the experimental one, which does not allow this model to be considered reliable (Fig. 6a, blue curve). Thus, based on the modeling results of the Si $L_{2,3}$ X-ray emission spectrum of the $Ag_{55}Si_{45}$ film, it was found that the best agreement between the simulated spectrum and the experiment is achieved when using the reference spectrum of Ag_2Si. However, due to the presence of statistical intensity fluctuations characteristic of a limited signal acquisition time, as well as the inclusion of multiple components in the model, for clarity, a comparison of the spectral feature positions of the reference spectra $AgSi_3$, Ag_2Si, and Ag_3Si with the difference spectra of the $Ag_{55}Si_{45}$ film (Fig. 7) was performed. The difference spectra of the $Ag_{55}Si_{45}$ film (Fig. 7, black dots) were obtained by subtracting the SiO_2, $SiO_{1.3}$, and *a*-Si components from the experimental spectrum in the proportion indicated in Table 1. It can be

Table 1. Phase composition of the $Ag_{55}Si_{45}$ film based on the modeling of the X-ray emission Si $L_{2,3}$-spectrum using three different silver silicide references: $AgSi_3$, Ag_2Si, and Ag_3Si

The silver silicide spectrum used in the model	Phase composition					
	SiO_2, %	$SiO_{1.3}$, %	*a*-Si, %	$AgSi_3$, %	Ag_2Si, %	Ag_3Si, %
$AgSi_3$	45	5	35	15	–	–
Ag_2Si	20	30	20	–	30	–
Ag_3Si	40	5	20	–	–	35

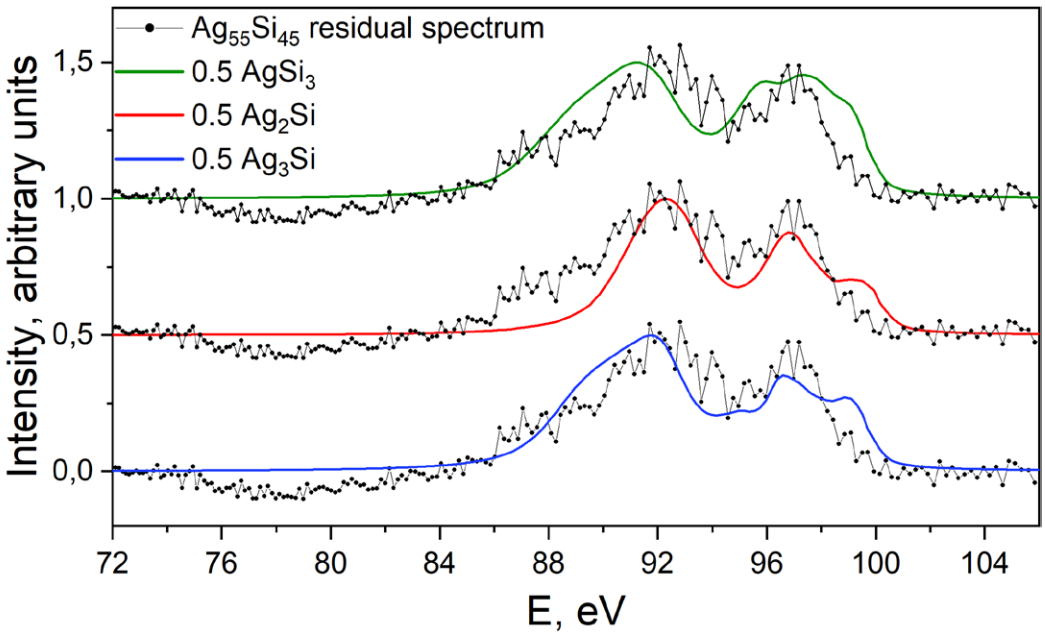

Fig. 7. Residual spectra of the $Ag_{55}Si_{45}$ film after subtraction of the *a*-Si, $SiO_{1.3}$, and SiO_2 components, as well as the spectra of silver silicides $AgSi_3$ (green line), Ag_2Si (red line), and Ag_3Si (blue line). The experimental spectrum is represented by dots

seen from Fig. 7 that the difference spectra of the $Ag_{55}Si_{45}$ film have two intensity maxima at ~ 92 and 97 eV. The spectra of all silicides also reveal the presence of two intensity maxima in the given energy regions. However, the high-energy maximum of the $AgSi_3$ phase is strongly broadened compared to the difference spectrum and has a high density of states near the top of the valence band, which is characteristic of higher silicides [48]. In turn, the spectrum of the Ag_2Si phase demonstrates similarity in the position and width of the intensity maxima to the difference spectrum (Fig. 7). The spectrum of the Ag_3Si phase also shows agreement in the position with the main and additional maxima of the difference spectrum of the $Ag_{55}Si_{45}$ film, and the main difference lies in the high intensity near the top of the VB. Differences in the intensity of the Si $L_{2,3}$ spectra near VB indicate the absence of the Ag_3Si phase in the studied sample.

Thus, due to the best agreement between the experimental Si $L_{2,3}$ X-ray emission spectrum of the $Ag_{55}Si_{45}$ film and the reference spectrum of the Ag_2Si phase, the formation of this metastable phase in the Ag-Si film during ion-beam sputtering of a composite target has been established. It should be noted, however, that the possibility of forming other silicides in Ag-Si films cannot be completely ruled out, although their detection is a challenging task.

4. Conclusions

As a result of X-ray diffraction studies of the $Ag_{55}Si_{45}$ film, obtained by ion-beam sputtering of a composite Ag-Si target, it was found that the film consists of silver nanoparticles with an average size of ~ 15 nm, as well as a solid solution based on Ag-Si, as evidenced by an additional reflex on the diffractogram in the angular range where the main maxima of the $AgSi_3$, Ag_2Si, and Ag_3Si phases are located. However, according to X-ray diffraction data, it is almost impossible to unambiguously identify the phase of silver silicide formed in the film.

At the same time, the analysis of X-ray emission Si $L_{2,3}$-spectra shows that the $Ag_{55}Si_{45}$ film is a complex composite material and contains phases of amorphous silicon *a*-Si, SiO_2, suboxide $SiO_{1.3}$, as well as a significant presence (~ 30 % of the total number of silicon atoms) of the silver silicide phase. Comparison of the experimental X-ray emission Si $L_{2,3}$-spectrum of the $Ag_{55}Si_{45}$ film with the theoretically calculated spectra of the $AgSi_3$, Ag_2Si, and Ag_3Si phases shows the best agreement with the spectrum of the Ag_2Si phase. Moreover, the Ag_2Si phase was identified by the authors of studies [26, 28–30].

Thus, based on X-ray diffraction data, X-ray emission spectroscopy, and theoretical calculations of the electronic density of states, it has been established that a metastable Ag_2Si phase is formed in the $Ag_{55}Si_{45}$ film produced by ion-beam sputtering.

Contribution of the authors

The authors contributed equally to this article.

Conflict of interests

The authors declare that they have no known competing financial interests or personal relationships that could have influenced the work reported in this paper.

The online version https://journals.vsu.ru/kcmf *contains supplementary material*

References

1. Yang Z. W., Meng L. Y., Lin J. S., ... Li J. F. 3D hotspots platform for plasmon enhanced Raman and second harmonic generation spectroscopies and quantitative analysis. *Advanced Optical Materials*. 2019;7: 3–8. https://doi.org/10.1002/adom.201901010

2. Ermina A. A., Solodovchenko N. S., Levitskii V. S., ... Zharova Y. A. Plasmonic disordered array of hemispherical AgNPs on SiO_2@c-Si: their optical and SERS properties. *Materials Science in Semiconductor Processing*. 2024;169: 107861. https://doi.org/10.1016/j.mssp.2023.107861

3. Dzhagan V., Mazur N., Kapush O., ... Yukhymchuk V. Self-organized SERS substrates with efficient analyte enrichment in the hot sSpots. *ACS Omega*. 2024;9(4): 4819–4830. https://doi.org/10.1021/acsomega.3c08393

4. Kukushkin V. I., Van'kov A. B., Kukushkin I. V. Relationship between the giant enhancement of the Raman scattering and luminescence on nanostructured metallic surfaces. *Journal of Experimental and Theoretical Physics Letters*. 2013;98(6): 342–347. https://doi.org/10.1134/S0021364013190089

5. Ghosh R., Ghosh J., Das R., ... Giri P. K. Multifunctional Ag nanoparticle decorated Si nanowires for sensing, photocatalysis and light emission applications. *Journal of Colloid and Interface Science*. 2018;532: 464-473. https://doi.org/10.1016/j.jcis.2018.07.123

6. Poletaeva D. A., Khakina E. A., Kukushkin V. I., ... Kotelnikov A. I. Application of SERS spectroscopy for detection of water-soluble fullerene C60 derivatives and

their covalent conjugates with dyes. *Doklady Physical Chemistry*. 2015;460(1): 1–5. https://doi.org/10.1134/S0012501615010017

7. Morawiec S., Mendes M. J., Priolo F., Crupi I. Plasmonic nanostructures for light trapping in thin-film solar cells. *Materials Science in Semiconductor Processing*. 2019;92: 10–18. https://doi.org/10.1016/j.mssp.2018.04.035

8. Atwater H. A., Polman A. Plasmonics for improved photovoltaic devices. *Nature Materials*. 2010;9: 205–213. https://doi.org/10.1038/nmat2629

9. Polat D. B., Eryilmaz L., Keles O. Generation of AgSi film by magnetron sputtering for use as anodes in lithium ion batteries. *ECS Meeting Abstracts*. 2015;MA2015-01: 514–514. https://doi.org/10.1149/ma2015-01/2/514

10. Liu B., Xu G., Jin C., ... Zhou L. The Si/Ag_2Si/Ag particles with the enhanced mechanical contact as anode material for lithium ion batteries. *Materials Letters*. 2020;280: 128536. https://doi.org/10.1016/j.matlet.2020.128536

11. Li R., Yang H., Zhang Y., ... Huang P. Physical mechanisms and enhancement of endurance degradation of SiO_x:Ag-based volatile memristors. *2023 Silicon Nanoelectronics Workshop (SNW)*. 2023;40: 117–118. https://doi.org/10.23919/SNW57900.2023.10183918

12. Ding X., Huang P., Zhao Y., Feng Y., Liu L. Understanding of the volatile and nonvolatile switching in Ag-based memristors. *IEEE Transactions on Electron Devices*. 2022;69: 1034–1040. https://doi.org/10.1109/TED.2022.3144373

13. Dias C., Lv H., Picos R., ...Ventura J. Bipolar resistive switching in Si/Ag nanostructures. *Applied Surface Science*. 2017;424: 122–126. https://doi.org/10.1016/j.apsusc.2017.01.140

14. Sarkar D. K., Cloutier F., El Khakani M. A. Electrical switching in sol-gel derived Ag-SiO_2 nanocomposite thin films. *Journal of Applied Physics*. 2005;97: 2–7. https://doi.org/10.1063/1.1870112

15. Jo S. H., Kim K. H., Chang T., Gaba S., Lu W. Si memristive devices applied to memory and neuromorphic circuits. In: *Proceedings of 2010 IEEE International Symposium on Circuits and Systems*, May 2010, IEEE; 2010. p. 13–16. https://doi.org/10.1109/iscas.2010.5537135

16. Huang C. Size-dependent behavior and challenges in Ag/Al_2O_3/Au memristors: an investigation into miniaturization effect. *Mechanical Engineering and Materials Science Independent Study*. 2023. https://doi.org/10.7936/r37p-cf73

17. Xu W., Wang J., Yan X. Advances in memristor-based neural networks. *Frontiers in Nanotechnology*. 2021;3: 645995. https://doi.org/10.3389/fnano.2021.645995

18. Zhang B., Kutalek P., Knotek P., ... Wagner T. Investigation of the resistive switching in Ag_xAsS_2 layer by conductive AFM. *Applied Surface Science*. 2016;382: 336–340. https://doi.org/10.1016/j.apsusc.2016.04.152

19. Jeong W. H., Han J. H., Choi B. J. Effect of Ag concentration dispersed in HfO_x thin films on threshold switching. *Nanoscale Research Letters*. 2020;15(1): 27 https://doi.org/10.1186/s11671-020-3258-6

20. Yoo J., Woo J., Song J., Hwang H. Threshold switching behavior of Ag-Si based selector device and hydrogen doping effect on its characteristics. *AIP Advances*. 2015;5(12): 127221. https://doi.org/10.1063/1.4938548

21. Ilyas N., Wang J., Li C., ... Li W. Controllable resistive switching of STO: Ag/SiO_2-based memristor synapse for neuromorphic computing. *Journal of Materials Science & Technology*. 2022;97: 254–263. https://doi.org/10.1016/j.jmst.2021.04.071

22. Cha J. H., Yang S. Y., Oh J., ... Choi S. Y. Conductive-bridging random-access memories for emerging neuromorphic computing. *Nanoscale*. 2020;12: 14339–14368. https://doi.org/10.1039/d0nr01671c

23. Sokolov A. S., Abbas H., Abbas Y., Choi C. Towards engineering in memristors for emerging memory and neuromorphic computing: a review. *Journal of Semiconductors*. 2021;42(1): 013101. https://doi.org/10.1088/1674-4926/42/1/013101

24. Raeis-Hosseini N., Lim S., Hwang H., Rho J. Reliable $Ge_2Sb_2Te_5$-integrated high-density nanoscale conductive bridge random access memory using facile nitrogen-doping strategy. *Advanced Electronic Materials*. 2018;4(11). https://doi.org/10.1002/aelm.201800360

25. Olesinski R. W., Gokhale A. B., Abbaschian G. J. The Ag-Si (Silver-Silicon) system. *Bulletin of Alloy Phase Diagrams*. 1989;10(6): 635–640. https://doi.org/10.1007/BF02877631

26. Anantharaman T. R., Luo H. L., Element W. Formation of new intermetallic phases in binary eutectic systems by drastic undercooling of the melt. *Nature*. 1966;210.(5040): 1040–1041. https://doi.org/10.1038/2101040a0

27. Terekhov V. A., Domashevskaya E. P., Kurganskii S. I., ... Agapov B. L. Formation of the Al_3Si metastable phase in Al-Si films obtained by ion-beam sputtering according to experimental and theoretical data. *Thin Solid Films*. 2023;772: 139816. https://doi.org/10.1016/j.tsf.2023.139816

28. Suryanarayana C. A new metastable phase in the silver-silicon system. *Journal of the Less Common Metals*. 1974;35(2): 347–352. https://doi.org/10.1016/0022-5088(74)90248-3

29. Lee W. S., Chen T. H., Lin C. F., Wu C. L. Microstructural evolution of nanoindented Ag/Si thin-film under different annealing temperatures. *Materials Transactions*. 2011;52(10): 1868–1875. https://doi.org/10.2320/matertrans.M2011160

30. Liu B., Xu G., Jin C., ... Zhou L. The Si/Ag_2Si/Ag particles with the enhanced mechanical contact as anode material for lithium ion batteries. *Materials Letters*. 2020;280: 128536. https://doi.org/10.1016/j.matlet.2020.128536

31. Materials Explorer Database. *Data retrieved from the Materials explorer for $AgSi_3$ (mp-978524) database: version 2025.06.09*. Available at: https://next-gen.materialsproject.org/materials/mp-978524

32. Materials Explorer Database. *Data retrieved from the Materials Explorer for Ag_3Si (mp-1219243) database: version 2025.06.09*. Available at: https://next-gen.materialsproject.org/materials/mp-1219243?material_ids=mp-1219243

33. Nakayama K. S., Nishijima M., Zhang Y., ... Suganuma K. Metastable phases of Ag–Si: amorphous Si and Ag-nodule mediated bonding. *Scientific Reports*. 2024;14(1): 1–9. https://doi.org/10.1038/s41598-024-70298-6

34. Cassidy C., Singh V., Grammatikopoulos P., ... Sowwan M. Inoculation of silicon nanoparticles with silver atoms. *Scientific Reports*. 2013;3: 1–7 https://doi.org/10.1038/srep03083

35. Barkov K. A., Terekhov V. A., Nesterov D. N., ... Sitnikov A. V. Formation of silver nanocrystals in Ag-Si composite films obtained by ion beam sputtering. *Condensed Matter and Interphases*. 2024;26(3), 407–416. https://doi.org/10.17308/kcmf.2024.26/12215

36. Zimkina T. M., Fomichev V. A. *Ultrasoft X-ray spectroscopy.*. Leningrad University Pub. House; 1971. 125 p.

37. Zimmermann P., Peredkov S., Abdala P. M., ... van Bokhoven J. A. Modern X-ray spectroscopy: XAS and XES in the laboratory. *Coordination Chemistry Reviews*. 2020;423: 213466. https://doi.org/10.1016/j.ccr.2020.213466

38. Terekhov V. A., Kashkarov V. M., Manukovskii E. Yu., Schukarev A. V., Domashevskaya E. P. Determination of the phase composition of surface layers of porous silicon by ultrasoft X-ray spectroscopy and X-ray photoelectron spectroscopy techniques. *Journal of Electron Spectroscopy and Related Phenomena*. 2001;114–116: 895–900. https://doi.org/10.1016/S0368-2048(00)00393-5

39. Blaha P., Schwarz K., Tran F., ... Marks L. D. WIEN2k: An APW+lo program for calculating the properties of solids. *The Journal of Chemical Physics*. 2020;152(7): 074101. https://doi.org/10.1063/1.5143061

40. Momma K., Izumi F. VESTA 3 for three-dimensional visualization of crystal, volumetric and morphology data. *Applied Crystallography*. 2011;44(6): 1272–1276. https://doi.org/10.1107/S0021889811038970

41. *SpringerMaterials: The Landolt-Börnstein Database. Data retrieved from the SpringerMaterials for Structural data № 0450926 database: version 2025*. Available at: https://materials.springer.com/isp/crystallographic/docs/sd_0450926

42. Langford J. I., Wilson A. J. C. Scherrer after sixty years: a survey and some new results in the determination of crystallite size. *Journal of Applied Crystallography*. 1978;11: 102–113. https://doi.org/10.1107/S0021889878012844

43. Hassanzadeh-Tabrizi S. A. Precise calculation of crystallite size of nanomaterials: a review. *Journal of Alloys and Compounds*. 2023:968: 171914. https://doi.org/10.1016/j.jallcom.2023.171914

44. Kurganskii S. I., Pereslavtseva N. S. Electronic structure of $FeSi_2$. *Physics of the Solid State*. 2002;44(4): 704–708. https://doi.org/10.1134/1.1470562

45. Kurganskii S. I., Pereslavtseva N. S. Electronic structure of cobalt disilicide film. *Physics of the Solid State*. 2000;42(8): 1542–1547. https://doi.org/10.1134/1.1307068

46. Pereslavtseva N. S, Kurganskii S. I. Electronic structure and spectral properties of nickel disilicide films. *Physics of the Solid State*. 1999;41(11): 1906–1910. https://doi.org/10.1134/1.1131124

47. Sarkar D. K., Dhara S., Nair K. G. M., Chowdhury S. Studies of phase formation and chemical states of the ion beam mixed Ag/Si (1 1 1) system. *Nuclear Instruments and Methods in Physics Research Section B: Beam Interactions with Materials and Atoms*. 2000;168(2): 215–220. https://doi.org/10.1016/S0168-583X(99)00876-9

48. Weijs P. J. W., Van Leuken H., De Groot R. A., ... Buschow K. H. J. X-ray-emission studies of chemical bonding in transition-metal silicides. *Physical Review B*. 1991;44(15): 8195. https://doi.org/10.1103/PhysRevB.44.8195

* *Translated by author of the article*

Information about the authors

Konstantin A. Barkov, Cand. Sci. (Phys.-Math.), Head of the Laboratory, Department of Solid State Physics and Nanostructures, Voronezh State University (Voronezh, Russian Federation).
https://orcid.org/0000-0001-8290-1088
barkov@phys.vsu.ru

Vitaly V. Babakov, student, Department of Solid State Physics and Nanostructures, Voronezh State University (Voronezh, Russian Federation).
https://orcid.org/0009-0002-8282-2034
babakov_vv@phys.vsu.ru

Gennady P. Potudansky, Lead Data Analyst, RT Labs JSC (Voronezh, Russian Federation).
https://orcid.org/0000-0002-4186-5081
potudanskiy@phys.vsu.ru

Sergey A. Ivkov, Cand. Sci. (Phys.-Math.), Leading Electronics Engineer, Department of Solid State Physics and Nanostructures, Voronezh State University (Voronezh, Russian Federation).
https://orcid.org/0000-0003-1658-5579
ivkov@phys.vsu.ru

Yaroslav A. Peshkov, Cand. Sci. (Phys.-Math.), Research Associate, Department of Solid State Physics and Nanostructures, Voronezh State University (Voronezh, Russian Federation).
https://orcid.org/0000-0003-0939-0466
tangar77@mail.ru

Ivan V. Polshin, student, Department of Solid State Physics and Nanostructures, Voronezh State University (Voronezh, Russian Federation).
https://orcid.org/0009-0008-7639-6538
polshin@phys.vsu.ru

Evgenii S. Kersnovsky, student, Department of Solid State Physics and Nanostructures, Voronezh State University (Voronezh, Russian Federation).
https://orcid.org/0009-0006-8215-6077
kersnovsky@phys.vsu.ru

Selby Y. Khydyrova, postgraduate student, Department of Electronic Technologies in Mechanical Engineering, Bauman Moscow State Technical University (Moscow, Russian Federation).
https://orcid.org/0000-0002-5510-0899
hydyrova@bmstu.ru

Konstantin M. Moiseev, Assistant Professor, Department of Electronic Technologies in Mechanical Engineering, Bauman Moscow State Technical University (Moscow, Russian Federation).
https://orcid.org/0000-0002-8753-7737
mkm430@ya.ru

Igor E. Zanin, Cand. Sci. (Phys.-Math.), Assistant Professor, General Physics Department, Voronezh State University (Voronezh, Russian Federation).
iezan@mail.ru

Alexandra K. Pelagina, Engineer-Physicist, Voronezh State University (Voronezh, Russian Federation).
Pisliaruk@phys.vsu.ru

Nikita S. Buylov, Cand. Sci. (Phys.-Math.), Assistant Professor, Department of Solid State Physics and Nanostructures, Voronezh State University; Engineer, Research Institute of Electronic Technology (Voronezh, Russian Federation).

https://orcid.org/0000-0003-1793-4400

buylov@phys.vsu.ru

Tran Van Tu, PhD, Lecturer, Faculty of Fundamental Sciences, Department of Physics, University of Medicine and Pharmacy at Ho Chi Minh city (Ho Chi Minh city, Viet Nam).

tranvantu@ump.edu.vn

https://orcid.org/0000-0002-3892-3578

Alexandr E. Nikonov, Cand. Sci. (Phys.-Math.), Research Engineer, Department of Solid-State Electronics, Voronezh State Technical University (Voronezh, Russian Federation).

nikonov.sasha1994@gmail.com

Aleksandr V. Sitnikov, Dr. Sci. (Phys.-Math.), Full Professor, Departments of Solid-State Electronics, Voronezh State Technical University (Voronezh, Russian Federation).

https://orcid.org/0000-0002-9438-9234

sitnikov04@mail.ru

Received January 29, 2025; approved after reviewing February 21, 2025; accepted for publication March 17, 2025; published online April 01, 2026.

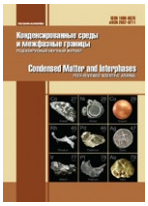

ISSN 1606-867X (Print)
ISSN 2687-0711 (Online)
Condensed Matter and Interphases
Kondensirovannye Sredy i Mezhfaznye Granitsy
https://journals.vsu.ru/kcmf/

Original articles

Research article
https://doi.org/10.17308/kcmf.2026.28/13556

Electrochemical reduction of nitrate ions on copper coatings of various roughness under conditions of mixed transport and kinetic control

F. A. Vdovenkov, P. P. Tarakanov, O. A. Kozaderov✉, P. V. Fomin

Voronezh State University,
1 Universitetskaya pl., Voronezh 394018, Russian Federation

Abstract

Objectives: In this work, the influence of electrode surface roughness on the kinetics of the non-stationary electrochemical process of cathodic reduction of nitrate ion under conditions of mixed transport-kinetic control under potentiostatic polarization conditions is established.

Experimental: The research was carried out on two copper coatings obtained by galvanostatic deposition from a copper sulfate electrolyte, which was supplemented with various organic additives to vary the roughness of the synthesized copper coatings. The kinetics of the electrochemical reduction of nitrate ions on the obtained copper coatings were studied by transient electrochemical methods of voltammetry and chronoammetry in an aqueous deaerated solution of 10 mM KNO_3 + 100 mM H_2SO_4. Potentiostatic measurements were performed at a cathodic potential of -470 mV, corresponding to a mixed transport-kinetic control. The surface roughness of the synthesized copper coatings was evaluated using atomic force microscopy and underpotential deposition of lead monolayer.

Conclusion: Based on the previously developed theoretical model of the electrochemical process occurring in a mixed transport-kinetic mode on a rough electrode, an approach is proposed for estimating the main parameters of the kinetic stage, taking into account normalization to the real surface area, using the example of the electrichemical reduction of nitrate ions on copper coatings of various roughness. Within the framework of this approach, it was found that a rougher copper coating is characterized by higher values of the heterogeneous constant of the rate and density of the exchange current, which indicates an increase in the electrocatalytic activity of copper in the reaction under study during the transition to electrodes with increased roughness.

Keywords: Surface roughness, Copper coating, Nitrate ion, Electrochemical reduction, Mixed kinetics, Atomic force microscopy, Voltammetry, Chronoamperometry

Funding: The study received financial support from the Ministry of Science and Higher Education of the Russian Federation within the framework of State Contract with universities regarding scientific research in 2025–2027, project No. FZGU-2025-0001.

Acknowledgements: The AFM studies were performed on the equipment of the Center for the Collective Use of Scientific Equipment of Voronezh State University.

For citation: Vdovenkov F. A., Kozaderov O. A., Tarakanov P. P., Fomin P. V. Electrochemical reduction of nitrate ions on copper coatings of various roughness under conditions of mixed transport and kinetic control. *Condensed Matter and Interphases*. 2026;28(1): 28–39. https://doi.org/10.17308/kcmf.2026.28/13556

Для цитирования: Вдовенков Ф. А., Козадеров О. А., Тараканов П. П., Фомин П. В. Электровосстановление нитрат-иона на медных покрытиях различной шероховатости в условиях смешанного транспортно-кинетического контроля. *Конденсированные среды и межфазные границы*. 2026;28(1): 28–39. https://doi.org/10.17308/kcmf.2026.28/13556

✉ Oleg A. Kozaderov, e-mail: ok@chem.vsu.ru

1. Introduction

Surface roughness is an important property of solid electrodes. The generally accepted quantitative characteristic for its estimation is the roughness factor $f_r = S_{real}/S_{geom}$, which is equal to the ratio of the true (S_{real}) to the visible area (S_{geom}) of the electrode surface [1, 2]. The roughness effect is not purely geometric, since the formation of a rough (morphologically heterogeneous) surface can lead not only to an increase in surface area, but also to the appearance of new active reaction and adsorption centers on it [3], changes in the kinetic parameters of the electrode reaction [4, 5], changes in corrosion resistance [6–8] and double-layer characteristics [9]. As a consequence, for a correct assessment of the electrocatalytic activity and adsorption capacity of the electrode, it is necessary to normalize the extensive parameters of the kinetics of the electrode reaction (current, impedance, admittance), double electric layer (differential and integral capacitance) and adsorption to the roughness factor when calculating them. Otherwise, the claimed "increase in electrocatalytic activity" may simply be the result of an increase in surface area without any real catalytic effect.

In this case, the procedure for finding the current density as a measure of the rate of the electrode process occurring on a rough electrode is generally not trivial, since it depends on the nature of kinetic constraints. So, if the limiting stage of the electrochemical reaction is charge transfer, then the current density $i = I/S_{real} = I/(S_{geom} \cdot f_r)$ should be calculated by dividing the current I by the true area of the electrochemically active electrode surface. Considering that electrocatalytic processes controlled by the charge transfer stage are mainly carried out on highly developed, dispersed electrodes, the main problem in this case is the determination of the roughness factor f_r [10], but not the task of calculating the rate of the electrode process.

In the case of diffusion-controlled processes, the procedure for taking into account the roughness factor becomes significantly more complicated, since their rate, generally speaking, should be normalized not to the surface area of the electrode, but to the surface area of the diffusion front [11]. At the same time, in the non-stationary mass transfer mode, the geometry of the diffusion front changes over time: it repeats the profile of the electrode surface at short times and is almost completely smoothed out at sufficiently long times. This is explained by the fact that during the initial period of the process, the thickness of the diffusion layer d is very small and does not exceed the size of the micro-dimensions, whereas during the propagation of the diffusion front deep into the phase, on the contrary, it becomes so large that the diffusion flux practically ceases to be sensitive to the roughness of the electrode surface [12].

The most difficult situation is when a non-stationary electrochemical process takes place in the mode of mixed transport and kinetic control. In this case, the contributions of the stages of charge transfer and mass transfer to the kinetics of the electrode process are comparable, and their ratio varies over time. Such processes play a special role in the formation of metal coatings, including in microelectronics, when it is necessary to carry out uniform electrodeposition of metal onto the surface of a rather complex micro- and/or macrogeometric profile.

In [13], a mathematical model was constructed of the process occurring at potentiostatic polarization in the mode of mixed diffusion-kinetic control on an electrode with an average surface roughness ($1 < f_r \leqslant 3$) of a harmonic, fractal, or irregular profile. The simulation results showed that the i,t-chronoamperograms of rough and flat electrodes are related by a ratio $i(t)_{rough} = i(t)_{flat} \cdot \varphi(k, D, f_r, \lambda, t)$ in which $\varphi(k, D, f_r, \lambda, t)$ is a roughness function. It depends in a complex way on the roughness factor f_r, the average size of the irregularities λ, as well as on the ratio of the heterogeneous rate constant k of the electrode process (charge transfer stage) and the diffusion coefficient of the electroactive reagent D, varying over time from $\varphi = f_r$ to $\varphi = 1$.

The range of electrode processes occurring in the mode of mixed transport-kinetic control is very wide. For instance, the complex process of cathodic reduction of the nitrate ion is very sensitive morphologically and structurally [14–19]. The cathodic reduction of NO_3^- ions is of great practical importance due to the need to control the nitrate content in aqueous media, as well as a method for obtaining nitrogen-containing

compounds, primarily ammonia as a starting substance in the production of nitrogen fertilizers. In this work, the process of the electrochemical reduction of NO_3^- ions is considered as a model for detecting the effect of surface roughness of the electrode.

Among the transition metals of the IB-group, copper exhibits the highest activity and selectivity in the cathodic reduction of nitrates [20], with ammonium ion being the main product in an acidic medium [21]. To vary the roughness of a copper electrode, our work uses the method of electrodeposition from sulfate electrolytes of copper plating, the introduction of organic additives into which makes it possible to obtain coatings with variable roughness [22].

The study of the role of roughness in the catalytic activity of electrodeposited copper coatings is complicated by the fact that the process of the cathodic reduction of NO_3^- ions is multielectron and multistage. As a consequence, the identification of a purely catalytic effect requires the determination of the kinetic parameters of the electrochemical stage, primarily the heterogeneous charge transfer rate constant. The transient electrochemical methods can be used to find the kinetic current. The potentiodynamic method (chronovoltammetry) allows us to identify the general kinetic patterns of the cathodic process involving the nitrate ion, as well as the potential range of its electroreduction. In turn, the potentiostatic method (chronoamperometry) makes it possible to evaluate the contributions of the diffusion and electrochemical stages to the overall rate of the process. In this paper, these problems are solved under conditions of mixed transport-kinetic control using a previously developed theoretical model of the electrode process on a geometrically inhomogeneous electrode surface of medium roughness [13]. Such electrodes can be used as electrochemical sensors to determine the concentration of nitrate ions in aqueous media.

The aim of the work is to establish the influence of the medium roughness of the electrode surface on the kinetics of the non-stationary electrochemical process of cathodic reduction of nitrate ion under conditions of mixed transport-kinetic control under potentiostatic polarization.

The tasks of the work are as follows:

1. To synthesize copper coatings with different roughness by electrodeposition and to determine the main microscopic and integral parameters of their surface morphology.

2. To determine the range of electroreduction potentials of the nitrate ion in an acidic sulfate medium on the obtained copper coatings under the potentiodynamic conditions of cathodic polarization, to establish the general nature of the kinetic limitations of the process and to determine the conditions for the implementation of mixed transport-kinetic control.

3. To identify the role of the roughness of synthesized copper coatings in the kinetics of cathodic reduction of NO_3^- ions under conditions of mixed transport-kinetic control.

2. Experimental

The studies were carried out on two copper coatings with a thickness of ~1 μm obtained by galvanostatic deposition at a current density of -15 mA/cm^2 from acidified solutions of copper sulfate onto a carbon-metal electrode (NTF Volta LLC). To vary the morphological state of the copper coatings, various organic additives were introduced into the sulfate solution of copper plating [22] (Table 1): polyethylene glycol of various molar weights (PEG-1500, PEG-4000), disodium salt of 4,4-dithiobenzenedisulfonic acid (DTBS) and 2-aminobenzothiazole (ABT). A copper plate was used as an auxiliary electrode during electrodeposition, and the silver chloride reference electrode (OOO NPP Tomanalit) was located in a separate vessel, which was connected to the cell by an electrolytic bridge filled with agar-agar with a saturated solution of potassium nitrate.

Table 1. Composition of solutions for galvanostatic deposition of copper coatings

Coating	Composition
No. 1	156 g/l $CuSO_4 \cdot 5H_2O$ + 10 g/l H_2SO_4 + 50 mg/l HCl + 0.5 g/l PEG-1500
No. 2	156 g/l $CuSO_4 \cdot 5H_2O$ + 10 g/l H_2SO_4 + 50 mg/l HCl + 0.12 g/l DBTA + 0.5 g/l PEG-4000 + 0.5 g/l ABT

Before coating, the surface of the carbon-metal electrode was standardized by sequential polishing on a velvet fabric with a diamond suspension, reducing the grain size (1.5, 1.0, 0.5 microns) to a mirror surface. After polishing, the electrode was washed twice with distilled water (bidistillate). Next, to clean its surface from abrasive particles and degrease it, it was sequentially placed in an ultrasonic bath for 3 minutes, first in a container with acetone and then with bidistillate, after which the surface of the electrode was dried using filter paper.

The kinetics of the model reaction of the electroreduction of nitrate ion on the obtained copper coatings was studied by transient electrochemical methods of voltammetry and chronoammetry. Cathodic polarization curves were recorded over a range from an open-curcuit potential value to –700 mV at various potential scan rates (from 10 to 100 mV/s). Chronoamperometric measurements were carried out at a cathodic potential of –470 mV, corresponding to the implementation of a mixed transport-kinetic control, recording current decay curves for 1000 s. A working solution of 10 mM KNO_3 + 100 mM H_2SO_4 was deaerated with chemically pure argon directly in an electrochemical cell for 90 minutes before the experiment. Electrochemical measurements were carried out in a three-electrode glass cell with undivided cathode and anode spaces. The reference electrode was a silver chloride electrode (OOO NPP Tomanalit), an auxiliary graphite electrode.

All solutions were prepared with water of analytical quality (GOST R 52501-2005) using a Livam UPVA-5 system (electrical conductivity 0.8–1.0 μS/cm) using reagents of analytical grade.

Electrochemical studies were performed on IPC-compact or P-20X potentiostats. The potentials are given relative to a standard hydrogen electrode. The current density is calculated per unit geometric surface area of the electrode.

The morphological state of the surface and quantitative parameters of the microgeometry of synthesized copper coatings were evaluated using atomic force microscopy (AFM) data. The AFM method was performed using a Solver P47PRO device in a semi-contact scanning mode of a sample using HA_FM composite cantilevers (resonant frequency 74.025 kHz, elastic constant of the cantilever console 3.5 N/m, radius of the probe tip curvature was 10 nm). AFM images were obtained at three different 10x10 mm^2 scan zones. The roughness parameters were found according to the statistical processing of AFM data in the Gwyddion software package.

The area of electrodeposited copper coatings was determined by the underpotential Pb monolayer deposition (UPD Pb) in an argon-deaerated solution of 1 mM $PbCl_2$ + 1 mM $HClO_4$ at a potential scan rate of 10 mV/s in accordance with the procedure described in [23]. 10 cycles were recorded in the range of potentials from 130 to -320 mV, and after stabilization of the voltammogram (Fig. 1), a charge corresponding to the deposition of a monolayer of lead was found:

$$Q_{\text{UPD,Pb}} = \frac{1}{V}\int_{E_1}^{E_2} i(E)\,dE\,, \qquad (1)$$

where $Q_{\text{UPD,Pb}}$ is the charge, mC/cm^2; V is the potential scan rate, mV/s; $i(E)$ is the current density at a given potential; E is the potential, mV.

The roughness factor was calculated using the formula:

$$f_r = \frac{Q_{\text{UPD,Pb}}}{Q_S}, \qquad (2)$$

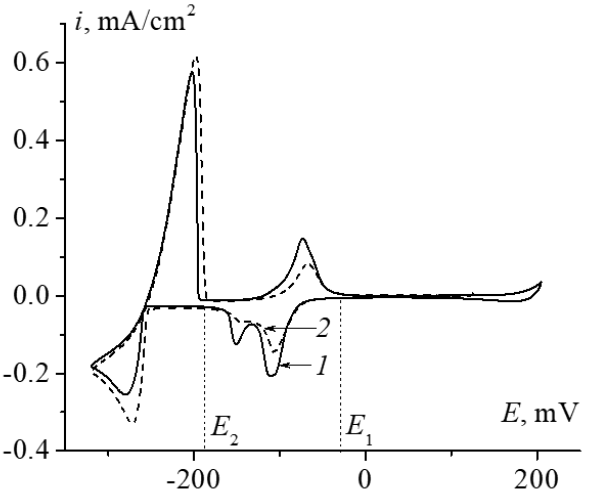

Fig. 1. Cyclic voltammograms obtained for coatings No. 1 (*1*) and No. 2 (*2*) in a solution of 1 mM $PbCl_2$ + 0.01 M $HClO_4$ at a scan rate of 10 mV/s

where Q_s is the charge required to form a monolayer of lead, which was assumed to be equal to ~250 mC/cm^2 [23].

3. Results and discussion

3.1. Morphology and roughness of electrodeposited copper coatings

Fig. 2 shows surface images, as well as 3D and 2D profiles of synthesized galvanic copper coatings obtained by atomic force microscopy. It can be seen that both coatings are morphologically heterogeneous, while the maximum height of irregularities for coating No. 1, deposited from a solution with the addition of polyethylene glycol PEG-1500, is higher than for coating No. 2, obtained from an electrolyte containing a complex of organic additives. This is consistent with the data from [22], in which scanning electron microscopy confirmed the smoothing of the surface of an electroplated copper coating deposited from a sulfate solution in the presence of PEG, DTBS, and ABT. A visual comparison of the morphology of the obtained coatings is confirmed by the analysis of quantitative parameters characterizing the surface roughness (Table 2). Indeed, the average and root mean square (RMS) roughness decreases by about one and a half times during the transition from coating No. 1 to No. 2, while the average distance between neighboring irregularities, on the contrary, increases. This is reflected in a decrease in the ratio of the total area of the scanned zone to its projection, which is indicated in Table 2 by f_r(AFM). However, this value, which is quite close to unity, turned out to be significantly underestimated compared to the roughness factor f_r(UPD) obtained by the electrochemical method. This can be explained by the fact that the atomic force microscopy method allows us to characterize the roughness of a relatively small area of the electrode surface limited by the AFM scanning area (in this work, 10×10 μm^2 = 10^{-6} cm^2). While electrochemical methods make it possible to determine the surface area of the electrode as a whole. The geometric area of the working electrode in operation is 0.07 cm^2, which exceeds the size of the AFM scanning site by 7·10^4 times. As a result, the AFM method makes it possible to register irregularities at the nano and micro levels, but it cannot, in principle, detect morphological irregularities on a larger scale that exceed the size of the scanning zone, which, however, contribute to the result of electrochemical measurements of the electrode area. At the same time, the previously detected decrease in the degree of morphological disorder during the transition from coating No. 1 to No. 2 continues in both cases of f_r(AFM) and f_r(UPD).

3.2. Voltammetry of electroreduction of nitrate ion on copper coatings

When potassium nitrate is introduced into a sulfuric acid solution, a maximum is recorded on the cathodic voltammograms in the range from –100 to –600 mV of both studied copper coatings (Fig. 3a). Considering that in the absence of KNO_3, the peaks on the polarization curves are not revealed in the same potential range (dotted line in Fig. 3a), the observed maximum in the voltammogram can be attributed to the process of the cathodic reduction of NO_3^- ions.

An increase in the potential scan rate V leads to an increase in the current density of the cathodic peak i_{max}, and this dependence is linearized in coordinates $i_{max} - V^{0.5}$ (Fig. 4a), which confirms the non-stationary nature of the diffusion transfer stage. Note that the obtained linear dependences are not extrapolated to the origin, which indicates the occurrence of a secondary cathodic process; the reaction of hydrogen evolution in the acid solution under study seems to be the most likely. In turn, the dependence of the peak potential E_{max} on lg$V$ is

Table 2. Roughness parameters of copper coatings

Parameter	Coating No. 1	Coating No. 1
RMS roughness (S_q), nm	53±5	32±2
Average roughness (S_a), nm	42±4	25±2
Average distance between neighbor irregularities (λ), nm	965±33	1561±107
Roughness factor f_r (AFM)	1.07±0.01	1.03±0.01
Roughness factor f_r (UPD)	2.56±0.02	1.89±0.02

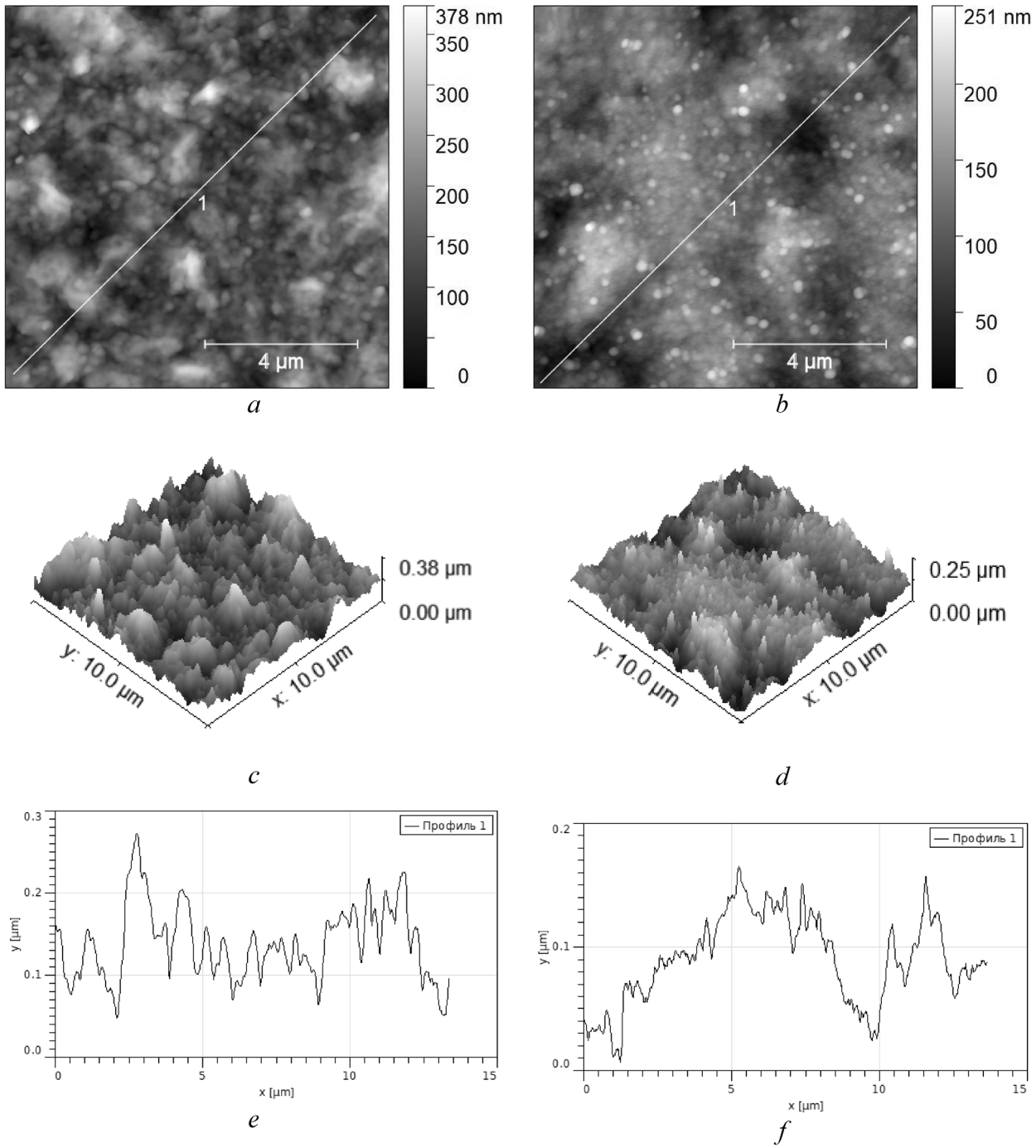

Fig. 2. AFM images of the surface (*a, b*), three-dimensional (*c, d*) and two-dimensional profiles (*d, e*) of copper coatings No. 1 (*a, c, e*) and No. 2 (*b, d, e*).

linear (Fig. 4b). As the scan rate increases, the peak potential becomes more negative. This indicates the irreversibility of the slow charge transfer stage of the process under study [24].

A comparison of the voltammograms on synthesized copper coatings (Fig. 3b) shows that the cathodic peak on the rougher coating No. 1 is formed at less negative potentials. The shift of the peak potential to the negative direction during the transition to a less rough coating is also confirmed by data obtained at different potential scan rates (Fig. 4a). Indeed, the E_{max}–lg$V$ dependence for the coating No. 2 shifts by about 25 mV in the negative direction. Considering that the open-circuit potential practically does not change during the transition from one coating

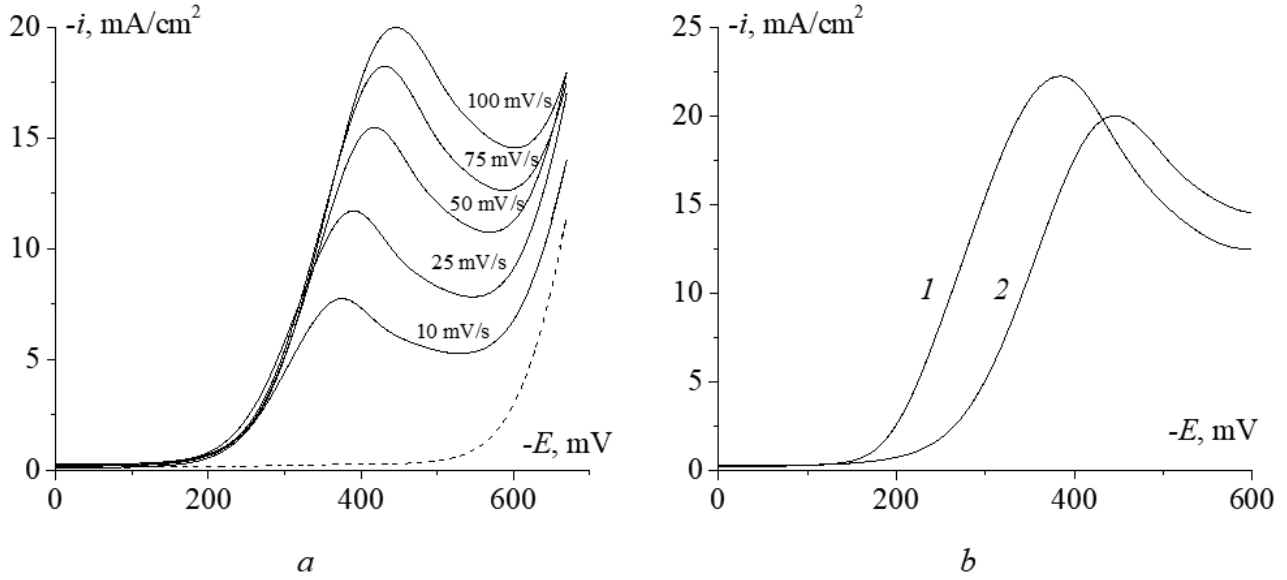

Fig. 3. Cathode voltammograms obtained in a solution of 10 mM KNO_3 + 100 mM H_2SO_4: (*a*) at different potential scan rates on copper coating No. 2; (*b*) at a rate of 25 mV/s on copper coatings No. 1 (*1*) and No. 2 (*2*). The dotted line is voltammogram obtained on copper coating No. 2 in a background solution of 100 mM H_2SO_4 at 25 mV/s

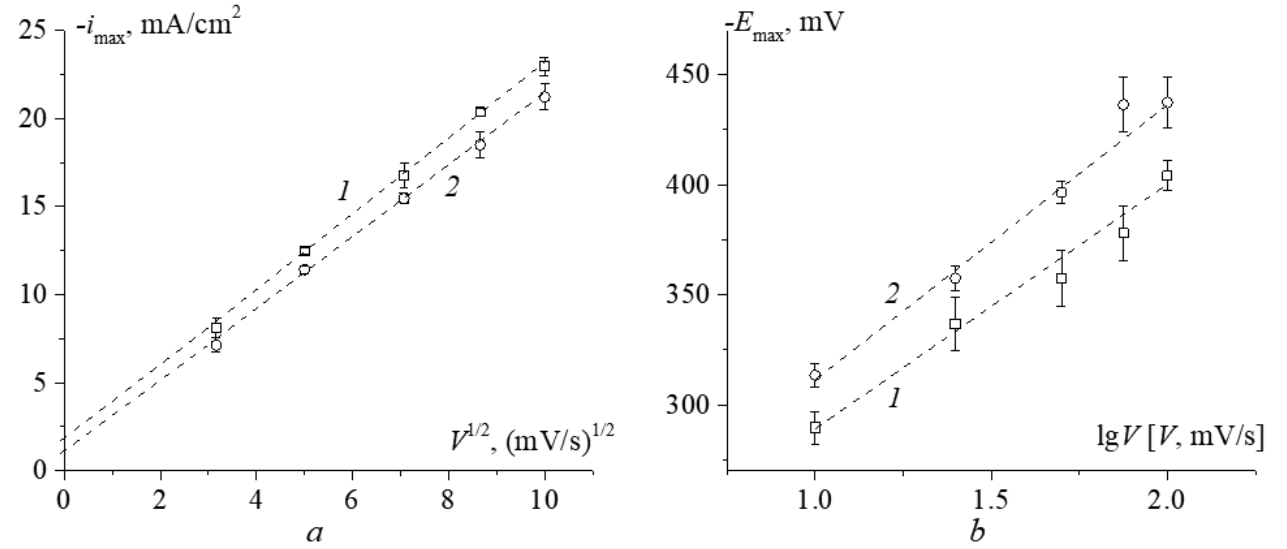

Fig. 4. Criterion dependences on the scan rate of maximum current density (*a*) and potential (*b*) of cathodic voltammograms of nitrate ion reduction in a solution of 10 mM KNO_3 + 100 mM H_2SO_4 on copper coatings No. 1 (*1*) and No. 2 (*2*)

to another, it can be concluded that the process of electroreduction of nitrate ion on a rougher coating No. 1 is characterized by a lower value of electrode polarization compared to coating No. 2.

In this case, the i_{max},$V^{1/2}$ dependences obtained for the two coatings, on the contrary, are quite close. The question arises: should the peak current density i_{max}, calculated for the geometric surface area of the electrode, be additionally normalized for the coating roughness factor? First, a preliminary estimation shows that such a correction by dividing by f_r leads to a fundamentally different result, namely, the i_{max} for the smoother coating No. 2 becomes higher than for coating No. 1, which contradicts the data on a decrease in cathodic polarization on the rougher coating No. 1. Secondly, a procedure is currently theoretically justified for the correct consideration of the roughness factor in voltammetry of only reversible [25] and

completely irreversible [26] electrode processes. In the first case, the rate constant of the charge transfer stage k is very high, and the limiting stage is non-stationary diffusion transfer. A characteristic feature of this mode is the absence of dependence of the peak potential on the scan rate. Obviously, this situation is not realized in the system under study. For a completely irreversible process, on the contrary, the value of the constant k is very small, so the limiting stage is charge transfer. According to the theory of voltammetry of an irreversible process on a rough electrode [26], taking into account the roughness of the electrode surface is mandatory and amounts to dividing the current by the roughness factor only under conditions of high potential scan rates, namely, under the condition $\upsilon \gg 1$ where the dimensionless potential scan rate is determined by the expression:

$$\upsilon = (nF\lambda^2/RTD)\cdot V. \quad (3)$$

Here F is the Faraday constant, R is the universal gas constant, T is the temperature, and D is the diffusion coefficient of the nitrate ion. In this paper, according to [27], $1.85\cdot10^{-5}$ cm^2/s is assumed. The total number of electrons involved in electroreduction was assumed to be n = 8. Indeed, according to the literature data [28-30] on copper surfaces in acidic solutions, the process of nitrate ion cathodic reduction is eight-electron and can be described by the following equation [31]:

$$NO_3^- + 10H^+ + 8e^- \rightarrow NH_4^+ + 3H_2O. \quad (4)$$

Assuming that the electrode process is completely irreversible, the estimate of the dimensionless rate for the system under study leads to values of υ = 0.002–0.02. This means that the potential scan rates V used in the work are so low that the condition $u \ll 1$ is fulfilled, under which, according to [26], the roughness factor is not required, since by the time the peak is reached on the voltammogram, the diffusion front becomes flat. Therefore, the current density must be calculated for the geometric surface area of the electrode. Thus, the maximum currents on coatings No. 1 and No. 2 would have to coincide. However, this conclusion is valid only if a completely irreversible process is implemented, which, apparently, is not performed in the system under study due to mixed kinetic control, which causes the observed slight discrepancy in $i_{max}, V^{1/2}$ dependencies (Fig. 4a).

3.3. Chronoamperometry of nitrate ion electroreduction under the mixed diffusion-kinetic control

The results of potentiostatic studies at E = –470 mV were used to quantify the role of morphological heterogeneity of the coatings in the mixed kinetics of electroreduction of NO_3^- ions. The choice of this value of the cathodic potential is due to the fact that, according to the results of potentiodynamic measurements, it corresponds to the maximum or decrease of the current on the voltammogram (Fig. 3a), when the contribution of diffusion mass transfer to the kinetics of the electrode process becomes significant enough, and therefore the probability of mixed kinetic control at the potentiostatic polarization is high. The shape of the current decay curves in Cottrell coordinates (Fig. 5) confirms this assumption. Indeed, at short times, the current is weakly time-dependent, which corresponds to a noticeable contribution from the kinetic stage. However, over time, a decrease in current becomes pronounced, and the rectification of the chronoamperogram in Cottrell coordinates observed at sufficiently long times indicates diffusion control of the process.

To interpret the obtained chronoamperograms and estimate the kinetic parameters of the charge transfer stage on two copper coatings of different roughness (heterogeneous rate constant k and exchange current density $i_0 = nFkc^v$), we used the chronoamperogram equation obtained earlier in [13] for the electrochemical process occurring on a rough electrode in the mode of mixed transport-kinetic control:

$$i(t)_{rough} = nFkc^v \cdot \exp\left(\frac{k^2 t}{D}\right)\cdot \mathrm{erfc}\left(\frac{kt^{1/2}}{D^{1/2}}\right)\cdot \varphi\left(k, D, f_r, \lambda, t\right). \quad (5)$$

Here $\varphi\left(k, D, f_r, \lambda, t\right)$ is the roughness function, which is the ratio of currents across rough and flat electrodes. The analysis showed [13] that the roughness function is equal to unity φ = 1 under the condition $\left(k^2 t / D\right) \gg 1$, i.e., at long times, and this condition is facilitated by the pronounced slowness of the diffusion stage when $\left(k\lambda / D\right) \gg 1$. In another limitimg case, when $\left(k^2 t / D\right) \ll 1$, i.e.

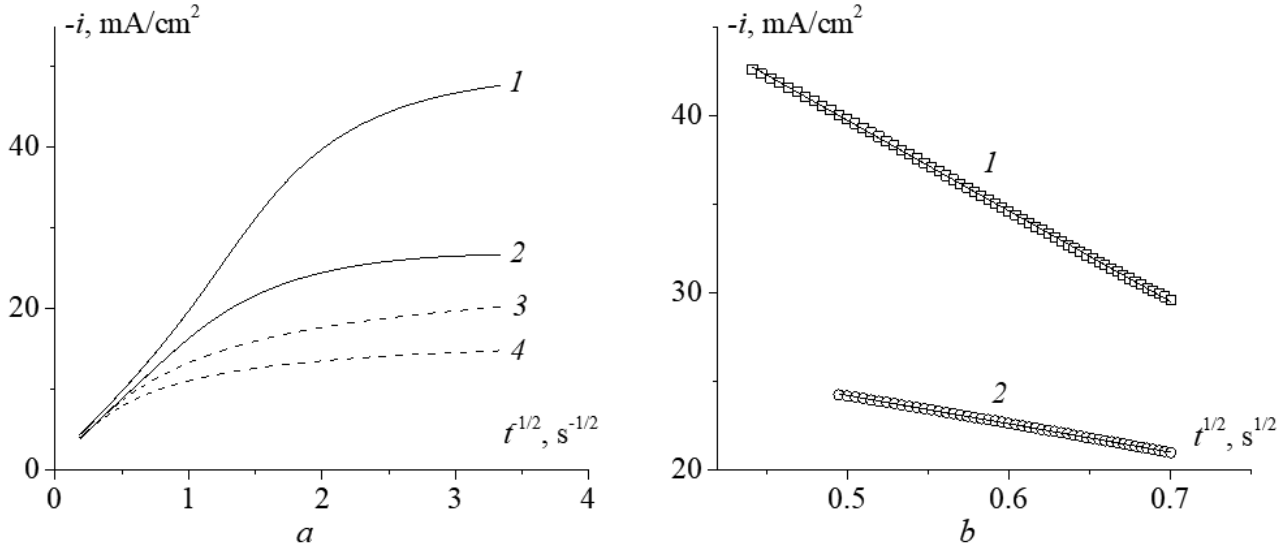

Fig. 5. (*a*) – Chronoamperograms of copper coatings No. 1 (*1*) and No. 2 (*2*) in a solution of 10 mM KNO_3 + 100 mM H_2SO_4 at a potential of -470 mV, rearranged in Cottrell coordinates. (*b*) – Initial sections of the current decay curves, linearized in the criterion $i,t^{1/2}$ coordinates

at short times, the roughness function is equal to the roughness factor $\varphi = f_r$, and the fulfillment of this condition is facilitated by the slowness of the charge transfer stage, when $(k^2t / D) \ll 1$. In the region of intermediate values, the roughness function gradually changes over time from f_r to 1 within the transition region. The position of the boundaries of this region strongly depends on the ratio of the rates of the kinetic and diffusion stages: as k decreases (the charge transfer stage slows down), the transition region shifts towards longer times and widens. Obviously, in this case, taking into account the roughness when calculating the current density is the most difficult, since it requires an estimation of the functional dependence $\varphi(k, D, f_r, \lambda, t)$.

Taking into account the properties of the roughness function, we obtained asymptotic relations for the chronoamperogram (5), which in two limiting cases is described by the following expressions:

$$i(t)_{\text{rough}} = \begin{cases} f_r \cdot nFkc^v \left(1 - \frac{2}{\pi^{1/2}} \frac{k}{D^{1/2}} t^{1/2}\right), \text{if } \left(\frac{k^2 t}{D}\right) \ll 1, & 6(\text{a}) \\ \frac{nFD^{1/2}c^v}{(\pi t)^{1/2}}, \text{if } \left(\frac{k^2 t}{D}\right) \gg 1. & 6(\text{б}) \end{cases}$$

It can be seen that at long times, the chronoamperogram does not include the roughness factor and is described by the well-known Cottrell equation [24], i.e. it corresponds solely to the diffusion control of the process on a flat electrode. This is confirmed by the linearization of the experimental current decay curves of both coatings at long times (Fig. 5a). Their coincidence for two coatings of different roughness is consistent with the fact that the roughness factor is not included in expression (6b), i.e. morphological heterogeneity no longer affects the rate of the electrode process in this time interval. Using formula (6b) and the slope of the linear sections of the $i,t^{1/2}$ curves (Fig. 5a), the total number of electrons involved in the process of electroreduction of the nitrate ion $n \approx 8$ was found, which is consistent with the literature data [28–31].

On the other hand, according to the ratio (6a), at short times the chronoamperogram should be linearized in the coordinates $i - t^{1/2}$, which is observed in the case of both copper coatings (Fig. 5b). Numerical comparison of expression (6a) with the initial sections of the experimental current decay curves using the roughness factor f_r (Table. 2), the total number of electrons $n = 8$ and the diffusion coefficient $D = 1.85 \cdot 10^{-5}$ cm^2/s [27], the rate constant of the charge transfer stage k and the exchange current density $i_0 = nFkc^v$ were found (Table 3).

A comparison of the obtained values shows that the kinetic stage of nitrate ion cathodic

Table 3. Kinetic parameters of the electrochemical stage on copper coatings

Parameter	Coating No. 1 (f_r = 2.56)	Coating No. 2 (f_r = 1.89)
Heterogeneous rate constant k, cm/s	$(3.3\pm0.1)\cdot10^{-3}$	$(2.1\pm0.2)\cdot10^{-3}$
Плотность тока Exchange current density i_0, mA/cm^2	25.5±0.8	16.2±1.5

reduction on a rougher copper electrode is characterized by the higher rate constant and higher exchange current density. This indicates an increase in the electrocatalytic activity of copper in the reaction under study during the transition to electrodes characterized by a higher roughness factor.

It is important to note that this conclusion was obtained taking into account the normalization of the process rate to the true surface area within the framework of the theoretical model of chronoamperometry of an electrochemical process proceeding on a rough electrode in the mode of transport-kinetic control. Therefore, the revealed increase in the rate constant is not apparent, since it is not caused solely by a purely geometric increase in the overall surface area of the copper electrode.

Possible reasons for the increase in k and i_0 during the transition from coating No. 2 to coating No. 1 may be a change in the structure of the polycrystalline sample with the release of more catalytically active crystalline faces to the surface, an increase in the number of active adsorption centers due to an increase in the proportion of surface areas of small curvature, an increase in the concentration of surface defects of the sample. The identification of specific causes of the observed increase in the electrocatalytic activity of the copper coating was not an objective of this work and requires additional research.

The approach used in the work to determine the parameters of the kinetic stage allows us to correctly estimate the role of morphological heterogeneity in changing the electrocatalytic activity of a rough electrode, on the surface of which a complex electrochemical process takes place in the mode of transport-kinetic control. Within the framework of this approach, the contribution of the non-kinetic (diffusion) stage to the value of the rate of the process under study is quantified, and a purely geometric effect associated only with a change in the surface area of the electrode is revealed.

4. Conclusion

Two copper coatings with the different roughness factors (2.56±0.02 amd 1.89±0.02) and the size of the irregularities (the mean roughness of the coatings is 42±4 and 25±2 nm) were synthesized by galvanostatic electrodeposition from aqueous sulfate solutions with organic additives. The electroreduction of the nitrate ion in an acidic aqueous solution on both obtained coatings corresponds to the range of cathodic potentials from –100 to –600 mV relative to the standard hydrogen electrode. Analysis of characteristic parameters of voltammetry (maximum current density and peak potential) revealed the non-stationary nature of the diffusion transfer stage, the irreversibility of the slowed electrochemical stage of the process under study, and a decrease in electrode polarization on a rougher coating.

A mode of mixed transport-kinetic control of the process of nitrate ion electroreduction in an acidic medium at potentiostatic cathodic polarization has been revealed using the non-stationary chronoamperometry method. It is shown that the roughness effect does not contribute to the kinetics of the process at long times, when the non-stationary diffusion of NO_3^- ions is the rate-controlling stage.

Within the framework of the previously developed theoretical model of an electrochemical process occurring in a mixed kinetic mode on a rough electrode, it is shown that the current density recorded during the initial period of current decay should be normalized by the roughness factor. Based on this, an approach is proposed for estimating the main kinetic parameters of the charge transfer stage for a process occurring on rough electrodes in a mixed transport-kinetic mode. The approach is based on comparing the initial sections of the experimental current decay curves with an asymptotic relation describing the chronoamperogram at short times.

The application of this approach to the analysis of the data obtained for the two copper

coatings synthesized in the work made it possible to establish that the heterogeneous rate constant and the exchange current density of the nitrate ion electroreduction increase with increasing roughness factor. This effect is not caused by a purely geometric increase in the true surface area of the electrode, and therefore it can be concluded that the electrocatalytic activity of copper in the reaction under study increases during the transition to rougher electrodes.

Author contributions

The authors contributed equally to this article.

Conflict of interests

The authors declare that they have no known competing financial interests or personal relationships that could have influenced the work reported in this paper.

References

1. Trasatti S., Parsons R. Interphases in systems of conducting phases (Recommendations 1985). *Pure and Applied Chemistry*. 1986;58(3): 437–454. https://doi.org/10.1351/pac198658030437

2. Bard A. J., Inzelt G., Scholz F. (Eds.). *Electrochemical dictionary*. Berlin, Heidelberg: Springer Berlin Heidelberg; 2012. https://doi.org/10.1007/978-3-642-29551-5

3. Jiang K., Huang Y., Zeng G., Toma F.M., Goddard III W. A., Bell A. T. Effects of surface roughness on the electrochemical reduction of CO_2 over Cu. A*CS Energy Letters*. 2020;5(4): 1206–1214. https://doi.org/10.1021/acsenergylett.0c00482

4. Popov K. I., Živković P. M., Nikolić N. D., Branković G. The effect of the electrode surface roughness at low level of coarseness on the polarization characteristics of electrochemical processes. *Electrochimica Acta*. 2010;55(6): 1919–1925. https://doi.org/10.1016/j.electacta.2009.10.085

5. Xie X., Holze R. Electrode kinetic data: geometric vs. real surface area. *Batteries*. 2022;8(10):146. https://doi.org/10.3390/batteries8100146

6. Dobri G., Banu A., Donath C., ... Marcu M. Effect of surface roughness on the electrochemical behavior and corrosion resistance of TiTaNbZrAg alloy with different amounts of tantalum in bulk composition. *Materials*. 2024;17(21): 5217. https://doi.org/10.3390/ma17215217

7. Xu R., Jin X., Bi H., Zhang Zh., Li M. Effect of surface roughness on contact resistance and electrochemical corrosion behavior of 446 stainless steel in simulated anode environments for proton exchange membrane fuel cell. *Journal of Solid State Electrochemistry*. 2024;28: 3087–3098. https://doi.org/10.1007/s10008-024-05864-z

8. Kim Y., Yoo M., Moon M. Effects of surface roughness on the electrochemical properties and galvanic corrosion behavior of CFRP and SPCC alloy. *Materials*. 2020;13(18): 4211. https://doi.org/10.3390/ma13184211

9. Douglass Jr. E. F., Driscoll P. F., Liu D., Burnham N. A., Lambert C. R., McGimpsey W. G. Effect of electrode roughness on the capacitive behavior of self-assembled monolayers. *Analytical Chemistry*. 2008:80(20): 7670–7677. https://doi.org/10.1021/ac800521z

10. Trasatti S., Petrii O. A. Real surface area measurements in electrochemistry. *Journal of Electroanalytical Chemistry*. 1992;327(1-2): 353–376. https://doi.org/10.1016/0022-0728(92)80162-W

11. Bard A. J., Faulkner L. R. *Electrochemical methods: fundamentals and applications*. *2nd Edition*. New York: John Wiley & Sons; 2001.

12. Kozaderov O. A. Surface roughness effect in the kinetics of heterogeneous processes. *Condensed Matter and Interphases*. 2017;19(1): 6–21. (in Russ.) https://doi.org/10.17308/kcmf.2017.19/171

13. Vdovenkov F. A., Kolosov A. N., Kuzmenko G. A., Kozaderov O. A. Simulation of a non-stationary electrochemical process on rough electrodes under mixed kinetic-diffusion control. *Condensed Matter and Interphases*. 2025;27(1): 592–605 https://doi.org/10.17308/kcmf.2025.27/13297

14. Lebedeva O., Kuznetsova I., Kultin D., ... Kustov L. Efficiency of the electrocatalytic nitrate reduction to ammonia: do the surface nanostructures play an essential role? *Catalysts*. 2025;15(7): 666. https://doi.org/10.3390/catal15070666

15. Pérez-Gallent E., Figueiredo M. C., Katsounaros I., Koper M. T. M. Electrocatalytic reduction of nitrate on copper single crystals in acidic and alkaline solutions. *Electrochimica Acta*. 2017;227: 77–84. https://doi.org/10.1016/j.electacta.2016.12.147

16. Farina R., D'Arrigo G., Alberti A., ... Libertino S. Copper micro-flowers for electrocatalytic sensing of nitrate ions in water. *Sensors*. 2024;24(14): 4501. https://doi.org/10.3390/s24144501

17. Hou T., Shan T., Rong H., Zhang J. Nitrate electroreduction to ammonia over copper-based catalysts. *ChemSusChem*. 2025;18(9): e202402331. https://doi.org/10.1002/cssc.202402331

18. Farina R., D'Arrigo G., Alberti A., ... Libertino S. Electrochemical growth of copper crystals on SPCE for electrocatalysis nitrate reduction. *Nanomaterials*. 2024;14(21): 1704. https://doi.org/10.3390/nano14211704

19. Shih Y.-J., Wu Z.-L., Lin C.-Y., Huang Y.-H., Huang C.-P. Manipulating the crystalline morphology and facet orientation of copper and copper-palladium nanocatalysts supported on stainless steel mesh with the aid of cationic surfactant to improve the electrochemical reduction of nitrate and N_2 selectivity. *Applied Catalysis B: Environmental*. 2020;273: 119053. https://doi.org/10.1016/j.apcatb.2020.119053

20. Dima G. E., De Vooys A. C. A., Koper M. T. M. Electrocatalytic reduction of nitrate at low concentration on coinage and transition-metal electrodes in acid solutions. *Journal of Electroanalytical Chemistry*. 2003;554–555: 15–23. https://doi.org/10.1016/S0022-0728(02)01443-2

21. Rosca V., Duca M., De Groot M. T., Koper M. T. M. Nitrogen cycle electrocatalysis. *Chemical Reviews*. 2009;109(6): 2209–2244 https://doi.org/10.1021/cr8003696

22. Kozaderov O., Sotskaya N., Yudenkova L., Buylov N., Ilina E. Electrocrystallization and morphology of copper coatings in the presence of organic additives. *Coatings*. 2023;13(11): 1896. https://doi.org/10.3390/coatings13111896

23. Giri S. D., Sarkar A. Estimating surface area of copper powder: A comparison between electrochemical, microscopy and laser diffraction methods. *Advanced Powder Technology*. 2018;29(12): 3520–3526. https://doi.org/10.1016/j.apt.2018.09.034

24. Galus Z. *Fundamentals of electrochemical analysis*. Chichester: Ellis Horwood: New York: Halsted Press, a division of Wiley; 1974. 520 p.

25. Kozaderov O. A., Lozovskii V. V., Vvedenskii A. V. Chronovoltammetry of the anodic dissolution of Ag-Au alloys in nitrate environments. *Protection of Metals*. 2008;44(4): 333–342. https://doi.org/10.1134/S0033173208040036

26. Bedova E. V., Kolganova D. I., Kozaderov O. A. Voltamperometry of a kinetically irreversible electrochemical process on a rough electrode. *Condensed Matter and Interphases*. 2020;22(2): 211–218. https://doi.org/10.17308/kcmf.2020.22/2833

27. Abir A. Y., Nizam Uddin S. M., Hasan M., ... Hasnat M. A. Cu-electrodeposited gold electrode for the sensitive electrokinetic investigations of nitrate reduction and detection of the nitrate ion in acidic medium. *Results in Chemistry*. 2023;5: 100702. https://doi.org/10.1016/j.rechem.2022.100702

28. Butcher D. P., Gewirth D. P. Nitrate reduction pathways on Cu single crystal surfaces: effect of oxide and Cl^-. *Nano Energy*. 2016;29: 457–465. https://doi.org/10.1016/j.nanoen.2016.06.024

29. Bae S.-E., Stewart K. L., Gewirth A. A. Nitrate adsorption and reduction on Cu(100) in acidic solution. *Journal of the American Chemical Society*. 2007;129(33): 10171–10180. https://doi.org/10.1021/ja071330n

30. Bae S. E., Gewirth A. A. Differential reactivity of Cu(111) and Cu(100) during nitrate reduction in acid electrolyte. *Faraday Discuss*. 2008;140: 113-23; https://doi.org/10.1039/b803088j

31. Pletcher D., Poorabedi Z. The reduction of nitrate at a copper cathode in aqueous acid *Electrochimica Acta*. 1979;24: 1253–1256. https://doi.org/10.1016/0013-4686(79)87081-4

Information about the authors

Frol A. Vdovenkov, postgraduate student, Department of Physical Chemistry, Faculty of Chemistry, Voronezh State University (Voronezh, Russian Federation).

https://orcid.org/0009-0009-4737-9218-

f.vdovenkov@gmail.com

Oleg A. Kozaderov, Dr. Sci. (Chem.), Leading Researcher at the Laboratory of organic additives for the processes of chemical and electrochemical deposition of metals and alloys used in the electronics industry, Voronezh State University (Voronezh, Russian Federation).

https://orcid.org/0000-0002-0249-9517

ok@chem.vsu.ru

Pavel P. Tarakanov, student, Department of Physical Chemistry, Faculty of Chemistry, Voronezh State University (Voronezh, Russian Federation).

https://orcid.org/0009-0005-6901-8772

tarakanov.pavlik2015@yandex.ru

Pavel V. Fomin, student, Department of Physical Chemistry, Faculty of Chemistry, Voronezh State University (Voronezh, Russian Federation).

https://orcid.org/0009-0008-7167-7795

pavel1.fomin@bk.ru

Received April 28, 2025; approved after reviewing May 26, 2025; accepted for publication September 15, 2025; published online April 01, 2026.

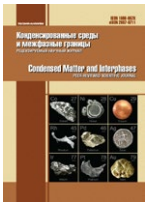

ISSN 1606-867X (Print)
ISSN 2687-0711 (Online)
Condensed Matter and Interphases
Kondensirovannye Sredy i Mezhfaznye Granitsy
https://journals.vsu.ru/kcmf/

Original articles

Research article
https://doi.org/10.17308/kcmf.2026.28/13558

Silicon nanowires modified with Au/Ag nanoparticles for the label-free detection of prostate-specific antigen using surface-enhanced Raman spectroscopy

K. A. Gonchar[1,2]✉, N. Yu. Saushkin[3], J. V. Samsonova[3], L. A. Osminkina[1,2]✉

[1]Lomonosov Moscow State University, Faculty of Physics,
1, Leninskie Gory, Building 2, Moscow 119991, Russian Federation

[2]Institute of Biological Instrumentation, Russian Academy of Sciences,
7, Institutskaya st., Pushchino 142290, Russian Federation

[3]Lomonosov Moscow State University, Faculty of Chemistry,
1, Leninskie Gory, Building 3, Moscow 119991, Russian Federation

Abstract

Objective: Prostate-specific antigen (PSA) is an important biomarker widely used for the early diagnosis of prostate cancer. In this work, substrates based on silicon nanowires coated with bimetallic gold and silver nanoparticles (AuAg@SiNWs) are presented for the highly sensitive detection of PSA using surface-enhanced Raman spectroscopy (SERS).

Experimental: The fabrication of AuAg@SiNWs was based on simple and readily accessible chemical etching and metal deposition techniques, making the approach suitable for scaling and potential biomedical applications. The thickness of the silicon nanowire array was approximately 800 nm, while the bimetallic nanoparticle layer was formed predominantly in the upper region of the nanostructures and exhibited a thickness of 100–200 nm. To ensure the biospecificity of the sensor, the surfaces of the AuAg@SiNW substrates were functionalized with antibodies.

Analysis of the SERS spectra revealed a clear dependence of the intensity of characteristic amide bands (in particular, at 1294 and 1030 cm^{-1}) on the PSA concentration, starting from 1 ng/mL. The calculated calibration curve in the concentration range of 0.001–1 μg/mL demonstrated a high degree of linearity (R^2 = 0.96), while the stable presence of characteristic spectral features at a concentration of 1 ng/mL indicates the high functional sensitivity of the proposed platform.

Conclusions: The results obtained demonstrate that AuAg@SiNW-based substrates possess significant potential for label-free and highly sensitive detection of protein cancer biomarkers, including PSA, and can be used as a platform for the development of compact biosensors for laboratory diagnostics and point-of-care applications.

Keywords: Silicon nanowires, Prostate-specific antigen (PSA), Surface-enhanced Raman spectroscopy

Funding: This research was supported by the Russian Science Foundation (Grant No. 22-72-10062; https://rscf.ru/en/project/22-72-10062/).

Acknowledgments: The authors acknowledge the use of equipment from the Educational and Methodological Center for Lithography and Microscopy of Lomonosov Moscow State University, as well as the Shared Research Facilities Center of Lomonosov Moscow State University "Technologies for the Fabrication of Novel Nanostructured Materials and Their Comprehensive Characterization." The equipment was acquired by Lomonosov Moscow State University within the framework of the national project "Science and Universities" and the MSU Development Program.

For citation: Gonchar K. A., Saushkin N. Yu., Samsonova J. V., Osminkina L. A. Silicon nanowires modified with Au/Ag nanoparticles for the label-free detection of prostate-specific antigen using surface-enhanced Raman spectroscopy. *Condensed Matter and Interphases*. 2026;28(1): 40–45. https://doi.org/10.17308/kcmf.2026.28/13558

✉ Kirill A. Gonchar, e-mail: k.a.gonchar@gmail.com
✉ Lyubov A. Osminkina, e-mail: osminkina@physics.msu.ru

Для цитирования: Гончар К. А., Саушкин Н. Ю., Самсонова Ж. В., Осминкина Л. А. Кремниевые нанонити, модифицированные наночастицами Au/Ag, для безметочной диагностики онкомаркера ПСА методом спектроскопии гигантского комбинационного рассеяния. *Конденсированные среды и межфазные границы*. 2026;28(1): 40–45. https://doi.org/10.17308/kcmf.2026.28/13558

1. Introduction

Cancer remains one of the major threats to human survival due to its significant impact on global health. Prostate cancer is the most common malignancy among men over the age of 50. Early diagnosis of prostate cancer is closely associated with prostate-specific antigen (PSA), which is regarded as the gold-standard biomarker. PSA is a 34 kDa single-chain glycoprotein secreted by the prostate gland [1]. It is well known that an increase in serum PSA concentration in prostate cancer is caused by tumor cell proliferation, disruption of the affected organ, and subsequent leakage of the antigen into the systemic circulation. PSA concentrations exceeding 4 ng/mL are detected in approximately 80–90 % of patients with prostate cancer and in 10–20 % of patients with benign prostatic hyperplasia.

At present, several methods are used for the determination of PSA levels, including enzyme-linked immunosorbent assay (ELISA) [2], immunochromatographic analysis [3], chemiluminescent immunoassay [4], silicon nanowire-based field-effect transistor sensors [5], and Raman scattering techniques [6]. One of the increasingly popular approaches for PSA detection is surface-enhanced Raman spectroscopy (SERS) [7–9]. SERS is a modification of conventional Raman scattering in which a strong enhancement of the signal from molecules adsorbed on nanostructured noble metal surfaces, most commonly gold or silver, is observed. The efficiency of SERS is largely determined by the morphology of the nanostructure, the type of metal used, and the distance between the analyte molecules and the metal surface.

Nanostructured silicon substrates have been actively investigated in recent years as a basis for the development of SERS-active sensing chips. Their key advantage lies in a high degree of structural tunability, which enables targeted modification of the silicon morphology at the synthesis stage. Among such substrates are silicon nanowires (SiNWs) fabricated by metal-assisted chemical etching (MACE) [10, 11]. By varying the MACE parameters, it is possible to control key structural characteristics, including pore size, nanowire height and diameter, nanostructure density and orientation, as well as the degree of their mutual aggregation. To impart SERS activity, SiNWs are additionally decorated with silver and/or gold nanoparticles [12, 13]. These structures have already demonstrated their effectiveness in the detection of bacteria [12], as well as in studies of bacterial sensitivity to antibiotics [13].

In [14], the feasibility of PSA detection by SERS using aptamer-functionalized SiNWs was demonstrated. However, that study employed exclusively silver nanoparticles, which, despite their high signal enhancement efficiency, are susceptible to oxidation and structural degradation during storage. This significantly reduces the reproducibility and long-term stability of the SERS response, particularly when operating in biological fluids. Such substrates are therefore less reliable than bimetallic Au/Ag systems, which provide more stable plasmonic behavior and improved chemical stability of the surface.

The aim of the present study is to develop and evaluate the performance of SERS-active substrates based on silicon nanowires modified with gold and silver nanoparticles for highly sensitive PSA detection using immobilized antibodies as the bioselective recognition element.

2. Experimental

SiNWs modified with gold and silver nanoparticles (AuAg@SiNWs) were fabricated by metal-assisted chemical etching (MACE) of a p-type crystalline silicon (c-Si) wafer with (100) crystallographic orientation and a resistivity of 0.8–1.2 Ω·cm. Prior to etching, the c-Si wafer was sequentially cleaned in acetone and isopropanol using an ultrasonic bath, followed by immersion in 5 M HF to remove the native oxide layer from the surface.

During the first stage, gold nanoparticles were deposited onto the c-Si surface by immersing the wafer into a solution of 0.01 M $AuCl_3$ and 5 M HF mixed in a volume ratio of 1:1 for 15 s. During

the second stage of the MACE process, the gold nanoparticle-coated c-Si wafer was placed into a solution of 30 % H_2O_2 and 5 M HF with a volume ratio of 1:10 for 2 min. During this step, localized etching occurred beneath the gold nanoparticles, enabling their penetration into the c-Si substrate and resulting in the formation of SiNWs.

Afterwards, the obtained SiNW arrays were sequentially immersed in a solution of 0.02 M $AgNO_3$ and 5 M HF mixed in a volume ratio of 1:1, followed by immersion in a solution of 0.01 M $AuCl_3$ and 5 M HF with the same volume ratio, for 30 s in each solution. As a result, SiNWs modified with silver and gold nanoparticles (AuAg@SiNWs) were obtained.

The morphology of the fabricated AuAg@SiNWs was examined using a scanning electron microscope (SEM, Carl Zeiss SUPRA 40).

The feasibility of PSA signal registration by SERS under conditions of nonspecific interaction with different types of substrates was initially evaluated. It was established that, in the absence of antibodies providing specific antigen binding, PSA detection using these nanostructured substrates was not possible. Therefore, to ensure the specific interaction of PSA with the AuAg@SiNW surface, preliminary functionalization of the substrates with antibodies capable of covalent attachment to gold nanoparticles via thiol groups was required.

The reduction of disulfide bonds in antibody molecules to generate free thiol groups was performed according to the procedure described in [15]. Briefly, 12 mg of 2-mercaptoethanolamine was added to 1 mg of monoclonal antibodies (mAbs) specific to PSA (clone 5A6, HyTest) dissolved in 10 mM phosphate-buffered saline (PBS, pH 7.3) containing 5 mM EDTA, followed by incubation for 1.5 h at 37 °C. Low-molecular-weight reaction components were removed using a PD-10 desalting gel-filtration column based on Sephadex G-25 (GE Healthcare).

For long-term storage, the resulting solution of reduced antibodies was stored at –20 °C in 50 % glycerol. AuAg@SiNW substrates were incubated in a solution of reduced antibodies (10 μg/mL in physiological saline) for 1 h at room temperature under gentle agitation, followed by three washing steps (1 min each) with physiological saline containing 0.1 % Tween 20. Subsequently, the AuAg@SiNW substrates with immobilized reduced antibodies were incubated in PSA solutions prepared in physiological saline over a concentration range of 0-1000 ng/mL for 1 h at room temperature under gentle agitation, followed by three washing steps (1 min each) with physiological saline containing 0.1 % Tween 20.

SERS spectra were recorded using a confocal microscope Confotec™ MR350 with laser excitation at a wavelength of 633 nm and a laser power of 1 mW.

3. Results and discussion

An SEM micrograph of the fabricated AuAg@SiNW substrates is shown in Fig. 1. The SiNW layer has a thickness of approximately 800 nm, whereas the bimetallic nanoparticle layer formed in the upper region of the nanowires ranges from 100 to 200 nm in thickness. Such a layer thickness suggests sufficiently dense nanoparticle coverage to achieve efficient plasmonic enhancement. Larger particles observed on the surface of the SiNWs correspond to silver nanoparticles, while the bright spots on their surface are attributed to gold nanoparticles. The bright features located at the SiNW/c-Si substrate interface correspond to gold nanoparticles that penetrated into the silicon during the formation of the nanowires.

Fig. 2 presents a SERS spectrum recorded from antibody-functionalized AuAg@SiNW substrates after incubation with a PSA solution at a concentration of 1 μg/mL. The peak at 520 cm^{-1} corresponds to the optical phonon mode of c-Si, which forms the basis of the nanowire structure.

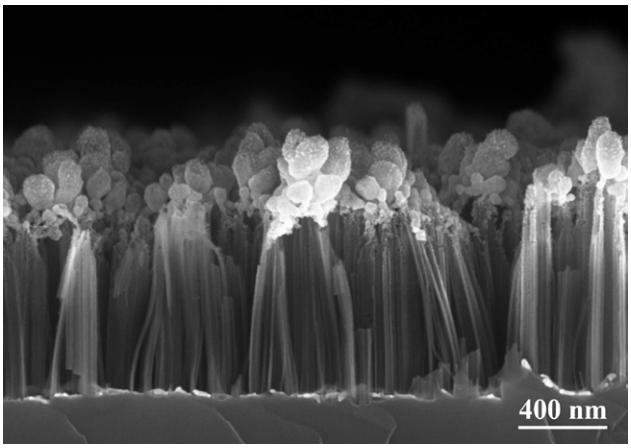

Fig. 1. SEM micrograph of a sample AuAg@SiNWs

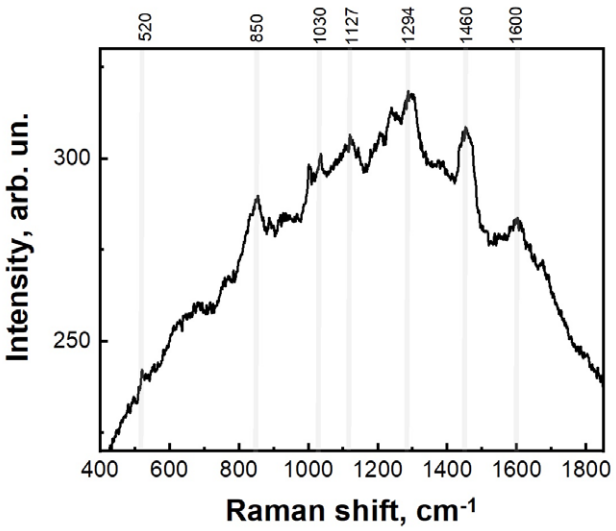

Fig. 2. SERS spectrum of PSA adsorbed on an AuAg@SiNW substrate at a concentration of 1 μg/mL

The increased background signal is attributed to photoluminescence originating from the SiNWs.

The remaining peaks in the spectrum can be attributed to vibrational modes of protein biomolecules. The band at 1000 cm^{-1} corresponds to the symmetric ring breathing mode of the phenyl group, which is characteristic of the aromatic α-amino acid phenylalanine, a constituent of most proteins. Bands in the range of 1110–1260 cm^{-1} are assigned to amide III vibrations, while the band at 1294 cm^{-1} is associated with C–N and N–H stretching modes within the amide III region. The peak at 1460 cm^{-1} is related to deformation vibrations of the C–NH bond in amide II, whereas the signal at 1600 cm^{-1} corresponds to C=O stretching vibrations of the peptide bond in the amide I region [14, 16]. These observations confirm the feasibility of efficient and reliable PSA protein detection using the developed AuAg@SiNW composite substrates via surface-enhanced Raman spectroscopy.

Fig. 3 shows SERS spectra recorded from AuAg@SiNW substrates after incubation with PSA solutions at different concentrations, ranging from 1 μg/mL to 1 ng/mL. The spectrum corresponding to the highest PSA concentration is shown at the top (black), while the spectrum of the control substrate functionalized with antibodies but without PSA is shown at the bottom (violet). The spectra are presented after subtraction of the photoluminescence background and are vertically offset for clarity.

It should be noted that the spectra of PSA and antibodies exhibit similar spectral features, which is attributable to their common protein nature. However, in the PSA spectra, pronounced bands at 1294 cm^{-1} and 1030 cm^{-1} are clearly observed, with intensities significantly exceeding those of the corresponding signals in the antibody spectra. This indicates a contribution of PSA molecules to the enhanced SERS response and confirms the possibility of their selective detection against a protein background.

Fig. 4 presents the calibration curve of the SERS signal intensity at 1294 cm^{-1} as a function of PSA concentration in the range from 1 ng/mL to 1 μg/mL. Linear fitting of the experimental data is described by the equation $y = 1969.1 + 411.4x$, with a coefficient of determination of $R^2 = 0.96$, indicating a strong correlation between antigen concentration and spectral response intensity. The observed linear relationship confirms the feasibility of quantitative PSA analysis based on the intensity of the amide band in the SERS spectrum. In the low-concentration region, starting from 1 ng/mL, a distinct specific signal

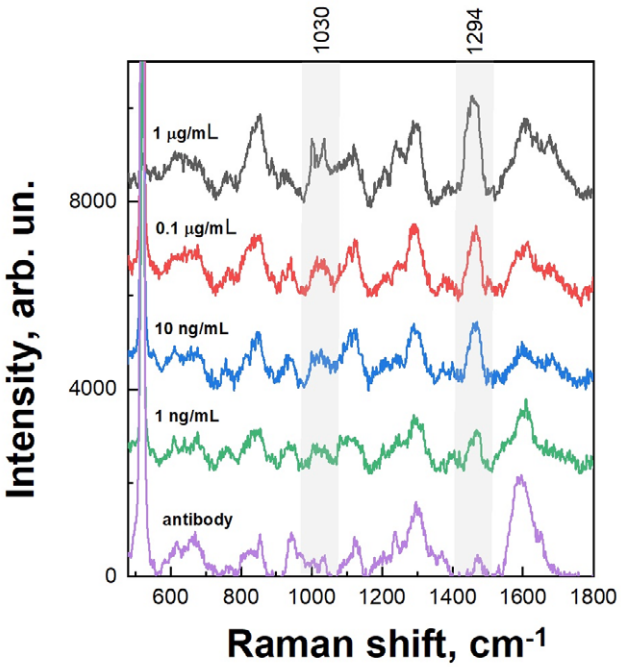

Fig. 3. SERS spectra recorded from AuAg@SiNW substrates after incubation with PSA solutions at different concentrations, ranging from 1 μg/mL to 1 ng/mL

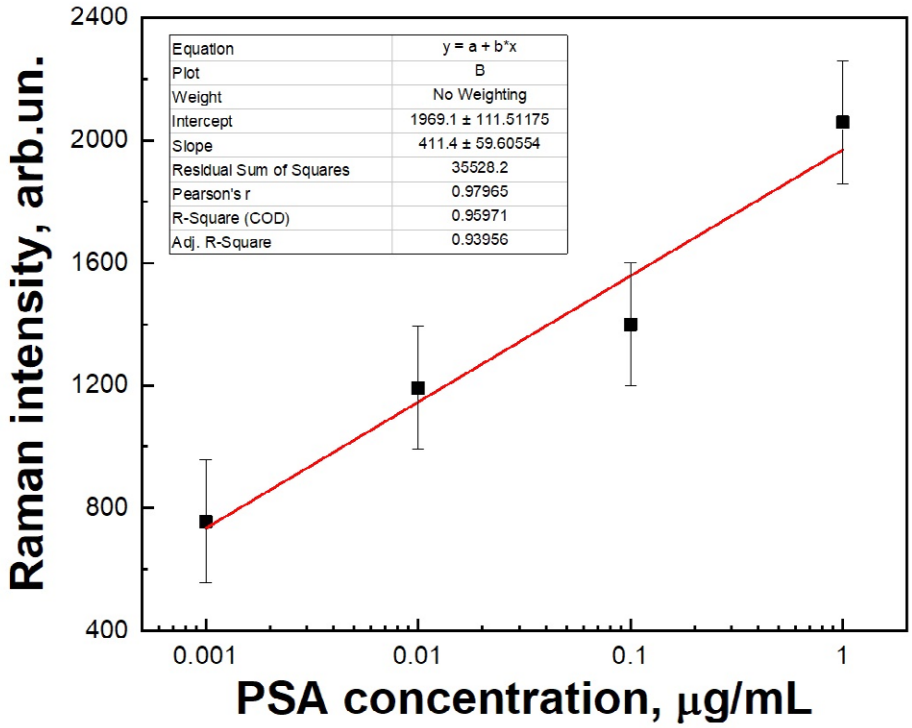

Fig. 4. Calibration curve of the SERS signal intensity at 1294 cm^{-1} as a function of PSA concentration in the range from 1 μg/mL to 1 ng/mL

is clearly detected, demonstrating the high sensitivity of the developed sensing platform.

4. Conclusions

This work presents the development and experimental evaluation of reproducible and sensitive SERS substrates based on arrays of silicon nanowires modified with bimetallic gold and silver nanoparticles (AuAg@SiNWs). The chemical etching and metal deposition methods employed are technologically simple, scalable, and compatible with silicon microelectronics, making the proposed approach promising for practical implementation.

The thickness of the SiNW arrays was approximately 800 nm, while the bimetallic nanoparticle layer was predominantly formed in the upper region of the nanostructures with a thickness of 100–200 nm. Such an architecture ensures dense and localized placement of metal nanoparticles, facilitating the formation of plasmonic hot spots and efficient signal enhancement.

To ensure biospecificity, the surface of the AuAg@SiNW substrates was functionalized with antibodies specific to prostate-specific antigen. Analysis of the SERS spectra revealed a clear dependence of the intensity of characteristic amide bands (in particular, at 1294 and 1030 cm^{-1}) on PSA concentration, starting from 1 ng/mL. The calculated calibration curve in the concentration range of 0.001–1 μg/mL exhibited a high degree of linearity (R^2 = 0.96). The stable presence of characteristic spectral features at a PSA concentration of 1 ng/mL indicates the high functional sensitivity of the developed platform.

The obtained results confirm that AuAg@SiNW-based substrates have high potential for highly sensitive detection of protein cancer biomarkers such as PSA and may serve as a basis for the development of compact biosensors for laboratory diagnostics and point-of-care applications.

Author contributions

The authors contributed equally to this article.

Conflict of interests

The authors declare that they have no known competing financial interests or personal relationships that could have influenced the work reported in this paper.

References

1. Pinsky P. ., Prorok P. C., Yu K., ... Andriole G. L. Extended mortality results for prostate cancer screening in the PLCO trial with median follow-up of 15 years. *Cancer*. 2017;123(4): 592–599. https://doi.org/10.1002/cncr.30474

2. Zangar R. C., Daly D. S., White A. M. ELISA microarray technology as a high-throughput system for cancer biomarker validation. *Expert Review of Proteomics*. 2006;3(1): 37–44. https://doi.org/10.1586/14789450.3.1.37

3. Li X., Li W., Yang Q., ... Chang J. Rapid and quantitative detection of prostate specific antigen with a quantum dot nanobeads-based immunochromatography test strip. *ACS Applied Materials & Interfaces*. 2014;6(9): 6406–6414. https://doi.org/10.1021/am5012782

4. Zhao L., Sun L., Chu X. Chemiluminescence immunoassay. *TrAC Trends in Analytical Chemistry*. 2009;28(4): 404–415. https://doi.org/10.1016/j.trac.2008.12.006

5. Presnova G., Presnov D., Krupenin V., ... Rubtsova M. Biosensor based on a silicon nanowire field-effect transistor functionalized by gold nanoparticles for the highly sensitive determination of prostate specific antigen. *Biosensors and Bioelectronics*. 2017;88: 283–289. https://doi.org/10.1016/j.bios.2016.08.054

6. Correia N. A., Batista L. T. A., Nascimento R. J. M., ... Pinheiro A. L. B. Detection of prostate cancer by Raman spectroscopy: a multivariate study on patients with normal and altered PSA values. *Journal of Photochemistry & Photobiology B: Biology*. 2020;204: 111801. https://doi.org/10.1016/j.jphotobiol.2020.111801

7. Cheng Z., Choi N., Wang R., ... Choo J. Simultaneous detection of dual prostate specific antigens using surface-enhanced Raman scattering-based immunoassay for accurate diagnosis of prostate cancer. *ACS Nano*. 2017;11(5): 4926–4933. https://doi.org/10.1021/acsnano.7b01536

8. Hao T., Wu X., Xu L., ... Xu C. Ultrasensitive detection of prostate-specific antigen and thrombin based on gold-upconversion nanoparticle assembled pyramids. *Small*. 2017;13(19): 1603944. https://doi.org/10.1002/smll.201603944

9. Zhao J., Wang J., Liu Y., ... Zhao B. Detection of prostate cancer biomarkers via a SERS-based aptasensor. *Biosensors and Bioelectronics*. 2022;216: 114660. https://doi.org/10.1016/j.bios.2022.114660

10. Gonchar K. A., Bozh'ev I. V., Shalygina O. A., Osminkina L. A. Optical properties of silicon nanowires obtained by metal-assisted chemical etching using gold nanoparticles. *Journal of Experimental and Theoretical Physics Letters*. 2023;117(1-2): 115–120. https://doi.org/10.31857/S1234567823020052

11. Shatskaia M. G., Nazarovskaia D. A., Gonchar K. A., ... Osminkina L. A. Photoluminescent porous silicon nanowires as contrast agents for bioimaging. *Condensed Matter and Interphases.*, 2024;6(1): 161–167. https://doi.org/10.17308/kcmf.2024.26/11819

12. Nazarovskaia D. A., Domnin P. A., Gyuppenen O. D., ... Osminkina L. A. Advanced bacterial detection with SERS-active gold- and silver-coated porous silicon nanowires. *Bulletin of the Russian Academy of Sciences: Physics*. 2023;87(Suppl. 1): S41–S46. https://doi.org/10.1134/S1062873823704385

13. Nazarovskaia D. A., Domnin P. A., Gyuppenen O. D., ... Osminkina L. A. Bimetallic AuAg-coated porous silicon nanowire platform for rapid SERS-based antibiotic susceptibility testing. *Results in Surfaces and Interfaces*. 2025;19: 100524. https://doi.org/10.1016/j.rsurfi.2025.100524

14. Ouhibi A., Raouafi A., Lorrain N., Guendouz M., Raouafi N., Moadhen A. Functionalized SERS substrate based on silicon nanowires for rapid detection of prostate specific antigen. *Sensors & Actuators: B. Chemical*. 2021;330: 129352. https://doi.org/10.1016/j.snb.2020.129352

15. Karyakin A. A., Presnova G. V., Rubtsova M. Y., Egorov A. M. Oriented immobilization of antibodies onto the gold surfaces via their native thiol groups. *Analytical Chemistry*. 2000;72(16): 3805–3811. https://doi.org/10.1021/ac9907890

16. Ten G. N., Gerasimenko A. Y., Shcherbakova N. E., Baranov V. I. Interpretation of IR and Raman Spectra of Albumin. *Izvestiya of Saratov University. Physics*. 2019;19(1): 43-57. https://doi.org/10.18500/1817-3020-2019-19-1-43-57

Information about the authors

Kirill A. Gonchar, Cand. Sci. (Phys.–Math.), Senior Researcher, Faculty of Physics, Lomonosov Moscow State University (Moscow, Russian Federation); Institute of Biological Instrumentation Russian Academy of Sciences (Pushchino, Russian Federation).

https://orcid.org/0000-0002-2301-2886

k.a.gonchar@gmail.com

Nikolay Yu. Saushkin, Cand. Sci. (Chem.), Researcher, Faculty of Chemistry, Lomonosov Moscow State University (Moscow, Russian Federation).

https://orcid.org/0000-0002-4565-2075

sushk_90@mail.ru

Jeanne V. Samsonova, Cand. Sci. (Chem.), Senior Researcher, Department of Chemistry, Lomonosov Moscow State University (Moscow, Russian Federation).

https://orcid.org/0000-0002-0670-0951

jvsamsonova@gmail.com

Liubov A. Osminkina, Cand. Sci. (Phys.–Math.), Leading Researcher, Department of Physics, Lomonosov Moscow State University (Moscow, Russian Federation); Institute of Biological Instrumentation, Russian Academy of Sciences (Pushchino, Russian Federation).

https://orcid.org/0000-0001-7485-0495

osminkina@physics.msu.ru

Received April 18, 2025 approved after reviewing April 30, 2025; accepted for publication May 12, 2025; published online April 01, 2026.

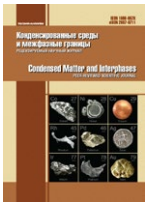

ISSN 1606-867X (Print)
ISSN 2687-0711 (Online)
Condensed Matter and Interphases
Kondensirovannye Sredy i Mezhfaznye Granitsy
https://journals.vsu.ru/kcmf/

Original articles

Research article
https://doi.org/10.17308/kcmf.2026.28/13590

Thermodynamic study of the BiSI-BiSeI system by the electromotive force method

A. A. Qurbanov[1], E. J. Ahmadov[2]✉, G. M. Shukurova[3], I. J. Alverdiyev[1], Y. I. Jafarov[3]

[1]Ganja State University,
187, H. Aliyev av., Ganja AZ-2000, Azerbaijan

[2]Institute of Chemistry,
113, H. Javid av., Baku AZ-1143, Azerbaijan

[3]Baku State University,
23, Z. Khalilov st., Baku Az-1148, Azerbaijan

Abstract

Objectives: Chalcohalides of arsenic subgroup elements and solid solutions based on them are of great interest as functional materials exhibiting thermoelectric, photoelectric, piezoelectric, optical, and other properties.

Experimental: This paper presents the results of a study of the thermodynamic properties of BiSI, BiSeI, and $BiS_{1-x}Se_xI$ solid solutions using electromotive force (EMF) analysis. For this study, concentration cells of the type

(–) Bi (solid)/liquid electrolyte, Bi^{3+}/(Bi in alloy) (solid) (+)

were constructed and their EMFs were measured in the temperature range of 300-370 K. An ionic liquid, namely, morpholine formate, was used as the electrolyte. To select the compositions of the right-hand electrodes, solid-state equilibria in the BiSI-BiSeI-BiI_3 system were studied using X-ray diffraction analysis. Continuous solid solutions of the BiSI-BiSeI boundary system were shown to form stable tie-line with BiI_3. Using these data and literature information on boundary systems, a fragment of the solid-phase equilibria diagram for the Bi-S-Se-I system was constructed. Based on constructed diagram, the $BiS_{1-x}Se_xI$ solid solutions of various compositions with a 2–3 mol % excess of BiI_3 and $S_{1-x}Se_x$ were selected as electrode-alloys for the aforementioned concentration cells. The partial molar functions of bismuth in the alloys were calculated from the obtained pairs of *E*(mV) and *T*(K) values.

Conclusions: The constructed phase diagram made it possible to determine the virtual reactions of potential formation corresponding to the aforementioned partial molar functions and calculate the standard thermodynamic functions of formation and the standard entropies of bismuth thio- and selenoidide and $BiS_{1-x}Se_xI$ solid solutions. The calculations were performed using literature data on the corresponding standard integral thermodynamic functions of the BiI_3 compound and $S_{1-x}Se_x$ alloys involved in potential-forming reactions. The thermodynamic functions of the BiSI and BiSeI compounds were compared with existing fragmentary literature data, and for solid solutions, they were determined for the first time.

Keywords: Bismuth chalcoiodides, Phase diagram, Solid solutions, EMF method, Thermodynamic functions, Ionic liquid

For citation: Qurbanov A. A., Ahmadov E. J., Shukurova G. M., Alverdiyev I. J., Jafarov Y. I. Thermodynamic study of the BiSI-BiSeI system by the electromotive force method. *Condensed Matter and Interphases*. 2026; 28(1): 46–56. https://doi.org/10.17308/kcmf.2026.28/13590

Для цитирования: Гурбанов А. А., Ахмедов Э. Дж., Шукурова Г. М., Алвердиев И. Дж., Джафаров Я. И. Термодинамическое исследование системы BiSI-BiSeI методом электродвижущих сил. *Конденсированные среды и межфазные границы*. 2026; 28(1): 46–56. https://doi.org/10.17308/kcmf.2026.28/13590

✉ Elvin J. Ahmadov, e-mail: elvin.j.ahmadov@gmail.com

1. Introduction

Compounds of the B^VXHal type (B^V = As, Sb, Bi; X = S, Se, Te; Hal = Cl, Br, I) and phases based on them have recently attracted considerable research interest due to their thermoelectric, photoelectric, piezoelectric and optical properties and are considered promising for several practical applications in modern high technologies [1–7]. In addition, a number of compounds of this type are Rashba semiconductors and are considered good candidates for use in spintronic devices [8–11].

The search and development of methods for obtaining new multicomponent phases and materials is based on data from fundamental research on phase equilibria and the thermodynamic properties of the corresponding systems [12–15]. One of the rational approaches to the comprehensive investigation of these characteristics is the incorporation of the electromotive force (EMF) method into the traditional set of experimental methods for studying phase equilibria [15]. The EMF method, being one of the most accurate equilibrium methods of chemical thermodynamics [16–18], is widely used for the comprehensive investigation of phase equilibria and thermodynamic properties of inorganic systems. Thermodynamic data obtained by this method, in addition to internal consistency within an individual phase, are also characterized by mutual consistency of their values for all phases of the system and with the phase diagram [15].

In practical thermodynamic investigations, various modifications of concentration cells with liquid [19–23] and solid electrolytes [24–28] are employed. It should be noted that in most cases, when studying chalcogenide and chalcohalide systems by this method, it is advisable to conduct experiments in the subsolidus region of the phase diagram, i.e., below the melting point of the corresponding chalcogen. The most widely used electrolytes for such measurements have been glycerol solutions of alkali metal salts, the application of which has made it possible to carry out thermodynamic studies even at room temperature [16, 17, 29–31]. A number of studies [32-35] have demonstrated the possibility of using ionic liquids as electrolytes in such low-temperature EMF measurements.

To obtain new sets of mutually consistent data for antimony and bismuth chalcoiodides, we have carried out systematic investigations of phase equilibria and thermodynamic properties of a series of ternary B^V-X-Hal systems [36–40], as well as some more complex systems including these elements [41–45].

This study aimed to investigate solid-phase equilibria in the composition area BiSeI-BiSI-BiI_3 (A) of the quaternary Bi-S-Se-I system and to determine the thermodynamic functions of the ternary BiSI, BiSeI compounds, and $BiS_{1-x}Se_xI$ solid solutions by the EMF method.

The BiSeI-BiSI and $Bi_{19}S_{27}I_3$-"$Bi_{19}Se_{27}I_3$" sections of the indicated system were studied by us in [46, 47]. It was shown that the first is characterized by the formation of a continuous series of solid solutions, and the second – a wide area of solid solutions (up to 70 mol %) based on $Bi_{19}S_{27}I_3$.

2. Experimental

For the thermodynamic study of solid solutions along the BiSI-BiSeI section, concentration cells of the type

(-) Bi (solid) / liquid electrolyte,
Bi^{3+} / (Bi in alloy) (solid) (+) (1)

were assembled and their EMF values were measured in the temperature range of 300–370 K.

As it is known [15], when planning thermodynamic experiments by the EMF method, it is necessary to have reliable data on phase equilibria in the studied system in the temperature range of EMF measurements. Taking this into account, we first carried out experiments to determine the nature of solid-phase equilibria in the BiSI-BiSeI-BiI_3 (A) subsystem. For this purpose, the BiI_3, BiSeI, and BiSI compounds were synthesized. At the same time, high-purity elementary components (not less than 99.999 %) purchased from the Alfa Aesar company were used. The synthesis was carried out by co-melting of stoichiometric amounts of constituent elements, weighed with an accuracy of 10^{-4} g on analytical balances. The synthesis was carried out in evacuated quartz ampoules (~10^{-2} Pa) at temperatures 30–50 K higher than their melting temperatures. Taking into account the high vapor pressure

of elemental iodine, sulfur, and selenium at the synthesis temperatures [48], the synthesis was performed in a two-zone inclined furnace. The temperature in the upper "cold" zone was maintained slightly below the boiling point of iodine, while the temperature in the "hot" zone was set at 30–50 K above the melting point of the synthesized compound. Taking into account that the ternary compounds BiSeI and BiSI melt with decomposition by peritectic reactions, the samples were ground into powder, pressed into tablets, and annealed at 750 K for 300 hours to ensure complete homogenization. The phase purity of all the synthesized initial compounds was verified by X-ray diffraction analysis (XRD) and differential thermal analysis (DTA), and the results coincided with literature data [36, 41, 49].

Alloys of various compositions of system (A) were prepared by melting the synthesized and identified initial compounds at 850 K in vacuumed quartz ampoules, which, after fusion, were subjected to stepwise homogenizing annealing: at 650 K for 300 h and 370 K for 100 h.

Powder diffraction patterns of annealed alloys revealed that all alloys in the studied system consist of two-phase mixtures of $BiS_{1-x}Se_xI$ and BiI_3. As an example, Fig. 1 presents the powder diffraction pattern of a sample with the nominal composition 40 mol % BiSI + 40 mol % BiSeI + 20 mol % BiI_3 (sample 1). Thus, according to the XRD data, the solid-phase equilibria diagram of system (A) at room temperature has the form shown in Fig. 2.

For the correct selection of the compositions of the electrode alloys of cells of type (1), it is advisable to consider the ray lines originating from the bismuth corner (reference electrode) of the concentration tetrahedron Bi-S-Se-I and passing through the BiSI-BiSeI section, on which the investigated $BiS_{1-x}Se_xI$ solid solutions are located. For this purpose, using Fig. 2 and the literature data on the boundary systems BiSI-BiI_3 [36], BiSeI-BiI_3 [41] and the binary S-Se system [49], we constructed a fragment of the solid-phase equilibrium diagram of the indicated quaternary system (Fig. 3). As can be seen, the indicated ray sections (red straight lines), passing through the investigated section (points 1, 2, 3, 4), reach the stable BiI_3-S-Se plane (shaded triangle). In this case, the rays passing through the extreme points 1 and 4, corresponding to the compositions

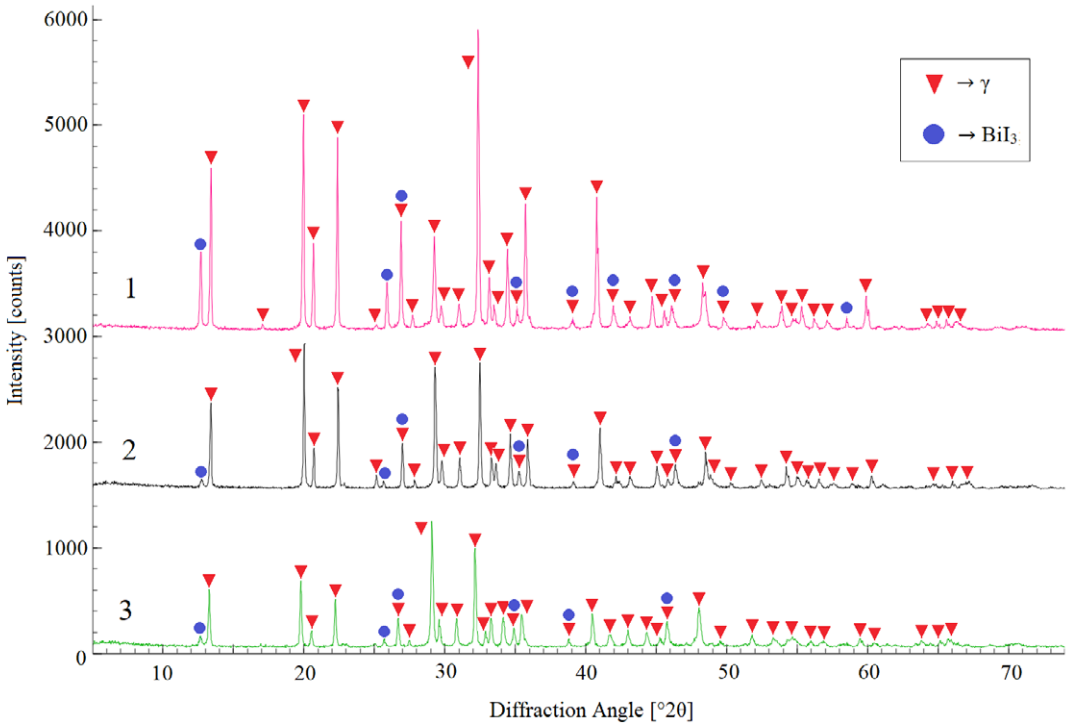

Fig. 1. Powder diffraction patterns of samples 1–3 in Fig. 2

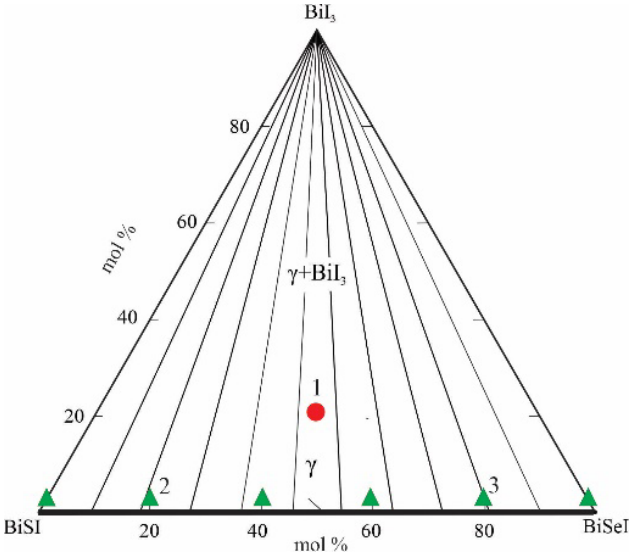

Fig. 2. Solid-phase equilibria diagram of the BiSeI-BiSI-BiI_3 system

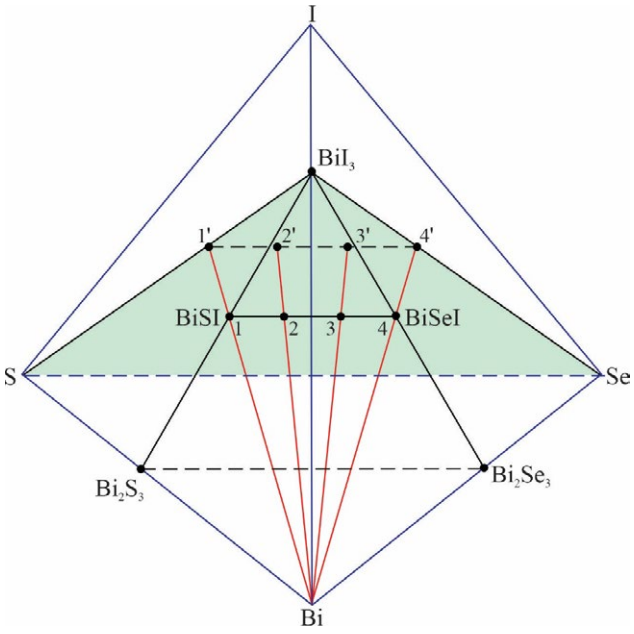

Fig. 3. Fragment of the solid-phase equilibria diagram of the Bi-S-Se-I concentration tetrahedron

of the BiSI and BiSeI compounds, reach the lateral sides BiI_3-S (point 1′) and BiI_3-Se (point 2′), respectively.

The ray lines passing through the intermediate compositions of the BiSI-BiSeI section (for example, points 2 and 3) reach points 2′ and 3′. According to the phase diagram of the S-Se system [49], alloys on the BiI_3-S-Se concentration plane, depending on the S : Se ratio, consist of mixtures of BiI_3 with single- or two-phase alloys of this binary system.

Taking the above into account, $BiS_{1-x}Se_xI$ samples with a small (2–3 mol %) excess of BiI_3 and $S_{1-x}Se_x$ were used as electrode alloys in type (1) cells. All of these samples are compositionally aligned with the above-discussed ray lines and consist of heterogeneous mixtures of $BiS_{1-x}Se_xI$, bismuth triiodide, and $S_{1-x}Se_x$ alloys. To bring the electrode alloys into a state as close as possible to equilibrium, after melting, they were subjected to annealing under the above-mentioned conditions.

Fig. 1 presents the powder diffraction patterns of samples 2 and 3 marked in Fig. 2. As can be seen, both samples exhibit a high degree of crystallinity; their diffraction patterns are identical and consist of reflection lines of γ-solid solutions of 20 and 80 mol % BiSeI compositions [46]. The absence of diffraction lines of BiI_3 and $S_{1-x}Se_x$ alloys is due to their insignificant number.

To prepare the right-hand electrodes of the cells of type (1), the annealed alloys were ground into powder and then pressed into tablets with a diameter of 7 and a thickness of 3–4 mm onto molybdenum current wires.

An ionic liquid (morpholinium formate) with the addition of $BiCl_3$ was used as the electrolyte. To obtain the ionic liquid, morpholine, formic acid, and anhydrous $BiCl_3$ were purchased from Alfa Aesar. The ionic liquid was prepared in accordance with the procedure described in [50]: morpholine was poured into a three-necked round-bottomed flask immersed in an ice-water bath and equipped with a reflux condenser, a dropping funnel for adding acid, and a thermometer to monitor the temperature. Formic acid was slowly (60 min) added dropwise with vigorous stirring. Considering the exothermic nature of this reaction, the temperature of the mixture was maintained below 25 °C using an ice bath. Stirring was continued for 4 h. The residual amine or acid was evaporated under reduced pressure (1–5 mmHg), and the remaining liquid was additionally dried at 80 °C under the same conditions.

To conduct EMF measurements, an electrochemical cell of design described in [32]

was assembled, evacuated, filled with argon to a pressure of ~40 kPa, and placed in a specially made tubular resistance furnace, where it was thermostatted at a temperature of ~360 K for three days. The temperature of the cell was measured using chromel-alumel thermocouples and a mercury thermometer with an accuracy of ±0.5 °C.

The EMF was measured using a high-resistance (input resistance 10^9 Ohm) digital voltmeter Keithley 2100 $6^{1/2}$, in the temperature range of 300–370 K. The choice of the upper limit of measurements is because at higher temperatures, the alloys of the S-Se system melt [49], which leads to a change in the phase composition of the electrode alloys.

The first equilibrium values were obtained after thermostating the cell under the above-mentioned conditions, and subsequent measurements were taken approximately every 4 h after the set temperature was established. Values of EMF were considered equilibrium when repeated measurements at a given temperature differed from each other by no more than 0.5 mV, regardless of the direction of the temperature change.

3. Results and discussion

Fig. 4 shows the EMF measurement data for cells of type (1). As can be seen, the numerical values of EMF decrease monotonically with increasing selenium concentration in the $BiS_{1-x}Se_xI$ solid solutions, and for each sample, its temperature dependence is linear. Considering this, for thermodynamic calculations, the experimental data were processed by the least-squares method, and linear equations of the type

$$E = a + bT \pm t\left[(S_E^2 / n) + S_b^2 \cdot (T - \overline{T})^2\right]^{1/2} \quad (2)$$

recommended in modern thermodynamic literature [16, 17] were obtained. In equation (2), n is the number of pairs of E and T values; S_E and S_b are the variances of individual EMF measurements and the b-factor, respectively. $\overline{T}$ – is the average absolute temperature; t is the Student's criterion. At a confidence level of 95 % and a number of experimental points $n \geqslant 20$, the Student's t-test is $t \geqslant 2$. The resulting equations of type (2) are presented in Table 1.

From the data in Table 1, using the thermodynamic relations [16, 17]:

$$\Delta\overline{G}_{Bi} = -zFE \quad (3)$$

$$\Delta\overline{H}_{Bi} = -z\left[E - T\left(\frac{\partial E}{\partial T}\right)_P\right] = -zFa \quad (4)$$

$$\Delta\overline{S}_{Bi} = zF\left(\frac{\partial E}{\partial T}\right)_P = zFb \quad (5)$$

(F = Faraday constant, 96485 C·mol^{-1}; z = cation charge, Bi^{3+}), the relative partial Gibbs free energy, enthalpy, and entropy of bismuth in the

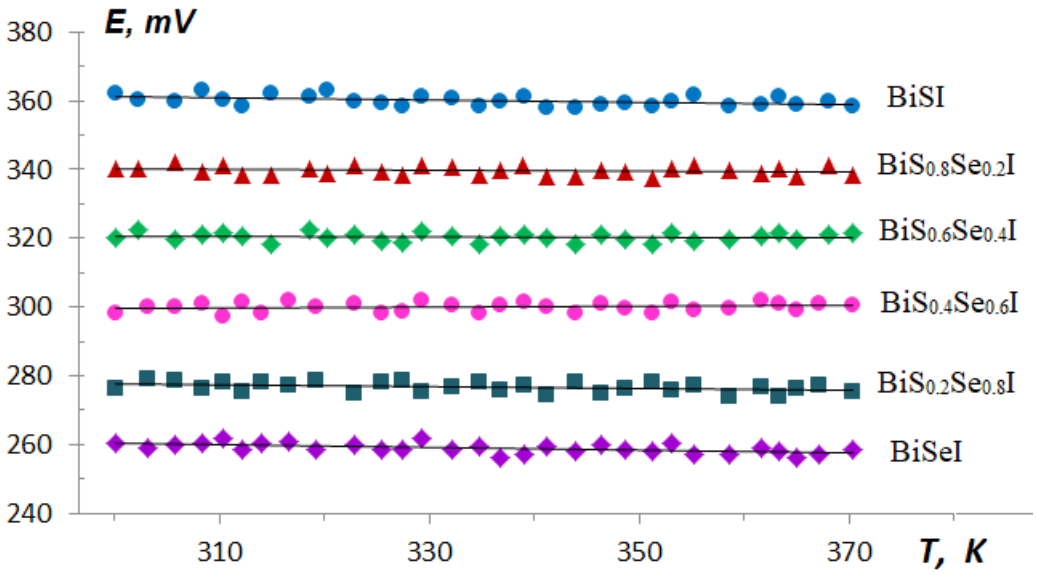

Fig. 4. EMF measurement data for type (1) cells for $BiS_{1-x}Se_xI$ alloys

Table 1. Equations for the temperature dependences of EMF for $BiS_{1-x}Se_xI$ alloys of various compositions in the temperature range 300–370 K

Phase	E, mV = $a + bT \pm 2\tilde{S}_E(T)$
BiSI	$370.35 - 0.0308T \pm 2\left[\frac{1.80}{30} + 1.4 \cdot 10^{-4}(T - 336.6)^2\right]^{1/2}$
$BiS_{0.8}Se_{0.2}I$	$344.48 - 0.0145T \pm 2\left[\frac{1.41}{30} + 1.1 \cdot 10^{-4}(T - 336.6)^2\right]^{1/2}$
$BiS_{0.6}Se_{0.4}I$	$322.13 - 0.0055T \pm 2\left[\frac{1.52}{30} + 1.2 \cdot 10^{-4}(T - 336.6)^2\right]^{1/2}$
$BiS_{0.4}Se_{0.6}I$	$296.54 + 0.0101T \pm 2\left[\frac{1.84}{30} + 1.4 \cdot 10^{-4}(T - 335.4)^2\right]^{1/2}$
$BiS_{0.2}Se_{0.8}I$	$279.70 - 0.0103T \pm 2\left[\frac{1.69}{30} + 1.3 \cdot 10^{-4}(T - 335.4)^2\right]^{1/2}$
BiSeI	$272.09 - 0.0394T \pm 2\left[\frac{1.48}{30} + 1.1 \cdot 10^{-4}(T - 335.4)^2\right]^{1/2}$

Table 2. Partial molar functions of bismuth in $BiS_{1-x}Se_xI$ alloys at 298 K

Phase	$-\Delta\overline{G}_{Bi}$	$-\Delta\overline{H}_{Bi}$	$\Delta\overline{S}_{Bi}$, J·K^{-1}·mol^{-1}
	kJ·mol^{-1}		
BiSI	104.54±0.15	107.20±1.5	-8.93±3.41
$BiS_{0.8}Se_{0.2}I$	98.46±0.13	99.71±1.01	-4.20±3.01
$BiS_{0.6}Se_{0.4}I$	92.77±0.13	93.24±1.05	-1.60±3.13
$BiS_{0.4}Se_{0.6}I$	86.71±0.15	85.84±1.16	2.94±3.44
$BiS_{0.2}Se_{0.8}I$	80.07±0.14	80.96±1.11	-2.99±3.30
BiSeI	75.36±0.13	78.76. ±1.04	-11.39±3.09

alloys were calculated. The resulting partial molar functions are presented in Table 2, and their concentration dependence graphs are shown in Fig. 5.

As can be seen from Fig. 5, all three functions are continuous functions of composition, which is in accordance with the formation of continuous solid solutions in the studied system.

To calculate the integral thermodynamic functions of BiSI, BiSeI compounds, and $BiS_{1-x}Se_xI$ solid solutions of various compositions, we determined the equations of potential-forming reactions using the schematic solid-phase equilibria diagram of the Bi-S-Se-I system (Fig. 3) [15]. It is easy to show that for BiSI and BiSeI compounds, they have the form:

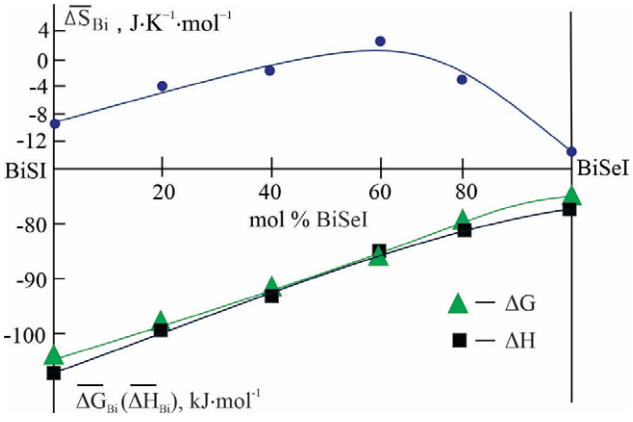

Fig. 5. Concentration dependences of the partial molar functions of bismuth in the BiSI-BiSeI system at 300 K

$Bi\ (solid) + 0.5\ BiI_3\ (solid) + 1.5S\ (solid) = 1.5\ BiSI\ (solid)$ (6)

$Bi\ (solid) + 0.5BiI_3\ (solid) + 1.5Se\ (solid) = 1.5BiSeI\ (solid)$ (7)

In accordance with these equations, the standard Gibbs free energy of formation and the enthalpy of formation of the specified ternary compounds were calculated using the relations:

$$\Delta_f Z^0(BiSI) = \frac{2}{3}\Delta\overline{Z}_{Bi} + \frac{1}{3}\Delta_f Z^0(BiI_3) \quad (8)$$

$$\Delta_f Z^0(BiSeI) = \frac{2}{3}\Delta\overline{Z}_{Bi} + \frac{1}{3}\Delta_f Z^0(BiI_3) \quad (9)$$

where $Z \equiv G$, H, and the standard entropies are according to

$$S^0(BiSI) = \frac{2}{3}[\Delta\overline{S}_{Bi} + S^0(Bi)] + \frac{1}{3}S^0(BiI_3) + S^0(S) \quad (10)$$

$$S^0(BiSeI) = \frac{2}{3}[\Delta\overline{S}_{Bi} + S^0(Bi)] + \frac{1}{3}S^0(BiI_3) + S^0(Se). \quad (11)$$

On the other hand, as shown above, the ray lines passing through different compositions of γ-solid solutions reach the BiI_3-S-Se concentration triangle. Therefore, the overall potential-forming reaction for them has the form

$Bi\ (solid) + 0.5BiI_3\ (solid) + 1.5(S_{1-x}Se_x)\ (solid) = 1.5\ BiS_{1-x}Se_xI\ (solid)$ (12)

According to equation (12), the standard thermodynamic functions of solid solution formation are calculated using the relations:

$$\Delta_f Z^0(BiS_{1-x}Se_x) = \frac{2}{3}\Delta\overline{Z}_{Bi} + \frac{1}{3}\Delta_f Z^0(BiI_3) + +\Delta_f Z^0(S_{1-x}Se_x), \quad (13)$$

and the standard entropies are –

$$S^0(BiS_{1-x}Se_x) = \frac{2}{3}[\Delta\overline{S}_{Bi} + S^0(Bi)] + \frac{1}{3}S^0(BiI_3) + S^0(S_{1-x}Se_x). \quad (14)$$

In calculations using equations (8)–(11) and (13)–(14), the values of standard entropies of bismuth, sulfur, and selenium recommended in modern reference literature (S^0(Bi) = 56.90±0.42, S^0(S) = 31.92±0.21, S^0(Se) = 42.13±0.21 J·mol^{-1}·K^{-1}) [51] were used, as well as the standard integral thermodynamic functions of BiI_3 compounds and binary $S_{1-x}Se_x$ alloys (x = 0.2, 0.4, 0.6, 0.8). For $S_{1-x}Se_x$ alloys, the values of $\Delta_f H^0$ and $\Delta_f S^0$ were taken from [52], and the standard entropy was calculated by combining the data from [52] with the above-given values of the standard entropies of elemental sulfur and selenium (Table 3). For BiI_3, the values of the functions $\Delta_f H^0$ and S^0 given in the reference books [53, 54] were used, and $\Delta_f G^0$ was calculated based on them (Table 4).

The obtained values of the standard integral thermodynamic functions are presented in Table 4. As can be seen, our data on ternary compounds are very close to those given in [32]. Thermodynamic data for $BiS_{1-x}Se_xI$ solid solutions have been determined for the first time. Their analysis shows a consistent decrease in the numerical values of the Gibbs free entropy and enthalpy with increasing selenium concentration. The behavior of the functions $\Delta_f S^0$ and S^0 is different: the formation of solid solutions is accompanied by an increase in the values of these functions from the stoichiometric compositions of the ternary compounds and passes through a maximum at approximately the composition $BiS_{0.4}Se_{0.6}I$, which is apparently associated with the contribution of the configurational entropy of the solid solutions.

Table 3. Standard integral thermodynamic functions of $S_{1-x}Se_x$ alloys [52]

Phase	$-\Delta_f G^0$ (298 K)	$-\Delta_f H^0$ (298 K)	$\Delta_f S^0$ (298 K)	S^0 (298 K)
	kJ·mol^{-1}		J·K^{-1}·mol^{-1}	
$S_{0.8}Se_{0.2}$	0.54	-0.8	4.5	38.5±0.3
$S_{0.6}Se_{0.4}$	0.84	-0.8	5.5	41.5±0.3
$S_{0.4}Se_{0.6}$	0.88	-1.0	6.3	44.4±0.3
$S_{0.2}Se_{0.8}$	0.69	-0.8	5.0	45.1±0.3

Table 4. Standard integral thermodynamic functions of the BiI_3, BiSI, BiSeI compounds and $BiS_{1-x}Se_xI$ solid solutions

Фаза	$\Delta_f G^0$(298 K)	$\Delta_f H^0$(298 K)	$\Delta_f S^0$ (298 K)	S^0 (298 K)
	kJ·mol^{-1}		J·K^{-1}·mol^{-1}	
BiI_3 [53, 54]	148.8±8.0	150.6±6.3	–	224.7±6.3
BiSI [32]	119.5±2.7	121.2±2.5	–	141.1±3.9
BiSI	119.3±2.8	121.7±2.9	−8.1±4.3	138.8±4.8
$BiS_{0.8}Se_{0.2}I$	115.3±2.8	115.9±2.8	−2.0±4.3	148.0±4.8
$BiS_{0.6}Se_{0.4}I$	112.3±2.8	111.6±2.9	2.3±4.2	152.7±4.7
$BiS_{0.4}Se_{0.6}I$	108.2±2.9	106.4±3.0	6.0±4.3	158.9±4.9
$BiS_{0.2}Se_{0.8}I$	103.7±2.9	103.5±3.0	0.7±4.4	154.6±4.9
BiSeI	99.8±2.8	102.7±2.8	−9.7±4.2	147.4±4.6
BiSeI [32]	100.0±2.8	102.4±2.5	–	148.6±3.6

4. Conclusions

Thus, we present new, consistent sets of thermodynamic data for the phases of the BiSI-BiSeI system, obtained by measuring the EMF of concentration cells with an ionic liquid as the electrolyte relative to a bismuth electrode. To rationally plan experiments and process their results, a solid-phase equilibria diagram of the BiSI-BiSeI-BiI_3 system and a fragment of the phase diagram of the Bi-S-Se-I system in the corresponding region were constructed using X-ray diffraction (XRD). The relative partial Gibbs free energy, enthalpy, and entropy of bismuth in the alloys were calculated from the EMF measurements. Based on the schematic phase diagram of the Bi-S-Se-I system, the virtual potential-forming reactions responsible for the indicated partial molar quantities were established. Using the obtained equations of potential-forming reactions, the standard thermodynamic functions of formation and the standard entropy of BiSI and BiSeI compounds, as well as $BiS_{1-x}Se_xI$ solid solutions of compositions x = 0.2, 0.4, 0.6, 0.8, were calculated. The thermodynamic functions of BiSI and BiSeI compounds are in good agreement with the literature, whereas those for solid solutions have been determined for the first time.

Contribution of the authors

A. A. Qurbanov – literature search, experimental research, participation in writing the original text. E. J. Ahmadov – processing of experimental data, participation in writing the article. G. M. Shukurova – participation in research and discussion of results. I. J. Alverdiev – scientific supervision, participation in discussion of results and text editing. Y. I. Jafarov – development of methodology of thermodynamic experiments and participation in text editing.

Conflict of interests

The authors declare that they have no known competing financial interests or personal relationships that could have influenced the work reported in this paper.

References

1. Mistewicz K., Das T. K., Nowacki B., … Masiuchok O. Bismuth sulfoiodide (BiSI) nanorods: synthesis, characterization, and photodetector application. *Scientific Reports*. 2023;13: 8800. https://doi.org/10.1038/s41598-023-35899-7

2. Peng B., Xu K., Zhang H., … Soukoulis C. M. 1D SbSeI, SbSI, and SbSBr with high stability and novel properties for microelectronic, optoelectronic, and thermoelectric applications. *Advanced Theory and Simulation*. 2018;1(1): 1700005. https://doi.org/10.1002/adts.201700005

3. Ganose A. M., Butler K. T., Walsh A., Scanlon D. O. Relativistic electronic structure and band alignment of BiSI and BiSeI: candidate photovoltaic materials. *Journal of Materials Chemistry A*. 2016;4: 2060–2068. https://doi.org/10.1039/C5TA09612J

4. Koc H., Palaz S., Mamedov A. M., Ozbay E. Optical, electronic, and elastic properties of some $A^5B^6C^7$ ferroelectrics (A=Sb, Bi; B=S, Se; C=I, Br, Cl): first principle calculation. *Ferroelectrics*. 2017;511: 22–34. https://doi.org/10.1080/00150193.2017.1332967

5. Xiong G. H., Liu T., Huang H. H., Wang J. Thermoelectric properties of Janus BiXI (X = S and Se) monolayers: a first-principles study. *Journal of Applied Physics*. 2024;136(18): 185102. https://doi.org/10.1063/5.0221109

6. Khan W., Hussain S., Minar J., Azam S. Electronic and thermoelectric properties of ternary chalcohalide semiconductors: first principles study. *Journal of Electronic Materials*. 2018;47: 1131–1139. https://doi.org/10.1007/s11664-017-5884-z

7. Govindaraj P., Venugopal K. Intrinsic ultra-low lattice thermal conductivity in orthorhombic BiSI: an excellent thermoelectric material. *Journal of Alloys and Compounds*. 2022;929: 167347. https://doi.org/10.1016/j.jallcom.2022.167347

8. Guo S. D., Guo X. S., Liu Z. Y., Quan Y. N. Large piezoelectric coeffcients combined with high electron mobilities in Janus monolayer XTeI (X=Sb and Bi): a first-principle study. *Journal of Applied Physics*. 2020;127(6): 064302. https://doi.org/10.1063/1.5134960

9. Zhuang H. L., Cooper V. R., Xu H., Ganesh P., Hennig R. G., Kent P. R. C. Rashba effect in single-layer antimony telluroiodide SbTeI. *Physical Review B*. 2015;92: 115302. https://doi.org/10.1103/PhysRevB.92.115302

10. Landolt G., Eremeev S. V., Koroteev Y. M., … Dil J. H. Disentanglement of surface and bulk rashbaspin splittings in noncentrosymmetric BiTeI. *Physical Review Letters*. 2012;109: 116403. https://doi.org/10.1103/PhysRevLett.109.116403

11. Li T., Xu Y., Li M., … Ju W. A study of the Rashba effect in two-dimensional ternary compounds ABC monolayers (A = Sb, Bi; B = Se, Te; C = Br; I). *Physical Chemistry Chemical Physics*. 2023;25: 3182–3189. https://doi.org/10.1039/D2CP05002A

12. Babanly M. B., Yusibov Y. A., Imamaliyeva S. Z., Babanly D. M., Alverdiyev I. J. Phase diagrams in the development of the argyrodite family compounds and solid solutions based on them. *Journal of Phase Equilibria and Diffusion*. 2024;45: 228–255. https://doi.org/10.1007/s11669-024-01088-w

13. Babanly M. B., Mashadieva L. F., Imamaliyeva S. Z., Babanly D. M., Taghiyev D. B., Yusibov Y. A. Complex copper-based chalcogenides: a review of phase equilibria and thermodynamic properties. *Condensed Matter and Interphases*. 2024;26(4): 579–619. https://doi.org/10.17308/kcmf.2024.26/12367

14. Babanly M. B., Mashadiyeva L. F., Babanly D. M., Imamaliyeva S. Z., Tagiev D. B., Yusibov Yu. A. Some issues of complex studies of phase equilibria and thermodynamic properties in ternary chalcogenide systems involving emf measurements (Review). *Russian Journal of Inorganic Chemistry*. 2019;64(13): 1649–1671. https://doi.org/10.1134/S0036023619130035

15. Babanly M. B., Mashadiyeva L. F., Babanly D. M., Imamaliyeva S. Z., Tagiev D. B., Yusibov Yu. A. Some issues of complex studies of phase equilibria and thermodynamic properties in ternary chalcogenide systems involving emf measurements (Review). *Russian Journal of Inorganic Chemistry*. 2019;64(13): 1649–1671. https://doi.org/10.1134/S0036023619130035

16. Morachevsky A. G., Voronin G. F., Geyderich V. A. Kutsenok I. B. *Electrochemical methods of investigation in hermodynamics of metal systems**. Moscow: Akademkniga Publ.; 2003. 334 p. (In Russ.)

17. Babanly M. B., Yusibov Y. A. Electrochemical methods in thermodynamics of inorganic systems*. Baku: BSU Publ.; 2011. 306 p. (in Russ.)

18. Ipser H., Mikula A., Katayama I. Overview: The emf method as a source of experimental thermodynamic data. *CALPHAD: Computer Coupling of Phase Diagrams and Thermochemistry*. 2010;34(3): 271–278. https://doi.org/10.1016/j.calphad.2010.05.001

19. Voronin M. V., Osadchii E. G. Determination of thermodynamic properties of silver selenide by the galvanic cell method with solid and liquid electrolytes. *Russian Journal of Electrochemistry*. 2011;47(4): 420–426. https://doi.org/10.1134/S1023193511040203

20. Levanov A. V., Isaikina O. Y., Lunin V. V. Determining the potential of a silver/silver chloride electrode at different temperatures. *Russian Journal of Physical Chemistry A*. 2019;93: 770–773. https://doi.org/10.1134/S0036024419040186

21. Vassiliev V., Gong W. Electrochemical cells with the liquid electrolyte in the study of semiconductor, metallic and oxide systems. *Electrochemical Cells – New Advances in Fundamental Researches and Applications*. InTech. 2012. pp. 71–102. https://doi.org/10.5772/39007

22. Mammmadov F. M., Imamaliyeva S. Z., Akhmedov E. J., Tagiyev D. B., Babanly M. B. Thermodynamic properties of iron-gallium sulfides. *Russian Journal of Physical Chemistry A*. 2024;68(14): 3522–3529. https://doi.org/10.1134/S0036024424703126

23. Mammadov F. M., Babanly D. M., … Babanly M. B. Solid-phase relations in the FeSe-Ga_2Se_3-Se system and thermodynamic investigation of the $FeGa_2Se_4$ compound and $(FeSe)_{1-x}(Ga_2Se_3)_x$ solid solutions. Chemical Thermodynamics and Thermal Analysis. 2025;19: 100207. https://doi.org/10.1016/j.ctta.2025.100207

24. Kristavchuk A. V., Zabolotskaya A. V., Voronin M. V., Chareev D. A., Osadchii E. G. Temperature dependence of tellurium fugacity for the kotulskite (PdTe)–merenskyite ($PdTe_2$) equilibrium determined by the method of a solid-state galvanic cell. *Physics and Chemistry of Minerals*. 2021;48: 16. https://doi.org/10.1007/s00269-021-01141-x

25. Osadchii E. G., Voronin M. V. Thermodynamic properties of $RuTe_2$ evaluated by emf measurements on a solid state electrochemical cell. *Inorganic Materials*. 2024;60(3): 832–837. https://doi.org/10.1134/S0020168524701061

26. Moroz M. V., Tesfaye F., Demchenko P., Prokhorenko M., Prokhorenko, S., Reshetnyak O. Non-activation synthesis and thermodynamic properties of ternary compounds of the Ag-Te-Br system. *Thermochimica Acta*. 2021;698: 178862. https://doi.org/10.1016/j.tca.2021.178862

27. Moroz M., Tesfaye F., Demchenko P., … Gladyshevskii R. Synthesis, thermodynamic properties, and structural characteristics of multicomponent compounds in the Ag-Ni-Sn-S system. *JOM*. 2023;75: 2016–2025. https://doi.org/10.1007/s11837-023-05784-9

28. Alverdiev I. D., Imamalieva S. Z., Babanly D. M. Yusibov Yu. A., Tagiev D. B., Babanly M. B. Thermodynamic study of siver-tin selenides by the emf method with Ag_4RbI_5 solid electrolyte. *Russian Journal of Electrochemistry*. 2019;55: 467–474. https://doi.org/10.1134/S1023193519050021

29. Imamaliyeva S. Z., Mehdiyeva I. F., Qasymov V. A., Babanly D. M., Taghiyev D. B., Babanly M. B. Solid-phase equilibria and thermodynamic properties of phases in the Tm–Te system. *Russian Journal of Physical Chemistry A*.

2021;95(4): 926–932. https://doi.org/10.1134/S0036024421050149

30. Imamaliyeva S. Z., Babanly D. M., Zlomanov V. P., Taghiyev D. B., Babanly M. B. Thermodynamic properties of terbium tellurides. *Condensed Matter and Interphases*. 2020;22(4): 453–459. https://doi.org/10.17308/kcmf.2020.22/3116

31. Mammadov F. M., Babanly D. M., Imamaliyeva S. Z., Zeynalova G. S., Ahmadov E. I., Babanly M. B. Solid-phase equilibria in the FeS-In_2S_3-S system, thermodynamic properties of the $FeIn_2S_4$ compound and $(FeS)_{1-x}(In_2S_3)_x$ solid solutions. *The Journal of Chemical Thermodynamics*. 2026;213: 107585. https://doi.org/10.1016/j.jct.2025.107585

32. Imamaliyeva S. Z., Musayeva S. S., Babanly D. M., Jafarov Y. I., Taghiyev D. B., Babanly M. B. Determination of the thermodynamic functions of bismuth chalcoiodides by emf method wıth morpholinium formate as electrolyte. *Thermochimica Acta*. 2019;679: 178319. https://doi.org/10.1016/j.tca.2019.178319

33. Aliev Z. S., Musayeva S. S., Imamaliyeva S. Z., Babanly M. B. Thermodynamic study of antimony chalcoiodides by emf method with an ionic liquid. *Journal of Thermal Analysis and Calorimetry*. 2018;133: 1115–1120. https://doi.org/10.1007/s10973-017-6812-4

34. Hasanova G. S., Aghazade A. I., Babanly D. M., Imamaliyeva S. Z., Yusibov Y. A., M. B. Babanly. Experimental study of the phase relations and thermodynamic properties of BiSe system. *Journal of Thermal Analysis and Calorimetry*. 2022;147: 6403–6414. https://doi.org/10.1007/s10973-021-10975-0

35. Hasanova G. S., Aghazade A. I., Imamaliyeva S. Z., Yusibov Y. A., Babanly M. B. Refinement of the phase diagram of the Bi-Te system and the thermodynamic properties of lower bismuth Tellurides. *JOM*. 2021;73(5): 1511–1521. https://doi.org/10.1007/s11837-021-04621-1

36. Aliev Z. S., Musayeva S. S., Jafarli F. Y., Amiraslanov I. R., Shevelkov A. V. Babanly M. B. The phase equilibria in the Bi–S–I ternary system and thermodynamic properties of the BiSI and $Bi_{19}S_{27}I_3$ ternary compounds. *Journal of Alloys and Compounds*. 2014;610: 522–528. https://doi.org/10.1016/j.jallcom.2014.05.015

37. Babanly M. B., Tedenac J.-C., Aliev Z. S., Balitsky D. V. Phase eqilibriums and thermodynamic properties of the system Bi-Te-I. *Journal of Alloys and Compounds*. 2009;481(1-2): 349–353. https://doi.org/10.1016/j.jallcom.2009.02.139

38. Aliyev Z. S., Musaeva S. S., Babanly D. M., Shevelkov A. V., Babanly M. B. Phase diagram of the Sb-Se-I system and thermodynamic properties of SbSeI. *Journal of Alloys and Compounds*. 2010;505(2): 450–455. https://doi.org/10.1016/j.jallcom.2010.06.103

39. Aliyev Z. S., Babanly M. B. Shevelkov A. V., Babanly D. M., Tedenac J.-C. Phase diagram of the Sb-Te-I system and thermodynamic properties of SbTeI. *International Journal of Materials Research*. 2012;103(3): 290–295. https://doi.org/10.3139/146.110646

40. Aliev Z. S., Musayeva S. S., Babanly M. B. The phase relations in the Sb-S-I system and thermodynamic properties of SbSI. *Journal of Phase Equilibria and Diffusion*. 2017;38(12): 887–896. https://doi.org/10.1007/s11669-017-0601-4

41. Aliev Z. S., Ahmadov E. C., Babanly D. M., Amiraslanov I. R., Babanly M. B. The Bi_2Se_3-Bi_2Te_3-BiI_3 system: synthesis and characterization of the $BiTe_{1-x}Se_xI$ solid solutions. *Calphad*. 2019;66: 101650. https://doi.org/10.1016/j.calphad.2019.101650

42. Ahmadov E. J., Aliev Z. S., Babanly D. M., Imamaliyeva S. Z., Gasymov V. A., Babanly M. B. The quasi-ternary system Bi_2S_3–Bi_2Te_3–BiI_3. *Russian Journal of Inorganic Chemistry*. 2021;66: 538–549. https://doi.org/10.1134/S0036023621040021

43. Ahmadov E. J., Orujlu E. N., Babanly D. M., … Babanly M. B. Phase equilibria of the $Sb_2Te_3+2BiI_3 \leftrightarrow Bi_2Te_3+2SbI_3$ reciprocal system: synthesis and characterization of the cation-substituted $Bi_{1-x}Sb_xTeI$ solid solutions. *Journal of Alloys and Compounds*. 2022;929: 167388. https://doi.org/10.1016/j.jallcom.2022.167388

44. Ahmadov E. J. Physico-chemical interaction in the BiSI–BiTeI system. *Azerbaijan Chemical Journal*. 2020;1: 36–40. https://doi.org/10.32737/0005-2531-2020-1-36-40

45. Ahmadov E. J., Babanly D. M., Aliyev Z. S., Zlomanov V. P. Phase equilibria in the system SbTeI-BiTeI. *New Materials, Compounds and Applications*. 2019;3(2): 87–93. Available at: https://jomardpublishing.com/UploadFiles/Files/journals/NMCA/V3N2/Ahmadov%20et%20al.pdf

46. Qurbanov A., Ahmadov E., Alverdiyev I., Jafarov Y. Phsico-chemical interaction in the BiSI-BiSeI system. *Baku State University Journal of Chemistry and Material Sciences*. 2024;1(4): 6–12. https://doi.org/10.30546/209501.201.2024.1.04.061

47. Qurbanov A. A., Ahmadov E. J., Aghazade A. I., Aghayeva A. R., Gasymov V. A., Alverdiyev I. J. Phase equilibria in the $Bi_{19}S_{27}I_3$-"$Bi_{19}Se_{27}I_3$" system and characterization of solid solutions. *Azerbaijan Chemical Journal*. 2026;2: 145–152. https://doi.org/10.32737/0005-2531-2026-2-145-152

48. Emsley J. *The elements*. Oxford: Clarendon, Oxford University Publ.; 1998. 292 p.

49. Massalski T. B., Okamoto H., Subramanian P. R., Kacprzak L. *Binary alloy phase diagrams*. 2nd ed. Ohio: ASM International, Materials Park Publ.; 1990. 3589 p.

50. Brigouleix C., Anouti M., Jacquemin J., Caillon-Caravanier M., Galiano H., Lemordant D. Physicochemical characterization of morpholinium cation based protic ionic liquids used as electrolytes. *The Journal of Physical Chemistry B*. 2010;114(5): 1757–1766. https://doi.org/10.1021/jp906917v

51. Data base of thermal constants of substances. Digital version. Eds.: Iorish V.S., Yungman V.S., 2006. http://www.chem.msu.ru/cgi-bin/tkv.pl

52. Guan P. W., Shang S. L., Lindwall G., Anderson T., Liu Z. K. First-principles calculations and thermodynamic modeling of the S-Se system and implications for chalcogenide alloys. *Journal of Alloys and Compounds*. 2017;694: 510–521. https://doi.org/10.1016/j.jallcom.2016.10.037

53. Kubaschewski O., Alcock C. B., Spencer P. J. *Materials thermochemistry*. Oxford: New York: Pergamon Publ.; 1993. 363 p.

54. Barin I. *Thermochemical data of pure substances*. Third edition. New York: Willey Publ.; 2008. 1936 p.

** Translated by author of the article*

Information about the authors

Abbas A. Qurbanov, graduate student, Ganja State University (Ganja, Azerbaijan).
https://orcid.org/0009-0009-3295-6684
qurbanov777abbas@gmail.com

Elvin J. Ahmadov, PhD (in Chem.), Leading Researcher, Institute of Chemistry (Baku, Azerbaijan).
https://orcid.org/0000-0002-7616-9553
elvin.j.ahmadov@gmail.com

Guntakin M. Shukurova, PhD (in Chem.), Baku State University (Baku, Azerbaijan).
https://orcid.org/0009-0005-5916-7467
gunteksh@hotmail.com

Isfandiyar J. Alverdiyev, Dr. Sci. (Chem.), Associate Professor, Dean of the Faculty of Chemistry and Biology, Ganja State University (Ganja, Azerbaijan).
https://orcid.org/0000-0003-0446-8850
ialverdiyev73@gmail.com

Yasin I. Jafarov, Dr. Sci. (Chem.), Professor, Baku State University (Baku, Azerbaijan).
https://orcid.org/0000-0002-3968-8725
yasin_cafarov@mail.ru

Received September 18, 2025; accepted after reviewing October 13, 2025; accepted for publication November 15, 2025; published online April 01, 2026.

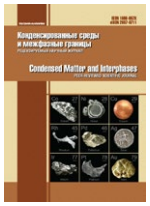

ISSN 1606-867X (Print)
ISSN 2687-0711 (Online)
Condensed Matter and Interphases
Kondensirovannye Sredy i Mezhfaznye Granitsy
https://journals.vsu.ru/kcmf/

Original articles

Research article
https://doi.org/10.17308/kcmf.2026.28/13559

Kinetics of cathodic deposition of copper from an acid sulfate solution in the presence of organic disulfides

E. A. Ilina, O. A. Kozaderov✉, N. V. Sotskaya, A. D. Golovinsky, E. D. Kolbeshkina, V. A. Polikarchuk

Voronezh State University,
1 Universitetskaya pl., Voronezh 394018, Russian Federation

Abstract

Objectives: In this work, we established the kinetic patterns and evaluated the main parameters of heterogeneous nucleation and growth of a new phase during the electrocrystallization of copper during cathode deposition from an acid sulfate solution in the presence of organic disulfides (disodium salts of 3,3′-dithiodipropanedisulfonic acid, 4,4′-dithiodibenzene disulfonic acid and 3,3’-dithiodi(4-aminobenzene)sulfonic acids). The additives under study contain a disulfide group (-S-S-), which is characteristic of accelerators of the copper cathode deposition process in the implementation of electrochemical void-free filling of through holes (through silicon vias) of silicon wafers used in microelectronics in the manufacture of microcircuits.

Experimental: Electrodeposition of copper coatings was carried out from aqueous sulfate solutions of copper plating in galvanostatic mode. Using scanning electron microscopy, it was found that in the presence of all the studied organic disulfides, copper crystallites with clearer edges are formed in the acid sulfate electrolyte of copper plating than in solutions without additives. The presence of aromatic groups in the structure of the accelerator molecule increases the size of the crystallites of the galvanic copper deposit, and the additional introduction of terminal amino groups into the disulfide structure, on the contrary, leads to a decrease in the size of the crystallites. The latter can be explained by the bifunctional nature of 3,3′-dithiodi(4-aminobenzene)sulfonic acid, capable of exhibiting both an accelerating and leveling effect due to the presence of a disulfide group and an amino group in the structure, respectively. The kinetics of cathodic deposition of copper coatings was studied using transient electrochemical methods of voltammetry, chronopotentiometry, and chronoammetry. In the presence of the studied additives, the overvoltage of copper electrodeposition decreases, while the kinetics of the process does not change: the charge transfer stage proceeds irreversibly, the activation of nucleation sites is progressive, and the growth of a new phase is controlled by the diffusion of copper ions from the solution to the cathode surface.

Conclusions: The functionalization of aliphatic disulfide by the introduction of aromatic and amino groups does not lead to significant changes in the parameters of heterogeneous nucleation and the growth of a new phase during cathodic deposition of copper from an acid sulfate solution. However, the rate of electrocrystallization increases with the transition from aliphatic disulfide (disodium salt of 3,3′-dithiodipropanedisulfonic acid) to disodium salt of 3,3’-dithiodi(4-aminobenzene)sulfonic acid, which contains both aromatic groups and amino groups in its structure.

Keywords: Copper, Cathodic deposition, Organic disulfides, Kinetics, Voltammetry, Chronopotentiometry, Phase formation

Funding: The study received financial support from the Ministry of Science and Higher Education of the Russian Federation within the framework of State Contract with universities regarding scientific research in 2025–2027, project No. FZGU-2025-0001.

Acknowledgements: The SEM studies were performed on the equipment of the Center for the Collective Use of Scientific Equipment of Voronezh State University.

For citation: Ilina E. A., Kozaderov O. A., Sotskaya N. V., Golovinsky A. D., Kolbeshkina E. D., Polikarchuk V. A. Kinetics of cathodic deposition of copper from an acid sulfate solution in the presence of organic disulfides. *Condensed Matter and Interphases*. 2026;28(1): 57–68. https://doi.org/10.17308/kcmf.2026.28/13559

✉ Oleg A. Kozaderov, e-mail: ok@chem.vsu.ru

Для цитирования: Е. А. Ильина, О. А. Козадеров, Н.В. Соцкая, А. Д. Головинский, Е. Д. Колбешкина, В. А. Поликарчук. Кинетика электрокристаллизации меди из кислого сульфатного раствора в присутствии органических дисульфидов. *Конденсированные среды и межфазные границы*. 2026;28(1): 57–68. https://doi.org/10.17308/kcmf.2026.28/13559

1. Introduction

The process of copper cathodic deposition forms the basis of TSV (through silicon vias) technology used in microelectronics to form electrical contacts (interposers) between different levels of semiconductor devices [1–3]. The technology is based on creating interconnections in the holes of a silicon wafer by filling them with metal, which must be superconformal. This means that when creating interposers, it is necessary to exclude the formation of voids in the forming galvanic deposits [4, 5]. This process cannot be implemented in simple copper deposition electrolytes containing only two main components: copper sulfate and sulfuric acid. The fact is that such electrolytes have a low scattering capacity, which negatively affects the deposition quality in micro-sized holes with a high aspect ratio "depth/height". In this regard, special functional additives are introduced into the electrolyte, among which accelerators play a special role [6–10].

Accelerator molecules are adsorbed mainly in the depth of the micro-holes, which provides a superconformal "bottom-up" filling mode. This is facilitated by the relatively small size and sufficiently high diffusion mobility of accelerator molecules. In addition, their composition and structure play an important role. The most common are organic disulfides containing a disulfide (-S-S-) bond, for example, bis-(3-sulfopropyl)-disulfide (SPS) [11, 12]. According to modern concepts, during the first stage of the mechanism of the accelerating action, SPS molecules decompose to form monomers – 3-mercaptopropanesulfonic acid (MPS). This stage occurs either in the volume of the solution [13, 14] or on the surface of the cathode [15]. Next, MPS forms a thiolate complex with a Cu^+ ion, which is formed during the first stage of the cathodic reduction of Cu^{2+} ions [16]. The subsequent reduction of the Cu^+-MPS thiolate complex to copper proceeds faster than the process of purely electrochemical conversion of Cu^{2+} in the absence of organic disulfide in the electrolyte. In this case, the rate of copper electrodeposition correlates with the concentration of the thiolate complex [17]. The accelerating effect is manifested in the presence of chloride ions [18, 19], which promote chemisorption of Cu^+ ions and increase their concentration on the cathode surface, thereby reducing the capacity of the double electric layer and polarization, which ultimately creates favorable conditions for nucleation and growth of a new copper phase. In addition, an accelerator can contribute to a change in the contribution of these stages to the deposition kinetics, which, in turn, leads to morphological changes due to the formation of crystallites of a different size [19].

Along with accelerators, an important component of TSV electrolytes are levelers, which are most often used as nitrogen-containing aromatic compounds, including heterocyclic ones [20, 21]. Their functional N-containing groups, including amino groups, contribute to the adsorption of leveler molecules on the copper surface [22]. As a result, the adsorption of a leveler is most pronounced, first of all, in areas with high cathodic current density, which prevents the unwanted deposition of copper in the upper part of TSV holes, but has almost no effect on electrodeposition in areas with low current density (i.e. in the depth of the TSV holes).

The simultaneous action of an accelerator and a leveler ensures superconformal filling of TSV structures with copper. At the same time, both the selection of the most appropriate deposition regime in the presence of both additives and the selection of their optimal concentrations is a difficult task [23, 24]. Therefore, an urgent problem of TSV technology is the search for a single bifunctional additive that would combine the properties of an accelerator and a leveler. Obviously, the use of such a universal additive will simplify the process of optimizing the copper plating regime and reduce the cost of an electrolyte. In addition, it will help to increase its environmental friendliness by reducing the total number of organic components. One of the approaches to finding such a universal additive is to evaluate the possibility and conditions of using already known commercial organic

additives as the only additional component of a copper electrolyte providing superconformal filling [25–27]. In addition, it seems promising to modify the accelerator molecule by introducing functional groups that are characteristic of leveler molecules. It was found [28] that the introduction of nitrogen into the MPS molecule promotes the manifestation of compounds such as 3-S-thiuronium propanesulfonate and 3-(benzothiazolyl-2-mercapto)-propyl sulfonate, along with accelerating, also leveling action. In [29], the possibility of implementing superconformal deposition using a single additive 3-(1-pyridinio)-1-propanesulfonate was shown, the dual effect of which (leveling in the upper part and accelerating in the lower part of the TSV hole) is explained within the framework of model concepts of the dual nature of the molecule due to the presence of a nitrogen-containing heterocycle and a sulfonic acid groups.

When functionalizing an accelerator molecule, the general requirements for it must be met: the presence of a terminal sulfonate group, $-SO_3$, is mandatory, since it accelerates copper deposition, while additives containing terminal groups, -COOH, -OH, and $-CH_3$, do not affect the rate of the process [21]. In addition, the introduction of additional groups into the accelerator molecule should not lead to changes in the kinetics and parameters of electrocrystallization [19]. Thus, along with an assessment of the overall effect of functionalized accelerator molecules on the rate and polarization of the electrochemical copper plating process, it is advisable to study the kinetics of nucleation and growth of a new phase in their presence. Indeed, based on the results of a potentiostatic study of this process, it is possible to evaluate the effect of various additives on the main parameters of phase formation: the density of nucleation sites, rate constant, and the mechanism of their activation [30, 31]. It should be borne in mind that the process of copper cathodic deposition can be complicated by the adsorption of solution components on the electrode surface, as well as by the side reaction of hydrogen evolution [32], since the pH of the copper deposition solution is quite low. The data obtained on the kinetics of copper coating formation, as well as on the patterns and parameters of electrocrystallization, will make it possible to draw a reasonable conclusion and can be used as the basis for further research on the possibility of using universal additives combining the properties of an accelerator and an leveler to purposefully regulate the filling process of TSV structures by varying the structure of accelerator molecules.

In this work we study the role of the functionalization of the bis-(3-sulfopropyl) disulfide molecule, used as an accelerator in TSV technology, by introducing electron-donating aromatic groups and amino groups into the structure of its molecule, in the electrocrystallization kinetics of copper electrodeposition.

The purpose of the work is to establish kinetic patterns and evaluate the main parameters of heterogeneous nucleation and growth of a new phase during electrocrystallization of copper during cathodic deposition from an acid sulfate solution in the presence of organic disulfides of various structures and compositions.

Work objectives:

1. To identify the role of the structure of organic disulfides in the non-stationary electrochemical deposition of copper from a sulfate solution.

2. To determine the effect of the structure of organic disulfides on the morphology of electrodeposited copper coatings.

3. To establish the parameters of heterogeneous nucleation during electrodeposition of copper in the presence of the studied organic disulfides and to evaluate the effect of the introduction of aromatic groups, as well as terminal amino groups into their structure, on the kinetics of copper electrocrystallization.

2. Experimental

Electrodeposition of copper coatings was carried out from aqueous solutions of the following composition: (1) – 156 g/L $CuSO_4 \cdot 5H_2O$ + 10 g/L H_2SO_4 + 50 mg/L Cl^- (pH 1.3); (2) – 12.5 g/L $CuSO_4 \cdot 5H_2O$ + 0.8 g/L H_2SO_4 + 50 mg/L Cl^- (pH 2.1) at room temperature (~20 °C) in a three-electrode electrochemical cell with undivided cathode and anode spaces, without mixing, under conditions of natural aeration. Solution (1) was used for galvanostatic deposition and morphology analysis of the obtained coatings, solution (2) was used for

non-stationary electrochemical measurements and study of copper electrocrystallization kinetics. The thickness of the coatings, determined by the gravimetric method, averages 5.571±0.003 microns.

A copper electrode reinforced in polymerized epoxy resin was used as a working electrode in non-stationary studies. To determine the coating morphology and the current efficiency, deposition was performed on a copper plate. Before electrochemical studies, the working electrode was cleaned on sandpaper with a grain size of P2500, polished on vacuum rubber with Al_2O_3 powder with a grain size of F800, washed with distilled water, cleaned using an ultrasonic bath, then the surface was degreased with isopropyl alcohol, rinsed again with distilled water and dried with filter paper. The preparation of the copper plate surface for electrochemical deposition included degreasing with isopropyl alcohol, rinsing with distilled water, etching in HNO_3 for 7 seconds, repeated rinsing with distilled water and drying with filter paper. The auxiliary electrode was a platinum plate, and a silver chloride electrode (SCE) was used as a reference electrode, connected to the working solution by an electrolytic bridge filled with a saturated solution of potassium nitrate.

The kinetics of cathodic deposition of copper coatings was studied using transient electrochemical methods of voltammetry, chronopotentiometry, and chronoammetry. The measurements were carried out using a computerized P-40X potentiostat/galvanostat. The potentials are given relative to a standard hydrogen electrode. The current density i is calculated per unit of the visible (geometric) area of the electrode, which is 0.045 cm^2. Chronopotentiograms of copper deposition were recorded at a current density of $i = -1.5$ A/dm^2 for 1000 s. Cathodic potentiodynamic curves were recorded by changing the electrode potential over time t from an open-circuit value to $E = -1000$ mV with a scan rate $\upsilon = dE/dt$. The kinetics of electrocrystallization was studied by chronoamperometry method, recording current I,t-transients at different deposition potentials E_{dep} (–200 mV, –300 mV) in the region of the voltammetric maximum. The current efficiency was determined by gravimetric method. The morphology of the coatings was studied by scanning electron microscopy on a JSM-6380LV JEOL installation.

The following organic disulfides were used as additives in concentration of 0.14 mmol/L: disodium salt of 3,3′-dithiodipropanedisulfonic acid (SPS), disodium salt of 4,4′-dithiodibenzenedisulfonic acid (DTBS), and disodium salt of 3,3′-dithiodi(4-aminobenzenesulfonic acid)-acids (AFDS) (Fig. 1). The DTBS molecule contains aromatic groups, and amino groups are additionally introduced into the AFDS molecule.

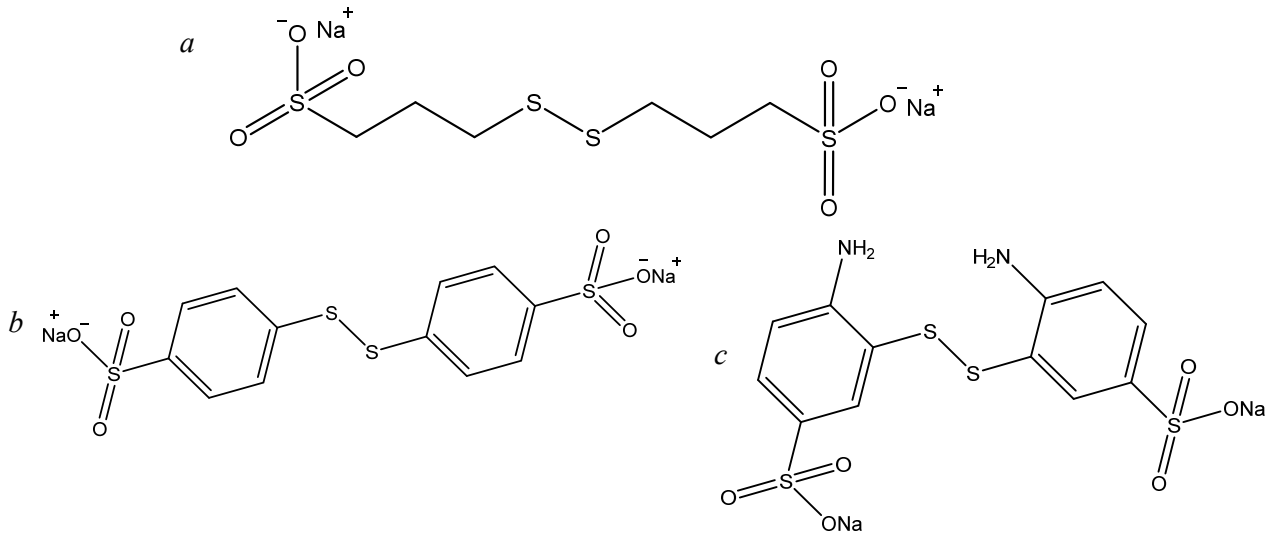

Fig. 1. Molecular structure of the studied organic disulfides: (a) – SPS, (b) – DTBS, (c) – AFDS

3. Results and discussion

The cathodic chronopotentiograms (Fig. 2) obtained in the studied electrolytes show a shift of the electrode potential in the negative direction relative to the open-circuit value (325±4 mV vs. standard hydrogen electrode). It can be seen that during galvanostatic deposition of copper, the introduction of all the studied organic disulfides – both aliphatic SPS and aromatic DTBS and AFDS – such a potential shift is expressed to a lesser extent compared with a solution containing no additives. This indicates a decrease in the electrode polarization of the deposition process, i.e. an acceleration of the cathodic reduction of copper from the sulfate electrolyte in the presence of SPS, DTBS, or AFDS. When aromatic groups are introduced into the structure of the disulfide molecule, the deposition potential shifts by about 15 mV in the positive direction relative to the solution containing the aliphatic chain (SPS). The presence of terminal amino groups in the disulfide structure (AFDS), in turn, leads to an even greater refinement of the deposition potential (~35 mV). Indeed, the greatest potential shift in the positive direction relative to the solution without additives is observed with the addition of AFDS, the smallest with the addition of SPS.

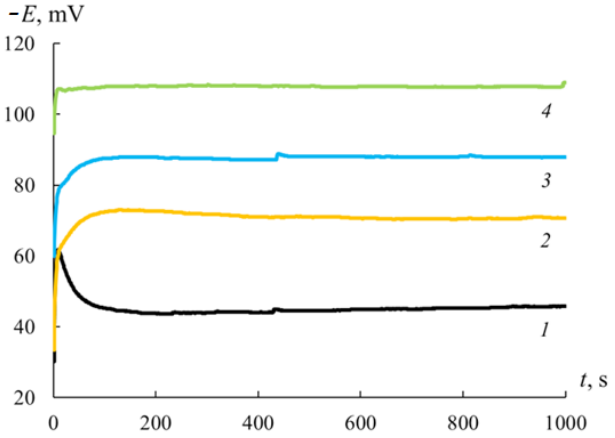

Fig. 2. Chronopotentiograms of copper deposition from solution (1) at i = -1.5 A/dm^2 in the absence of additives (*1*) and in the presence SPS (*2*), DTBS (*3*) and AFDS (*4*)

SEM images of the surface of copper coatings obtained from solutions of various compositions are shown in Fig. 3. The surface of the coating obtained from an electrolyte without additives is characterized by a coarse-grained structure with partial blurring of the grain boundaries. The effect of organic disulfides is manifested in the formation of crystallites with clearer edges. The introduction of the DTBS additive does not significantly affect the size of the crystallites, the use of the SPS additive leads to a decrease, and the AFDS leads to a significant decrease in the size of the crystallites. Thus, the introduction of an aromatic group accelerator (DTBS) into the structure of the molecule increases the size of the crystallites compared to a solution containing an aliphatic chain (SPS). On the contrary, additional functionalization of aromatic disulfide by introducing terminal amino groups (AFDS) into its structure leads to significant grinding of crystallites. This may be due to the fact that the presence of nitrogen in the AFDS molecule contributes to the manifestation, along with the accelerating, also the leveling effect of the additive, which is consistent with [28, 29].

A comparative analysis of the cathodic polarization curves (Fig. 4) shows that the shape of the voltammograms does not change when the studied additives are introduced into the sulfate

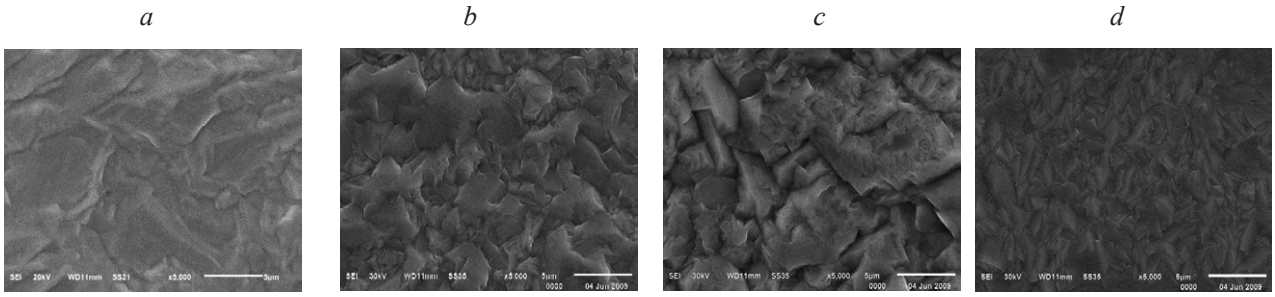

Fig. 3. SEM images obtained with magnification x5000 of the surface of copper coatings galvanostatically deposited (current density i = –1.5 A/dm^2, deposition time 1000 s) from solution (1) without additives (*a*) and in the presence of organic additives SPS (*b*), DTBS (*c*) and AFDS (*d*)

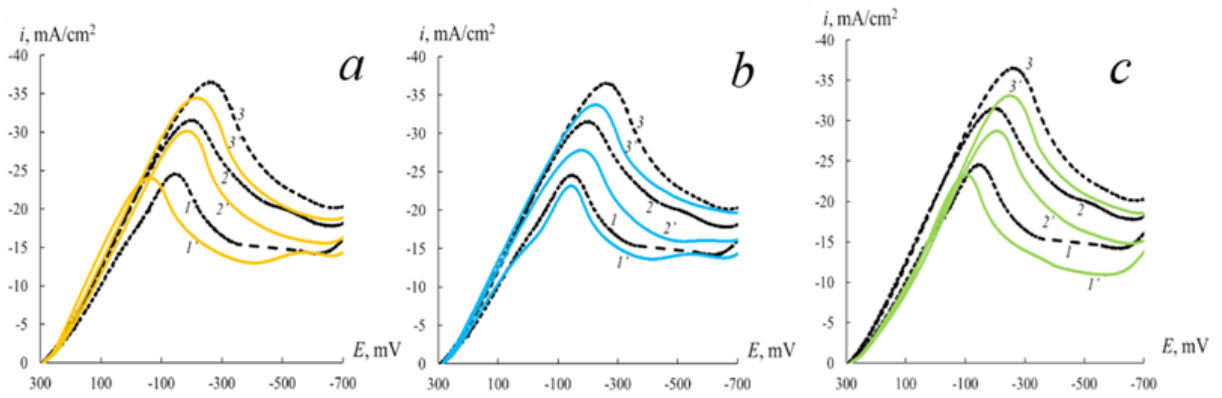

Fig. 4. Cathodic voltammograms obtained in solution (2) at υ = 100 (1,1′), 200 (2,2′), 300 (3,3′) mV/s in the absence of additives (1,2,3) and with the introduction of organic additives (1′,2′,3′): SPS (*a*), DTBS (*b*) and AFDS (*c*)

solution of copper plating. At the same time, the current density of the voltammetric maximum i_{max} decreases with the introduction of the studied disulfides compared with the solution without additives. The peak potential E_{max} shifts slightly to the positive region, with the exception of the solution containing the AFDS additive. The greatest shift to the positive area is observed when using an SPS additive based on an aliphatic structure. In addition, unlike DTBS and AFDS, in the case of SPS, acceleration of the process is observed at $E > E_{max}$ (Fig. 4). The totality of these data confirms the purely accelerating effect of SPS. The presence of aromatic groups (DTBS) in the structure of the molecule leads to a slight decrease in the current density of the voltammetric maximum i_{max} and a shift in the potential of the maximum E_{max} to a negative region compared with a solution containing an aliphatic chain (SPS). The additional introduction of terminal amino groups into the disulfide structure (AFDS) leads to a more noticeable shift of the maximum potential E_{max} to the negative region.

Thus, based on the observed changes in the voltammetric response, it is difficult to unambiguously judge the accelerating or inhibitory effect of the additives under study on the copper deposition process. This can be explained by the fact that the ratio of the contributions of the accelerating and leveling effects of the functionalized additives DTBS and AFDS changes in a complex way during recording the polarization curve under potentiodynamic conditions, and at $E < E_{max}$, the non-stationary mass transfer stage has the greatest effect on the kinetics of the process, which is apparently weakly sensitive to the presence of organic additives in solution. The diffusion limitations of the process are confirmed by the linear dependence of the maximum current density i_{max} vs. root of the potential scan rate $\upsilon^{1/2}$ (Fig. 5a). The i_{max} – $\upsilon^{1/2}$ curves for all additives are close and do not extrapolate to the origin, probably due to a parallel side process (for example, hydrogen evolution). Indeed, the current efficiency according to gravimetric measurements is 85±4 %. At the same time, a significant shift of the maximum potential to the negative side with an increase in the scan rate indicates the irreversibility of the charge transfer stage (Fig. 5b).

The role of organic disulfides in the kinetics of electrocrystallization was established by determining the parameters of nucleation and growth of a new phase during copper deposition. The kinetics of the process is usually determined under the assumption of instantaneous or continuous activation of nucleation sites [33] within the framework of the 3D nucleation model proposed by Scharifker and Hills [34]. However, a preliminary comparison of the experimental chronoamperograms with the theoretical equations of the Scharifker-Hills model showed their significant discrepancy, which made it impossible to establish the nucleation kinetics, much less to quantify the characteristics of the copper electrocrystallization. The most likely causes of the revealed deviation are the significant contribution of the hydrogen evolution reaction, as well as the presence of substances capable of adsorption in the solution. In this regard, for

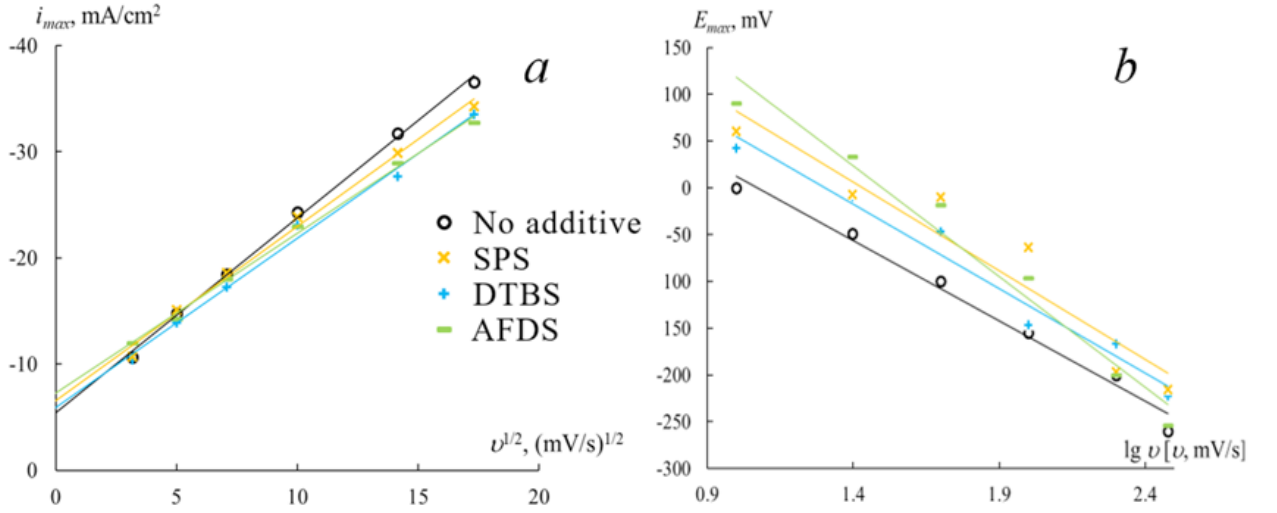

Fig. 5. (*a*) – Current density of the voltammetric maximum vs. root of the potential scan rate, (*b*) – potential of the voltammetric maximum vs. decimal logarithm of the potential scan rate obtained in solution (2) without additives and with the introduction of organic additives SPS, DTBS and AFDS

further analysis, we used an extended model of nucleation and growth of a new phase [32], which takes into account that diffusion-controlled electrodeposition of metal occurs together with hydrogen reduction and adsorption of solution components. The extended model makes it possible to describe the potentiostatic transient current $i(t)$ obtained during electrodeposition as the sum of three components:

$$i(t) = i_{Cu}(t) + i_H(t) + i_{ads}(t). \quad (1)$$

Here, the current density i_H determines the rate of the proton reduction reaction [32] and can be described by the ratio:

$$i_H(t) = P_1 S(t), \quad (2)$$

in which the coefficient $P_1 = z_H F k_H$ includes the charge $z_H F$ responsible for the reduction of 1 mole of protons ($z_H = 1$, $F = 96485$ C/mole), k_H is the rate constant of the proton reduction reaction. The fraction of the surface occupied by electrodeposited copper

$$S(t) = (2c_0 M/\pi\rho)^{1/2}\theta(t) \quad (3)$$

it includes c_0 – the initial volume concentration of copper ions (0.05 M), M – the molar mass of copper (63.5 g/mole), r – the density of the copper deposit (8.96 g/cm^3), as well as the function

$$q(t) = \{1-\exp\{-P_2[t-(1-\exp(P_3 t))/P_3]\}\}. \quad (4)$$

Here, the parameters $P_2 = N_0 \pi k D$ and $P_3 = A$ include the density of active nucleation sites on the electrode surface (N_0), the diffusion coefficient of copper ions (D), the nucleation rate (A), and the constant $k = (8\pi c_0/\rho)^{1/2}$.

The current density i_{Cu}, which determines the rate of the diffusion-controlled copper reduction process, is determined as follows [32]:

$$i_{Cu}(t) = P_4 t^{-1/2}\theta(t), \quad (5)$$

where $P_4 = 2FD^{1/2}c_0/\pi^{1/2}$.

Finally, the third term i_{ads} is due to the adsorption process described in [32] as an exponential decrease in current:

$$i_{ads}(t) = K_1 \exp(-K_2 t). \quad (6)$$

Thus, the total current density will be described by the following expression:

$$i(t) = \left\{P_1^* + P_4 t^{-1/2}\right\} \times \left\{1-\exp\left\{-P_2\left[t-\frac{1-\exp(P_3 t)}{P_3}\right]\right\}\right\} + K_1 \exp(-K_2 t), \quad (7)$$

where $P_1^* = P_1(2c_0 M/\pi\rho)^{1/2}$.

To identify the effect of organic disulfides on the stage of heterogeneous nucleation during cathodic deposition of copper, kinetic parameters of the electrocrystallization process were obtained by approximating equation (7) and experimental chronoamperograms recorded at potentials in the vicinity of the voltammetric peak: –200 and –300 mV. Experimental chronoamperograms have the shape of a curve with a maximum (Fig. 6),

which is typical for nucleation processes: a sharp increase in current during the initial period of the electrodeposition process is followed by a decrease in current and its tending to a constant value. Their comparison with the current transients found in accordance with the extended model of the 3D nucleation process shows that the use of generalized equation (7) made it possible to obtain a complete coincidence of experimental and theoretical chronoamperograms. In addition, *i*,*t*-curves were calculated for three parallel processes (electrocrystallization, hydrogen evolution, and adsorption). As expected, the rate of adsorption is higher in solutions containing additives than in their absence. The current caused by the hydrogen evolution reaction increases and reaches a constant value, which does not significantly depend on the presence of additives.

The nucleation current is characterized by the formation of a maximum in the initial period

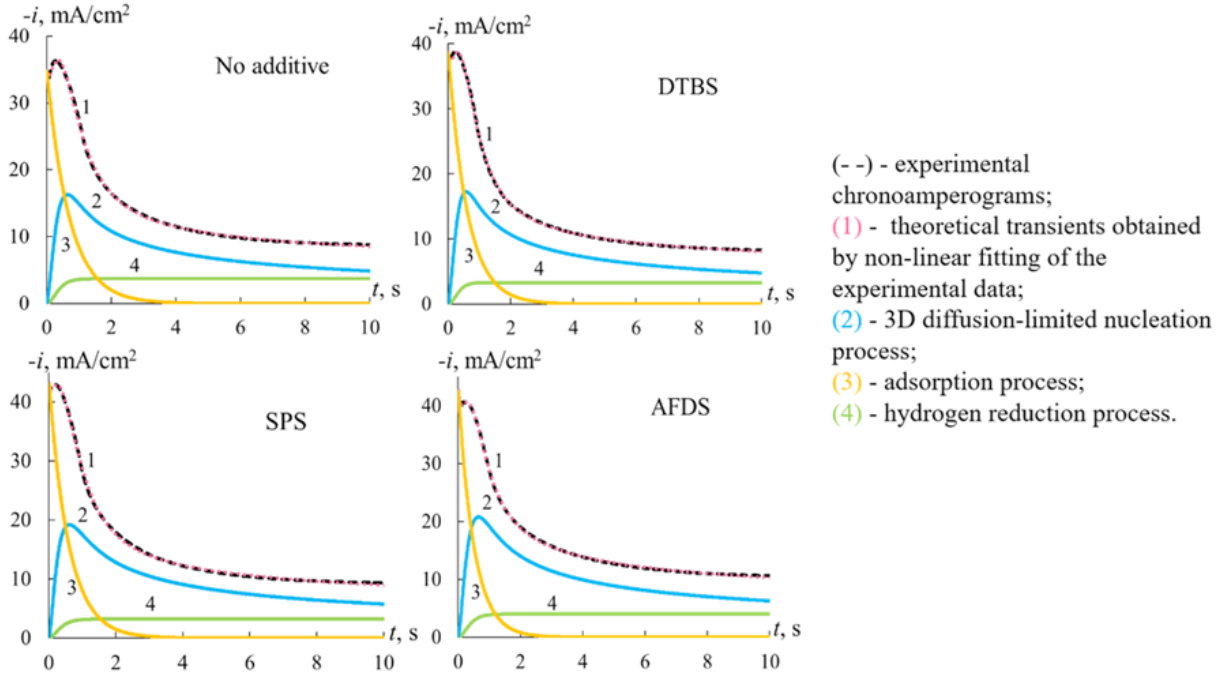

Fig. 6. Experimental and theoretically calculated chronoamperograms obtained by electrodeposition of copper at a potential of -300 mV

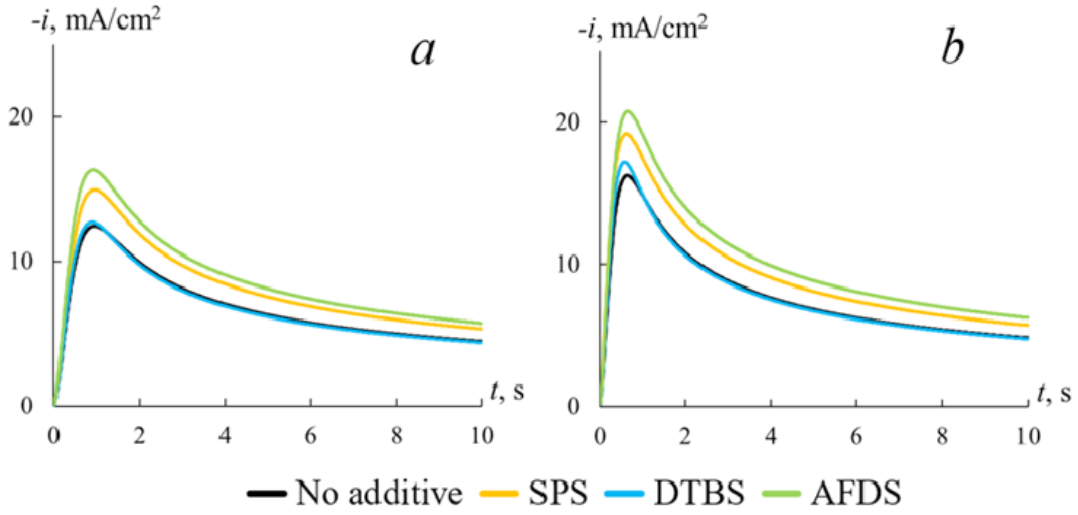

Fig. 7. Partial curves of copper electrocrystallization at a cathode potential of -200 mV (*a*) and -300 mV (*b*)

of the process, the height of which depends on the deposition potential and the presence of additives in the electrolyte (Fig. 7). With an increase in the cathodic potential, the rate of electrocrystallization increases, as with the introduction of all the studied organic disulfides into the solution. At the same time, DTBS gives a minimal accelerating effect (4–5 %), while SPS and AFDS increase the nucleation current by 17–22 % and 24–34 %, respectively.

Using the extended electrocrystallization model, it was also possible to determine the values of kinetic parameters of electrodeposition at the stage of nucleation and growth of a new phase, including in the presence of organic disulfides (Fig. 8). The analysis shows that the transition from aliphatic (SPS) to functionalized (DTBS, AFDS) organic disulfides is unsystematic and to a small extent affects both the density of nucleation sites and the rate constant of activation of potential nucleation sites, which on average are $N_0 = (1.3\pm0.3)\cdot10^{-5}$ cm^{-2} and $A = (2.8\pm0.6)$ cm^{-1}, respectively. It is known that, depending on the value of parameter A, the activation process can be classified as instantaneous if $At \gg 1$, otherwise as continuous [34]. The estimation of At value by the time the maximum is reached on the nucleation curve ($t \approx 1$ s) leads, both in the case of a solution without additives and with additives, to the value of $At \approx 3$, which allows us to consider the activation of nucleation sites as continuous.

Thus, despite the introduction of aromatic groups and/or amino groups into the structure of DTBS and AFDS disulfides, the kinetics and parameters of electrocrystallization do not change significantly, which is a prerequisite [19] when choosing a universal organic additive that exhibits accelerating and leveling effects depending on the current distribution inside the TSV structure. At the same time, the results of non-stationary electrochemical studies and scanning electron microscopy allow us to consider the addition of AFDS, characterized by the presence of both aromatic groups and amino groups in its structure, the most promising as a bifunctional additive in relation to cathodic deposition of copper, since for this compound the most pronounced effect of accelerating the rate of electrocrystallization is observed (Fig. 7), on the one hand, and a noticeable morphological smoothing of the surface, on the other hand (Fig. 3), while maintaining the kinetics and parameters of copper electrocrystallization.

4. Conclusion

The introduction of organic disulfides (disodium salts of 3,3′-dithiodipropanedisulfonic acid, 4,4′-dithiodibenzene disulfonic acid and

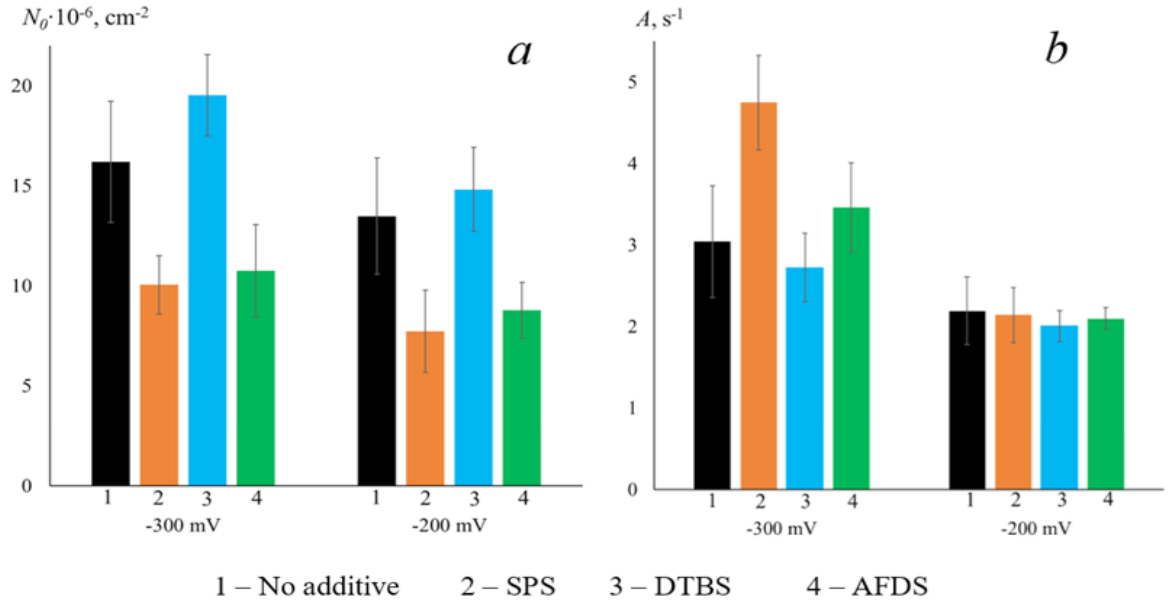

Fig. 8. Kinetic parameters of nucleation: *a* – nucleation active site densities (N_0), *b* – activation rate constant of potential nucleation active site (A)

3,3′-dithiodi(4-aminobenzenesulfonic acid) into an acidic sulfate solution leads to a decrease in the cathodic polarization of the copper reduction process during galvanostatic deposition, which confirms the accelerating effect of these additives. The functionalization of the aliphatic disulfide (SPS) molecule by including aromatic groups in the structure enhances the deposition potential by about 15 mV, while the additional introduction of amino groups into the disulfide structure leads to an even greater (about 35 mV) shift in the deposition potential to the positive side.

Scanning electron microscopy revealed that in the presence of the studied additives of organic disulfides, crystallites with more pronounced faces form on the surface of the copper coating. Moreover, if the introduction of a 4,4′-dithiodibenzene disulfonic acid salt does not significantly affect the size of the crystallites, then the use of 3,3′-dithiodi(4-aminobenzenesulfonicacid leads to their significant reduction. According to literature data, this effect can be explained by the presence of amino groups responsible for the leveling effect in the molecule of the AFDS accelerator. The dual nature of functionalized additives in relation to the copper deposition process is indirectly confirmed by the results of potentiodynamic measurements, the analysis of the critical parameters of which allowed us to establish that the charge transfer stage during copper deposition is irreversible, and the process is complicated by the non-stationary diffusion of ions of the deposited metal to the cathode surface.

The role of organic disulfides in the kinetics of electrocrystallization has been established taking into account the double-layer and adsorption processes which occur during the initial deposition period, as well as the side reaction of hydrogen evolution, the contribution of which is confirmed by the value of the current efficiency of 85±4 %. It was found that the rate of electrocrystallization increases with the introduction of all the studied organic disulfides into the solution (DTBS by 4–5 %, SPS by 17–22 %, and AFDS by 24–34 %), which confirms their accelerating effect. However, the kinetics of 3D nucleation during copper deposition in the presence of the studied additives remains unchanged and corresponds to the mechanism of continuous activation of nucleation sites. During the functionalization of organic disulfide molecules, their density and the rate constant of activation vary slightly and unsystematically, averaging $(1.3\pm0.3)\cdot10^{-5}$ cm^{-2} and 2.8 ± 0.6 cm^{-1}, respectively.

Contribution of the authors

Ilina E. A. – conducting electrochemical research, writing a text. Kozaderov O. A. – scientific guidance, research concept, methodology development, text editing, final conclusions. Sotskaya N. V. – conducting research, editing text. Golovinsky A. D. – conducting electrochemical research. Kolbeshkina E. D. – conducting electrochemical research. Polikarchuk V. P. – conducting organic synthesis.

Conflict of interests

The authors declare that they have no known competing financial interests or personal relationships that could have influenced the work reported in this paper.

References

1. Lau J. Overview and outlook of through-silicon via (TSV) and 3D integrations. *Microelectronics International*. 2011;28(2): 8–22. https://doi.org/10.1108/13565361111127304

2. Morrow P. R., Park C. M., Ramanathan S., Kobrinsky M. J., Harmes M. Three-dimensional wafer stacking via Cu-Cu bonding integrated with 65-nm strained-Si/low-k CMOS technology. *IEEE Electron Device Letters*. 2006;27(5): 335–337. https://doi.org/10.1109/led.2006.873424

3. Wang F., Zeng P., Wang Y., Ren X., Xiao H., Zhu, W. High-speed and high quality TSV filling with the direct ultrasonic agitation for copper electrodeposition. *Microelectronic Engineering*. 2017;180: 30–34. https://doi.org/10.1016/j.mee.2017.05.052

4. Josell D., Moffat T. Superconformal copper deposition in through silicon vias by suppression-breakdown. *Journal of the Electrochemical Society*. 2018;165(2): 23–30. https://doi.org/10.1149/2.0061802jes

5. Burkett S. L., Jordan M. B., Schmitt R. P., Menk L. A., Hollowell A. E. Tutorial on forming through-silicon vias. *Journal of Vacuum Science & Technology A*. 2020;38(3): 31202. https://doi.org/10.1116/6.0000026

6. Gavrilov S. A., Belov A. N. *Electrochemical processes in micro- and nanoelectronics technology: textbook. manual 2nd ed*[*]. Moscow: RIOR: INFRA-M Publ.; 2019. 240 p. Available at: https://library.atu.edu.kz/flgl/48784.pdf

7. Kondo K., Matsumoto T., Watanabe K. Role of additives for copper damascene electrodeposition: experimental study on inhibition and acceleration effects. *Journal of the Electrochemical Society*. 2004;151: 250. https://doi.org/10.1149/1.1649235

8. Chan P.-F., Chiu Y.-D., Dow W.-P., Krug K., Lee Y.-L., Yau S. Use of 3,3-thiobis(1-propanesulfonate) to accelerate microvia filling by copper electroplating. *Journal of the Electrochemical Society*. 2013;160(12): 3271–3277. https://doi.org/10.1149/2.047312jes

9. Wang F., Zhou K., Zhang Q., ... Feng W. Effect of molecular weight and concentration of polyethylene glycol on through-silicon via filling by copper. *Microelectronic Engineering*. 2019;215: 111003. https://doi.org/10.1016/j.mee.2019.111003

10. Aleshina V. Kh., Grigoryan N. S., Asnis N. A., Abrashov A. A., Fadeeva V. A., Chudnova T.A. Effect of organic additives on copper electrodeposition in the manufacture of printed boards. *International Journal of Corrosion and Scale Inhibition*. 2023;12(1): 126–144. https://doi.org/10.17675/2305-6894-2023-12-1-7

11. Dow W.-P., Chiu Y.-D., Yen M.-Y. Microvia filling by Cu electroplating over a Au seed layer modified by a disulfide. *Journal of the Electrochemical Society*. 2009;156: 155. https://doi.org/10.1149/1.3117562

12. Sun Q., Cao H., Ling H., Li M. Analysis of accelerator consumption in TSV copper electroplating. In: *Proceedings – 2013 14th International Conference on Electronic Packaging Technology*. 2013: 818–821. https://doi.org/10.1109/ICEPT.2013.6756589

13. Chrzanowska A., Mroczka R., Florek M. Effect of interaction between dodecyltrimethylammonium chloride (DTAC) and bis(3-sulphopropyl) disulphide (SPS) on the morphology of electrodeposited copper. *Electrochimica Acta*. 2013;106: 49–62. https://doi.org/10.1016/j.electacta.2013.05.061

14. Wang F., Le Y. Bis-(3-sulfopropyl) disulfide acceleration of copper electrodeposition via molecular dynamics and quantum chemical calculations. *International Journal of Electrochemical Science*. 2020;15(6): 4931–4943. https://doi.org/10.20964/2020.06.11

15. Arnold M., Emnet C., Fluegel A., ... Broekmann P. Alternative pathway of SPS action: impact on electrochemistry and additive action. *ECS Meeting Abstracts*. 2010;2(34): 2036–2036. https://doi.org/10.1149/MA2010-02/34/2036

16. Garcia-Cardona E., Wong E. H., Barkey D. P. NMR spectral studies of interactions between the accelerants SPS and MPS and copper chlorides. *Journal of the Electrochemical Society*. 2011;158(3): 143–148. https://doi.org/10.1149/1.3529937

17. Schmitt K. G., Schmidt R., Gaida J., Gewirth A. A. Chain length variation to probe the mechanism of accelerator additives in copper electrodeposition. *Physical Chemistry Chemical Physics*. 2019;21(30):16838–16847. https://doi.org/10.1039/c9cp00839j

18. Pasquale M.A., Gassa L.M., Arvia A.J. Copper electrodeposition from an acidic plating bath containing accelerating and inhibiting organic additives. *Electrochimica Acta*. 2008;53(20): 5891–5904. https://doi.org/10.1016/j.electacta.2008.03.073

19. Guo L., Li S., He Z., ... Yang G. Electroplated copper additives for advanced packaging: a review. *ACS Omega*. 2024;9(19): 20637–20647. https://doi.org/10.1021/acsomega.4c01707

20. Jin S., Kim S.-M. Jo Y., Lee W. Y., Lee S.-Y., Lee M.-H. Unraveling adsorption behaviors of levelers for bottom-up copper filling in through-silicon-via. *Electronic Materials Letters*. 2022;18(1): 583–591. https://doi.org/10.1007/s13391-022-00364-6

21. Dow W.-P., Li C.-C., Su Y.-C., ... Hsu S. Microvia filling by copper electroplating using diazine black as a leveler. *Electrochimica Acta*. 2009;54(2): 5894-5901. https://doi.org/10.1016/j.electacta.2009.05.053

22. Wang C., Zhang J., Yang P., An M. Electrochemical behaviors of Janus Green B in through-hole copper electroplating: an insight by experiment and density functional theory calculation using Safranine T as a comparison. *Electrochimica Acta*. 2013;92: 356–364. https://doi.org/10.1016/j.electacta.2013.01.064

23. Wu H., Wang Y., Li Z., Zhu W. Investigations of the electrochemical performance and filling effects of additives on electroplating process of TSV. *Scientific Reports*. 2020;10(1): 9204. https://doi.org/10.1038/s41598-020-66191-7

24. Sun J.-J., Kondo K., Okamura T. Oh S., ... Takahashi K. High-aspect-ratio copper via filling used for three-dimensional chip stacking. *Journal of the Electrochemical Society*. 2003;150(6). https://doi.org/10.1149/1.1572154

25. Tang J., Zhang Y., Zhang X., Guo J. D., Shang J. K. Copper bottom-up filling for through silicon via (TSV) using single JGB additive. *ECS Electrochemistry Letters*. 2015;4(9): 28–30. https://doi.org/10.1149/2.0101509eel

26. Wang F., Le Y. Experiment and simulation of single inhibitor SH110 for void-free TSV copper filling. *Scientific Reports*. 2021;11(1). https://doi.org/10.1038/s41598-021-91318-9

27. Wang C., Zhang J., Yang P., Zhang B., An M. Through-hole copper electroplating using nitrotetrazolium blue chloride as a leveler. *Journal of the Electrochemical Society*. 2013;160(3): 85–88. https://doi.org/10.1149/2.035303jes

28. Chen T.-C., Tsai Y.-L., Hsu C.-F., Dow W.-P., Hashimoto Y. Effects of brighteners in a copper plating bath on throwing power and thermal reliability of plated through holes. *Electrochimica Acta*. 2016;212: 572–582. https://doi.org/10.1016/j.electacta.2016.07.007

29. Le Y., Fu-liang W. Void free TSV copper filling using single additive 3-(1-pyridinio)-1-propanesulfonate (PPS). In: *2020 3rd International Conference on Advanced Electronic Materials, Computers and Software Engineering (AEMCSE)*. 2020: 636–640. https://doi.org/10.1109/AEMCSE50948.2020.00139

30. Kozaderov O., Sotskaya N., Yudenkova L., Buylov N., Ilina E. Electrocrystallization and morphology of copper coatings in the presence of organic additives. *Coatings*. 2023;13(11): 1896. https://doi.org/10.3390/coatings13111896

31. Ilina E. A., Kozaderov O. A., Sotskaya N. V., Vandyshev D. Y., Polikarchuk V. A., Shikhaliev K. S. Kinetics of copper electrocrystallization from an acid sulfate solution in the presence of N-methyl polyvinylpyridine-methyl sulfate. *Condensed Matter and Interphases*. 2025;27(3): 368–379. https://doi.org/10.17308/kcmf.2025.27/13013

32. Garfias Garcia E., Romero-Romo M., María T., Ramírez-Silva, Palomar-Pardavé M. Overpotential nucleation and growth of copper onto polycrystalline and single crystal gold electrodes. *International Journal of Electrochemical Science*. 2012;7(4): 3102–3114. https://doi.org/10.1016/S1452-3981(23)13938-1

33. Zhang Q., Yu X., Hua Y., Xue W. The effect of quaternary ammonium-based ionic liquids on copper

electrodeposition from acidic sulfate electrolyte. *Journal of Applied Electrochemistry*. 2015;45: 79–86. https://doi.org/10.1007/s10800-014-0774-z

34. Scharifker B., Hills G. Theoretical and experimental studies of multiple nucleation. *Electrochimica Acta*. 1983;28(7): 879–889. https://doi.org/10.1016/0013-4686(83)85163-9

Information about the authors

Evgenia A. Ilina, Junior Researcherat the Laboratory of organic additives for the processes of chemical and electrochemical deposition of metals and alloys used in the electronics industry, Voronezh State University (Voronezh, Russian Federation).
https://orcid.org/0009-0004-4825-5894
zhenya.ali@yandex.ru

Oleg A. Kozaderov, Dr. Sci. (Chem.), Leading Researcher at the Laboratory of organic additives for the processes of chemical and electrochemical deposition of metals and alloys used in the electronics industry, Voronezh State University (Voronezh, Russian Federation).
https://orcid.org/0000-0002-0249-9517
ok@chem.vsu.ru

Nadezhda V. Sotskaya, Cand. Sci. (Chem.), Associate Professor at the Department of Physical Chemistry, Voronezh State University (Voronezh, Russian Federation).
https://orcid.org/0000-0003-4088-1546
nvs@chem.vsu.ru

Andrey D. Golovinsky, student at the Department of Physical Chemistry, Voronezh State University (Voronezh, Russian Federation).
https://orcid.org/0009-0001-1352-3738
golovinskiiandrei773@gmail.com

Elizaveta D. Kolbeshkina, student at the Department of Physical Chemistry, Voronezh State University (Voronezh, Russian Federation).
https://orcid.org/0009-0004-3941-0047
elsvtkolb@gmail.com

Vladimir A. Polikarchuk, Cand. Sci. (Chem.), Junior Researcher at the Laboratory of organic additives for the processes of chemical and electrochemical deposition of metals and alloys used in the electronics industry, Voronezh State University (Voronezh, Russian Federation).
https://orcid.org/0009-0001-7339-5803
polikarchyk@mail.ru

Received November 24, 2025; approved after reviewing January 12, 2026; accepted for publication January 15, 2026; published online April 01, 2026.

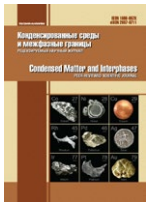

ISSN 1606-867X (Print)
ISSN 2687-0711 (Online)
Condensed Matter and Interphases
Kondensirovannye Sredy i Mezhfaznye Granitsy
https://journals.vsu.ru/kcmf/

Original articles

Research article
https://doi.org/10.17308/kcmf.2026.28/13588

Microstructural and hydrophilic properties of acrylonitrile-butadiene-styrene copolymer ABS samples with different 3D-printed patterns

A. S. Lenshin[1], V. E. Frolova[1], V. A. Makagonov[2], A. K. Pelagina[1], E. P. Domashevskaya[1]✉

[1]Voronezh State University,
1, Universitetskaya pl., Voronezh 394018, Russian Federation

[2]Voronezh State Technical University,
14, Moskovsky pr., Voronezh 94026, Russian Federation

Abstract

Objectives: The aim of this study is to investigate the influence of different 3D printing patterns, under identical thermal and mechanical parameters of the 3D printing process itself, on the microstructural and hydrophilic properties of amorphous ABS copolymer samples printed with five different 3D printing patterns by sequentially depositing layers using FDM (Fused Deposition Modeling).

Conclusions: The results of studying the printed samples using SEM, X-ray diffraction, IR spectroscopy, and contact angle measurements showed that the combination of thermal and mechanical effects during 3D printing in the studied extrusion mode does not cause noticeable orientation of the polymer chains of the original amorphous ABS copolymer, does not disrupt its intrastructural chemical bonds, and the surface of all printed samples with five different patterns is hydrophilic. Moreover, the printed sample with the most complex geometry is the 1_Hilbert pattern, which has the most distorted morphology and surface defects and exhibits the highest contact angle ($\varphi = 67^{o}$), exceeding the corresponding values in samples with other patterns ($\varphi \approx 60^{o}$) by ~10 %, and has a hydrophilic surface.

Keywords: Acrylonitrile-butadiene-styrene copolymer ABS, Various 3D-printed patterns, Printed samples, Surface morphology, Amorphous state, IR spectra, Contact angles, Hydrophilic surface.

Funding: This work was supported in part by the Ministry of Education and Science of the Russian Federation under a state assignment for universities in the field of scientific activity, project no. FZGU-2026-0009, and the Advanced Engineering School of VSU.

For citation: Lenshin A. S., Frolova V. E., Makagonov V. A., Pelagina A. K., Domashevskaya E. P. Microstructural and hydrophilic properties of acrylonitrile-butadiene-styrene copolymer ABS samples with different 3D-printed pattern designs. *Condensed Matter and Interphases*. 2026;28(1): 69–80. https://doi.org/10.17308/kcmf.2026.28/13588

Для цитирования: Леньшин А. С., Фролова В. Е., Макагонов В. А., Пелагина А. К., Домашевская Э. П. Микроструктурные и гидрофильные свойства образцов из сополимера акрилонитрил-бутадиен-стирол ABS с различными модельными рисунками 3D-печати. *Конденсированные среды и межфазные границы*. 2026;28(1): 69–80. https://doi.org/10.17308/kcmf.2026.28/13588

✉ Evelina P. Domashevskaya, e-mail: ftt@phys.vsu.ru

1. Introduction

Thermoplastic polymers play an important role in various engineering fields due to their excellent functional and technological properties. Along with other thermoplastics, acrylonitrile-butadiene-styrene copolymer (ABS) is widely used as a structural material. ABS consists of varying amounts of polyacrylonitrile (15–30 %), polybutadiene (5–35 %), and polystyrene (40–60 %) and is widely used in the aerospace and defense industries, automotive manufacturing, and in electrical, telecommunications, and computer technologies [1]. The advantages of ABS copolymer also include the ability to manufacture various products with matte and mirror-like surfaces. ABS exhibits good impact resistance, toughness, rigidity, heat resistance, elasticity, and environmental friendliness. It is tolerant to moisture, inorganic acids and salts, solvents, lubricating oils, and alkalis. A significant advantage of ABS thermoplastic is its recyclability. The chemical formula of the acrylonitrile-butadiene-styrene (ABS) copolymer consists of three parts: $(C_8H_8)_x \cdot (C_4H_6)_y \cdot (C_3H_3N)_z$ [2].

The structural formula of the ABS copolymer [3, 4] is shown in Fig. 1.

The melting point of the ABS copolymer ranges from 220 °C to 260 °C, but it begins to soften at approximately 105 °C. Different grades of ABS may have slightly different melting points, but this range is generally typical. It should also be noted that the glass transition of the ABS copolymer occurs in the temperature range of approximately 60÷65 °C.

ABS products are recommended for use in temperatures ranging from –20 to 80 °C, as their mechanical properties vary with temperature [3].

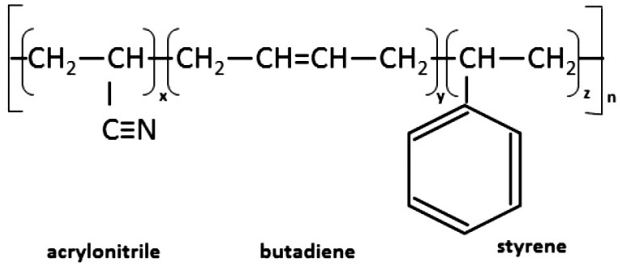

Fig. 1. Structural formula of the acrylonitrile-butadiene-styrene (ABS) copolymer [3, 4]

However, the material easily withstands short-term exposure to temperatures up to +100°C, as well as long-term heating at +75÷80 °C. The rigidity, mechanical strength, and durability of ABS significantly exceed those of high-impact polystyrene and other polymers. To increase impact resistance, viscosity, and heat resistance, the ratio of polybutadiene, polystyrene, and polyacrylonitrile copolymers in ABS can be varied, allowing for the production of different grades of ABS by varying the component proportions [3].

The properties of ABS products also depend to some extent on the conditions under which the material is processed into the final object. For example, high-temperature molding improves the gloss and heat resistance of products, while the highest impact resistance is achieved with low-temperature molding. Fibers (usually fiberglass) and additives can be blended with resin granules to impart strength to the final product and increase its maximum operating temperature. Pigments can also be added to ABS, as its natural color ranges from translucent ivory to white. Additives are also used to protect against ultraviolet radiation [2].

ABS copolymers are resistant to aqueous acids, alkalis, concentrated hydrochloric and phosphoric acids, as well as animal, vegetable, and mineral oils. They are soluble in esters, acetone, chloroform, and ethylene dichloromethane, and exhibit low resistance to chlorinated solvents, alcohols, and aldehydes [2].

Although ABS thermoplastics are primarily used in mechanical applications, they also exhibits electrical properties that are quite stable over a wide frequency range. Temperature and humidity have virtually no effect on these properties within the permissible operating temperature range [4]. However, when exposed to high temperatures, such as during wood combustion, ABS plastics are highly flammable. They melt and then boil, after which the vapors turn into an intense hot flame, releasing toxic decomposition products. The toxicity of ABS thermoplastics are characterized in [5].

Of particular importance to modern materials science is the fact that, along with other thermoplastics, acrylonitrile butadiene styrene is a common material used in 3D printers [6] as ABS

filament because it is inexpensive, durable, highly stable, and can be post-processed in various ways, including sanding, painting, gluing, casting, and chemical smoothing.

It is known [6] that ABS deforms when used in 3D printing due to shrinkage that occurs during cooling during the printing process. However, shrinkage can be reduced by printing samples on a heated print surface, using glue to ensure good adhesion of the first layer of the print to the print surface, or printing with edges/rafts at the base of the print to improve adhesion to the print surface [6].

The aim of this study is to investigate the influence of different 3D printing patterns under identical thermal and mechanical parameters of the 3D printing process on the microstructural and hydrophilic properties of ABS copolymer samples printed with five different 3D printing patterns by sequentially depositing layers using Fused Deposition Modeling (FDM). Structural and optical characterization methods enable rapid characterization and comparison of acrylonitrile-butadiene-styrene polymer compounds [7]. Furthermore, infrared calibration curves are extremely useful in analyzing the composition of ABS plastic. Analyses based on this method provide information that can be used to predict the physical properties of the formed plastic [7–12].

Therefore, to achieve our goal of studying the influence of the 3D printing process on the microstructural and hydrophilic properties of ABS-printed samples, we used scanning electron microscopy (SEM), X-ray diffraction (XRD), IR spectroscopy, and contact angle measurements to determine surface wettability.

The prerequisites for studying the influence of different patterns on the properties of ABS samples in this work are the differences in the chemical formula of ABS, and especially its structural formula (with a long repeat period), from the corresponding parameters of two other thermoplastics, PETG and PLA, and the observed tendency for the contact angle to increase (hydrophilicity to decrease) in printed samples with the most complex pattern, i.e., 1_Hilbert: up to 4 % [13] in the PETG sample and up to 10 % [14] in the PLA sample. We previously conducted similar studies of the effect of the 3D printing process on the microstructural and hydrophilic properties of samples with the same pattern printed from two other thermoplastic polymers: polyethylene terephthalate-glycol (PETG) and polylactic acid (PLA). Therefore, when discussing the results obtained in this study, we will compare them with similar results for two other polymers published in our papers [13] and [14].

Despite the presence of papers in modern scientific journals devoted to modeling the properties, computer design, and improvement of polymer models and computer programs, we did not find any studies on the possible influence of pattern designs on polymer properties. Only one theoretical study on modeling the influence of the structure of an amorphous-crystalline polymer on its deformation properties [15] showed that the deformation characteristics of the polymer depend significantly on the relative positions of the crystalline and amorphous phases of the polymer in accordance with the five structural models considered: 1 – ideal phase mixing; 2 – square lattice of the crystalline phase; 3 – square lattice of the amorphous phase; 4 – staggered phase arrangement; 5 – random phase arrangement.

However, in the theoretical modeling conducted in [15], deformation and structural rearrangements of the amorphous phase were not taken into account. Whereas in the following sections of the article, we will show that the polymer we studied, both in the initial ABS filament state and in the printed samples, contains only one amorphous phase. It is this circumstance that determines the novelty and relevance of our experimental study of the possible influence of different geometry of the 3D printing model pattern on the microstructural and hydrophilic properties of ABS printed samples with five different model patterns.

2. Experimental. Research objects and methods

The test specimens were made from colorless MAKO 1.75 Natural ABS Filament with a diameter of 1.75 mm using the Fused Deposition Modeling (FDM) method on a Hercules Original 3D printer at an extruder temperature of 240 °C and a

power of 500 W. Table 1 presents the 3D printer parameters used to print specimens with five different patterns. Using the parameters listed in Table 1, five cylindrical specimens with different 3D patterns were printed.

Fig. 2 shows the five types of patterns studied. The patterns shown in Fig. 2 were taken from the Prusa Slicer modeling software. After constructing five models with different 3D patterns, five samples with five different 3D patterns (1_Hilbert, 2_Concentric, 3_Archimedian, 4_Rectilinear, 5_Octagram) were printed from these models.

The printed colorless samples have the same cylindrical shape with a diameter of 20 mm and a thickness of 5 mm. Along with the printed samples, the original filamentary acrylonitrile-butadiene-styrene (ABS filament) sample was studied, so the next section presents the results of the microstructural properties of the six samples.

Scanning electron microscopy (SEM) of the surfaces of the five printed samples with different patterns was performed on a JSM 6510LV scanning electron microscope at the VSU Center for Collective Use. To obtain better contrast in the SEM micrographs, surface morphology studies of the printed samples were performed on the surfaces of samples coated with a very thin gold layer (a few nanometers thick) at various magnifications of ×40, ×1000, and ×5000.

Table 1. 3D printing parameters on a Hercules Original printer

3D Printing Parameter	Value
Value layer thickness / extruder nozzle diameter	0.8 mm
Filling density	20 %
Filling speed	50 mm/s
Filling model patterns	5 types
Sample thickness	5.0 mm
Extruder nozzle temperature	240 °C

X-ray diffraction (XRD) analysis of the printed samples and the original ABS filament was performed at the Voronezh State Technical University using a BRUCKER D2 Phaser diffractometer (with a copper anode), at a high voltage of U = 30 kV and anode current of I = 10 mA in the Bragg angle range $2\theta = 5–80^{\circ}$.

IR spectroscopy is a universal method for obtaining information on the molecular structure of substances and allows one to determine the nature of atomic groups, the nature of chemical bonds, and their changes under external conditions [16, 17]. The molecular structures of the ABS filament and five 3D-printed samples with different patterns were studied by measuring IR transmission spectra on a Brucker Vertex 70 FTIR spectrometer at the Voronezh State University Center for Collective Use in the range of 400–4000 cm^{-1}.

The surface wettability of five flat 3D-printed samples with different patterns was determined using a unique contact angle measuring setup (Fig. 3), which we manufactured on a Hercules Original 3D printer. The setup consists of a stand with a sample holder on which a flat sample is placed. A droplet meter is placed on the stand, which creates droplets on the sample surface to measure the contact angle. A webcam is mounted opposite the stand containing the sample, displaying the droplet image on the screen. The contact angle of the sample, φ^{o}, is measured using the Pic-pic graphics editing program.

A liquid droplet on the surface of a solid, depending on the nature of the sample, the liquid itself, and the environment in which it is located,

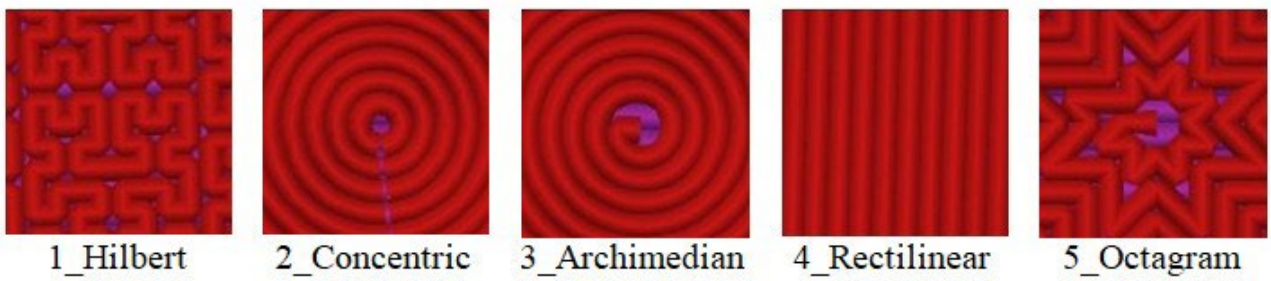

Fig. 2. Five types of 3D printed patterns on ABS (acrylonitrile butadiene styrene) polymer samples: 1_Hilbert, 2_Concentric, 3_Archimedian, 4_Rectilinear, 5_Octagram

can spread completely or partially, taking on the appearance shown in Fig. 4. The angle φ between the tangent to the droplet surface and the surface of the solid, measured toward the droplet surface, is called the contact angle φ° [18, 19]. Only those liquids that lower the surface tension of the solid at the interface with air (φ < 90°) wet a solid surface. Solid surfaces wetted by water are called hydrophilic. For hydrophobic surfaces, the contact angle φ > 90°.

Using the methods listed above, we answer questions about the influence of the technological process and the geometry of the pattern on the surface morphology of printed samples, their microstructure, and surface wettability. Answers to these questions are contained in the following sections of the article.

3. Results and discussion

3.1. Sample morphology based on scanning electron microscopy (SEM) data

Fig. 5 shows SEM micrographs obtained at different magnifications of ×40, ×1000, and ×5000 for five samples printed from ABS filament with different patterns.

The SEM results for the five printed samples, compared with the model types in Fig. 2, show that the polymer fills the sample volumes during 3D printing not as continuous smooth layers, but as layers with a morphology structured more or less in accordance with its pattern and a low filling density of approximately 20 %.

Sample 1_Hilbert, with the most complex pattern, exhibits the greatest distortion of its geometry during 3D printing. For example, in Fig. 2, the 1_Hilbert pattern shows only right angles in its complex geometry, whereas the SEM micrograph of the sample printed using this model (Fig. 5, 1.1_Hilbert X40) shows no undistorted rectangular shapes.

The micrographs of samples with patterns 4_Rectilinear and 5_Octagram most accurately and contrastingly reflect the geometry of the 3D printed pattern.

A comparison of Fig. 5 and Fig. 2 shows that the surface micrographs of two samples with similar circular patterns, 2_Concentric and 3_Archimedian (Fig. 2), adequately reflect the curvilinear geometry of the circular arc in the two printed samples with these patterns to a more or less equal degree (Fig. 5).

3.2. X-ray diffraction of the original ABS filament sample and printed ABS copolymer samples

The diffractograms of five printed samples with different 3D patterns and the original ABS polymer filament are shown in Fig. 6. The XRD results, obtained in the Bragg angle range 2θ = 5–80°, showed that all five samples with different 3D patterns made of amorphous ABS polymer filament are indeed amorphous, just like the original ABS filament itself. All diffractograms contain two broad bands of diffraction reflections:

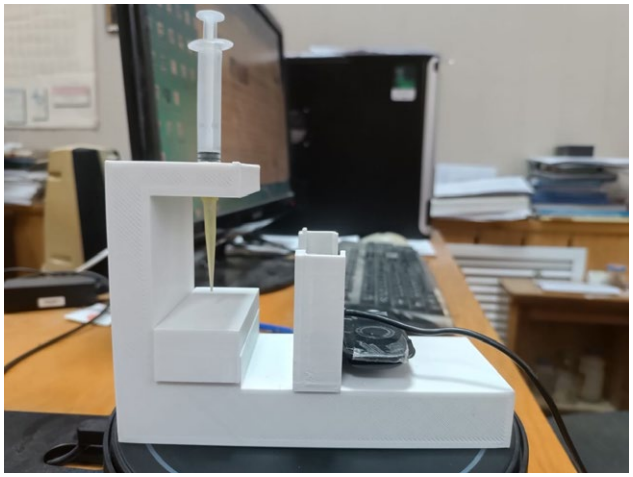

Fig. 3. The original setup for measurement of the contact angle, printed on a Hercules Original 3D printer

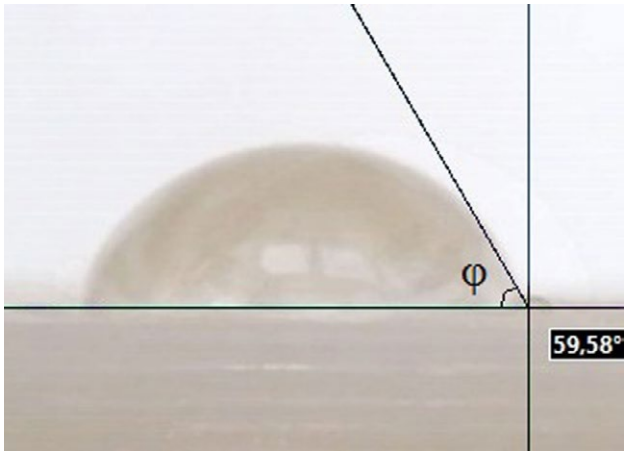

Fig. 4. Contact angle φ on the hydrophilic surface of one of the printed samples with the 3_Archimedean pattern

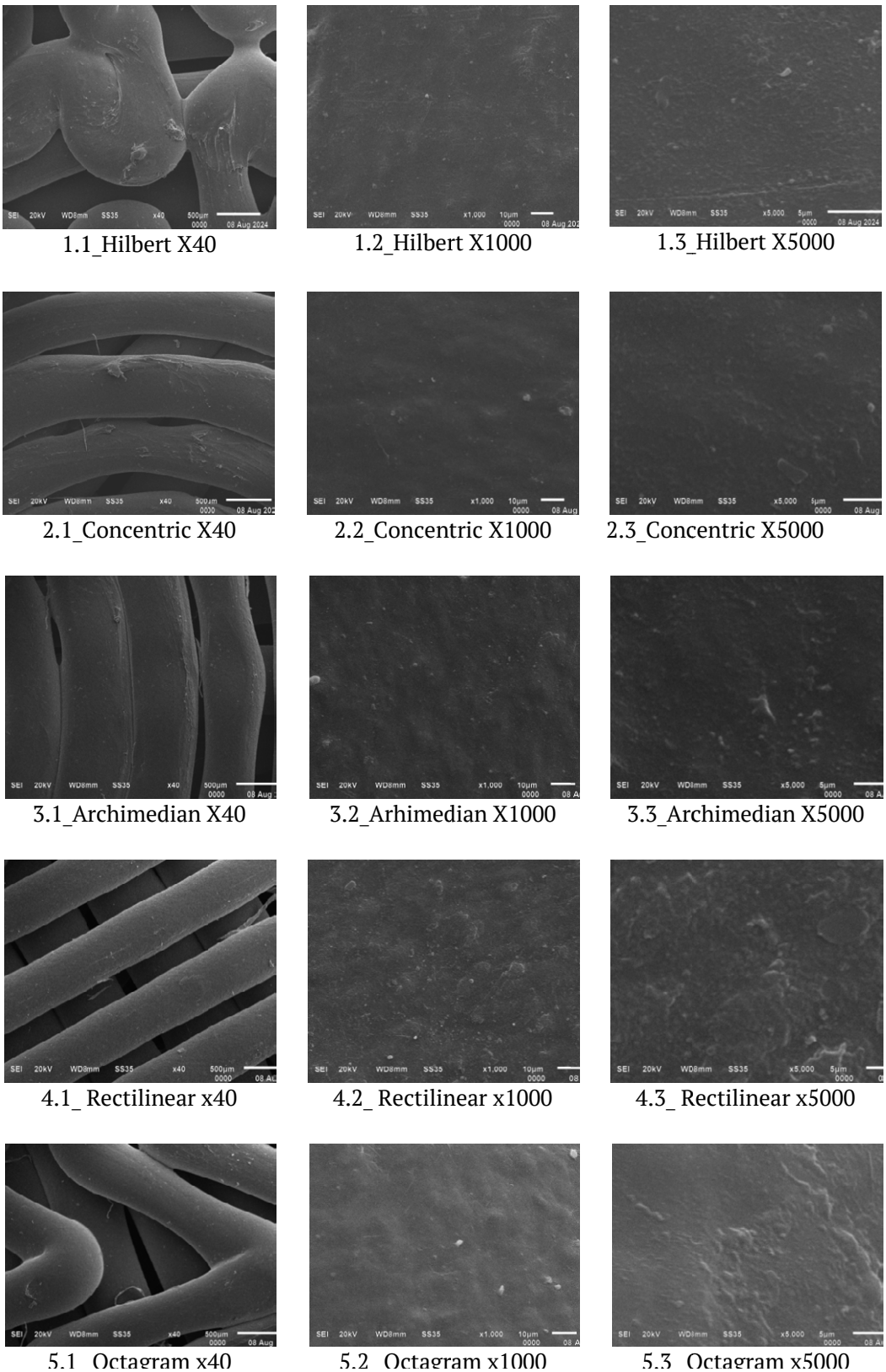

Fig. 5. SEM micrographs at ×40, ×1000, and ×5000 magnification for ABS samples with different patterns: 1_Hilbert, 2_Concentric, 3_Archimedian, 4_Rectilinear, 5_Octagram

a main band with a maximum near 2θ ≈ 20° and a shoulder at 2θ ≈ 12°, and a second, low-intensity band with a maximum at 2θ ≈ 43°.

It should be noted that the diffraction band shapes we obtained are in good agreement with the X-ray structural data reported for ABS in the literature [9–12]. Furthermore, a comparison of our X-ray structural data for ABS with our results for two other polymers, PETG [13] and PLA [14], indicates some differences in the shape and position of the X-ray diffraction bands of the original amorphous filamentary samples and different degrees of influence of the 3D printing process on the microstructural properties of samples printed from three different polymers.

Thus, in our previous work we established that the differences in the diffraction patterns of printed PETG samples from the diffraction pattern of the original PETG filament are due to the greater ordering of the polymer chains in the printed samples with different patterns, which occurs under thermal and mechanical influences on the original filament sample during 3D printing and is manifested in an increase by an order of magnitude in the relative intensity of the main diffraction maximum of the amorphous PETG polymer in all printed samples compared to the original amorphous filament [13].

We discovered even greater differences between the diffraction patterns of the printed samples and the diffraction pattern of the original amorphous filament during 3D printing from the PLA polymer. These differences were due to partial crystallization of the initially misoriented polymer chains of amorphous PLA, resulting in the formation of an orthorhombic α-Poly(L-lactide) phase, which occurs in the extruder under thermal and mechanical influences on the original amorphous filamentary sample [14].

Moreover, the most noticeable crystallization with the formation of the orthorhombic α-phase of PLA occurs in the printed samples with the 3_Archimedian and 5_Octagram patterns, which the extruder produces continuously within each layer during continuous layer-by-layer accumulation of the total sample thickness of 5 mm.

Thus, a comparative analysis of the shape and relative intensity of X-ray diffraction patterns of samples made from three different thermoplastic polymers indicates the greatest stability of the amorphous microstructure of ABS copolymer with respect to thermal and mechanical influences during printing on a Hercules Original 3D printer and the preservation of the original amorphous state in all printed samples across the five model patterns.

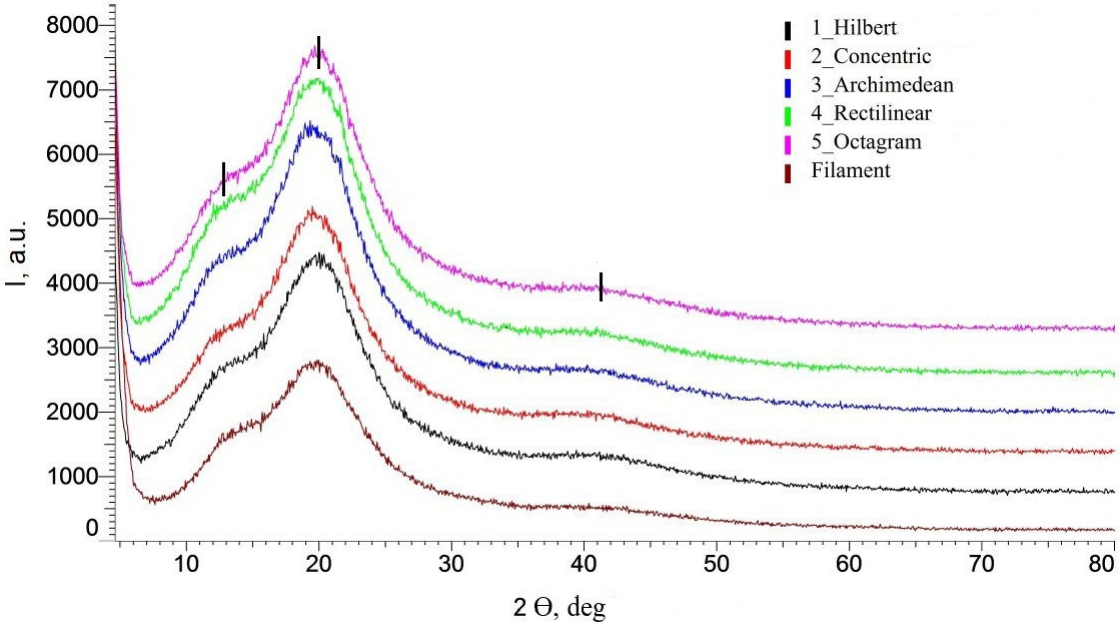

Fig. 6. X-ray diffractograms obtained in the Bragg angle range 2θ = 5–80° for the original filament and five samples printed from ABS filament with different patterns: 1_Hilbert, 2_Concentric, 3_Archimedian, 4_Rectilinear, 5_Octagram

3.3. IR spectra of the original ABS filaments and printed ABS copolymer samples

IR spectroscopy is a non-destructive optical method used to solve specific problems, including determining the fundamental characteristics of a molecule, quantitatively analyzing known phases in a substance, identifying chemical compounds, and elucidating their structure [18–20]. This optical method is based on measuring the intensity of infrared (IR) radiation absorbed or reflected by a given material. This intensity is associated with vibrational and rotational oscillations of molecular fragments and manifests itself in the intensity distribution in absorption bands depending on the wavelength (λ) or its reciprocal, which is known as the wavenumber (ν). Fig. 7 shows the IR transmission spectra for the original filament sample (ABS Filament) and five 3D-printed samples with different pattern designs.

Table 2 presents the identification of all vibration modes of ABS molecular fragments in the original filament (ABS filament) and the five printed ABS samples.

The IR spectroscopy results show that the wavenumbers and relative intensities of the absorption bands for all five printed samples with different patterns are similar and coincide, within the measurement accuracy, with the corresponding values of the main absorption bands of the original ABS filament used in 3D printing our samples and with literature data for ABS copolymer [9–11]. This means that its intrastructural chemical bonds are not subject to mechanical and thermal influences during 3D printing, just as its amorphous microstructure, which we discussed above based on XRD data, is not subject to these influences.

3.4. Surface wettability of printed ABS specimens with different patterns

Surface wettability is a manifestation of intermolecular interactions at the interface of

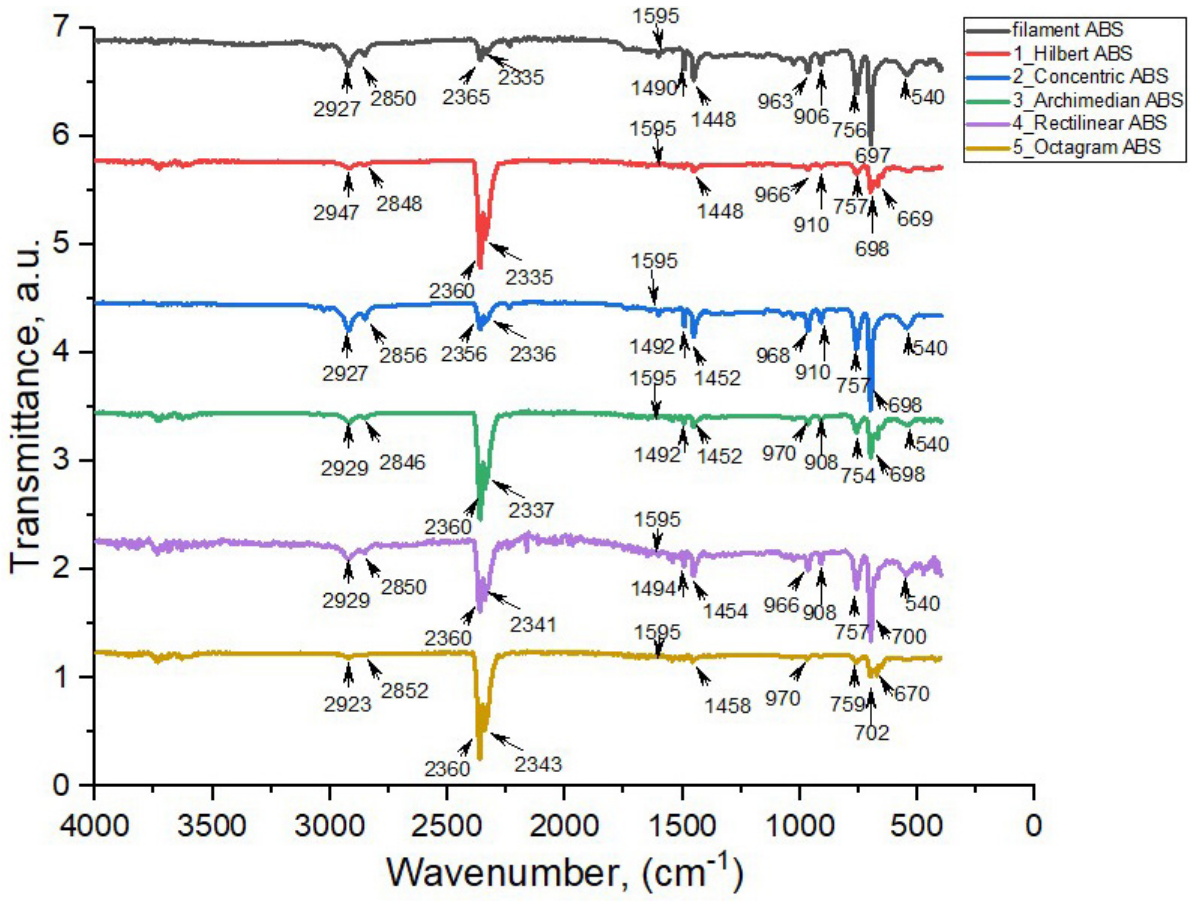

Fig. 7. IR transmission spectra from the original ABS filament and five printed samples with different patterns.

Таблица 2. Моды колебаний ИК-спектров исходного нитевидного образца Filament ABS и напечатанных образцов с различными модельными рисунками

Identification of vibration modes	Vibration modes ABS, cm^{-1}						
	Filament ABS	1_Hilbert	2_Concentric	3_Archimedian	4_Rectilinear	5_Octagram	ABS [references]
Nitrile	540	539	540	540	540	539	539 [10]
C-H out of plane bond	697	700	698	698	700	702	696 [10]
=C-H out of plane bond	756	757	757	754	757	759	757 [10]
C-H bending for H atoms attached to alkene carbons in butadiene	906 963	910 966	910 968	908 970	908 966	– 970	911 [12] 967 [12] 955 [10]
C-H bending asymmetry Scissor mode of CH_2 groups	1448	1448	1452	1452	1454	1458	1453 [12] 1450 [10]
C-H bend asymmetry Aromatic ring in styrene	1490	–	1492	1492	1494	–	1494 [11] 1492 [10]
C=C (styrene)	1595	1595	1595	1595	1595	1595	1589[10]
Bending of the N–C bond in acrylonitrile	2365 2335	2360 2335	2356 2336	2360 2337	2360 2341	2360 2343	2356 [10] 2238 [12]
Aromatic and aliphatic C-H stretching modes	2850 2927	2848 2947	2856 2927	2846 2929	2850 2929	2852 2923	2800–3200 [12] 2922 [10]

three phases: solid, liquid, and gas, resulting in a liquid spreading across the surface of a solid [19–21]. Since contact angle measurements are only performed on flat specimens, this section presents wettability results for five printed specimens.

Fig. 8 shows photographs of droplets taken using the original contact angle measurement setup on the surface of five printed ABS specimens with different 3D printed patterns. Contact angle measurements of water droplets on the surface of the specimens were taken at six points for each specimen, which were then averaged to an accuracy of one degree.

Table 3 presents the average contact angle values for the five printed specimens.

A comparative analysis of the surface contact angles of the samples in Table 3 and Fig. 8 shows that the average contact angles for all printed samples vary within the range of $\varphi = 59 \div 67°$. The large deviation of all average contact angle values toward smaller values relative to a right angle of 90° indicates that the surfaces of all five printed ABS copolymer samples with different patterns are hydrophilic.

Moreover, sample 1_Hilbert, with the most complex pattern geometry and the most distorted morphology, exhibits the highest average contact angle of $\varphi = 67°$, i.e., it is less hydrophilic than the others.

Four samples with other patterns, whose surface micrographs in Fig. 5 reflect the geometry of their pattern to a less distorted degree, have similar contact angles of approximately $\varphi \approx 60°$. Thus, one can see some influence of the more complex geometry of the 1_Hilbert pattern in the 3D-printed sample, manifested in the distorted surface morphology in Fig. 5, also on the wettability of its surface, towards a decrease in hydrophilicity (Table 3).

In printed samples with the same patterns from another thermoplastic polymer, polylactide (PLA), we previously found [14] that the sample with the same 1_Hilbert pattern geometry also exhibits the highest contact angle $\varphi = 59°$ compared to other samples ($\varphi = 50–55°$).

Since the wettability of a solid surface is a manifestation of intermolecular interactions at the interface between a liquid and a solid surface, it can be assumed that one mechanism for this interaction

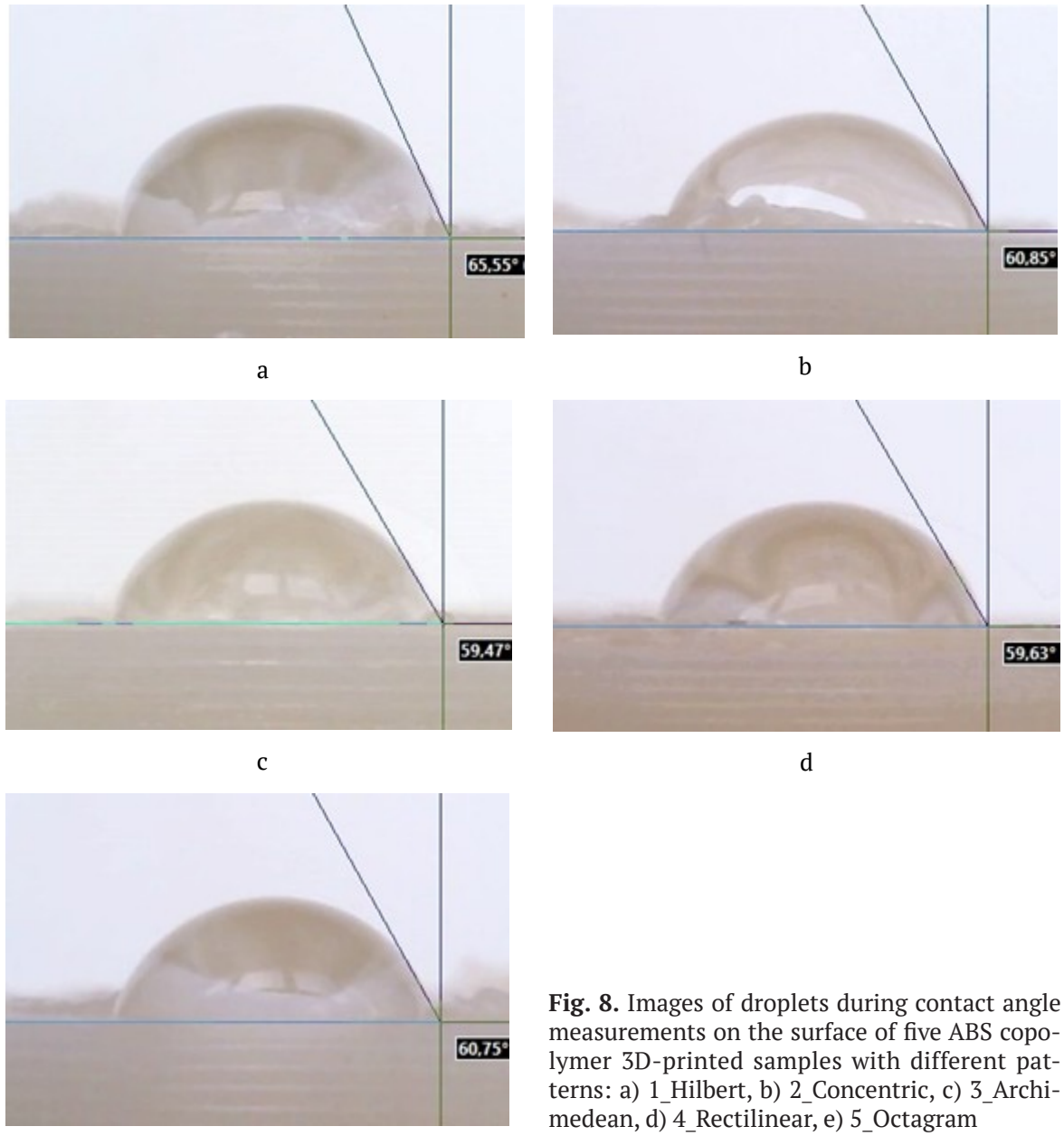

a b c d e

Fig. 8. Images of droplets during contact angle measurements on the surface of five ABS copolymer 3D-printed samples with different patterns: a) 1_Hilbert, b) 2_Concentric, c) 3_Archimedean, d) 4_Rectilinear, e) 5_Octagram

Table 3. Average contact angle values (φ°) on the surface of ABS samples with different 3D-printed patterns

Sample number and model pattern type	Average values of wetting edge angle φ°
1_Hilbert	67
2_Concentric	60
3_Archimedian	63
4_Rectilinear	59
5_Octagram	59

may be the participation of the polar groups of the ABS polymer in the formation of hydrogen bonds with water molecules on the surface of all five samples. This leads to a significant decrease in the contact angles relative to 90° and the hydrophilicity of all ABS-printed samples. Moreover, sample 1_Hilbert, with the most complex pattern, the most distorted morphology, and surface defects, exhibits the highest average contact angle (φ = 67°), i.e., it is less hydrophilic due to the greatest difficulties in forming hydrogen bonds with water molecules on its surface.

3. Conclusion

The results obtained in studying the effect of the 3D printing process on the microstructural and hydrophilic properties of ABS copolymer samples obtained by sequentially depositing copolymer layers using the FDM method on a Hercules Original 3D printer with five different model patterns showed:

– All five samples, printed with different 3D patterns from amorphous ABS filament, retain the original amorphous state of the filamentous sample.

– A comparative analysis of the shape and relative intensity of the XRD diffraction patterns of the ABS samples with the X-ray diffraction data of two other polymers, PETG and PLA, indicates the greatest resistance of the amorphous microstructure of the ABS copolymer under study to thermal and mechanical stress during 3D printing compared to the other two polymers.

– The intrastructural chemical bonds of ABS are also not susceptible to the mechanical and thermal effects of the 3D printing process, and therefore the wavenumbers and relative intensities of the IR spectral bands of all five printed samples with different pattern designs have similar values, which coincide, within the measurement accuracy, with the corresponding values of the main absorption bands of the original ABS filament and with literature data.

– The average contact angles of the printed ABS copolymer samples with five different patterns vary within the range of $\varphi = 59 \div 67°$, significantly less than a right angle, and therefore the surfaces of all printed samples are hydrophilic.

– The printed sample with the most complex geometry, the most distorted morphology, and the most surface defects, the 1_Hilbert pattern, exhibits the highest contact angle ($\varphi = 67°$), exceeding the corresponding values in samples with other pattern designs ($\varphi \approx 60°$) by ~10 %. It also has a less hydrophilic surface due to a possible reduction in hydrogen bonds with water molecules on its more defective surface.

Thus, the obtained results demonstrate that the thermal and mechanical effects of 3D printing in the studied extrusion mode do not cause a noticeable orientation of the polymer chains of the original amorphous ABS copolymer, do not disrupt its intrastructural chemical bonds, and the surfaces of the printed samples with five different pattern designs are hydrophilic.

Author contributions

The authors contributed equally to this article.

Conflict of interests

The authors declare that they have no known competing financial interests or personal relationships that could have influenced the work reported in this paper.

References

1. Kumar R. M., Rajini N. T., Kumar S. M., Mayandi K., Siengchin S., Ismail S. O. Thermal and structural characterization of acrylonitrile butadiene sstyrene (ABS) copolymer blended with polytetrafluoroethylene (PTFE) particulate composite. *Materials Research Express.* 2019;6(8): 085330. https://doi.org/10.1088/2053-1591/ab250f

2. Peters E. N. *Plastics: thermoplastics, thermosets, and elastomers*. Handbook of Materials Selection. Kutz M. (ed.). New York: John Wiley & Sons, Inc.; 2002. p. 363–365. https://doi.org/10.1002/9780470172551.ch11

3. Kutnjak-Mravlincic S., Sutlovic A., Glogar M. I., Ercegovic Ražic S., Godec D. Innovative development of batch dyed 3D printed acrylonitrile-butadiene-styrene objects. *Molecules.* 2021;26: 6637. https://doi.org/10.3390/molecules26216637

4. Kulich D. M., Gaggar S. K., Lowry V., Stepien R. Acrylonitrile–butadiene–styrene polymers. In: *Encyclopedia of Polymer Science and Technology.* Hoboken, NJ, USA: John Wiley & Sons; 2001. p. 174–201. https://doi.org/10.1002/0471440264.pst011

5. Mukhamedyanov E. R., Orlova N. Yu. Toxicity of non-engineering plastics during extrusion*. *Collection of scientific papers of the All-Russian scientific and practical conference. December 22–23, 2020.* Moscow: NRNU MEPhI; Snezhinsk: SFTI NRNU MEPhI; 2020: 56-59.

6. Harper C. A. *Handbook of plastic and elastomers*. New York: McGraw-Hill; 1997. p. 1–62. ISBN 0070266816

7. Rutkowski J. V., Levin B. C. Acrylonitrile-butadiene-styrene copolymers (ABS): pyrolysis and combustion products and their toxicity- a review of the literature. *Fire and Materials.* 1986;10(3-4): 93–105. https://doi.org/10.1002/fam.810100303

8. Steeman P. A., Meier R. J. The structure of styrene-acrylonitrile/bytadiene polymer studied by 2D-i.r. spectroscopy. *Polymers,* 1997;38(21): 5435–5462. https://doi.org/10.1016/s0032-3861(97)00074-8

9. Bandeira L. C., Campos B. M., Ciuffi K. J., ... Maia I. A. Calcium phosphate coatings by sol-gel on acrylonitrile-butadiene-styrene substrate. *Journal of the Brazilian Chemical Society.* 2017;28(6): 943–949. https://doi.org/10.21577/0103-5053.20160244

10. Boricha A. G., Murthy Z. V. P. Acrylonitrile-butadiene-styrene/chitosan blend membranes: preparation, characterization and performance for the separation of heavy metals. *Journal of Membrane Science.* 2009;339(1): 239–249. https://doi.org/10.1016/j.memsci.2009.04.057

11. Desrousseaux C., Cueff1 R., Aumeran C., ... Sautou V. Fabrication of acrylonitrile-butadiene-styrene nanostructures with anodic alumina oxide templates, characterization and biofilm development test for staphylococcus epidermidis. *PLOS ONE*. 2015;10(8): e0135632. https://doi.org/10.1371/journal.pone.0135632

12. Neher B., Gafur Md. A., Al-Mansur M. A., Bhuiyan Md. M. R., Qadir Md. R., Ahmed F. Investigation of the surface morphology and structural characterization of palm fiber reinforced acrylonitrile butadiene styrene (PF-ABS) composites. *Materials Sciences and Applications,* 2014;5: 378–386. https://doi.org/10.4236/msa.2014.56043

13. Lenshin A. S., Frolova V. E., Ivkov S. S., Domashevskaya E. P. Microstructural and hydrophilic properties of polyethylene terephthalate glycol polymer samples with different 3D printing patterns. *Condensed Matter and Interphases*. 2024;26(1): 78–87. https://doi.org/10.17308/kcmf.2024.26/11810

14. Lenshin A. S., FrolovaV. E., Kannykin S. V., Domashevskaya E. P. Microstructural and hydrophilic properties of polylactide polymer samples with various 3D printing patterns. *Polymers*. 2024;16: 1281. https://doi.org/10.3390/polym16091281

15. Oshmyan V. G., Timan S. A., Shamaev M. Yu. Modeling of ductile failure of polymer blends and composites with account of interface formation. *Polymer Science, Series A*. 2003;45(10): 1011–1018. Available at: https://elibrary.ru/item.asp?id=13425982]

16. Gremlikh G. U. *The language of spectra. Introduction to the interpretation of spectra of organic compounds**. Brooker. Opt.; 2002. 94 p. (in Russ.)

17. Hollas J. M. *Modern Spectroscopy. Fourth Edition*. The Atrium, Southern Gate, Chichester, West Sussex, England: John Wiley & Sons Ltd.; 2004. 452 p.

18. Tolstoy V. P., Chernyshova I. V., Skryshevsky V. A. *Handbook of infrared spectroscopy of ultrathin films*. Hoboken, New Jersey: John Wiley & Sons, Inc.; 2003. 739 p. https://doi.org/10.1002/047123432x

19. Kiselev M. G., Savich V. V., Pavich T. P. Determination of the contact wetting angle on flat surfaces. *Bulletin of BNTU*. 2006;1: 38–41. Available at: https://elibrary.ru/item.asp?id=21398120

20. Elesina V. V. *Wetting angle. Methodical recommendations**. Altai State Technical University named after I. I. Polzunov Publ.; 2019. 22 c. (in Russ.)

21. Pavlov I. N., Rinkevichyus B. S., Tolkachev A. V. A setup for visualizing the evaporation of a liquid drop using the method of frustrated total internal reflection of a laser beam. *Instruments and Experimental Techniques*. 2013;56(2): 242–246. https://doi.org/10.1134/s0020441213020103

** Translated by author of the article*

Information about the authors

Aleksandr S. Lenshin, Dr. Sci. (Phys.–Math.), Leading Researcher, Department of Solid State Physics and Nanostructures, Voronezh State University (Voronezh, Russian Federation).

https://orcid.org/0000-0002-1939-253X
lenshinas@mail.ru

Vera E. Frolova, Cand. Sci. (Phys.–Math.), Associate Professor, Department of Solid State Physics and Nanostructures, Voronezh State University (Voronezh, Russian Federation).

https://orcid.org//0009-0000-2880-8958
ternovaya@phys.vsu.ru

Vladimir A. Makagonov, Cand. Sci. (Phys.–Math.), Associate Professor, Department of Physics, Voronezh State Technical University (Voronezh, Russian Federation).

https://orcid.org/0000-0002-4024-4064
vlad_makagonov@mail.ru

Alexandra K. Pelagina, postgraduate student, Department of General Physics, Voronezh State University (Voronezh, Russian Federation).

https://orcid.org/0000-0003-2597-3602
pisliaruk@phys.vsu.ru

Evelina P. Domashevskaya, Dr. Sci. (Phys.–Math.), Professor, Consulting Professor, Department of Solid State Physics and Nanostructures, Voronezh State University (Voronezh, Russian Federation).

https://orcid.org/0000-0002-6354-4799
ftt@phys.vsu.ru

Received August 12, 2025; approved after reviewing September 17, 2025; accepted for publication October 15, 2025; published online April 01, 2026.

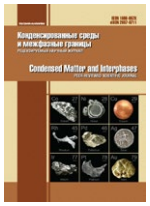

ISSN 1606-867X (Print)
ISSN 2687-0711 (Online)
Condensed Matter and Interphases
Kondensirovannye Sredy i Mezhfaznye Granitsy
https://journals.vsu.ru/kcmf/

Original articles

Research article
https://doi.org/10.17308/kcmf.2026.28/13591

Effect of Sr^{2+} ions on the gas-sensitive properties of $LaCrO_3$ and $GdCrO_3$

Ya. M. Nemykh[1]✉, V. F. Kostryukov[1], I. N. Gorbunov[1], E. V. Tomina[1,2]

[1]*Voronezh State University,*
1, Universitetskaya pl., Voronezh 394018, Russian Federation

[2]*Voronezh State Forestry University*
8, Timiryazeva st., Voronezh 394087, Russian Federation

Abstract

Objectives: Thin films obtained from $La_{1-x}Sr_xCrO_{3-\delta}$ and $Gd_{1-x}Sr_xCrO_{3-\delta}$ (x = 0.05, 0.10, and 0.15) synthesized by the modified citrate method were studied.

Experimental: An analysis of the phase composition, structure, and gas-sensitive properties of films in the presence of carbon monoxide was carried out. Doping with Sr^{2+} ions led to an increase in the defect rate of nanoparticles due to the formation of vacancies in the oxygen sublattice. This phenomenon had a positive effect on their gas-sensitive properties.

Conclusions: It was found that samples of $La_{0.9}Sr_{0.1}CrO_{3-\delta}$ and $Gd_{0.9}Sr_{0.1}CrO_{3-\delta}$ showed the highest sensory response at 180°C, 2.26 and 1.78, respectively. The results obtained confirmed the prospects of using these materials as gas sensors.

Keywords: Nanopowders, Perovskites, Gas-sensitive properties, Pechini method, $LaCrO_3$, $GdCrO_3$, Sr^{2+} doping

Acknowledgements: The research results were partially obtained on the equipment of the Voronezh State University Center for Collective Use: http://ckp.vsu.ru

For citation: Nemykh Y. M., Kostrukov V. F., Gorbunov I. N., Tomina E. V Effect of Sr^{2+} ions on the gas-sensitive properties of $LaCrO_3$ and $GdCrO_3$. *Condensed Matter and Interphases*. 2026;28(1): 81–91. https://doi.org/10.17308/kcmf.2026.28/13591

Для цитирования: Немых Я. М., Кострюков В. Ф., Горбунов И. Н., Томина Е. В. Влияние ионов Sr^{2+} на газочувствительные свойства $LaCrO_3$ и $GdCrO_3$. *Конденсированные среды и межфазные границы*. 2026;28(1): 81–91. https://doi.org/10.17308/kcmf.2026.28/13591

✉ Yaromir M. Nemykh, e-mail: yaromir0202@gmail.com

1. Introduction

Since the 1980s, gas sensors based on metal oxides, such as SnO_2, which are widely used in industry, have been actively studied. However, traditional metal oxide sensors are not able to cover the entire range of tasks of modern industry, which encourages the search for new materials [2]. One of the categories of such materials is compounds with a perovskite structure. Gas-sensitive materials with a perovskite structure have several advantages over binary oxides: high sensitivity, selectivity, and sensor signal values. Synthesis can be carried out at relatively low temperatures. Their gas-sensitive properties can be quite easily and widely controlled, changing both the composition of the material itself, and the nature and concentration of the dopant. In this case, doping can be carried out in two positions, and not in one as with simple oxides. This feature of perovskite-like compounds allows them to contain cationic and oxygen vacancies [3], endowing these compounds with variable electrical and redox properties, which have a decisive influence on gas-sensitive properties [4]. Doping allows you to change the electrical and sensory characteristics of the material, making it more selective.

Perovskite-based gas sensors provide reliable detection of harmful gases in the environment. Such sensors can operate in a wide temperature range and demonstrate selectivity to various gases, such as CO, NH_3, NO_2, etc. At the same time, the maximum values of the sensor signal are observed at lower temperatures. The reduction in comparison with tin and zinc oxides is up to 100°C. These materials are promising for creating sensors with low power consumption. The main mechanisms of sensitivity are chemisorption and catalytic processes occurring on the surface of oxide materials [5, 6].

There are various types of gas sensors based on perovskite-like materials, such as ferrites, cobaltites, stannites, manganites, and other complex oxides.

Ferrites are oxide compounds with the general formula $AFeO_3$, where A is a rare earth element. They show high sensitivity to various gases, especially hydrocarbons and CO. Among ferrites, the most interesting are $LaFeO_3$ and $YFeO_3$, which are successfully used in the detection of liquefied petroleum gases [7].

Cobaltites, such as $LaCoO_3$, have a high catalytic activity and are sensitive to alcohols, CO, and H_2. Doping with oxides such as ZnO improves their sensor characteristics, reducing the detection operating temperature. Due to their high thermal stability, cobaltites are promising materials for use in gas-sensitive sensors operating at elevated temperatures [8].

Stannites, represented by $BaSnO_3$ and $ZnSnO_3$ compounds and $ZnSnO_3$, exhibit sensitivity to NO_2 and n-propanol. They have good selectivity and stability, which makes them in demand for monitoring industrial emissions and indoor air quality. The high operating temperature of stannite-based sensors (up to 900°C) limits their use, but active research is aimed at reducing these temperatures by modifying the structure and morphology of the material [9, 10].

Manganites such as $YMnO_3$ show increased sensitivity to hydrogen sulfide (H_2S) and ammonia (NH_3). They have a stable structure and can operate at relatively low temperatures (about 100°C). Studies show that varying the composition of manganites makes it possible to control their sensory characteristics, which opens up prospects for their application in environmental monitoring and industrial safety [11].

Another promising group of materials is chromites of rare-earth elements, for example, $LaCrO_3$ [12] and $GdCrO_3$, which are studied in our laboratory [13]. They demonstrate resistance to high temperatures, which makes them promising for sensor applications. An analysis of the literature shows that doping of chromites can change their electronic and surface properties. In [14], a wide range of possibilities for modifying $LaCrO_3$ to change its physical properties was demonstrated, and in [15], the authors found that the mechanism of electrical conductivity $GdCrO_3$ is described by the Mott model of hopping conductivity with a variable hop length.

Thus, the aim of this work is to study the gas-sensitive properties of lanthanum and gadolinium chromites doped with Sr^{2+} ions. The synthesis and complex analysis of the

composition, structure, and sensory response of $La_{1-x}Sr_xCrO_{3-\delta}$ and $Gd_{1-x}Sr_xCrO_{3-\delta}$ (x = 0.05, 0.10, and 0.15) to the presence of carbon monoxide in the atmosphere was performed. The choice of strontium ion concentrations is determined, on the one hand, by the need for a sufficiently significant impact on the target characteristics, and, on the other hand, by the need to form a single-phase material.

2. Experimental

Nanopowders $Ls_{1-x}Sr_xCrO_{3-\delta}$ and $Gd_{1-x}Sr_xCrO_{3-\delta}$ (x = 0.05, 0.10, and 0.15) were synthesized by the modified citrate method [16]. This method is based on the complexation of cations with citric acid, followed by thermal decomposition. Lanthanum, gadolinium, strontium, and chromium nitrates, citric acid, and ammonium hydroxide were used as starting materials

First, the calculated amounts of nitrates of $La(NO_3)_3 \cdot 6H_2O$ (or $Gd(NO_3)_3 \cdot 6H_2O$), $Sr(NO_3)_2 \cdot 4H_2O$, and $Cr(NO_3)_3 \cdot 9H_2O$ were dissolved in distilled water with constant stirring. The resulting solution was boiled to form a sol, after which an ammonia solution was added dropwise until pH 7–8 was established. During the deposition, a gel was formed. The resulting gel was cooled to room temperature, after which, with constant stirring, citric acid was added to the system in a stoichiometric ratio of 3:1 with respect to the number of metal cations.

The solution was heated until the water completely evaporated and a gel-like precipitate was formed. The resulting gel was calcined at 300–350°C to remove organic compounds. The final formation of nanopowders was achieved by heat treatment in a muffle furnace at 700°C for 4 hours.

The resulting nanopowders were dispersed in ethyl alcohol with the addition of cetyltrimethylammonium bromide (CTAB) as a surfactant to form a paste, and then they were applied to a conductive element (silicon wafer) by spin-coating (SpinNXG-P1H installation) and annealed for 1 hour at a temperature of 100°C. The deposition mode (first 1 minute - 2000 rpm, then 20 minutes - 5000 rpm) was determined by calibration dependences and provided a fixed thickness of 150±7 nm [17, 18].

3. Study of composition and structure

X-ray phase analysis

The study of the phase compositions of $La_{1-x}Sr_xCrO_{3-\delta}$ and $Gd_{1-x}Sr_xCrO_{3-\delta}$ (x = 0.05, 0.10, and 0.15) was performed on a Thermo ARL X'TRA X-ray diffractometer (CuK_α radiation, λ = 1.5418 Å). When examining the X-ray diffraction patterns of the obtained samples (Fig. 1), it was found that all peaks in the graphs of the intensity dependence on the angle 2θ correspond to the perovskite structure, which is confirmed by comparison with the bases of X-ray diffractograms [19].

A detailed examination of the diffractograms shows a shift in the peaks of the doped samples (Tables 1, 2) relative to the undoped ones, which indicates a change in the lattice parameters due to strontium ions embedded in it.

The upward shift of the peaks of doped lanthanum chromite was about 0.06, 0.03, and 0.04 deg. for 5 at. %, 10 at. % and 15 at. % strontium, respectively. This is explained by the fact that the ionic radius of Sr (1.16 Å) is smaller than the ionic radius of La (1.50 Å), which leads to compression of the crystal lattice [20].

The lower shift of the peaks of doped gadolinium chromite were about 0.02, 0.03, and 0.03 deg. for 5 at. %, 10 at. % and 15 at. % strontium, respectively. This is explained by the fact that the ionic radius of Sr (1.16 Å) is larger than the ionic radius of Gd (0.98 Å), which leads to an increase in interplanar distances [20].

Based on the obtained data, the volume of unit cells of the synthesized samples was calculated in the absence and presence of doping. For unsubstituted lanthanum chromite, the unit cell volume was 234.34 $(Å)^3$, and for gadolinium chromite it was 222.95 $(Å)^3$. The tabulated values were 234, 46, and 223.71 $(Å)^3$, respectively (calculated on the basis of data from [19]). Doping with strontium ions led to a change in the unit cell volume. Lanthanum chromite doped with 10 at. % Sr the unit cell volume was 233.74 $(Å)^3$, while gadolinium chromite doped with 10 at. % Sr it was 223.57 $(Å)^3$. The results obtained, on the one hand, are in good agreement with the tabulated values, and, on the other hand, showed a regular change in the volume of unit cells when the initial cations were replaced during doping with a cation

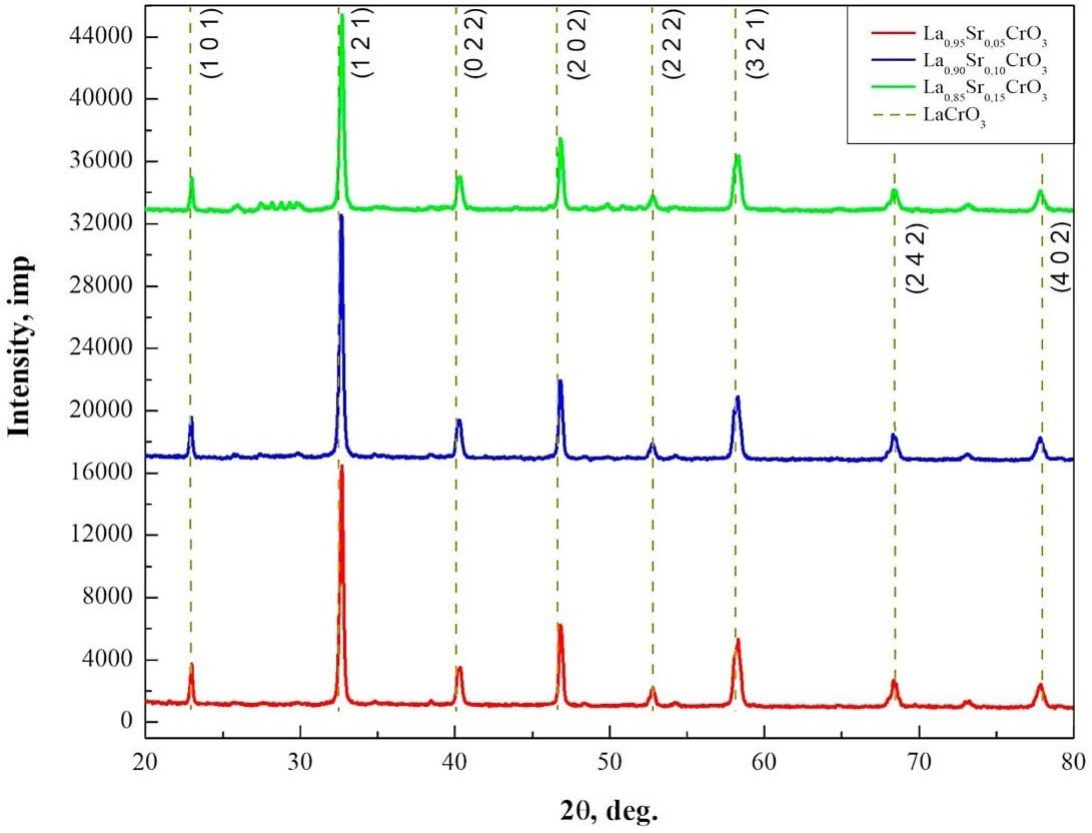

a

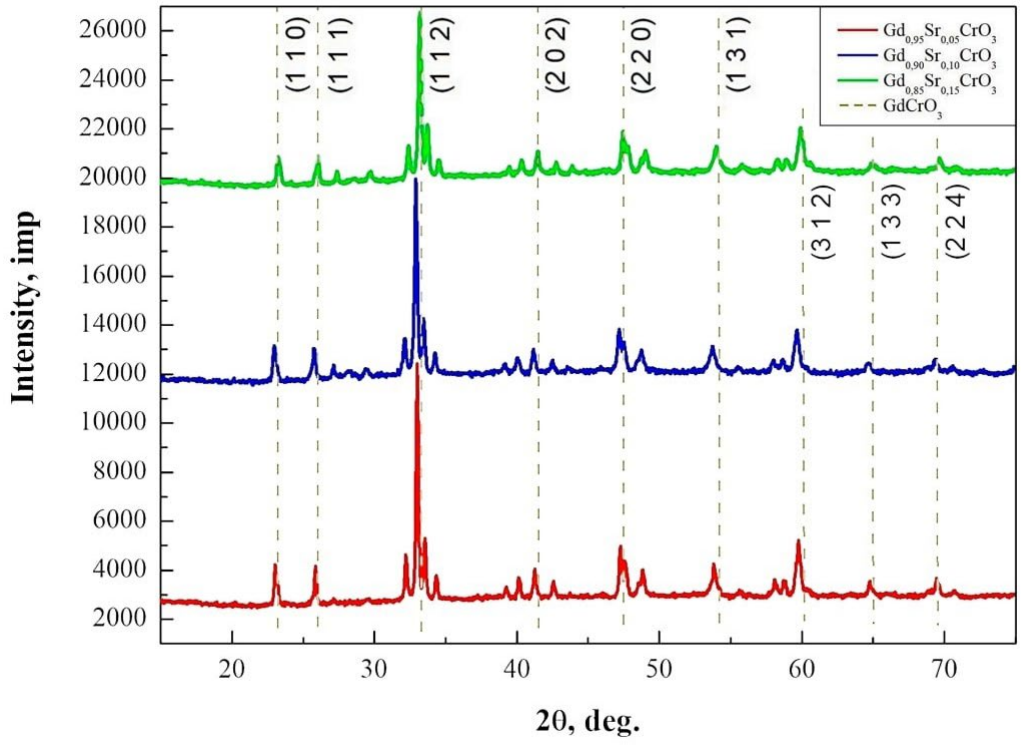

b

Fig. 1. Comparison of X-ray diffractograms of doped $La_{1-x}Sr_xCrO_{3-\delta}$ (a) and $Gd_{1-x}Sr_xCrO_{3-\delta}$ (b) nanopowders with individual samples

Table 1. 2θ value for a series of $La_{1-x}Sr_xCrO_{3-\delta}$ samples (x = 0.05, 0.10, and 0.15) relative to unsubstituted $LaCrO_3$

Sample	Value 2θ for unsubstituted sample / value 2θ for doped sample							
	(101)	(121)	(022)	(202)	(222)	(321)	(242)	(402)
$La_{0.95}Sr_{0.05}CrO_{3-\delta}$	22.90 / 22.96	32.60 / 32.72	40.12 / 40.10	46.76 / 46.82	52.68 / 52.72	58.26 / 58.32	68.30 / 68.36	77.72 / 77.82
$La_{0.9}Sr_{0.1}CrO_{3-\delta}$	22.90 / 22.92	32.60 / 32.64	40.12 / 40.14	46.76 / 46.80	52.68 / 52.72	58.26 / 58.28	68.30 / 68.32	77.72 / 77.76
$La_{0.85}Sr_{0.15}CrO_{3-\delta}$	22.90 / 22.96	32.60 / 32.66	40.12 / 40.16	46.76 / 46.82	52.68 / 52.74	58.26 / 58.24	68.30 / 68.34	77.72 / 77.80

Table 2. 2θ value for a series of $Gd_{1-x}Sr_xCrO_{3-\delta}$ samples (x = 0.05, 0.10, and 0.15) relative to unsubstituted $GdCrO_3$

Sample	Value 2θ for unsubstituted sample / value 2θ for doped sample							
	(110)	(111)	(112)	(202)	(220)	(131)	(312)	(133)
$Gd_{0.95}Sr_{0.05}CrO_{3-\delta}$	23.24 / 23.26	26.04 / 26.02	33.20 / 33.16	41.46 / 41.42	47.46 / 47.44	54.00 / 53.98	59.92 / 59.92	64.98 / 64.96
$Gd_{0.9}Sr_{0.1}CrO_{3-\delta}$	23.24 / 23.26	26.04 / 26.02	33.20 / 33.16	41.46 / 41.42	47.46 / 47.42	54.00 / 53.94	59.92 / 59.88	64.98 / 64.90
$Gd_{0.85}Sr_{0.15}CrO_{3-\delta}$	23.24 / 23.26	26.04 / 26.02	33.20 / 33.16	41.46 / 41.42	47.46 / 47.42	54.00 / 53.96	59.92 / 59.88	64.98 / 64.92

of a smaller (in the first case) and larger (in the second case) radius.

Local X-ray spectral microanalysis

The elemental composition of the powders was analyzed using a JEOL-6510LV scanning electron microscope with a Bruker energy dispersive microanalysis system. The results of the study are presented in Tables 3 and 4. This method is not able to estimate the oxygen content [21], so only the cation content is presented in the analysis results. In addition to the direct experimental data, Tables 3 and 4 add a column that shows the ratio of cations in the samples and characterizes the proximity of the composition of the obtained samples to the one specified during synthesis.

Both series of samples showed a fairly close correspondence to the required stoichiometric

Table 3. Result of elemental composition analysis of unsubstituted lanthanum chromite and strontium-doped lanthanum chromite nanopowders

Nominal composition of samples	Elemental composition, at. %			
	La	Sr	Cr	[Sr]/([Sr]+[La])
$LaCrO_3$	19.4	–	20.6	–
$La_{0.95}Sr_{0.05}CrO_{3-\delta}$	19.54	0.99	20.61	0.48
$La_{0.9}Sr_{0.1}CrO_{3-\delta}$	18.92	1.98	20.66	0.95
$La_{0.85}Sr_{0.15}CrO_{3-\delta}$	18.03	3.02	20.73	0.14

Table 4. Result of elemental composition analysis of unsubstituted gadolinium chromite and strontium-doped gadolinium chromite nanopowders

Nominal composition of samples	Elemental composition, at. %			
	Gd	Sr	Cr	[Sr]/([Sr]+[Gd])
$GdCrO_3$	23.9	–	24.2	–
$Gd_{0.95}Sr_{0.05}CrO_{3-\delta}$	19.42	0.91	21.06	0.045
$Gd_{0.9}Sr_{0.1}CrO_{3-\delta}$	19.03	1.86	21.03	0.089
$Gd_{0.85}Sr_{0.15}CrO_{3-\delta}$	18.23	2.89	21.22	0.137

ratio. At the same time, according to the results of the Local X-ray spectral microanalysis, it was found that in the $La_{1-x}Sr_xCrO_{3-\delta}$ system (x = 0.05, 0.10, and 0.15), strontium was embedded in a larger amount, which is associated with a simpler substitution of a large La^{3+} ion (ionic radius 1.50 Å) with a Sr^{2+} ion (ionic radius 1.04 Å) of a smaller size. In the $Gd_{1-x}Sr_xCrO_{3-\delta}$ system (x = 0.05, 0.10, and 0.15), strontium was embedded in a smaller amount, since the ionic radius of Gd is 0.96 Å [20].

At the same time, despite the fact that the oxygen content has not been experimentally determined, it can be assumed that in the synthesized samples there will be a certain lack of oxygen associated with the formation of vacancies in the oxygen sublattice, which arises due to the need to compensate for the positive charge during doping with double-charged strontium cations.

4. Particle size study

Transmission electron microscopy

In this work, the obtained powders were examined using a ZEISS Libra 120 transmission electron microscope. Sample preparation was carried out as follows. 5 ml of distilled water was poured into a glass, 0.15 g of gelatin, 1 mg of the test sample were added and placed on a heated magnetic stirrer. The agitator was used for more uniform distribution of nanoparticles in the prepared suspension. Next, objects were caught using a copper mesh with a carbon replica and inserted into the object holder. The results obtained are shown in Fig.2.

According to the TEM data, the particle size ranged from 25 to 35 nm. The dependence of the particle size during the transition from

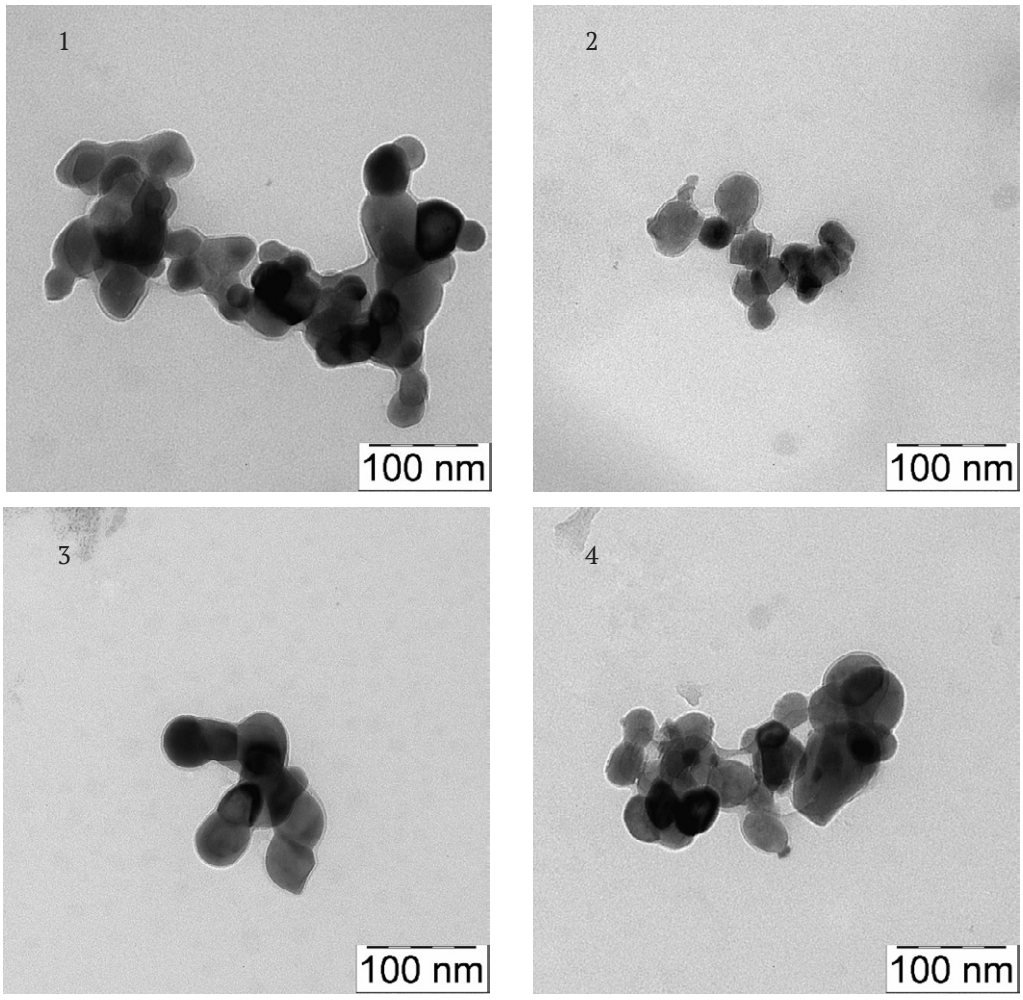

Fig. 2. TEM images of nanoparticles *1* – $LaCrO_3$; *2* – $La_{0,9}Sr_{0,1}CrO_{3-\delta}$; *3* – $GdCrO_{3-\delta}$; *4* – $Gd_{0.9}Sr_{0.1}CrO_{3-\delta}$

unsubstituted to doped chromites has not been established.

5. Investigation of gas-sensitive properties

The specific surface resistance of films made from nanopowders of the $La_{1-x}Sr_xCrO_{3-\delta}$ and $Gd_{1-x}Sr_xCrO_{3-\delta}$ systems (x = 0, 0.05, and 0.1) was measured by the four-probe Van der Pau method. The method was similar to that described in [22, 23]. The studies were performed in air (Fig. 3) and in the presence of carbon monoxide (Fig. 4). Measurements were performed 3 times for each of the samples. The gas concentration was 50 ppm, and the temperature range of the study was 20–400°C. The required carbon monoxide concentration was achieved by diluting the certified gas mixture with dry synthetic air. Measurements were carried out in a stationary system (a closed chamber with a volume of 50 ml). Before each new experiment, the system was purged with synthetic air.

The results of measuring the resistivity of doped samples were compared with the resistivity of unsubstituted $LaCrO_3$ and $GdCrO_3$.

During the measurement process, the analyzed reducing agent gas was adsorbed, during which the free electrons of the adsorbed gas transferred to the sensor surface, increasing the number of mobile charges and reducing the temperature of the onset of a sharp change in resistance.

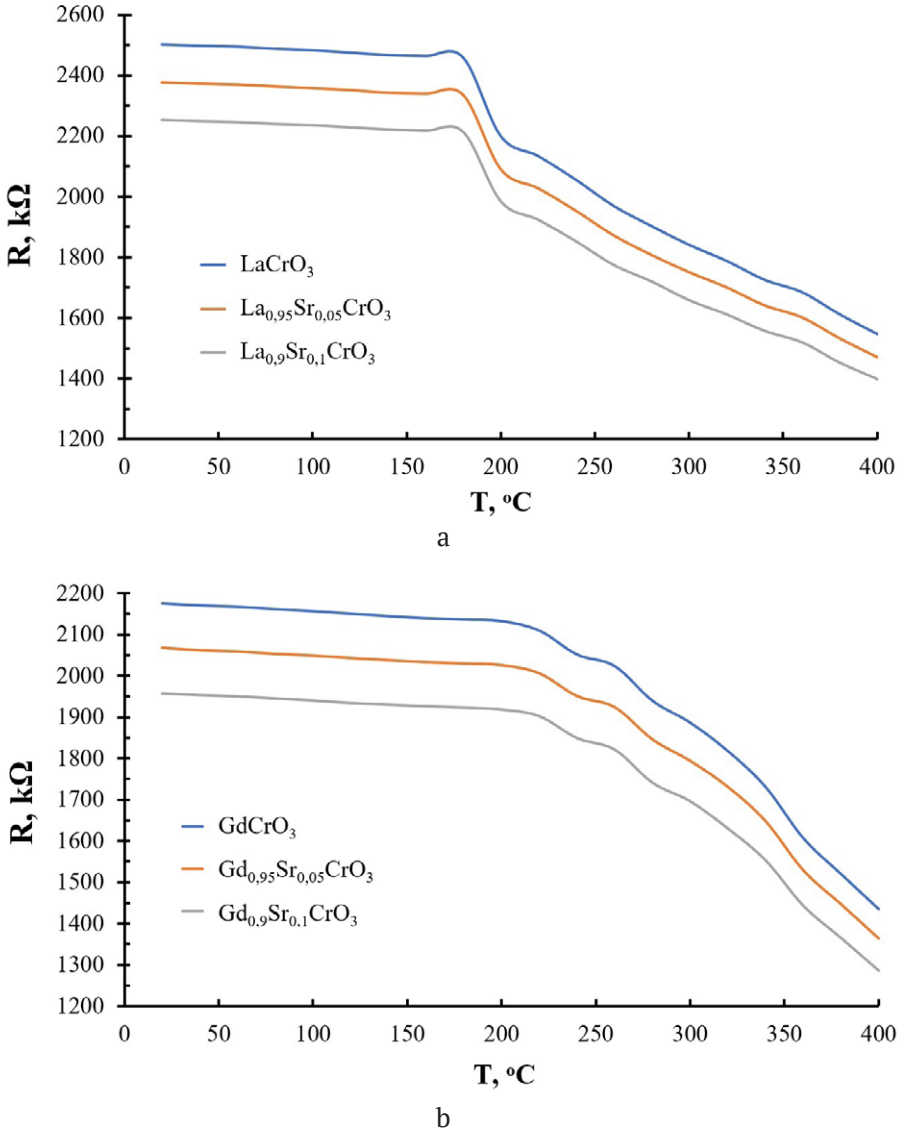

Fig. 3. Dependence of the resistivity of thin films of $La_{1-x}Sr_xCrO_{3-\delta}$ (x = 0, 0.05 and 0.1) (a) and $Gd_{1-x}Sr_xCrO_{3-\delta}$ (x = 0.05 and 0.1)

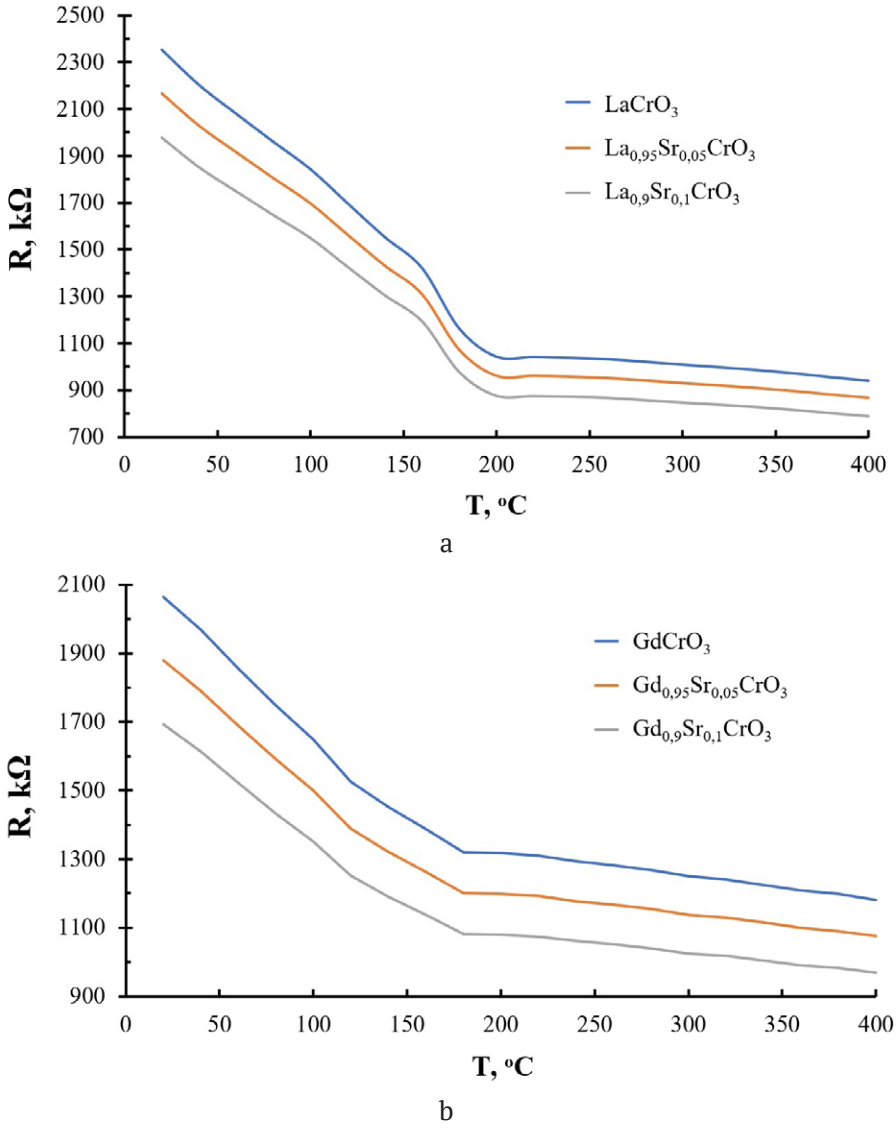

Fig. 4. Dependence of the resistivity of thin films of $La_{1-x}Sr_xCrO_{3-\delta}$ (x = 0, 0.05 and 0.1) (a) and $Gd_{1-x}Sr_xCrO_{3-\delta}$ (x = 0, 0.05 and 0.1) (b) in the presence of carbon monoxide (50 ppm) in the atmosphere

This phenomenon confirms that the resulting chromites are semiconductors.

The introduction of strontium ions into the crystal lattice of lanthanum chromite and gadolinium chromite reduced their resistivity. This is explained by the ionic structure of the crystal: the appearance of uncompensated charges during the substitution of La^{3+} or Gd^{3+} for Sr^{2+} contributed to the formation of oxygen vacancies, which led to a decrease in resistivity, indicating *n*-type conductivity in lanthanum and gadolinium chromites.

According to the results of measuring the resistivity of gadolinium and lanthanum chromites, the resistance of the former is lower. This is explained by the large number of oxygen vacancies in the samples of the $Gd_{1-x}Sr_xCrO_{3-\delta}$ (x = 0, 0.05, and 0.1) system detected by the local X-ray spectral microanalysis.

Based on the obtained values of the resistivity of the samples, the sensory response was calculated using the formula $S_r = R_a/R_g$, where S_r is the gas-sensitive response, R_a is the specific surface resistance of films in air, and R_g is the specific surface resistance of films in the presence of a reducing gas [24]. The dependences of the sensory response on temperature are shown in Fig. 5.

According to the data obtained, lanthanum chromite, unsubstituted and doped with strontium, exhibited the strongest sensory response to carbon

monoxide (CO) at 180°C. Unsubstituted and doped gadolinium chromite at similar temperatures also showed a peak value of the sensory response, but the value of the sensory response was lower than that of the lanthanum chromite samples. A comparison of the sensory responses of doped samples with unsubstituted samples showed that the introduction of strontium into the systems allowed a stronger sensory response, and an increase in the concentration of introduced strontium contributed to a strengthening of the response.

From Fig. 5a it follows that for the $La_{1-x}Sr_xCrO_{3-\delta}$ system (x = 0, 0.05, and 0.1) at 180°C, the sensory responses in the presence of carbon monoxide (50 ppm concentration) were 2.11, 2.18, and 2.26, respectively. The graph itself has a clear maximum, which indicates the accuracy of the gas sensor. For the $Gd_{1-x}Sr_xCrO_{3-\delta}$ (x = 0, 0.05, and 0.1) system (Fig. 5b), the sensory responses under similar conditions were 1.62, 1.69, and 1.78, respectively, which was weaker than the response of lanthanum chromites. The peak graph has similar values at 180 and 200°C.

The high values of sensory response for lanthanum chromites is due to its high resistivity, since during the adsorption of reducing agent gas on the film surface, the number of charge carriers in the system increased, which led to a sharp change in the resistivity.

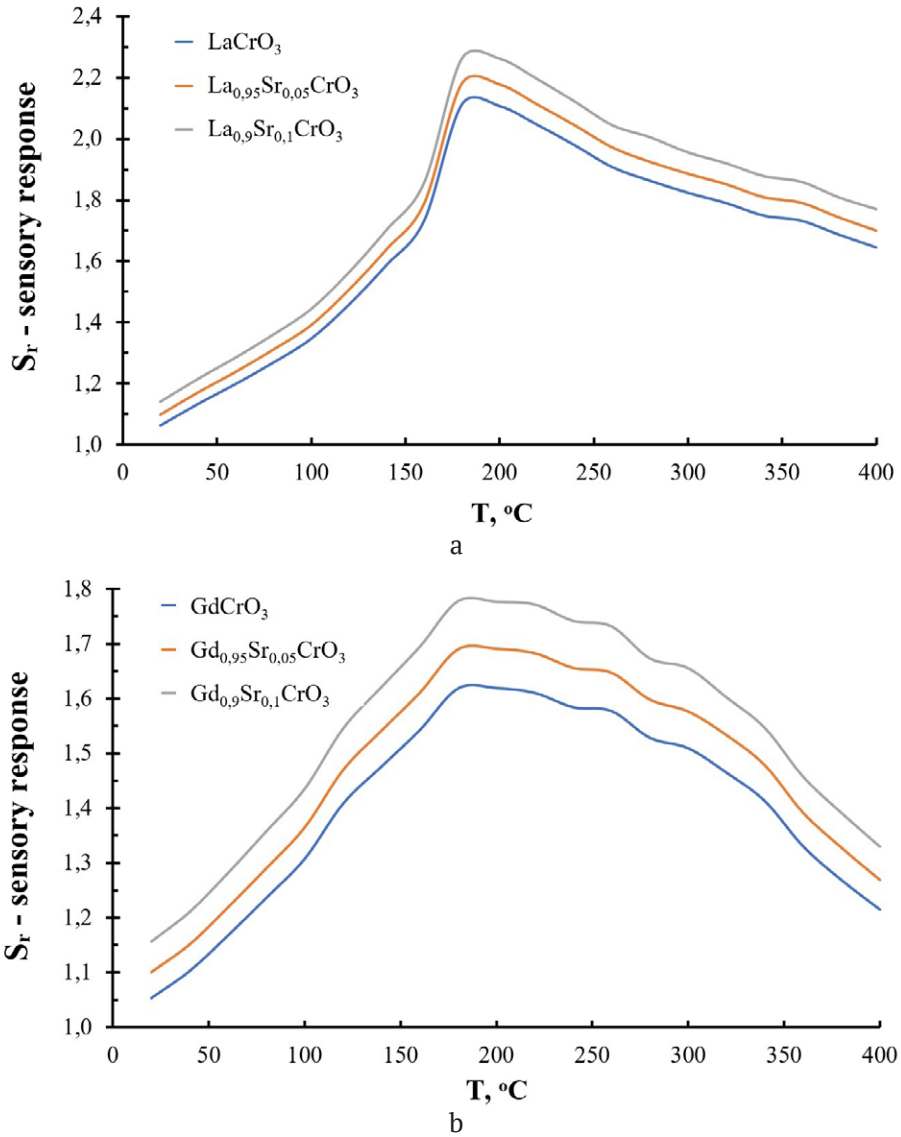

Fig. 5. Temperature dependence of the sensory response to carbon monoxide (50ppm) for thin films of $La_{1-x}Sr_xCrO_{3-\delta}$ (x = 0, 0.05 and 0.1) (a) and $Gd_{1-x}Sr_xCrO_{3-\delta}$ (x = 0, 0.05 and 0.1) (b)

6. Conclusions

Synthesis of $La_{1-x}Sr_xCrO_{3-\delta}$ and $Gd_{1-x}Sr_xCrO_{3-\delta}$ by the Pechini method made it possible to obtain materials with a high degree of uniformity and controlled particle size. The X-ray phase analysis confirmed the presence of a perovskite-like structure of the synthesized compounds and revealed the effect of doping with Sr^{2+} ions on the crystal lattice parameters. Dopant embedding was manifested in a change in interplanar distances associated with the difference in the ionic radii of the substituted element and the dopant. Strontium doping led to an increase in the concentration of oxygen vacancies, which had a positive effect on the sensory characteristics of the materials. Studies of gas-sensitive properties have shown that nanopowders exhibit the maximum response to CO at 180°C. The samples with the highest content of Sr^{2+} ions showed high sensitivity, which is explained by the optimal balance of the defective structure and mobility of charge carriers. The results obtained show the promise of using these nanomaterials for gas sensors.

Author contributions

The authors contributed equally to this article.

Conflict of interests

The authors declare that they have no known competing financial interests or personal relationships that could have influenced the work reported in this paper.

References

1. Anishhik V. M., Konjushko L. I., Jarmolovich V. A., Gorbachevskij D. A., Gerasimova T. G. Structure and properties of tin dioxide films. *Inorganic Materials*. 1995;31(4): 338–341. (in Russ.)

2. Rembeza E. S., Rembeza S. I., Svistova T. V., Dyrda N. N. Methods for improving gas-sensing properties of SnO_2 films for gas sensors. *Izvestija vysshih uchebnyh zavedenij. Jelektronika*. 2006;4: 3–8. (in Russ.). Available at: https://translit.ru/ru/bsi/

3. Kuklja M. M., Mastrikov Y. A., Jansang B., Kotomin E. A. The Intrinsic defects, disordering, and structural stability of $Ba_xSr_{1-x}Co_yFe_{1-y}O_{3-\delta}$ perovskite solid solutions. *The journal of Physical Chemistry C*. 2012;116: 18605–18611. https://doi.org/10.1021/jp304055s

4. Bulemo P. M., Kim I.-D. Recent advances in ABO_3 perovskites: their gas-sensing performance as resistive-type gas sensors. *Journal of the Korean Ceramic Societ*. 2020;57: 24–39. https://doi.org/10.1007/s43207-019-00003-1

5. Fergus J. W. Perovskite oxides for semiconductor-based gas sensors. *Sensors and Actuators B*. 2007;123: 1169–1179. https://doi.org/10.1016/j.snb.2006.10.051

6. Zhu L. Y., Ou L. X., Mao L. W., Wu X.-Y., Liu Y.-P., Lu H. L. Advances in noble metaldecorated metal oxide nanomaterials for chemiresistive gas sensors: Overview. *Nano-Micro Letters*. 2023;15(1). https://doi.org/10.1007/s40820-023-01047-z

7. Avadhesh K. Y., Rajnees K. S., Prabhakar S. Fabrication of lanthanum ferrite based liquefied petroleum gas sensor. *Sensors and Actuators B: Chemical*. 2016;229: 25–30. https://doi.org/10.1016/j.snb.2016.01.066

8. Wenbo Q., Zhenyu Y., Hongliang G., Renze Z., Fanli M. Perovskite-structured $LaCoO_3$ modified ZnO gas sensor and investigation on its gas sensing mechanism by first principle. *Sensors and Actuators: B. Chemical*. 2021;341: 1–15. https://doi.org/10.1016/j.snb.2021.130015

9. Cerda J., Arbiol J., Dezanneau G., Dıaz R., Morante J. R. Perovskite-type $BaSnO_3$ powders for high temperature gas sensor applications. *Sensors and Actuators: B. Chemical*. 2002;84: 21–25. https://doi.org/10.1016/s0925-4005(02)00005-9

10. Yaoyu Y., Yanbai S., Pengfei Z., Rui L., Ang L. Fabrication, characterization and n-propanol sensing properties of perovskite-type $ZnSnO_3$ nanospheres based gas sensor. *Applied Surface Science*. 2020;509: 1–10. https://doi.org/10.1016/j.apsusc.2020.145335

11. Balamurugan C., Lee D. W. Perovskite hexagonal $YMnO_3$ nanopowder as p-type semiconductor gas sensor for H_2S detection. *Sensors and Actuators B: Chemical*. 2015;221: 857–866. https://doi.org/10.1016/j.snb.2015.07.018

12. Prashant B. K., Kailas H. K., Uday G. D., Umesh J. T., Sachin G. S. Fabrication of thin film sensors by spin coating using sol-gel $LaCrO_3$ perovskite material modified with transition metals for sensing environmental pollutants, greenhouse gases and relative humidity. *Environmental Challenges*. 2021;3: 1–13. https://doi.org/10.1016/j.envc.2021.100043

13. Nemykh Ya. M., Kostryukov V. F., Gorbunov I. N. Synthesis of nanopowders of gadolinium chromite and lanthanum chromite with gas-sensitive properties. *Proceedings of Voronezh State University. Series: Chemistry. Biology. Pharmacy*. 2024;3: 13–21. (in Russ.). Available at: https://elibrary.ru/item.asp?id=72799790

14. Duran A., Falconi R., Mata J., Huerta L., Gonzalez M., Reguera E., Torres J. C. From $LaCrO_3$ towards $LaCr_{0,2}Mn_{0,2}Fe_{0,2}Al_{0,2}Ga_{0,2}O_3$ high-entropy ceramic compound: crystal structure, dielectric and magnetic properties. *Journal of the European Ceramic Society*. 2025;45: 1–19. https://doi.org/10.1016/j.jeurceramsoc.2024.116927

15. Javed M., Arif Khan A., Kazmi J., … Mohamed M. A. Variable range hopping transport and dielectric relaxation mechanism in $GdCrO_3$ rare-earth orthochromite perovskite. *Journal of Rare Earths*. 2023;42: 1304–1316. https://doi.org/10.1016/j.jre.2023.07.006

16. Moreno L. C., Valencia J. S., Landínez Téllez D. A., … Fajardo F. Preparation and structural study of $LaMnO_3$ magnetic material. *Magnetism and Magnetic Materials*. 2008;320(14): e19–e21. https://doi.org/10.1016/j.jmmm.2008.02.052

17. Yakimchu M. A., Eliseeva E. S., Kostryukov V. F. Nanocrystalline films based on $YCrO_3$ and $LaCrO_3$ yttrium

and lanthanum chromites doped with strontium ions Sr^{2+} as a basis for semiconductor gas sensors. *Condensed Matter and Interphases*. 2024;26(3): 536–546. https://doi.org/10.17308/kcmf.2024.26/12229

18. Kostryukov V. F., Parshina A. S., Mittova I. Ya. Preparation of gas-sensing thin Sr^{2+}-doped $YFeO_3$ films. *Inorganic Materials*. 2024;60(13): 1482–1490. https://doi.org/10.1134/s0020168525700232

19. JCPDS PCPDFWIN: A Windows-based retrieval and display program for accessing the ICDD PDF-2 database, International Centre for Diffraction Data. 1997.

20. Bugaenko L. T., Ryabykh S. M., Bugaenko A. L. A nearly complete system of average crystallographic ionic radii and its use for determining ionization potentials. *Moscow University Chemistry Bulletin*. 2008;63(6): 303–317. https://doi.org/10.3103/s0027131408060011

21. Krishtal M. M., Jasnikov I. S., Polunin V. I., Filatov A. M., Ul'janenkov A. G. *Scanning electron microscopy and X-ray spectral microanalysis**. Moscow: Tehnosfera Publ.; 2009. 208 p. (in Russ.)

22. *Four-probe method for measuring the electrical resistance of semiconductor materials: a teaching aid for the special practical course "Physics of semiconductor materials and devices" for students of the physics department**. N. A. Poklonskogo (ed.). Minsk: BGU Publ.; 1998. 46 p. (in Russ.)

23. Rembeza S. I., Svistova T. V., Rembeza E. S., Borsyakova O. I. The microstructure and physical properties of thin SnO_2 films. *Semiconductors*. 2001;35(7): 762–765. https://doi.org/10.1134/1.1385709

24. Kostryukov V. F., Parshina A. S., Sladkopevtsev B. V., Mittova I. Ya. Thin films on the surface of GaAs, obtained by chemically stimulated thermal oxidation, as materials for gas sensors. *Coatings (MDPI)*. 2022;12(12): 1819–1828. https://doi.org/10.3390/coatings12121819

** Translated by author of the article*

Information about the authors

Yaromir M. Nemykh, 2st year postgraduate student of the Department of Materials Science and Nanosystems Industry, Voronezh State University (Voronezh, Russian Federation).

https://orcid.org/0009-0009-3189-6018

yaromir0202@gmail.com

Viktor F. Kostryukov, Dr. Sci. (Chem.), Associate Professor at the Department of Materials Science and Industry of Nanosystems, Voronezh State University (Voronezh, Russian Federation).

https://orcid.org/0000-0001-5753-5653

vc@chem.vsu.ru

Ivan N. Gorbunov, 1st year Master's student of the Department of Materials Science and Industry of Nanosystems, Voronezh State University (Voronezh, Russian Federation).

https://orcid.org/0009-0001-5170-7909

wot4114@gmail.com

Elena V. Tomina, Dr. Sci. (Chem.), Head of the Department of Chemistry, Voronezh State Forestry University (Voronezh, Russian Federation)

https://orcid.org/0000-0002-5222-0756

tomina-e-v@yandex.ru

Received August 8, 2025; approved after reviewing October 3, 2025; accepted for publication October 15, 2025; published online April 01, 2026.

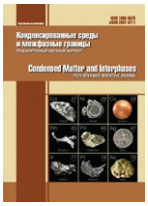

ISSN 1606-867X (Print)
ISSN 2687-0711 (Online)
Condensed Matter and Interphases
Kondensirovannye Sredy i Mezhfaznye Granitsy
https://journals.vsu.ru/kcmf/

Original articles

Research article
https://doi.org/10.17308/kcmf.2026.28/13561

Semi-empirical description of the regularity of change in thermal conductivity of single crystals based on the example of a concentration series of $Ba_{1-x}La_xF_{2+x}$ solid solutions

P. A. Popov[1], A. V. Shchelokov[1], N. V. Mitroshenkov[1], A. A. Kushnereva[1], V. A. Konyushkin[2], A. N. Nakladov[1], P. P. Fedorov[2], S. V. Kuznetsov[2]✉

[1]Petrovsky Bryansk State University
14, Bezhitskaya st., 241036 Bryansk, Russian Federation

[2]Prokhorov General Physics Institute of the Russian Academy of Sciences
38, Vavilov st., 119991 Moscow, Russian Federation

Abstract

Purpose: To study the thermal conductivity of single crystals of a $Ba_{1-x}La_xF_{2+x}$ solid solution and a semi-empirical description of changes in thermal conductivity depending on the lanthanum content.

Experimental: In the temperature range of 50–300 K, the thermal conductivity of single crystal $Ba_{1-x}La_xF_{2+x}$ samples with lanthanum content from $x = 0.001$ to $x = 0.300$ was determined by the experimental method of long heat flow.

Conclusions: A monotonic concentration dependence of thermal conductivity has been revealed. A semi-empirical expression has been proposed to approximate the experimental values of thermal conductivity.

Keywords: Barium difluoride, Lanthanum, Solid solution, Defect clusters, Thermal conductivity, Semi-empirical model

For citation: Popov P. A., Shchelokov A. V., Mitroshenkov N. V., Kushnereva A. A., Konyushkin V. A., Nakladov A. N., Fedorov P. P., Kuznetsov S. V. Semi-empirical description of the regularity of change in thermal conductivity of single crystals based on the example of a concentration series of $Ba_{1-x}La_xF_{2+x}$ solid solutions. *Condensed Matter and Interphases*. 2026;28(1): 92–102. https://doi.org/10.17308/kcmf.2026.28/13561

Для цитирования: Попов П. А., Щелоков А. В., Митрошенков Н. В., Кушнерёва А. А., Конюшкин В. А., Накладов А. Н., Федоров П. П., Кузнецов С. В. Полуэмпирическое описание закономерности изменения теплопроводности монокристаллов на примере концентрационной серии твердых растворов $Ba_{1-x}La_xF_{2+x}$ *Конденсированные среды и межфазные границы*. 2026;28(1): 92–102. https://doi.org/10.17308/kcmf.2026.28/13561

✉ Sergey V. Kuznetsov e-mail: kouznetzovsv@gmail.com

1. Introduction

Bulk crystalline materials based on calcium, strontium, and barium fluorides doped with rare earth elements are widely used as functional elements of photonics, scintillators [1–5], and elements of passive and active optics [6–10], both in the form of single crystals [11] and optical ceramics [12]. Besides its use in photonics, these solid solutions are used as ionic conductors [13–22], ion batteries [13–24], and catalysts [25]. The thermal conductivity of good-quality optical ceramics is no different from that of single crystals, allowing a comparison of their characteristics [26].

For various applications, one of the key characteristics is thermal conductivity, as it determines the material's ability to dissipate heat under various intense types of pumping. Solid solutions based on calcium, strontium, and barium fluorides, doped with rare earth elements, tend to form clusters of the R_6F_{36} type [27–31], which leads to a complex dependence of thermal conductivity on temperature. This is expressed by the fact that with an increase in the content of rare earth elements and with an increase in temperature from 50 to 300 K, a change in the nature of the temperature dependence is observed. At low rare earth element concentrations and low temperatures, the temperature dependence is typical of a crystalline material. As the rare earth content increases at low temperatures, the temperature dependence becomes more glass-like. Such complex behavior of the temperature dependence is extremely difficult to describe because the indicated patterns are observed for samples of the same solid solution with the same crystal structure. The best approximation based on a semi-empirical algorithm for describing the behavior of this type of materials was proposed in [32–33].

The processes of partial reduction of some trivalent ions to the divalent state (Sm, Eu, Dy, Yb, Tm) are often observed upon doping calcium, strontium, and barium fluorides with active rare earth ions [34–37]. To prevent this effect it was previously proposed to increase the complexity of the original matrix by adding optically inactive yttrium to the crystal composition. As a result, a new matrix for optical materials such as yttrofluorite (CaF_2:Y) was developed [38]. In addition to yttrium, various studies have proposed the use of lanthanum [39], which is a more effective ion for preventing the reduction of triply charged ions and preventing cluster formation. To reduce multiphonon relaxation processes, it is desirable to use matrices with lower phonon energy, therefore a barium fluoride matrix was chosen in preference to calcium and strontium fluorides.

The aim of the study was to investigate the patterns and mathematical description of the change in thermal conductivity in the temperature range of 50–300 K for the $Ba_{1-x}La_xF_{2+x}$ solid solution with a rare earth element content from 0.1 to 30.0 mol %.

To approximate the experimental values of thermal conductivity in the temperature range, we tested a simple semi-phenomenological model, which is significantly simpler than existing ones. The approximation does not have a strict physical justification, but it makes it possible to reliably describe the dependence of thermal conductivity on temperature and is useful for improving the theoretical understanding of heat transfer processes in media with a complex structure.

2. Experimental

Single crystals of $Ba_{1-x}La_xF_{2+x}$ solid solutions ($0.001 \leqslant x \leqslant 0.300$) were grown by the Bridgman technique in a vacuum growth oven using an Ar and CF_4 atmosphere in multi-cell graphite crucibles, allowing the growth of a concentration series of samples in one growth cycle. Barium fluoride (99.99 %, LANHIT) and lanthanum fluoride (99.99 %, LANHIT) were used as initial reagents.

The thermal expansion coefficient in the temperature range from 78 K to room temperature for samples containing 4, 10, and 20 mol % La was estimated based on the determination of the lattice parameters of the powders by the Debye-Scherrer method on a DRON-7.0 X-ray diffractometer (Burevestnik JSC, St. Petersburg, Russia) using an X-ray cryostat [40] in Cu-$K\alpha$ radiation with a wavelength of 1.54184 Å. Reflections from the {355} crystallographic plane were registered around diffraction angles of 146, 147, and 149°, respectively. The error in determining the lattice parameter over the entire temperature range studied did not exceed $\pm 1 \cdot 10^{-4}$ Å.

Thermal conductivity in the temperature range of 50–300 K was measured using the absolute stationary longitudinal heat flux method. The equipment and measurement technique are described in [41]. The samples were cylindrical with 9.6 mm in diameter and 22–26 mm in length. The thermal conductivity measurement error was within ±5 %.

3. Results

Prior to the study of the thermal and physical characteristics of $Ba_{1-x}La_xF_{2+x}$ solid solutions, the dependences of the lattice parameter and thermal expansion coefficient in the temperature range of thermal conductivity measurements were studied. The experimental points of the lattice parameter $a(T)$ for samples with a lanthanum content of 4, 10, and 20 mol. % are shown in Fig. 1. The behavior of $a(T)$ was typical for crystalline materials without anomalies, which indicates the high quality of the samples. The values of the lattice parameter a at T = 300 K were 6.1864, 6.1661, and 6.1360 Å for 4, 10, and 20 mol %, respectively. Data agree with the concentration dependence of $a(x)$ proposed in [42]. From the $a(T)$ data, the values of the thermal expansion coefficient (TEC) were calculated in accordance with the expression $\alpha = \frac{\Delta a}{\Delta T} \cdot \frac{1}{a}$. Fig. 1 shows the calculation results in comparison with previously obtained TEC data for the $Ba_{0.70}La_{0.30}F_{2.30}$ composition [43] and the BaF_2 matrix [44]. The analysis of the results demonstrated that a significant effect of lanthanum addition on the TEC is observed only in the low temperature range.

The thermal conductivity of $Ba_{1-x}La_xF_{2+x}$ samples with x = 0.008, 0.120 in the low temperature region and x = 0.045, 0.330, 0.460 with an increase in temperature to room temperature were studied [45–46]. Previously conducted studies [46–48] demonstrated that the thermal conductivity of the LaF_3 crystal is significantly lower than that of BaF_2.

The magnitude and temperature behavior of thermal conductivity are directly affected by heat capacity. Calorimetric studies of the $Ba_{1-x}La_xF_{2+x}$ solid solution in the range $T \leqslant 1$ K were summarized in [45]. The heat capacity of the $Ba_{0.70}La_{0.30}F_{2.30}$ crystal in the range of 63–313 K was investigated in [49]. The heat capacity of a $Ba_{0.51}La_{0.49}F_{2.49}$ sample in the range of 500–1000 K

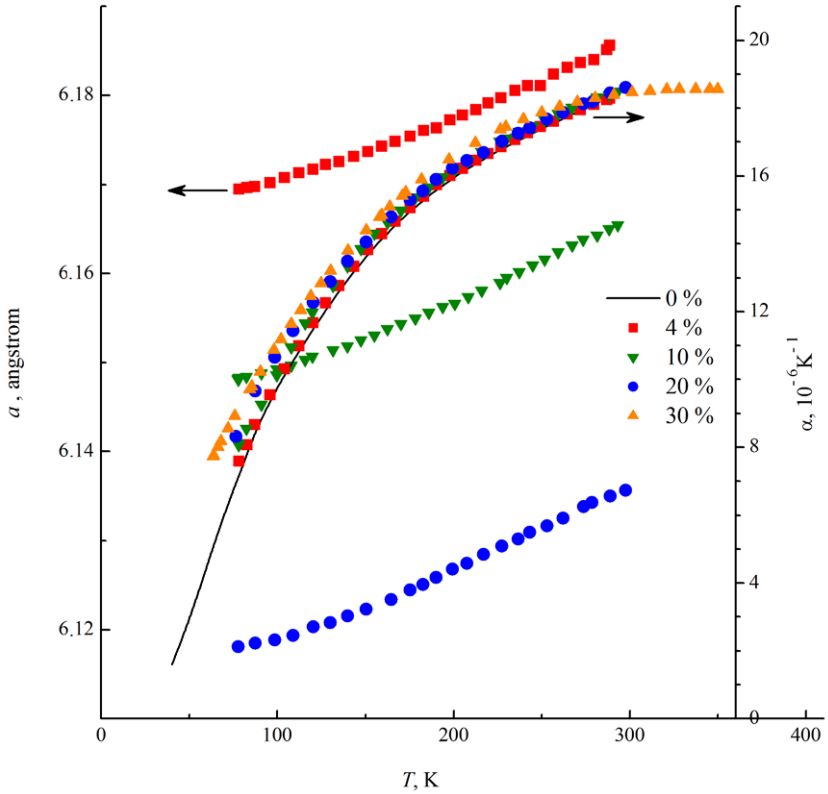

Fig 1. Temperature dependence of the lattice parameter and TEC of crystals of a $Ba_{1-x}La_xF_{2+x}$ solid solution

was measured [50]. In the temperature range from liquid nitrogen to room temperature, the effect of the LaF_3 doping has a character close to additive.

The thermal conductivity of the $Ba_{1-x}La_xF_{2+x}$ solid solution are presented graphically in Fig. 2 and in numerical form in Table 1. Fig. 2 includes data of $k(T)$ for previously studied samples using the experimental equipment and methods used in this study: BaF_2 corresponding to the composition $x = 0$ [48], and samples with $x = 0.25$ and $x = 0.30$ [51]. The markers in Fig. 2 show the experimental points $k(T)$ while lines show the results of calculations using Formula 1 (see below). A comparison of our $k(T)$ data with those presented graphically in [46] showed their close agreement.

An analysis of the results (Fig. 2) shows that the thermal conductivity value decreases sharply with an increase in the lanthanum content and the decreasing temperature dependence $k(T)$ weakens and turns into a weakly increasing one. A similar effect of trivalent rare earth elements introduced into crystals with a fluorite structure has been discovered for many heterovalent solid solutions of the type $M_{1-x}R_xF_{2+x}$, where M = Ca, Sr, Ba, Cd, R = REE [52–57]. This phenomenon was explained by the formation of large clusters of R_6F_{36} defects, which are highly efficient phonon scattering centers. The thermal conductivity of highly concentrated samples is lower than that of quartz glass (k = 1.36 $W \cdot m^{-1} \cdot K^{-1}$) at T = 300 K [58]). Crystals of the $Ba_{1-x}La_xF_{2+x}$ solid solution are characterized by high fluorine-ion conductivity, which increases with an increasing concentration of x [59–68]. The anticorrelation between the thermal conductivity and anionic conductivity of heterovalent solid solutions of fluorides with a fluorite structure, established in [69], is associated with the inelastic interaction of phonons and mobile fluorine ions. In accordance with the ion transport model proposed in [70], F^- ions occupy interstitial positions in $Ba_{1-x}La_xF_{2+x}$ crystal structure. A sharp decrease in thermal conductivity with a decrease in temperature to T = 50 K, as was noted for solid solutions of $Ca_{1-x}Y_xF_{2+x}$ [56, 71] and $Ba_{0.50}Ce_{0.50}F_{2.50}$ [51], was not observed for $Ba_{1-x}La_xF_{2+x}$ crystals. Monotonic increasing dependence $k(T)$ occurs only for one composition with the maximum lanthanum

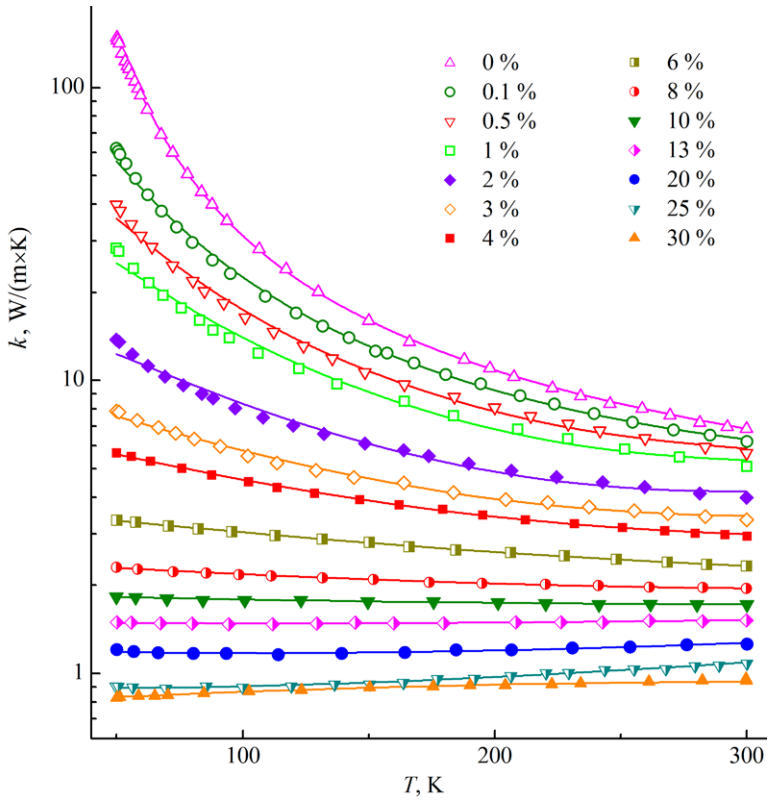

Fig. 2. Temperature dependence of thermal conductivity of single crystals of a $Ba_{1-x}La_xF_{2+x}$ solid solution (in the legend the La content is in mol %)

Table 1. Thermal conductivity values (W/(m·K) at different temperatures

Lanthanum content *x* mol. fraction	Temperature, K					
	50	100	150	200	250	300
0.001	62.1	21.8	13.1	9.42	7.36	6.20
0.005	39.9	16.6	10.6	8.11	6.56	5.66
0.01	28.3	13.3	9.08	7.03	5.87	5.10
0.02	13.8	7.91	6.06	5.01	4.42	3.98
0.03	7.86	5.62	4.61	4.00	3.63	3.35
0.04	5.67	4.56	3.86	3.44	3.17	2.95
0.06	3.34	3.03	2.79	2.59	2.44	2.33
0.08	2.30	2.18	2.09	2.03	1.98	1.95
0.10	1.83	1.79	1.76	1.74	1.73	1.72
0.13	1.50	1.48	1.49	1.49	1.50	1.52
0.20	1.21	1.16	1.18	1.20	1.23	1.26
0.25	0.904	0.898	0.936	0.976	1.03	1.08
0.30	0.828	0.865	0.893	0.914	0.929	0.939

content of x = 0.30. Obviously, a sharp decrease in the thermal conductivity of the crystals of this solid solution will occur with a more significant decrease in temperature. For three highly concentrated compositions (x = 0.25, x = 0.20, x = 0.13), the $k(T)$ curves have weakly defined minima, while for all other samples the $k(T)$ dependence is monotonously decreasing.

The concentration dependences of the thermal conductivity of the $Ba_{1-x}La_xF_{2+x}$ solid solution for temperatures (T = 50 K and T = 300 K) were shown in Fig. 3. Data analysis demonstrated that the $k(x)$ dependences are monotonic, allowing one to fairly confidently estimate the values of the thermal conductivity coefficient for intermediate (not studied) compositions.

Comparison between the concentration dependences of thermal conductivity $k(x)$ for the $Ba_{1-x}La_xF_{2+x}$ solid solution and the previously studied close analogue $Ba_{1-x}Yb_xF_{2+x}$ with an ytterbium content of up to x = 0.06 (Fig. 4) [48] was carried out. The thermal conductivity of $Ba_{1-x}La_xF_{2+x}$ crystals significantly exceeds that of the corresponding $Ba_{1-x}Yb_xF_{2+x}$ compositions due to size and weight factors. The radius of the barium cation is larger than that of lanthanum and ytterbium while the size of the lanthanum cation is larger than that of ytterbium [72]. Furthermore, the atomic masses of Ba and La are close and significantly smaller than the mass of Yb. As a result, the intensity of phonon-defect scattering in the case of the $Ba_{1-x}Yb_xF_{2+x}$ solid solution will be higher, and, consequently, the thermal conductivity will be lower than in the case of the $Ba_{1-x}La_xF_{2+x}$ solid solution with more homogeneous in cationic characteristics.

The experimental values of thermal conductivity $k(T)$ for studied $Ba_{1-x}La_xF_{2+x}$ crystals was described by expression (1) [33] based on the specific thermal resistance $w = 1/k$ of heterovalent solid solutions. It allows one to satisfactorily approximate the experimental values of $k(T)$ for $Ca_{1-x}Y_xF_{2+x}$ [71], $Ca_{1-x}Yb_xF_{2+x}$ [33], and $Ca_{1-x-y}Sr_xNd_yF_{2+y}$ solid solutions [73]. The expression has the form:

$$\frac{1}{k} = \frac{(1-A)}{\beta\sqrt{\frac{k_0}{d}}\cdot\arctan\left(\frac{\sqrt{k_0 d}}{\beta}\right)} + \frac{A}{D+BT+CT^2}. \qquad (1)$$

Here A is the contribution of thermal resistance associated with the introduction of trivalent rare earth ions and the formation of defect clusters ("amorphous component"); β is a parameter depending on the type of rare earth impurity; k_0 is the thermal conductivity coefficient of the undoped crystal; d is the concentration of the rare earth impurity (in the case of a two-component solid solution $Ba_{1-x}La_xF_{2+x}$ it is equal to the mole fraction x); T is the temperature in K. Parameters D, B, and C are coefficients of the polynomial describing the "amorphous component" of the thermal conductivity coefficient and have no explicit physical meaning. The phonon heat

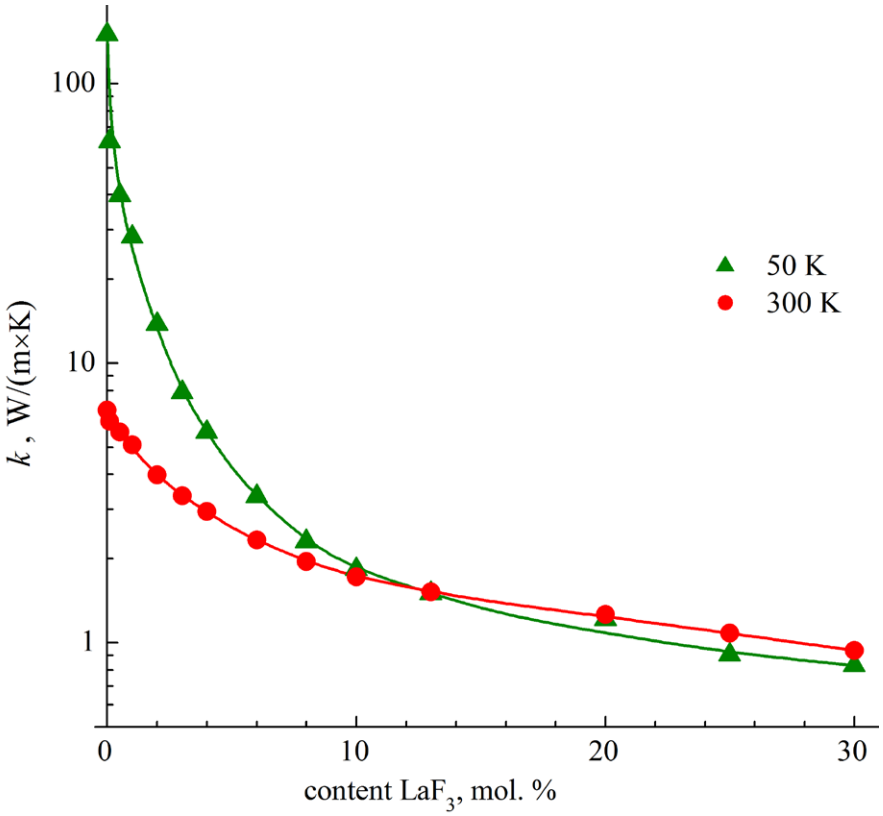

Fig. 3. Concentration dependence of thermal conductivity of a $Ba_{1-x}La_xF_{2+x}$ solid solution for different temperatures

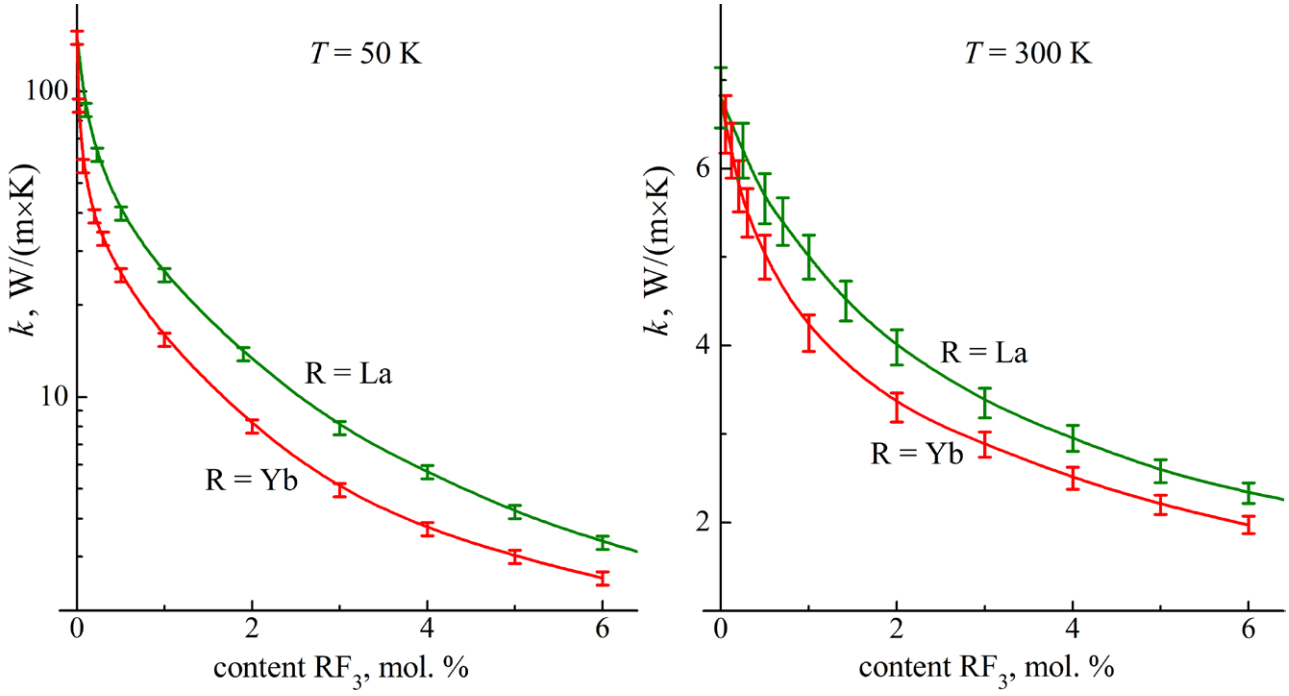

Fig. 4. Comparison of concentration dependences of thermal conductivity of $Ba_{1-x}La_xF_{2+x}$ and $Ba_{1-x}Yb_xF_{2+x}$ solid solutions (vertical frames correspond to the measurement error of thermal conductivity ± 5 %)

transfer model developed for single crystals is also conditionally applicable to amorphous media. In these media, the mean free path of phonons reaches its minimum value.

An approximation of the experimental data made it possible to achieve agreement with the corresponding calculated values of $k(T)$ at $\beta = 1$. As the coefficient k_0 for a nominally pure BaF_2 crystal, an approximating expression of the form was used:

$$k_0 = 1.49 + 1184 \exp\left(\frac{91.6}{T}\right) T^{-1} \quad (2).$$

The values of parameters A, B, C, and D for different compositions are given in Table 2. Their concentration dependences are summarized in Fig. 5. It is evident that the main changes in the values of these parameters occur within the concentration range $0 < x < 10$ mol %. At lanthanum concentrations greater than 10 mol %,

Table 2. The values of parameters A, B, C and D included in expression 1

LaF_3 content, mol %	A	C, $W \cdot m^{-1} \cdot K^{-3}$	B, $W \cdot m^{-1} \cdot K^{-2}$	D, $W \cdot m^{-1} \cdot K^{-1}$
0.1	0.10	$1.099 \cdot 10^{-4}$	$-5.841 \cdot 10^{-2}$	11.33
0.5	0.15	$1.137 \cdot 10^{-4}$	$-5.503 \cdot 10^{-2}$	9.599
1	0.22	$1.030 \cdot 10^{-4}$	$-5.068 \cdot 10^{-2}$	9.056
2	0.33	$5.769 \cdot 10^{-5}$	$-2.848 \cdot 10^{-2}$	5.762
3	0.40	$2.823 \cdot 10^{-5}$	$-1.452 \cdot 10^{-2}$	3.849
4	0.45	$1.510 \cdot 10^{-5}$	$-8.498 \cdot 10^{-3}$	3.013
5	0.51	$2.453 \cdot 10^{-6}$	$-1.978 \cdot 10^{-3}$	1.835
8	0.56	$1.732 \cdot 10^{-6}$	$-7.156 \cdot 10^{-4}$	1.338
10	0.60	$5.520 \cdot 10^{-7}$	$6.453 \cdot 10^{-5}$	1.105
13	0.63	$6.887 \cdot 10^{-7}$	$2.401 \cdot 10^{-4}$	0.9337
20	0.70	$1.993 \cdot 10^{-6}$	$-1.892 \cdot 10^{-4}$	0.8403
25	0.73	$2.161 \cdot 10^{-6}$	$1.266 \cdot 10^{-5}$	0.6490
30	0.76	$-1.088 \cdot 10^{-6}$	$8.417 \cdot 10^{-4}$	0.5947

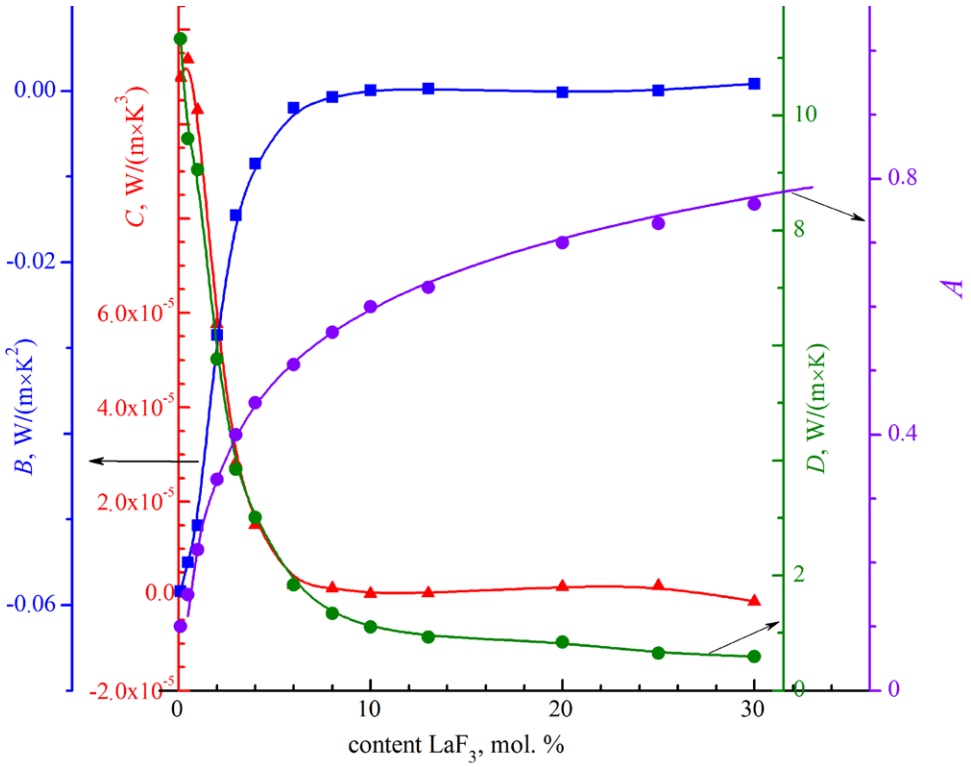

Fig. 5. Concentration dependences of the coefficients of the polynomial A, B, C, and D describing the "amorphous component"

the temperature dependences of the thermal conductivity of $Ba_{1-x}La_xF_{2+x}$ crystals practically disappear. To approximate the parameter $A(d)$, the formula $A = 1 + 0.16 \cdot \ln(0.8d)$ was used. Its largest value is obviously lower than $A_{max} = 1$, which corresponds to the intended relative meaning of this parameter.

4. Conclusion

For the first time, the thermal conductivity of single-crystal samples of the heterovalent solid solution $Ba_{1-x}La_xF_{2+x}$ ($0 \leqslant x \leqslant 0.30$) was experimentally studied in the temperature range of 50–300 K. It was noted that with increasing La content, the thermal conductivity decreases monotonically, and its temperature dependence changes from a strong decrease to a weak increase. Samples with high lanthanum content demonstrated thermal conductivity values close to those of optical glasses. The experimental results were accurately described by a semi-empirical expression that takes into account the contribution of the crystalline and amorphous components to the thermal resistance of the heterovalent solid solution. The values of the thermal expansion coefficient of $Ba_{1-x}La_xF_{2+x}$ crystals, experimentally determined in the temperature range (from liquid nitrogen to room temperature), have noticeable differences from the thermal expansion coefficient for the BaF_2 matrix only at low temperatures.

Author contributions

The authors contributed equally to this article.

Conflict of interests

The authors declare that they have no known competing financial interests or personal relationships that could have influenced the work reported in this paper.

References

1. Schotanus P., Dorenbos P., van Eijk C. W. E., Lamfers H. J. Suppression of the slow scintillation light output of BaF_2 crystals by La^{3+} doping. *Nuclear Instruments and Methods in Physics Research. A*. 1989;281(1): 162–166. https://doi.org/10.1016/0168-9002(89)91229-1

2. Herweg K., Nadig V., Schulz V., Gundacker S. On the prospects of BaF_2 as a fast scintillator for Time-of-Flight positron emission tomography systems. *IEEE Transactions on Radiation and Plasma Medical Sciences*. 2023;7(3): 241–252. https://doi.org/10.1109/TRPMS.2023.3237254

3. Belov M. V., Zavertyaev M. V., Kozlov V. A., Tskhay V. S. Scintillation properties of electromagnetic calorimeter modules based on BaF_2 crystals. *Bulletin of the Lebedev Physics Institute*. 2024;51(8): 273–277. https://doi.org/10.3103/S1068335624600475

4. Wojtowicz J., Glodoay J., Wisniewski D., Lempicki A. Scintillation mechanism in RE-activated fluorides. *Journal of Luminescence*. 1997;72–74: 731–733. https://doi.org/10.1016/S0022-2313(97)80790-9

5. Vladimirov S. V., Kaftanov V. S., Nilov A. F. ... Skvortsov V. N . Characteristics of BaF2 scintillation crystals. *Atomic Energy*.2001;90: 55–62. https://doi.org/10.1023/A:1011391923801

6. Shendrik R., Radzhabov E., Myasnikova A., ... Pankratov V. Ultrafast core-to-core luminescence in BaF_2 – LaF_3 single crystals. *Scientific Reports*. 2025;15: 26558. https://doi.org/10.1038/s41598-025-11505-w

7. Nepomnyashchikh A. I., Radzhabov E. A., Egranov A. V., Ivashechkin V. F. Luminescence of BaF_2–LaF_3. *Radiation Measurements*. 2001;33: 759–762. https://doi.org/10.1016/S1350-4487(01)00101-9

8. Radzhabov E. A., Shalaev A., Nepomnyashikh, A. I. Exciton luminescence suppression in BaF_2–LaF_3 solid solutions. *Radiation Measurements*. 1998;29(3-4): 307–309. https://doi.org/10.1016/S1350-4487(98)00048-1

9. Madirov E. I., Kuznetsov S. V., Konyushkin V. A., Busko D., Richards B. S., Turshatov A. Pushing the limits: down-converting Er^{3+}-doped BaF_2 single crystals with photoluminescence quantum yield surpassing 100%. *Advanced Optical Materials*. 2024;12(16): 2303094. https://doi.org/10.1002/adom.202303094

10. Kaminskii A. A. *Laser cystals, their physics and properties*. In: Springer Series in Optical Sciences. Berlin: Springer; 1990, vol. 14, 2nd ed. https://doi.org/10.1007/978-3-540-70749-3

11. Lu Z., Zhang Z., Jiang D., ... Su L. Thermo-mechanical properties and laser-induced damage behaviors in NYCF and NYSF crystals with different orientations. *Optics Express*. 2025;33(16): 33153–33168. https://doi.org/10.1364/OE.566275

12. Kuznetsov S. V., Aleksandrov A. A., Fedorov P. P. Optical fluoride nanoceramics. *Inorganic Materials*. 2021;57(6): 555–578. https://doi.org/10.1134/S0020168521060078

13. Sorokin N. I., Breiter M. W. Anionic conductivity and thermal stability of single crystals of solid solutions based on barium fluoride. *Solid State Ionics*. 1997;99(3-4): 241–250. https://doi.org/10.1016/S0167-2738(97)00190-2

14. Ivanov-Shits A. K., Sorokin N. I., Fedorov P. P., Sobolev B. P. Specific features of ion transport in nonstoichiometric fluorite-type $Ba_{1-x}R_xF_{2+x}$ (R=La–Lu phases). *Solid State Ionics*. 1989;31(4): 269–280. https://doi.org/10.1016/0167-2738(89)90466-9

15. Preishuber-Pflűgl F., Bottke P., Pregartner V., Bitschnauc B., Wilkening M. Correlated fluorine diffusion and ionic conduction in the nanocrystalline F^- solid electrolyte $Ba_{0.6}La_{0.4}F_{2.4}$ – ^{19}F $T_{1(\rho)}$ NMR relaxation vs. conductivity measurements. *Physical Chemistry Chemical Physics*. 2014;16(20): 9580–9590. https://doi.org/10.1039/C4CP00422A

16. Rammutla K. E., Comins J. D. High temperature raman scattering studies of $Ba_{1-x}La_xF_{2+x}$. *Radiation Effects and*

Defects in Solids. 1999;150(1–4): 347–353. https://doi.org/10.1080/10420159908226255

17. Den Hartog H. W., Langevoort J. C. Ionic thermal current of concentrated cubic solid solutions of SrF_2: LaF_3 and BaF_2: LaF_3. *Physical Review B*. 1981;24(6): 3547–3554. https://doi.org/10.1103/PhysRevB.24.3547

18. Den Hartog H. W., Pen K. F., Meuldijk J. Defect structure and charge transport in solid solutions $Ba_{1-x}La_xF_{2+x}$. *Physical Review B*. 1983;28(10): 6031–6040. https://doi.org/10.1103/PhysRevB.28.6031

19. Laredo E., Suarez N., Bello A., Puma M., Figueroa D., Schoonman J. Dislocation polarization and space-charge relaxation in solid solutions $Ba_{1-x}La_xF_{2+x}$. *Physical Review B*. 1985;32(12): 8325–8331. https://doi.org/10.1103/PhysRevB.32.8325

20. Wapenaar K. E. D., Koesveld J. L., Schoonmam J. Conductivity enhancement in fluorite-structured $Ba_{1-x}La_xF_{2+x}$ solid solutions. *Solid State Ionics*. 1981;2(3): 145–154. https://doi.org/10.1016/0167-2738(81)90172-7

21. Ivanov-Shits A. K., Sorokin N. I., Fedorov P. P., Sobolev B. P. Specific features of ion transport in nonstoichiometric $Sr_{1-x}R_xF_{2+x}$ phases (R=La-Lu, Y) with the fluorite-type structure. *Solid State Ionics*. 1989;31(4): 253–268. https://doi.org/10.1016/0167-2738(89)90465-7

22. Trnovcova V., Sorokin N. I., Fedorov P. P., Krivandina E. A., Šramkova T., Sobolev B. P. Electrical properties of heavily doped fluorite-structured BaF_2:RF_3 (R=rare earth element, Y, Sc) single crystals. *Ionics*. 2000;6(5): 351–358. https://doi.org/10.1007/BF02374152

23. Munnangi R., Mohammad I., Fichtner M. Room temperature fluoride ion batteries. *ECS Meeting Abstracts, Vol. MA2019-01, A02-Lithium Ion Batteries and Beyond*. 346. https://doi.org/10.1149/MA2019-01/2/346

24. Rongeat C., Munnangi A. R., Witter R., Fichtner M. Nanostructured fluorite-type fluorides as electrolytes for fluoride ion batteries. *The Journal of Physical Chemistry C*. 2013;117(10): 4943–4950. https://doi.org/10.1021/jp3117825

25. Astruc A., Celerier S., Pavon E., Mamede A.-S., Delevoye L., Brunet S. Mixed $Ba_{1-x}La_xF_{2+x}$ fluoride materials as catalyst for the gas phase fluorination of 2-chloropyridine by HF. *Applied Catalysis B: Environmental*. 2017;204: 107–118. https://doi.org/10.1016/j.apcatb.2016.11.019

26. Akchurin M. Sh., Gainutdinov R. V., Smolyanskii P. L., Fedorov P. P. Anomalously high fracture toughness of polycrystalline optical fluorite from the Suran deposit (South Urals). *Doklady Physics*. 2006;51(1): 10–12. https://doi.org/10.1134/S1028335806010034

27. Aminov L. K., Kurkin I. N., Kurzin S. P., Gromov I. A., Mamin G. V. Identification of the La_6F_{37} cubooctahedral clusters in mixed crystals $(BaF_2)_{1-x}(LaF_3)_x$ by the electron paramagnetic resonance method. *Physics of the Solid State*. 2007;49 (11): 2086–2090. https://doi.org/10.1134/S1063783407110121

28. Aminov L. K., Abdulsabirov R. Y., Korableva S. L., Kurkin I. N., Kurzin S. P. EPR of rare-earth ion clusters in mixed crystals $Ba_{1-x}La_xF_{2+x}$ doped with Yb^{3+} Ion. *Applied Magnetic Resonance*. 2005;29(4): 561–568. https://doi.org/10.1007/BF03166332

29. Fedorov P. P. Association of point defects in non-stoichiometric $M_{1-x}R_xF_{2+x}$ fluorite-type solid solutions. *Butlletí de les Societats Catalanes de Física, Química, Matemàtiques i Tecnologia*. 1991;12(2): 349–381. Режим доступа: https://raco.cat/index.php/ButlletiSCFQMT/article/view/221696

30. Moore D. S., Wright J. C. Laser spectroscopy of defect chemistry in CaF_2:Er. *The Journal of Chemical Physics*. 1981;74: 1626–1636. https://doi.org/10.1063/1.441303

31. Kazanskii S. A., Ryskin A. I., Nikiforov A. E., Zaharov A. Y., Ougrumov M. Y., Shakurov G. S. EPR spectra and crystal field of hexamer rare-earth clusters in fluorites. *Physical Review B*. 2005;72(1): 014127. https://doi.org/10.1103/PhysRevB.72.014127

32. Liu K., Bian G., Zhang Z., Ma F., Su L. Modelling and analyzing the glass-like heat transfer behavior of rare-earth doped alkaline earth fluoridecrystals. *CrystEngComm*. 2022;24(37): 6468–6476. https://doi.org/10.1039/D2CE00698G

33. Popov P. A., Shchelokov A. V., Fedorov P. P. Numerical model of temperature-dependent thermal conductivity in $M_{1-x}R_xF_{2+x}$ heterovalent solid Solution nanocomposites, where M stands for alkaline-earth metals and R for rare-earth Metals. *Nanosystems: Physics, Chemistry, Mathematics*. 2024;15(2): 255–259. https://doi.org/10.17586/2220-8054-2024-15-2-255-259

34. Kaczmarek S. M., Tsuboi T., Ito M., Boulon G., Leniec G. Optical study of Yb^{3+}/Yb^{2+} conversion in CaF_2 crystals. *Journal of Physics: Condensed Matter*. 2005;17(25): 3771–3786. https://doi.org/10.1088/0953-8984/17/25/005

35. Angervaks A. E., Shcheulin A. S., Ryskin A. I., ... Fedorov P. P. Di- and trivalent ytterbium distributions along a melt-grown CaF_2 crystal. *Inorganic Materials*. 2014;50(7): 733–737. https://doi.org/10.1134/S0020168514070024

36. Savchuk R. N., Omelchuk A. A., Kompanichenko N. M., Nagorny P. G. Reduction of rare earth element fluorides with zirconium. *Russian Journal of Inorganic Chemistry*. 2003;48(10): 1454–1458. Available at: https://elibrary.ru/item.asp?id=27970487

37. Azarov V. V., Skorobogatov B. S. Reduction of rare-earth ions in LaF_3 single crystals. *Izvestiya Akademii Nauk SSSR. Neorganicheskiye Materialy* (Inorganic Materials) 1968;4(10): 1748–1749.

38. Kaminskii A. A., Osico V. V., Prokhorov A. M., Voronko Yu. K. Spectral investigation of the stimulated radiation of Nd^{3+} in CaF_2–YF_3. *Physics Letters*. 1966;22(4): 419–421. https://doi.org/10.1016/0031-9163(66)91208-X

39. Kitajima S., Yamakado K., Shirakawa A., Ueda K., Ezura Y., Ishizawa H. Yb^{3+}-doped CaF_2–LaF_3 ceramics laser. *Optics Letters*. 2017;42(9): 1724–1727. https://doi.org/10.1364/OL.42.001724

40. Novikov V. V., Matovnikov A. V., Avdashchenko D. V., ... Shevelkov A. V. Low-temperature structure and lattice Dynamics of the thermoelectric clathrate $Sn_{24}P_{19.3}I_8$. *Journal of Alloys and Compounds*. 2012;520: 174–179. https://doi.org/10.1016/j.jallcom.2011.12.171

41. Popov P. A., Sidorov A. A., Kul'chenkov E. A., ... Fedorov P. P. Thermal conductivity and expansion of PbF_2 single crystal. *Ionics*. 2017;23(1): 233–239. https://doi.org/10.1007/s11581-016-1802-2

42. Sobolev B. P., Tkachenko N. L. Phase diagrams of BaF_2-(Y, Ln)F_3 systems. *Journal of the Less Common Metals*. 1982;85: 155–170. https://doi.org/10.1016/0022-5088(82)90067-4

43. Sidorov A. A., Popov P. A., Aksenov S. V., Begunov A. I., Fedorov P. P. Thermal expansion of solid solutions based on

calcium and barium fluorides. *Inorganic Materials*. 2013;49(5): 525–527. https://doi.org/10.1134/S0020168513040146

44. White G. K. Thermal eExpansion at low temperatures of the alkaline earth fluorides and PbF_2. *Journal of Physics C: Solid State Physics*.1980;13(26): 4905–4913. https://doi.org/10.1088/0022-3719/13/26/012

45. Cahill D. G., Pohl R. O. Low-energy excitations in the mixed crystal $Ba_{1-x}La_xF_{2+x}$. *Physical Review B*. 1989;39: 10477–10480. https://doi.org/10.1103/PhysRevB.39.10477

46. Cahill D. G., Watson S. K., Pohl R. O. Lower limit to the thermal conductivity of disordered crystals. *Physical Review B*, 1992;46(10): 6131–6140. https://doi.org/10.1103/PhysRevB.46.6131

47. Popov P A., Moiseev N. V., Filimonova A. V., ... Mironov I. Thermal conductivity of LaF_3-based single crystals and ceramics. *Inorganic Materials*. 2015;48(3): 304–308. https://doi.org/10.1134/S0020168512030120

48. Popov P. A., Fedorov P. P., Kuznetsov S. V., Konyushkin V. A., Osiko V. V., Basiev T. T. Thermal conductivity of single crystals of $Ba_{1-x}Yb_xF_{2+x}$ solid solution. *Doklady Physics*. 2008;53(7): 353–355. https://doi.org/10.1134/S1028335808070045

49. Moiseev N. V., Popov P. A., Reiterov V.M., Fedorov P. P. Heat Capacity and Thermodynamic Functions of $Ba_{0.70}La_{0.30}F_{2.30}$ heterovalent solid solution. *Condensed Matter and Interphases*. 2010;12(3): 243–246. Available at: https://journals.vsu.ru/kcmf/article/view/1121

50. Andeen N. H., Clausen K. N., Kjems J. K., Schoonman J. A Study of the Disorder in Heavy Doped $Ba_{1-x}La_xF_{2+x}$ by Neutron Scattering. *Journal of Physics C: Solid State Physics*. 1986;19(14): 2377–2389. https://doi.org/10.1088/0022-3719/19/14/004

51. Popov P. A., Fedorov P. P., Konyushkin V. A. Thermal conductivity of single crystals of $Ba_{1-x}R_xF_{2+x}$ (R=La, Ce, Nd, Gd) solid solutions. *Crystallography Reports*. 2017;62(2): 283–287. https://doi.org/10.1134/S1063774517020225

52. Popov P. A., Fedorov P. P., Konyushkin V. A., Nakladov A. N., Kuznetsov S. V., Osiko V. V., Basiev T. T. Thermal conductivity of single crystals of $Sr_{1-x}Yb_xF_{2+x}$ solid solution. *Doklady Physics*. 2008;53(8): 413–415. https://doi.org/10.1134/S1028335808080016

53. Popov P. A., Fedorov P. P., Kuznetsov S. V., Konyushkin V. A., Osiko V. V., Basiev T. T. Thermal conductivity of single crystals of $Ca_{1-x}Yb_xF_{2+x}$ solid solutions. *Doklady Physics*. 2008;53(4): P. 198-200. https://doi.org/10.1134/S102833580804006X

54. Popov P. A., Fedorov P. P., Osiko V. V., Reiterov V. M., Garibin E. A., Demidenko A. A., Mironov I. A. Thermal conductivity of single crystals of $Ca_{1-x}Er_xF_{2+x}$ and $Ca_{1-x}Tm_xF_{2+x}$ solid solutions. *Doklady Physics*. 2012;57(3): 97–99. https://doi.org/10.1134/S1028335812030111

55. Popov P. A., Fedorov P. P., Garibin E. A., Smirnov A. N., Gusev P. E., Krutov M. A. Thermal conductivity of $Ca_{1-x}Ho_xF_{2+x}$ optical ceramics. *Inorganic Materials*. 2012;48(8): 857–860. https://doi.org/10.1134/S002016851207014X

56. Popov P. A., Fedorov P. P., Osiko V. V. Thermal conductivity of single crystals of the $Ca_{1-x}Y_xF_{2+x}$ solid solution. *Doklady Physics*. 2014;59(5): 199–202. https://doi.org/10.1134/S1028335814050036

57. Popov P. A., Fedorov P. P., Konyushkin V. A. Heat conductivity of $Ca_{1-x}R_xF_{2+x}$ (R = La, Ce, Pr, $0 \leqslant x \leqslant 0.25$) heterovalent solid solutions. *Crystallography Reports*. 2015;60(5): 744–748. https://doi.org/10.1134/S1063774515050107

58. Sergeev O. A., Shashkov A. G., Umanskii A. S. Thermophysical properties of quartz glass. *Journal of Engineering Physics*. 1982;43(6): 1375–1383. https://doi.org/10.1007/BF00824797

59. Wapenaar K. E. D., Van Koesveld J. L., Schoonman J. Conductivity enhancement in fluorite-structured $Ba_{1-x}La_xF_{2+x}$ solid solutions. *Solid State Ionics*. 1981;2(3): 145–154. https://doi.org/10.1016/0167-2738(81)90172-7

60. Trnovcova V., Garashina L. S., Skubla A., ... Sobolev B. P. Structural aspects of fast ionic conductivity of rare earth fluorides. *Solid State Ionics*. 2003;157(1-4): 195–201. https://doi.org/10.1016/S0167-2738(02)00209-6

61. Hull S. Superionics: crystal structures and conduction. *Reports on Progress in Physics*. 2004;67(7): 1233–1314. https://doi.org/10.1088/0034-4885/67/7/R05

62. Düvel A., Bednarcik J., Šepelák V., Heitjans P. Mechanosynthesis of the fast fluoride ion conductor $Ba_{1-x}La_xF_{2+x}$: from the fluorite to the tysonite structure. *The Journal of Physical Chemistry* C. 2014;118(13): 7117–7129. https://doi.org/10.1021/jp410018t

63. Sobolev B. P., Sorokin N. I., Bolotina N. B. Nonstoichiometric single crystals $M_{1-x}R_xF_{2+x}$ and $R_{1-y}M_yF_{3-y}$ (M = Ca, Sr, Ba: R = rare earth elements) as fluorine-ionic conductive solid electrolytes. In: *Photonic & Electronic Properties of Fluoride Materials*. Tressaud A., Poeppelmeier K. (ed.). Elsevier; 2016. pp. 465–491. https://doi.org/10.1016/B978-0-12-801639-8.00021-0

64. Gschwind F., Rodrigues-Garsia G., ... Hörmann N. Fluoride ion batteries: theoretical performance, safety, toxicity, and a combinatorial screening of new electrodes. *Journal of Fluorine Chemistry*. 2016;182: 76–90. https://doi.org/10.1016/j.jfluchem.2015.12.002

65. Cheng X., Wang S., Lin X. Preparation and electrochemical properties of $Ba_{1-x}La_xF_{2+x}$ fluoride electrolyte. *IOP Conference Series: Materials Science and Engineering*. 2019;678: 012148. https://doi.org/10.1088/1757-899X/678/1/012148

66. Nikolaichik V. I., Sobolev B. P., Sorokin N. I., Avilov A. S. Electron diffraction study and ionic conductivity of fluorite $Ba_{1-x}La_xF_{2+x}$ and tysonite $La_{1-y}Ba_yF_{3-y}$ phases in the BaF_2-LaF_3 system. *Solid State Ionics*. 2022;386: 116052. https://doi.org/10.1016/j.ssi.2022.116052

67. Sorokin N. I. Concentration and mobility of charge carriers in the superionic conductor $Ba_{1-x}La_xF_{2+x}$ ($0.05 \leqslant x \leqslant 0.5$). *Physics of the Solid State*. 2024;66(1): 53–58https://doi.org/10.61011/PSS.2024.01.57854.253 Available at: https://journals.ioffe.ru/articles/viewPDF/57854

68. Andersen N. H., Clausen K. N., Kjems J. K., Schoonman J. A study of the disorder in heavily doped $Ba_{1-x}La_xF_{2+x}$ by neutron scattering, ionic conductivity and specific heat measurements. *Journal of Physics C: Solid State Physics*. 1986;19(14): 2377–2389. https://doi.org/10.1088/0022-3719/19/14/004

69. Fedorov P. P., Sorokin N. I., Popov P. A. Inverse correlation between the ionic and thermal conductivities of single crystals of $M_{1-x}R_xF_{2+x}$ (M = Ca, Ba; R–rare-earth element) fluorite solid solutions. *Inorganic Materials*. 2017;53(6): 626–632. https://doi.org/10.1134/S0020168517060036

70. Sorokin N. I., Karimov D. N. Crystallophysical model of ion transport in single crystals of $Ba_{1-x}La_xF_{2+x}$ and $Ca_{1-x}Y_xF_{2+x}$ superionics conductors. *Physics of the Solid State*. 2021;63(12): 1821–1832. https://doi.org/10.1134/S106378342110036X

71. Popov P. A., Shchelokov A. V., Konyushkin V. A., Nakladov A. N., Fedorov P. P. Application of the numerical model of temperature-dependent thermal conductivity in $Ca_{1-x}Y_xF_{2+x}$ heterovalent solid solution nanocomposites. *Nanosystems: Physics, Chemistry, Mathematics*. 2024;16(1): 67–73. https://doi.org/10.17586/2220-8054-2025-16-1-67-73

72. Shannon R. D. Revised effective ionic radii and systematic studies of interaction distance in halides and chalcogenides. *Acta Crystallographica Section A*. 1976;32(5): 751–767. https://doi.org/10.1107/S0567739476001551

73. Popov P. A., Shchelokov A. V., Zentsova A. A., Fedorov P. P. Thermal conductivity of single crystals of $Ca_{1-x-y}Sr_xNd_yF_{2+y}$ solid solution. *Inorganic Materials*. 2024;60(5): 590–600. https://doi.org/10.31857/S0002337X24050082

Information about the authors

Pavel A. Popov, Dr. Sci. (Phys.-Math.), Professor at the Department of Experimental and Theoretical Physics, Bryansk State Academician I. G. Petrovski University (Bryansk, Russian Federation).
https://orcid.org/0000-0001-7555-1390
tfbgubry@mail.ru

Alexander V. Shchelokov, graduate student at the Department of Experimental and Theoretical Physics, Bryansk State Academician I. G. Petrovski University (Bryansk, Russian Federation).
https://orcid.org/0009-0001-4090-2506
alexandershchelokov@mail.ru

Nikolay V. Mitroshenkov, Cand. Sci. (Phys.-Math.), Head of the Department of Experimental and Theoretical Physics, Bryansk State Academician I. G. Petrovski University (Bryansk, Russian Federation).
https://orcid.org/0000-0002-4418-9613
weerm@yandex.ru

Alena A. Kushnereva, master's student at the Department of Experimental and Theoretical Physics, Bryansk State Academician I. G. Petrovski University (Bryansk, Russian Federation).
https://orcid.org/0000-0002-9793-7099
alenazen01@mail.ru

Vasily A. Konyushkin, Senior Researcher, Prokhorov General Physics Institute of the Russian Academy of Sciences (Moscow, Russian Federation).
https://orcid.org/0000-0002-6028-8937
vasil@lst.gpi.ru

Andrey N. Nakladov, Junior Researcher, Prokhorov General Physics Institute of the Russian Academy of Sciences (Moscow, Russian Federation).
https://orcid.org/0000-0002-4060-8091
andy-nak@yandex.ru

Pavel P. Fedorov, Dr. Sci. (Chem.), Chief Researcher, Prokhorov General Physics Institute of the Russian Academy of Sciences (Moscow, Russian Federation).
https://orcid.org/0000-0002-2918-3926
ppfedorov@yandex.ru

Sergey V. Kuznetsov, Cand. Sci. (Chem.), Leading Researcher, Prokhorov General Physics Institute of the Russian Academy of Sciences (Moscow, Russian Federation).
https://orcid.org/0000-0002-7669-1106
kouznetzovsv@gmail.com

Received September 18, 2025; accepted after reviewing October 13, 2025; accepted for publication November 15, 2025; published online April 01, 2026.

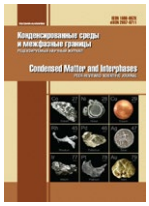

ISSN 1606-867X (Print)
ISSN 2687-0711 (Online)
Condensed Matter and Interphases
Kondensirovannye Sredy i Mezhfaznye Granitsy
https://journals.vsu.ru/kcmf/

Original articles

Research article
https://doi.org/10.17308/kcmf.2026.28/13562

Features of equilibrium uranium sorption on the fibrous carboxylated sorbent FORPAN from carbonate-containing solutions simulating seawater

M. A. Rahimli, S. R. Mamedova✉

Institute of Catalysis and Inorganic Chemistry,
113, H. Javid ave., Baku, AZ-1143, Azerbaijan

Abstract

Objectives: The purpose of this work is to study and identify the features of the equilibrium sorption of uranium from carbonate-containing solutions on a fibrous sorbent obtained (at the St. Petersburg Institute of Textile and Light Industry named after S. M. Kirov) by synthesizing carboxylated polyacrylonitrile (PAN) fiber with formaldehyde, with the common name of FORPAN.

Experimental: The equilibrium sorption of uranium by the carboxylated fibrous sorbent FORPAN from carbonate-containing solutions simulating seawater was studied in the range of initial concentrations ($3.36\cdot10^{-5}$–$7.13\cdot10^{-4}$ mol/l) and temperatures (293–338 K) at pH = 7.85. It was found that during the contact of the fiber with the carbonate-containing uranium solution, a sharp decrease in the pH of the solution and the cleavage of the tricarbonate uranilate complex occur due to the protolysis of carboxyl groups. Based on mathematical processing (using the least squares method) of the dependences of the equilibrium distribution coefficients of uranium (ml/g) on the equilibrium concentration of uranium in solution (mol/ml) at different temperatures, a generalized equation was obtained that made it possible to calculate the capacity of the fiber for uranium (mol/g) during its sorption from model solutions prepared based on Caspian Sea water in the range of studied concentrations and temperatures, as well as to calculate the capacity of the FORPAN sorbent relative to uranium in Caspian Sea water ($1.22\cdot10^{-5}$ mol/g = $2.9\cdot10^{-3}$ g/g) and the distribution coefficient of uranium in seawater ($1.6\cdot10^{4}$ ml/g) at T = 293.3 K.

Conclusions: Based on the conducted studies of the features of equilibrium sorption of uranium from model carbonate-containing solutions and the results obtained, FORPAN fiber can be recommended for the extraction uranium from dilute carbonate-containing solutions of natural waters, in particular from Caspian Sea water, with a uranium content of $2.5\cdot10^{-6}$ mol/l, in the range of relatively low temperatures of 293–307 K.

Keywords: Sorption, Uranium, Fibrous sorbent, Carbonate-containing solutions, Thermodynamics

For citation: Rahimli M. A., Mamedova S. R. Features of equilibrium uranium sorption on the fibrous carboxylated sorbent FORPAN from carbonate-containing solutions simulating seawater. *Condensed Matter and Interphases*. 2026;28(1): 103–114. https://doi.org/10.17308/kcmf.2026.28/13562

Для цитирования: Рагимли М. А., Мамедова С. Р. Особенности равновесной сорбции урана на волокнистом карбоксилированном сорбенте ФОРПАН из карбонатсодержащих растворов, моделирующих морскую воду. *Конденсированные среды и межфазные границы*. 2026;28(1): 103–114. https://doi.org/10.17308/kcmf.2026.28/13562

✉ Севиндж Рагим гызы Мамедова, e-mail: edu.office@kqki.science.az

1. Introduction

Ocean water is a virtually inexhaustible source of many elements, particularly uranium, copper, and cobalt, whose oceanic abundances are estimated at $4.2 \cdot 10^9$, $4.1 \cdot 10^9$, and $7.6 \cdot 10^7$ tons, respectively. Ocean water is promising not only for its inexhaustibility but also for its technological feasibility – its constant composition and potential for comprehensive use.

Attention to the ocean as a source of uranium is driven by the depletion of terrestrial reserves and the intensive development of nuclear energy. Given the trace concentrations of uranium in seawater (~ 3 μg/l) against the backdrop of its highly mineralized, complex salt composition, the need to select selective sorbents using highly effective methods for concentrating this element is of undeniable practical interest [1, 2]. Sorption methods are currently showing promise [3]. The authors used FIBAN C-1 (cation exchanger) and FIBAN AC-22V (aminocarboxyl polyampholyte) fiber ion exchangers under dynamic settings to determine various features of the sorption, extraction, and concentration of uranyl ions from model nitrate solutions. It was demonstrated that a high uranium sorption rate is coupled with effective uranium (VI) extraction and concentration. The following quantitative aspects of uranium sorption under dynamic conditions were computed: sorption rate, uranium content in the sorbent phase, dynamic exchange capacity, and overall dynamic exchange capacity.

The possibility of using many types of sorbents for these purposes has been investigated so far: natural and synthetic ion exchangers, complexing, modified, composite, and others. The efficiency of radionuclide extraction depends on the sorbent's selectivity in the presence of inorganic and organic components contained in aqueous media [4–7]. Thus, the authors [4] synthesized a new sorbent, 4XADMnO (Amberlite XAD-4 modified with manganese dioxide nanoparticles), to improve the sorption of UO_2^{2+} ions in aqueous media from low-level radioactive waste and characterized it using EDX, XRD, and FTIR analysis. It was established that the developed sorbent was successfully used for the sorption of UO_2^{2+} ions for safety purposes.

By adding hydrated zirconium dioxide to a gel-like anion-exchange resin, the authors [6] created organic-inorganic sorbents. Throughout the experiment, the solvent's surface tension, temperature, and solution concentration were all changed. Particles of different sizes are more common in the polymer matrix depending on the production technique. Research on the sorption of anionic uranyl complexes revealed that pseudo-first- or pseudo-second-order chemical reaction models describe the sorption rate. Compared to the original resin, samples altered with tiny particles (< 300 nm) show a greater sorption rate. Particle size reduction makes it easier for the sorbents to regenerate chemically.

When selecting a sorbent, it is necessary to consider: high sorption capacity and selectivity; good kinetic and mechanical properties in multiple sorption-regeneration cycles; and, most importantly, the sorbent's low cost.

According to numerous studies, sorbents based on metal oxides meet most of these requirements. In particular, titanium dioxide, as a sorbent, is distinguished by its radiation and chemical stability in acidic and alkaline solutions, and as an ion exchanger, it exhibits a satisfactory exchange rate, which is important when working in a column configuration. Hydrated titanium dioxide has been studied in considerable detail for a number of years as a sorbent for extracting uranium from seawater. It should be noted that mixed titanium oxide sorbents exhibit the best sorption characteristics, due to the introduction of an inert additive in the form of zirconium oxide (6 %) and others during synthesis, which has a significant impact on the change in the sorption properties of titanium dioxide (almost doubling its kinetic and equilibrium characteristics, significantly altering all energy parameters of the sorption process [8–12]).

For the selective concentration of radionuclides from neutral natural waters, complexing sorbents with phosphoric acid, amidoxime, hydroxamic, iminodiacetate, and other groups are also used, which are capable of binding radionuclides into corresponding complex compounds and effectively isolating them from natural waters with a high salt content and in the presence of natural ligands [13].

Currently, the sorption extraction of metals from solutions using fibrous sorbents, characterized by good kinetic properties and high element distribution coefficients during

sorption, allows them to be successfully used for the concentration and separation of trace elements from natural waters and other solutions, under both static and dynamic conditions [14]. The developed surface, providing good sorption and kinetic properties of fibrous sorbents, distinguishes them from granular sorbents, since they are convenient for practical use both in static conditions (a small amount of sorbent is required, especially when there is no need to regenerate the sorbent), and in a dynamic, columnar version, for concentrating microelements from large volumes of solutions, when after sorption the elements are usually eluted and then analyzed [15, 16].

Neutron activation sorption (NAS) is performed directly on the sorbent without elution or degradation, which increases the speed of the method and reduces contamination by foreign impurities.

The selection of the sorbent and sorption conditions ensures the separation of trace elements from large quantities of macroelements. Separation of elements using fibrous sorbents is based on differences in the sorbent's selectivity for metals, which in turn is due to differences in the stability of the complexes formed by metals in the sorbent phase.

The selectivity of a sorbent is determined primarily by the nature of its functional and analytical groups. The selective properties of sorbents are characterized by selectivity series. The presence of carboxyl groups determines the complexing properties of the ion exchanger. Metal ions such as Zn, Cd, Pb, Cu, U, and others form complexes of varying strength with acetate ions. For example, the strength of monoacetate complexes increases in the following order: $Zn^{2+} < Cd^{2+} < Pb^{2+} < Cu^{2+} < UO_2^{2+}$. According to Gregor, the strength of polyacrylate complexes increases in approximately the same direction. Interestingly, the strength of sulfate complexes of these metals is virtually identical.

A visual expression of sorbent selectivity is the dependence of element distribution coefficients on pH and component concentration.

The presence of complexing groups in ion-exchange fibers leads to an increased affinity of these ion exchangers for metal ions; such compounds exhibit specific properties and are highly selective for individual metal ions.

The most effective uranium sorbents known to date contain amidoxime (AO) or imide-dioxime (H_3JDO) functional groups capable of binding uranyl ions (UO_2^{2+}). This is the form in which uranium is most commonly found in seawater. Polyacrylonitrile (PAN) fibers are grafted with an H_3JDO group, which is selective for the uranyl ion. The adsorption capacity of such modified polymers can exceed 4 grams of uranium per gram of adsorbent [17]. Although the use of functional AO groups has significantly improved uranium extraction efficiency and is considered the most promising approach for extracting uranium from seawater, implementing these functional AO groups is a complex and expensive process. Furthermore, the effectiveness of these groups is significantly impacted by exposure to other ions. Furthermore, since these adsorbents are primarily available as powders or nanoparticles, their regeneration after uranium extraction is difficult.

Not all known uranium-adsorbing materials can be used in the industrial extraction of uranium from seawater, as they often bind more strongly to vanadium ions (VO^{3+}), the concentration of which in water exceeds the uranium content [18]. In order to comprehend the remarkably strong and selective vanadium binding by polyamidoximes, the authors of this research provided a thorough investigation combining ab initio modeling with thermochemical titration and XAFS spectroscopy. The adsorbent's cyclic imidodioxime group creates a special nonoxide complex called V^{5+}, which has the highest stability constant yet seen for V^{5+} species, even though the open-chain amidoxime functional groups do not bind vanadium. Vanadium is only bound by imidodioximes, according to XAFS data of the adsorbents after they were submerged in seawater. The observed fundamental results, according to the scientists, can help explain the widespread accumulation of vanadium in certain marine animals and offer suggestions for additional optimization of the selectivity of amidoxime-based sorbent materials. This is very expensive because it is necessary to separate the uranium from the vanadium after sorption.

Researchers from the Oak Ridge National Laboratory and the Lawrence Berkeley National Laboratory, led by A. Ivanov and Jan Arnold, turned their attention to siderophores (iron-transport

proteins). This class of chelating compounds with nitrogen and oxygen donor groups, used by some species of bacteria and fungi as reservoirs for sequestering excess iron, is considered a potential ligand for binding *f*-elements, which include uranium [19]. The authors synthesized an artificial siderophore: bis[hydroxy(methyl) amino]-4-mordoline-1,3-triazine (H_2BHT). They then modified the ethylene-acrylic acid copolymer by binding this ligand to it. Despite the relatively low capacity of the material, 0.1 g of uranium per 1 g of sorbent, the vanadium content did not affect uranium sorption, indicating that H_2BHT is more selective for uranium ions than for vanadium ions. Further work in this direction is underway [20–22]. In order to extract uranium from seawater, the authors [20] thoroughly reviewed materials developed between 2000 and 2016. They focused on recent advancements in the field of inorganic materials, polymeric adsorbents, and related research on amidoxime, and nanostructured materials like metal–organic frameworks, porous organic polymers, and mesoporous carbon materials. The difficulties of doing accurate and repeatable uranium adsorption tests were also covered in the article, along with the standardization of parameters required to guarantee accurate comparison of various adsorbents. The history of uranium extraction from saltwater and current research in this field are briefly described in Review [22]. The coordination chemistry of the project is described in full in the paper, along with the functional groups found on common polymer sorbents and their low-molecular-weight analogs. Uranium selectivity in comparison to other metals, especially vanadium, is still difficult to achieve, and future solutions will need techniques for both quantitative evaluation of bond strength and selectivity.

Among the most recent achievements, the works of the authors [23–25] are noteworthy. The scientists have developed a series of new porous materials with specific pores and functional groups (hydroxyl, carboxyl, amidoxime, phosphate, etc.) that are highly selective for uranium. The active groups, when coordinated in these porous materials, form specific sites for binding uranium, which, compared to other ions, have a higher affinity and selectivity for uranyl ions (UO_2^{2+}).

Along with studies of the properties of traditional sorbents, adsorption-photocatalytic and adsorption-electrocatalytic materials are being studied, containing both specific adsorption sites and photocatalytic or electrocatalytic fragments in their frameworks. These innovative strategies enable the conversion of uranyl ions into sorbable solid products (such as UO_2 or $Na_2O(UO_3{\cdot}H_2O)$), which increases the highly efficient extraction of uranium, as well as their resistance to biofouling. The development of such porous materials represents a breakthrough in the field of selective uranium extraction from seawater [23].

Since the efficiency of uranium extraction depends on the presence of active adsorption sites in adsorbents, maximizing the utilization factor of binding sites is necessary to improve the sorption capacity. For this purpose, microredox reactors operating on the principle of Cu(I) Cu(II) conversion are introduced into the sorbent (containing both amidoxime and carboxyl groups), which activates the regeneration of inactivated binding sites. This sorbent has a high adsorption capacity of 962.4 mg-U/gAds, excellent ability to resist fouling, and excellent uranium absorption (14.62 mg-U/gAds) from natural seawater in 56 days. These indicators allow us to consider the sorbent the best among high-performance materials for uranium sorption from seawater [24].

An effective sorbent for uranium extraction from seawater has been synthesized by introducing amidoxime groups (AO) and grafted polyamides (PA) onto the Ti_3C_2 surface using a simple, one-step hydrothermal method. The absorption of $[UO_2(CO_3)_3]_4$ by the Ti_3C_2-AO-PA sorbent is characterized by fast reaction kinetics (approximately 120 min), excellent sorption capacity (81.1 mg/g at pH 8.3), significantly high selectivity (32.8 mg-U/gAds), and excellent antibacterial properties against contamination (92.8 %).

X-ray absorption spectra (XPS) and density functional theory (DFT) computational studies also demonstrated the high extraction capacity of Ti_3C_2-AO-RA for uranium, primarily due to the complexation of AO and NH_2 with $[UO_2(CO_3)_3]^{4-}$. These findings suggest that the Ti_3C_2-AO-RA sorbent is promising for the rapid and selective adsorption of uranium from real seawater [25].

These latest advances demonstrate that uranium extraction from seawater is a promising approach for ensuring a continuous supply of uranium fuel for nuclear power.

The problem of creating efficient inorganic and fibrous sorption materials with sufficient mechanical strength, acceptable kinetics, and high sorption capacity remains relevant. The use of sorption materials is hampered by the lack of a wide range of options, as well as by insufficient understanding of the thermodynamics, kinetics, and mechanism of sorption.

This study aims to investigate the equilibrium sorption of uranium by FORPAN fibrous sorbent (synthesized at the S. M. Kirov St. Petersburg Institute of Textile and Light Industry) from carbonate-containing solutions simulating seawater over a wide range of concentrations ($3.36 \cdot 10^{-5}$ to $7.13 \cdot 10^{-4}$ mol/l) and temperatures (293 to 338 K). The study also includes calculating a generalized thermodynamic equation for uranium sorption by FORPAN fiber under these conditions.

2. Experimental

The studies were conducted using model solutions prepared using natural Caspian Sea water (with a uranium content of $2.5 \cdot 10^{-6}$ mol/l). For analytical control and experimental convenience, uranium-233, previously purified from decay products, was added as a radioactive indicator, along with various amounts of natural uranium in the form of a tricarbonate-uranilate complex to study sorption over wide ranges of temperatures (293–338 K) and concentrations ($3.36 \cdot 10^{-5} \div 7.13 \cdot 10^{-4}$ mol/l). The main requirement for the model solutions is the stability of the concentration and forms of existence of uranium under conditions of carbonate-bicarbonate equilibrium. The technique [26, 27] of preparing solutions with subsequent pH stabilization by bubbling air through the solutions and adjusting the pH with 0.01 M HCl and Na_2CO_3 solutions made it possible to obtain solutions with stable (for at least two years) uranium concentration and pH. The selected pH of the solutions (~ 7.85) corresponded to the pH measurements of seawater. Uranium in the model solutions, as in seawater, was in the ion-soluble form $[UO_2(CO_3)_3]^{4-}$. Radioactive indicator methods, as well as spectrophotometric methods with the Arsenazo-III reagent, were used to determine the uranium content in solutions and sorbent samples. Monitoring of α-radioactivity measurements was carried out using a 2154-1-1M PROTOKA device.

The kinetics of uranium sorption were carried out earlier [1] using the limited volume method on the fibrous sorbent FORPAN with the structural formula of the unit:

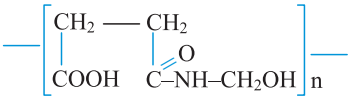

The experiments were carried out in a glass reaction vessel equipped with an electric stirrer and thermostat. At set intervals, at a given temperature (293, 308, 323, or 338 K), 10 ml of a uranium solution of a specified concentration, along with 0.01 g of air-dried fiber, were introduced into the vessel. The start time of the experiment was recorded. At set intervals, 0.025 ml samples of the solution were removed from the reaction vessel and analyzed for uranium content using the α-radiometric method.

Based on the initial concentration of uranium in the solution at each moment in time, the concentration of uranium in the solution at a given time τ ($C_{p,\tau}$), the amount of sorbed uranium in the solid phase ($C_{m,\tau}$) and the value of the distribution coefficient of uranium in the system at a given time ($K_{d,\tau}$) were calculated using the formulas:

$$C_{p,\tau} = C_{p,init} \frac{J_{p,t}}{J_{p,init}}, \quad (1)$$

$$C_{T,\tau} = \frac{C_{p,init} \cdot V}{m} \left(1 - \frac{J_{p,\tau}}{J_{p,init}}\right), \quad (2)$$

$$Kd,\tau = \frac{V}{m} \left(\frac{J_{p,init}}{J_{p,\tau}} - 1\right), \quad (3)$$

where $J_{p,\,init}$ and $J_{p,\tau}$ are the initial and determined α-radioactivity of the solution after a specified time, imp; $C_{p,\text{init}}$ and $C_{p,\tau}$ are the initial uranium concentration and the concentration at a specified time in the solution, mol/l; V is the volume of the solution, ml; m is the mass of the sorbent, g.

All kinetic dependences were satisfactorily described by the generalized Avrami-Erofeev-Kolmogorov kinetic equation using the Sakovich relation [1]. The equation parameters were processed using the least squares method.

Important information about sorption processes can be obtained by studying the thermodynamics of sorption of a given substance based on the temperature dependences of equilibrium distribution coefficients or sorption isotherms at different temperatures. Based on experimental data, uranium sorption by FORPAN fiber changed insignificantly over time upon reaching equilibrium between the "top" and "bottom" phases over a period of $1.4 \cdot 10^4$ s. This allowed the distribution coefficients (K_d) presented in Table 1 to be considered equilibrium, and the values of C_p and C_T were assumed to be equilibrium and designated $C_{p,\infty}$ and $C_{T,\infty}$, respectively.

Below in Fig. 1, based on the experimental results of Table 1, the dependences of the equilibrium distribution coefficients of uranium ($K_{d,\infty}$, ml/g) on the equilibrium concentration of uranium in solution ($C_{p,\infty}$, mol/ml) at various temperatures are shown. By extrapolating these dependences to any given equilibrium concentration of uranium in solution, an equation of the form can be obtained for each of them:

$$\ln K_{d,\infty} = a + b \ln C_{p,\infty}, \quad (4)$$

where $K_{d,\infty}$ is the equilibrium distribution coefficient of uranium in the system, ml/g, parameters a and b are constant values for a given pH value of the initial solution, calculated by mathematical processing using the least squares method (given in Table 2).

Uranium in seawater is dissolved as a stable tricarbonate-uranilate complex at pH > 7.5, with a carbonate ion content greater than $n \cdot 10^{-6}$ M. At carbonate ion content less than $n \cdot 10^{-6}$ M and pH < 7.5, it dissociates due to the formation of high concentrations of bicarbonate ions in solution, which do not interact with uranium.

The content of HCO_3 groups was determined using Reznikov's method, modified for the conditions of our experiment [28], the results of which are presented in Table 3.

The calculation of the entropy and enthalpy values of the uranium sorption process on the FORPAN fiber under study was carried out from the experimental results of the dependence of the equilibrium distribution coefficient of uranium on

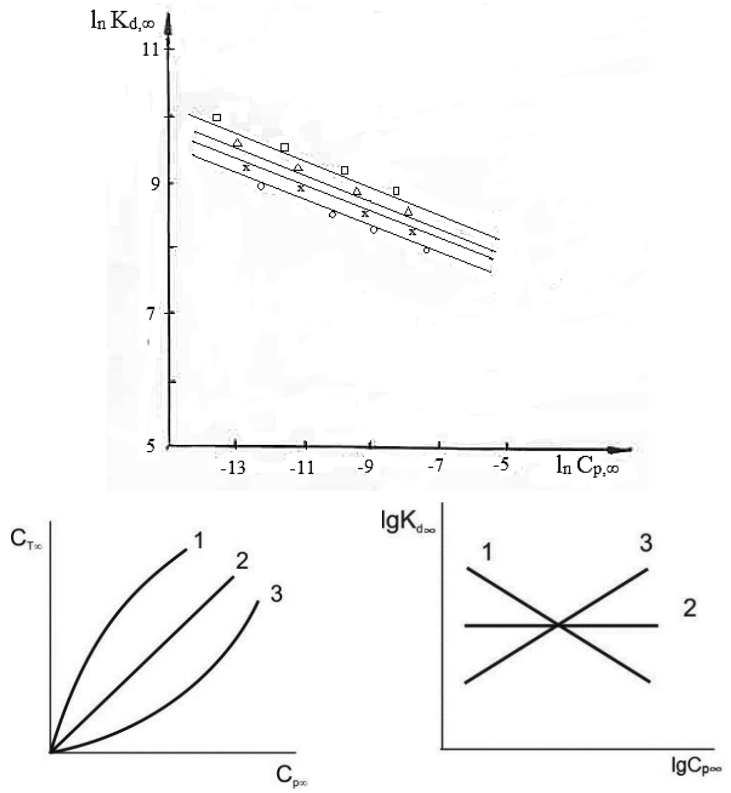

Fig. 1. Uranium sorption isotherm as a function of the equilibrium distribution coefficients ($K_{d,\infty}$) ml/g versus the equilibrium uranium concentration in solution ($C_{p,\infty}$, mol/l) using FORPAN fiber: *1* – 293 K; *2* – 308 K; *3* – 323 K; *4* – 338 K

Table 1. U^{233} sorption from model solutions with $C_{s.init.}$ = ($3.36\cdot10^{-5}$ – $7.13\cdot10^{-4}$) mol/l polyampholyte

Sorbent, structural formula of the unit, active groups	Brief characteristics of the sorbent, SEC, mol/g	Initial concentration of the solution, $C_{s.init}$ mol/l	$K_{d\infty}$, ml/g				Equilibrium time, $t_{\infty,C}$
			Temperature, K				
			293	308	232	338	
FORPAN O ‖ COOH–C– | $NHCH_2OH$ O ‖ COOH, C–NH	Obtained by synthesis of carboxylated PAN fiber with formaldehyde, COE_{NaOH} = 2.0	$3.36\cdot10^{-5}$ $1.15\cdot10^{-4}$ $2.7\cdot10^{-4}$ $7.13\cdot10^{-4}$	6670 4496 2165 1232	11195 7336 3544 1881	21764 13068 4124 2342	32260 16224 8773 3149	$1.4\cdot10^{4}$

Table 2. Parameters of the equation $\ln K_{d,\infty} = a + b\ln C_{p,\infty}$ (4) for four concentrations at a given temperature. Capacities (mol/g) calculated with the generalized parameters of equation (6)

Fiber	T, K	$\ln K_{d,\infty}$, mol/g	$\ln C_{p,\infty}$, mol/l	pH $C_{p,\infty}$	Parameters of equation (4)		The value of capacity according to the equation (6)	
					a	b	$\ln C_{B,\infty}$	mol/g
FORPAN	293	8.79	−12.13	5.1	3.72	−0.42	−10.87	$1.9\cdot10^{-5}$
		8.4	−10.77	7.22			−10.07	$4.2\cdot10^{-5}$
		7.68	−9.36	7.32			−9.25	$9.6\cdot10^{-5}$
		7.12	−8.05	7.42			−8.49	$2.1\cdot10^{-4}$
	308	9.3	−12.8	5	4.14	−0.41	−11.14	$1.45\cdot10^{-5}$
		8.97	−11.19	7.7			−10.23	$3.2\cdot10^{-5}$
		8.17	−9.95	7.8			−9.52	$7.3\cdot10^{-5}$
		7.54	−8.31	8.22			−8.60	$1.8\cdot10^{-4}$
	323	9.99	−13.43	5.1	3.64	−0.47	−11.38	$1.1\cdot10^{-5}$
		9.48	−11.71	7.7			−10.43	$2.9\cdot10^{-5}$
		8.34	−10.75	7.45			−9.90	$4.2\cdot10^{-5}$
		7.76	−8.45	7.85			−8.60	$1.8\cdot10^{-4}$
	338	10.38	−13.80	4.9	4.03	−0.45	−11.47	$1.0\cdot10^{-5}$
		9.69	−9.77	7.3			−9.29	$91\cdot10^{-5}$
		9.08	−8.48	7.7			−8.59	$1.8\cdot10^{-4}$
		8.05	−8.79	8.32			−8.44	$2.1\cdot10^{-4}$
The average values of the parameters $\bar{a}$ and $\bar{b}$ of the equation (4) a = (3.88±0.3); b = −0.43.±0.038								

Table 3. Uranium sorption from model carbonate-containing solutions on FORPAN fiber at T =293.15 K. Results of determination of bicarbonate ion and uranium content in solutions and sorbents

Initial concentration of uranium in solutions, mol/l	$3.36\cdot10^{-5}$	$1.15\cdot10^{-4}$	$7.13\cdot10^{-4}$
pH of the initial solution	7.85	7.87	7.89
The concentration of uranium in the equilibrium solution after sorption, mol/l	$4.4\cdot10^{-6}$	$2.09\cdot10^{-5}$	$3.21\cdot10^{-4}$
Concentration of uranium in the sorbent, mol/g	$2.92\cdot10^{-5}$	$9.41\cdot10^{-5}$	$3.95\cdot10^{-4}$
pH of the equilibrium solution	5.1	7.2	7.38
Concentration of HCO_3^- ion in the initial solution, mol/l	$1.04\cdot10^{-3}$	$5.25\cdot10^{-3}$	$3.01\cdot10^{-2}$
Concentration of HCO_3^- ion in solution after sorption, mol/l	$1.96\cdot10^{-3}$	$6.41\cdot10^{-3}$	$4.16\cdot10^{-2}$

temperature. These dependences were obtained for various initial uranium concentrations in solutions with a pH of 7.85 and are shown in Figure 2.

3. Results and discussion

The dependence $\ln Kd_{\infty} \rightarrow \ln C_{p,\infty}$ presented in Fig. 1 is similar to [29] the accepted representation of an isotherm of the $C_{T,\infty} \rightarrow C_{p,\infty}$ type, which can be successfully replaced by a representation in logarithmic coordinates, which makes it possible to easily, using extrapolation, estimate the capacity of the sorbent at any equilibrium concentration of the element in the solution for any form of sorption isotherm.

The calculated values of the uranium sorption isotherm parameters from model solutions are presented in Table 2.

By further mathematical processing of the values of the parameters *a* and *b* of equation (4) from temperature ($a \rightarrow \frac{1}{T}$ and $b \rightarrow \frac{1}{T}$), a generalized equation was derived that made it possible to calculate the equilibrium distribution coefficient K_d (ml/g) associated with temperature and the equilibrium concentration of the solution (mol/l), as well as the capacity of the fiber for uranium (mol/g) during its sorption from model solutions of seawater with pH 7.85–7.9 in a wide range of equilibrium concentrations of uranium in the solution (1.0 10^{-4}–1.0 10^{-9} mol/l) and temperatures (293–338 K):

$$\ln K_d = (5,271 - 0,72 \ln C_{p,\infty}) - \\ -(437,68 - 89,52 \ln C_{p,\infty}) / T. \quad (5)$$

Based on equation (5), we can write:

$$\ln C_{T,\infty} = (-5,271 + 0,28 \ln C_{p,\infty}) + \\ +(437,68 + 89,52 \ln C_{p,\infty}) / T. \quad (6)$$

Substituting into equation (6) the value of the uranium concentration in the water of the Caspian Sea, $2.5 \cdot 10^{-6}$ mol/l, we obtain the value of the capacity for seawater ($C_{T,S.W}$):

$$\ln C_{P,\ S.W} = -12.89$$

$$C_{T,\ S.W} = 1,22 \cdot 10^{-5} \text{ mol/ g} = 2,9 \cdot 10^{-3} \text{ l/ g} \quad (7)$$

Uranium sorption from natural waters and carbonate systems actively occurs with the participation of both anion exchangers and cation exchangers. However, under the same conditions, the absorption of uranium by cation exchangers is explained by the authors [30] by the fact that the presence of an ion exchanger shifts the equilibrium between the carbonate complex and the products of uranyl ion hydrolysis. It is necessary to take into account the participation of the HCO^{3-} ion in the carbonate equilibria system, which are interconnected with the pH of the solution, and determine the binding of uranium

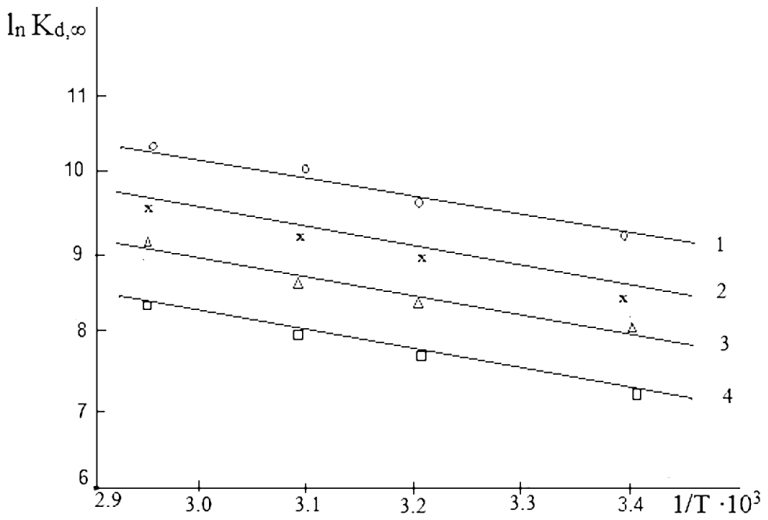

Fig. 2. Temperature dependences of the equilibrium distribution coefficient for uranium sorption using FORPAN fiber at different initial uranium concentrations in solution: $3.36 \cdot 10^{-5}$ M; *2* – $1.15 \cdot 10^{-4}$ M; *3* – $2.73 \cdot 10^{-4}$ M; *4* – $7.14 \cdot 10^{-4}$ M

into uranyl carbonate complexes according to the reactions:

$$HCO_3^- \leftrightarrow H^+ + CO_3^{2-},\ K = 4 \cdot 10^{11}$$

$$UO_2^{2+} + 2CO_3^{2-} \leftrightarrow \left[UO_2\left(CO_3\right)_2\right]^{2-},\ K = 10^{16}$$

$$\left[UO_2\left(CO_3\right)_2\right]^{2-} + CO_3^{2-} \leftrightarrow \left[UO_2(CO_3)_3\right]^{4-},\ K = 10^7$$

A comparison of the equilibrium constants for these reactions shows that, in the region of near-neutral and alkaline pH values, even a slight excess of carbonates above stoichiometric values is sufficient for the virtually complete binding of uranium into uranyl carbonate anions [31].

The carboxyl groups of FORPAN fiber, being acidic in nature and subject to the mechanism of carboxyl cation dissociation [32], partially or completely dissociate depending on the pH of the solution and are responsible for the sorption of uranium as a result of ion exchange. The amino groups are the basic groups, responsible for the formation of coordination bonds during sorption in a slightly acidic medium with a pH of 3–5. Taking this into account, the appearance of a negative charge in alkaline media and a positive charge in acidic media for FORPAN fiber can be represented by the following reaction equations:

$$R^{-COOH}_{-NH_2} + OH^- \rightarrow R^{-COO^-}_{-NH_3OH} \quad (a)$$

$$R^{-COO^-}_{-NH_3^+} + H^+ \rightarrow R^{-COOH}_{-NH_3^+} \quad (b)$$

At the initial moment of contact of the fiber with a carbonate-containing solution with a pH of 7.85, the fiber is charged negatively due to the protolysis of the carboxyl group according to reaction (a), which results in a decrease in the pH of the solution and the cleavage of the tricarbonate uranilate complex. In this case, the ion-exchange activity of the COOH groups is evident, and in solutions with neutral and slightly alkaline pH, the formation of stable carboxyl complexes of uranium is possible. In more acidic environments, carboxyl groups are protonated and are unable to form strong bonds with uranium, while in an alkaline environment, uranium can form complex compounds, including hydroxide complexes $UO_2(OH)_2$ and $UO_2(OH)_3$, which can compete with carboxyl complexes. As a result of the shift of the pH environment to the region of low pH values (~ 5–5.5), the process begins to proceed according to reaction (b), during which two types of bonding of the ligand groups of the fiber (ionic and coordination) occur, since in an acidic environment the amino group protonates and acquires a positive charge, turning into an ammonium ion ($-NH_3^+$), capable of participating in complex formation, however, in an alkaline environment it loses a proton and becomes neutral, which inhibits the further process of complex formation, or desorption of the complex may occur, which is reflected in the shift in the equilibrium between the forms of existence of uranium in the presence of fiber [33].

The experimental data obtained show that during the period of contact between the solution and deprotonated fiber from weakly alkaline and acidic solutions, sorption is characterized by high distribution coefficients (Table 1), which can be attributed to an increase in the HCO_3^- content in the solution. The observed increase in the solution concentration and pH, as well as a decrease in uranium sorption (reaching equilibrium), confirm the lack of correlation between uranium and carbonate ions in the fiber. As the uranium concentration and solution pH increase, the process proceeds with an increase in the ion-exchange mechanism.

A similar phenomenon in the sorption process was also discovered in [34] during a study of uranium(VI) sorption on goethite using X-ray absorption spectra (EXAFS), where in the presence of carbonate ions in the solution, an increase in uranium sorption was detected at low pH with the formation of complexes: $(>FeOH)_2UO_2(H_2O)$; $FeOCO_2UO_2$ and $(>FeOH)_2UO_2CO_3$, which were desorbed with an increase in the pH of the solution and were not recorded by the EXAFS spectra. Taking these complexes into account, the authors developed a thermodynamic model of surface complexation on goethite, corresponding to their experimental data on uranium sorption from aqueous solutions.

To study the thermodynamics of the process of uranium sorption from carbonate-containing solutions simulating seawater, the equation was first processed:

$$\ln K_d = A - B\frac{1}{T} \quad (8)$$

using the least squares method for various initial concentrations $3.36 \cdot 10^{-5} \div 7.13 \cdot 10^{-4}$ mol/l in the form of a dependence of $\ln K_d - \frac{1}{T}$ on each temperature (293, 308, 323, 338 K). By further processing the parameters A and B from the initial concentration in the form $(A - \ln C_{p,init})$ $(B - \ln C_{p,init})$, where $A = A' + B'$ $[A = (-1.17) + (-2.17)]$ and $B = A'' + B''$ $[B = 1276.7 + 472]$, generalized values of the parameters were obtained for any initial concentration:

$$A = A' + A'' \ln C_{p,init}, \quad (9)$$

$$B = B' + B'' \ln C_{p,init}. \quad (10)$$

As a result of mathematical processing of the entire set of obtained dependencies, a generalized semi-empirical thermodynamic equation was derived that relates the equilibrium distribution coefficient of uranium in the system ($K_{d,\infty}$), the initial concentration, and the temperature of the sorption experiment in the form:

$$\ln K_d = A' + A'' \ln C_{p,init} - \frac{B' + B'' \ln C_{p,init}}{T}. \quad (11)$$

Substituting the calculated values of the parameters into equation (11), $A' + A'' \ln C_{p,init} = (-1.17) + (-1276.7) \ln C_{p,init}$ and $B' + B'' \ln C_{p,init} = (2.17) + 472 \ln C_{p,init}$ a generalized equation of thermodynamics for the process of uranium sorption from model solutions of seawater in a wide range of initial uranium concentrations $3.36 \cdot 10^{-5} - 7.13 \cdot 10^{-4}$ mol/l and temperatures (293–308 K) at pH 7.85 for FORPAN fiber was obtained:

$$\ln Kd = (-1.17) + (-1276.7 \cdot \ln C_{p,init}) - \\ -(2.17 + 472 \cdot \ln C_{p,init}) / T. \quad (12)$$

The value of the uranium distribution coefficient in the water of the Caspian Sea ($K_{d,S.W}$) with a concentration of $2.5 \cdot 10^{-6}$ mol/l ($\ln C_{p,S.W} = -12.89$) at T = 293.3 K, calculated using equation (12), is equal to $\ln Kd_{S.W} = 9.7$ $K_{dS.W} = 1.6 \cdot 10^4$ mol/l.

The values of the parameters $A = A' + A'' \ln C_{p,init}$ and $B = B' + B'' \ln C_{p,init}$ of equation (12) correspond to the parameters of the known relationship:

$$\ln K_d = \frac{\Delta S}{R} - \frac{\Delta H}{RT}, \quad (13)$$

Where K_d is the equilibrium distribution coefficient of uranium in the system, ml/g; ΔS is the entropy of the uranium sorption reaction, J/mol deg; ΔH is the enthalpy of the uranium sorption reaction, J/mol; R is the universal gas constant, equal to 8.3143 J/mol deg; T is the experimental temperature, K.

The following formula was used to calculate the change in Gibbs free energy:

$$\Delta G = \Delta H - T\Delta S. \quad (14)$$

As can be seen from Table 4, the enthalpy value $\Delta H < 0$ is negative, i.e., the process is exothermic, with heat release. The heat of reaction for uranium sorption by the fiber under study is estimated to be in the range −28 ÷ −40 kJ/mol. These values are significantly lower than the heat of chemisorption reactions (50÷80 kJ/mol) and are close to the enthalpies characteristic of ion-exchange reactions, i.e., the process of uranium sorption from carbonate-containing solutions by FORPAN fiber proceeds via an ion exchange mechanism, along with complexation.

4. Conclusions

Based on a study of the fundamental principles of equilibrium uranium sorption by the fiber, it was established that the experimentally determined uranium distribution coefficients in the temperature range of 293–338 K are in equilibrium. It was found that during the period of fiber contact with a carbonate-containing uranium solution, the pH of the solution sharply decreases to 7.86, and the tricarbonate uranilate complex decomposes due to protolysis of carboxyl groups. This period is characterized by high uranium distribution coefficients and an increase in HCO^{3-} in the solution, confirming the lack of correlation between uranium and carbonate ions in the fiber.

The capacity of the fiber for uranium (mol/g) was calculated during its sorption from model solutions prepared based on Caspian Sea water in the range of studied concentrations and temperatures, and the capacity of the FORPAN sorbent relative to uranium in Caspian Sea water ($1.22 \cdot 10^{-5}$ mol/g = 2.9 10^{-3} g/g) and $K_{d,S.W}$ = $1.6 \cdot 10^4$ ml/g at T = 293.3 K was also calculated.

Table 4. Parameters of equation (8) for different initial concentrations of model solutions and the values of enthalpy, entropy and Gibbs free energy of the uranium sorption reaction on FORPAN fiber (T = 298.16 K), calculated based on the generalized parameters $A = A' + A''\ln C_{p,init}$; $B = B' + B''\ln C_{p,init}$

$C_{p,init}$ mol/l	$\ln C_{p,init}$	$A = A' + B'\ln C_{p,init}$	$B = A'' + B''\ln C_{p,init}$	$A_{gener.} = A' + A''\ln C_{p,init}$	$B_{gener} = B' + B''\ln C_{p,init}$	ΔS J/mol·degree	ΔH J/mol	ΔG кJ/mol
$3.36\cdot10^{-5}$	−10.3	20.907	−3584	13148	−4859	109.32	−40400	−72.998
$1.15\cdot10^{-4}$	−9.1	18.609	−2887	11610	−4293	96.535	−35694	−64.477
$2.73\cdot10^{-4}$	−8.2	17.350	−2843	10462	−3868	87.015	−32162	−58.1
$7.13\cdot10^{-4}$	−7.2	14.009	−2013	9237	−3415	76.801	−28394	−51.292

A generalized semiempirical thermodynamic equation for uranium sorption by the fiber under study was obtained. It relates the equilibrium distribution coefficient of uranium in the system, the initial concentration, and the temperature of the sorption experiment under given conditions. The parameters of this equation made it possible to calculate the entropy, enthalpy, and Gibbs energy of uranium sorption by FORPAN fiber. The enthalpy values ($\Delta H < 0$) are negative, indicating an exothermic process with the release of heat. The heat of reaction for uranium sorption by the fiber under study is estimated at values in the range of −28 ÷ −40 kJ/mol. These values turned out to be significantly lower than those for chemisorption processes, i.e., they are more consistent with ion-exchange processes, along with which complex formation also occurs.

Based on the conducted studies of the features of equilibrium sorption of uranium from model carbonate-containing solutions and the results obtained, FORPAN fiber can be recommended for the purpose of extracting uranium from dilute carbonate-containing solutions of natural waters, in particular, from the water of the Caspian Sea, with a uranium content of $2.5\cdot10^{-6}$ mol/l, in the range of relatively low temperatures of 293–308 K.

Author contributions

M. A. Rahimli – concept, writing, and scientific editing of the article; S. R. Mamedova – research and participation in literature analysis, and preparation of figures and tables.

Conflict of interests

The authors declare that they have no known competing financial interests or personal relationships that could have influenced the work reported in this paper.

References

1. Ragimli M. A., Nuriyev A. N. Sorption of uranium from carbonate solutions carboxylated fibrous sorbents. *Condensed Matter and Interphases*. 2013;15(4): 438–445. Available at: https://elibrary.ru/item.asp?id=20931239

2. Wang F., Liu Q., Li R., ... Wang J. Selective adsorption of uranium (VI) onto prismatic sulfides from aqueous solution. *Colloids and Surfaces A: Physicochemical and Engineering Aspects*. 2016;490: 215–221. https://doi.org/10.1016/j.colsurfa.2015.11.045

3. Perlova O. V., Tekmenzhi E. I., Perlova N. A., Polikarpov A. P. Recovery and concentration of uranium(VI) compounds from nitrate solutions by FIBAN fibrous ion exchangers under dynamic conditions. *Voprosy khimii I khimicheskoi tekhnologii*. 2019;5: 104–111. https://doi.org/10.32434/0321-4095-2019-126-5-104-111

4. Zidan W. I., Abo-Aly M. M., Elhefnawy O. A., Bakier E. Batch and column studies on uranium adsorpsion by Amberlite XAD-4 modified with nano-manganese dioxide. *Journal of Radioanalytical and Nuclear Chemistry*. 2015;304(2): 645–653. https://doi.org/10.1007/s10967-014-3833-3

5. Dzyazko Yu. S., Perlova O. V., Perlova N. A., ... Palchik A. V. Composite cation-exchange resins containing zirconium hidrophosphate for purification of water from U (VI) cations. *Desalination and Water Treatment* 2017;69: 142–152. https://doi.org/10.5004/dwt.2017.0686

6. Perlova O., Dzyazko Y., Halutska I., Perlova N., Palchik A. Anion exchange resin modified with nanoparticles of hydrated zirconium dioxide for sorption of soluble U (VI) compounds. *Springer Proceedings in Physics* 2018;210: 3–15. https://doi.org/10.1007/978-3-319-91083-3_1

7. Soldatov V. S., Zelenkovskii V. M., Orlovskaya L. A. Sorption of bivalent ions by a fibrous chelating ion exchanger and the structure of sorption complexes. *Reactive and Functional Polymers*. 2011;71(1): 49–61. https://doi.org/10.1016/j.reactfunctpolym.2010.11.003

8. Myasoedov B. F., Nuriyev A. N., Novikov Yu. P., ... Malykh T. G. Investigation of uranium sorption from carbonate-containing solutions by inorganic sorbents. VII. Thermodynamics of uranium sorption on titanium-containing sorbents with disordered structure*. *Radiochemistry*. 1984; 26(3): 285–288. (in Russ.)

9. Nuriyev A. N., Akperov G. A., Mamedov R. M., Dzhabbarova Z. A., Rahimli M. A., Efendieva Sh. Z. Investigation of uranium sorption from carbonate-containing solutions by inorganic sorbents. Kinetics and thermodynamics of uranium sorption on titanium-tin and titanium-manganese-containing sorbents*. *Radiochemistry*. 1998;40: 256–258 (in Russ.)

10. Nuriyev A. N., Rahimli M. A. The influence of mechanical processing on the structure and sorption properties of titanium containing a sorbent in the sorption of uranium from solutions modeling compositions of seawater. *Condensed Matter and Interphases*. 2017;19(13): 400–407. (in Russ.). https://doi.org/10.17308/kcmf.2017.19/217

11. Smirnova V. V. Effect of the structure, properties and surface treatment for titanium dioxide sorption activity. *Modern Problems of Science and Education*. 2012;5: 1–7. (inRuss.). Available at: https://elibrary.ru/item.asp?id=18318988

12. Smirnova V. V., Ilyin A. P. Influence of constant electric field on dioxide titanium sorption properties. *Fundamental Research*. 2013;6-6: 1366–1371. (in Rus.). Available at: https://fundamental-research.ru/ru/article/view?id=31742

13. Myasoedova G. V., Nikashina V. A. Sorption materials for radionuclide extraction from waters. *Rossiiskii khimicheskii zhurnal*. 2006;1(5): 55. Available at: https://elibrary.ru/item.asp?id=9316663

14. Kosandrovich E. G., Soldatov V. S. Fibrous ion exchangers. In: *Ion exchange technology I: theory and materials*. Inamuddin and M. Luqman (eds.). Dordrecht, Heidelberg, New York, London: Springer Science business Media. 2012. 199–271. https://doi.org/10.1007/978-94-007-1700-8_9

15. Perlova O. V., Sazonova V. F., Perlova N. A., Polikarpov A. P. Sorption of uranium (VI) compounds by fibrous cation exchanger Fıban K-1 from acidic media. *Voda: khimiya i ekologiya*. 2016;3: 53–59. (in Russ.). Available at: https://elibrary.ru/item.asp?id=26696988

16. Sazonova V. F., Perlova O. V., Perlova N. A., Polikarpov A. P. Sorption of uranium (VI) kompounds on fibrous anion exchanger surface from aqueous solutions. *Colloid Journal*. 2017;79(2): 270–277. https://doi.org/10.1134/S1061933X17020132

17. Sun Q., Aguila B, Perman J., ... Ma S. Bio – inspired nano- traps for uranium extraction from seawater and recovery from nuclear waste. *Nature Communications*. 2018;9: 1644. https://doi.org/10.1038/s41467-018-04032-y

18. Ivanov A. I., Leggett C. J., Parker B. F., ...Rao L. Origin of the unusually strong and selective binding of vanadium by polyamidoximes in seawater. *Nature Communications*. 2017; 8: 1560. https://doi.org/10.1038/s41467-017-01443-1

19. Mullen L., Gong C., Czerwinski K. Complexation of uranium (VI) with the siderophore desferrioxamine B. *Journal of Radioanalytical and Nuclear Chemistry*. 2017;273: 683–688. https://doi.org/10.1007/s10967-007-0931-5

20. Abney C. W., Mayes R. T., Saito T., Dai S. Materials for the recovery of uranium from seawater. *Chemical Review*. 2017;117: 13935. https://doi.org/10.1021/acs.chemrev.7b00355

21. Hadjithoma S., Papanikolaou M. G., Leontidis E., Kabanos T. A., Keramidas A. D. Bis (hydroxylamino)triazines: high selectivity and hydrolytic stability of hidroxylamine-based ligands for uranyl compared to vanadium (V) and iron (III). *Inorganic Chemistry*. 2018;57: 7631. https://doi.org/10.1021/acs.inorgchem.8b00582

22. Parker B. F., Zhang Z., Rao, L., Arnold J. An overview and recent progress in the chemistry of uranium extraction from seawater. *Dalton. Transactions*. 2018; 47: 639. https://doi.org/10.1039/C7DT04058J

23. Hao M., Xie Y., Chen Z., ... Wang X. Promising porous materials for uranium extraction from seawater. *Fundamental Research*. 2026;6(1): 170–172. https://doi.org/10.1016/j.fmre.2024.03.004

24. Zhang Y., Wang Y., Dong Z., ... Liu Y. Boosting uranium extraction from Seawater by microredox reactors anchored in a seaweed-like adsorbent. *Nature Communications*. 2024;15: 9124. https://doi.org/10.1038/s41467-024-53366-3

25. Zhang D., Liu L., Zhao B., Wang X., Pang H., Yu S. Highly efficient extraction of uranium from seawater by polyamide and amidoxime cofunctionalized MXene. *Environmental Pollution*. 2023;15: 120826. https://doi.org/10.1016/j.envpol.2022.120826

26. Nekrasova N.A., Kudryavtseva S.P., Milyutin V.V., Chuveleva E.A., Firsova L.A., Gelis V.M. Sorption of uranium from nitric acid solutions on various ion exchangers. *Radiochemistry*. 1984;50(2): 183–185. https://doi.org/10.1134/s1066362208020173

27. Rahimli M. A., Nuriyev A. N., Efendieva Sh. Z., et al. Effect of temperature on the composition and properties of fibrous sorbents PAN-PEI-FF and FORPAN before and after uranium sorption from carbonate-containing solutions*. *Azerbaijan Chemical Journal*. 2011;1: 23.

28. Laptev F. F. *Water analysis**. Moscow: Gostgeoltekhizdat Publ.; 1985. 42 p. (in Russ.)

29. Yang L., Li Y., Chen D., ... Tang J. Efficient cooperative extraction uranium(VI) from aqueous solution and seawater by a novel phosphate/amidoxime chitosan-based adsorbent. *Journal of Water Process Engineering*. 2024;61: 105197 https://doi.org/10.1016/j.jwpe.2024.105197

30. Guidez J., Gabriel S. Extraction of uranium from seawater: a few facts. *EPJ N - Nuclear Sciences & Technologies*, 2016;2: 10. https://doi.org/10.1051/epjn/e2016-50059-2

31. Shi S., Liu J., Shu J., ... Lan T. Uranium(VI) adsorption from carbonate solutions using cetyltrimethylammonium bromide modified purified-bentonite-MOF composite. *Applied Clay Science*. 2023;241: 106986. https://doi.org/10.1016/j.clay.2023.106986

32. Khokhlov V. Yu., Selemenev V. F., Zagorodniy A. A., Moiseeva I. V. The mechanism of dissociation of carboxyl cations*. *Russian Journal of Physical Chemistry*. 1995;69(12): 2138–2141. (in Russ.). Available at: https://elibrary.ru/item.asp?id=23630562

33. Kersten B., Akolkar R., Duval C. E. An electrochemical technique for sensing uranium adsorption and desorption. *Analytica Chimica Acta*. 2023; 1284: 342003. https://doi.org/10.1016/j.aca.2023.342003

34. Herman D. M., Peacock C. L., Hubbard G. Ch. Surface complexation of U(VI) on goethite (α-FeOOH). *Geochimica et Cosmochimica Acta*. 2008;72: 298–310. https://doi.org/10.1016/j.gca.2007.10.023

** Translated by author of the article*

Information about the authors

Manzar Ah. Rahimli, PhD, Associate Professor, Leading Researcher, Institute of Catalysis and Inorganic Chemistry (Baku, Azerbaijan).

https://orcid.org/0009-0004-8621-214X
manzar.rahimli@mail.ru

Sevinj R. Mamedova, PhD, Associate Professor, Senior Researcher, Institute of Catalysis and Inorganic Chemistry (Baku, Azerbaijan).

https://orcid.org/0009-0006-9608-8976
edu.office@kqki.science.az

Received April 28, 2025; approved after reviewing December 12, 2025; accepted for publication December 15, 2025; published online April 01, 2026.

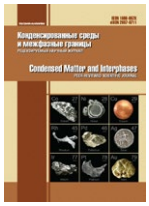

ISSN 1606-867X (Print)
ISSN 2687-0711 (Online)
Condensed Matter and Interphases
Kondensirovannye Sredy i Mezhfaznye Granitsy
https://journals.vsu.ru/kcmf/

Original articles

Research article
https://doi.org/10.17308/kcmf.2026.28/13563

Stability against crystallization and optical properties of $(Ga_{10}Ge_{15}Te_{75})_{100-x}(AgI)_x$ (x = 0–15 mol %) glasses

E. A. Tyurina[1], A. P. Velmuzhov[1]✉, M. V. Sukhanov[1], A. D. Plekhovich[1], D. G. Fukina[2], V. S. Shiryaev[1]

[1]G. G. Devyatykh Institute of Chemistry of High-Purity Substances of the Russian Academy of Sciences, 49, Tropinin st., Nizhny Novgorod 603951, Russian Federation

[2]Lobachevsky State University of Nizhny Novgorod, 23, Gagarin aven., Nizhny Novgorod 603950, Russian Federation

Abstract

Objectives: Germanium telluride based glasses, due to their wide transparency range and high refractive index, are promising optical materials for the middle infrared range. The tendency of such glasses to crystallize, which limits their practical application, requires the search for new compositions and the study of their properties. The aim of this work was to investigate the stability against crystallization and optical transparency of $(Ga_{10}Ge_{15}Te_{75})_{100-x}(AgI)_x$ (x = 0–15 mol %) glasses as new materials for fiber optics.

Experimental: The glasses were analyzed using differential scanning calorimetry, scanning electron microscopy combined with X-ray spectral microanalysis, and near- and mid-infrared spectroscopy. The main goal of the work is the establishment of high stability against crystallization of the studied glasses with a silver iodide content of 5–15 mol %.

Conclusions: This makes it possible to consider such glasses as one of the most promising materials for the production of fibers with low optical losses in the spectral range of 4–15 μm.

Keywords: Chalcogenide glass, Germanium telluride, Silver iodide, Crystallization, Middle infrared materials, Optical transmittance

Funding: The work was financially supported by the Russian Science Foundation (Project No. 25-13-20046, Russia), https://rscf.ru/project/25-13-20046/.

For citation: Tyurina E. A., Velmuzhov A. P., Sukhanov M. V., Plekhovich A. D., Fukina D. G. Stability against crystallization and optical properties of $(Ga_{10}Ge_{15}Te_{75})_{100-x}(AgI)_x$ (x = 0–15 mol %) glasses. *Condensed Matter and Interphases*. 2026;28(1): 115–125. https://doi.org/10.17308/kcmf.2026.28/13563

Для цитирования: Тюрина Е. А., Вельмужов А. П., Суханов М. В., Плехович А. Д., Фукина Д. Г. Кристаллизационная устойчивость и оптические свойства стекол системы $(Ga_{10}Ge_{15}Te_{75})_{100-x}(AgI)_x$ (x = 0–15 мол. %). *Конденсированные среды и межфазные границы*. 2026;28(1): 115–125. https://doi.org/10.17308/kcmf.2026.28/13563

✉ Aleksandr P. Velmuzhov, e-mail: velmuzhov.ichps@mail.ru

1. Introduction

Glasses based on the Ge – Te system are among the most promising optical materials for the middle infrared (mid-IR) range [1]. They have a wide transparency window extending from 2 to 30 μm (some compositions up to 35 μm [2]) and high refractive index values [3]. Optical fibers made of glasses based on the Ge–Te system are transparent up to 16 μm [4]. Therefore, these materials are used for the production of fiber-optic sensors [4, 5], transmission of CO_2 laser radiation with operating wavelengths of 9.3 and 10.6 μm [6], and for solving problems related to space exploration [7, 8].

The main disadvantage of glasses based on the Ge–Te binary system is a pronounced tendency to crystallization [9]. To increase their stability against crystallization, components promoting glass formation are added to their composition. The most suitable of these components is silver iodide. To date, glasses of the Ge – Te – AgI system are the only representatives of germanium telluride glassy materials that do not crystallize upon heating during analysis by differential scanning calorimetry at a heating rate of 10 K/min [10, 11]. The crystallization stability of these materials allows them to be used to manufacture optical fibers. However, optical losses in these fibers are high compared to Ge–S and Ge–Se systems [12]. One of the main reasons for this is partial crystallization of samples during fiber drawing [4]. Recently, the authors of the work fabricated a $(Ge_{21}Te_{79})_{50}(AgI)_{50}$ glass fiber with optical losses of less than 1 dB/m in the spectral range of 7.2–10.9 μm, which is a record among telluride systems [13]. One of the key areas for further reduction of optical losses in germanium telluride fibers is optimization of the chemical composition of the glass. In this regard, the study of novel glasses based on the Ge–Te–AgI system is an actual scientific task.

The aim of this work was to investigate the stability against crystallization and optical transparency of glasses of the $(Ga_{10}Ge_{15}Te_{75})_{100-x}(AgI)_x$ (x = 0–15 mol %) system as new materials for fiber optics. The choice of the system was due to the higher glass-forming ability of Ga – Ge – Te glasses compared to binary Ge – Te compositions. Within the Ga – Ge – Te system, one of the most stable against crystallization is the $Ga_{10}Ge_{15}Te_{75}$ composition [14], which was chosen as the base variant. There is only one publication in the literature on the study of the properties of glasses of the $(Ga_{10}Ge_{15}Te_{75})_{100-x}(AgI)_x$ system, the results of which indicate an unexpectedly low stability against crystallization [15], which, in the authors' opinion, requires clarification.

2. Experimental

2.1. Glass preparation

To avoid any misunderstandings in the chemical composition of telluride glasses containing silver iodide, available in the literature (e.g., [2] and [16]), the equations used to specify the component ratios are given below:

$$y(\mathrm{Ga}) = 0.1 \times (100 - 2x), \quad (1)$$

$$y(\mathrm{Ge}) = 0.15 \times (100 - 2x), \quad (2)$$

$$y(\mathrm{Te}) = 0.75 \times (100 - 2x), \quad (3)$$

$$y(\mathrm{Ag}) = n(I) = x, \quad (4)$$

where y(...) is the component concentration, at. %; x is the variable in the formula $(Ga_{10}Ge_{15}Te_{75})_{100-x}(AgI)_x$.

To prepare the glass, 6N gallium (JSC "Lankhit", Moscow, Russia), 5N germanium (JSC "Germanium", Krasnoyarsk, Russia), and 5N tellurium (JSC "ADV-Engineering", Zelenograd, Russia) were used. Silver iodide was prepared by passing 3N iodine (JSC "Khimreaktiv", Russia) over metallic silver (JSC "Novosibirsk Rare Metals Plant", Russia) in a vacuum silica-glass reactor. The iodine was preliminarily triple sublimated to remove metal impurities and water.

The $(Ga_{10}Ge_{15}Te_{75})_{100-x}(AgI)_x$ glasses were prepared by melting the batch in silica-glass glass ampoules with an internal diameter of 7 mm and a wall thickness of 1.5 mm. The ampoules were pre-washed with a mixture of hydrofluoric, hydrochloric, and nitric acids, deionized water, then dried and baked in a flow of especially pure oxygen at 980 °C to remove OH groups [17]. The batch was evacuated to a residual pressure of no more than 10^{-3} Pa, the ampoules were sealed-off. The homogenization of the glass-forming melt was carried out in a rocking muffle furnace at a temperature of 750–850 °C, depending on the glass composition, for 6 hours. The melt was quenched by quickly immersing the ampoules in

water. To relieve mechanical stress, the glasses were annealed at 150–170 °C for 30 minutes, with subsequent cooling to room temperature in the furnace off mode. To extract the samples, the ampoules were cut with a diamond disk. The resulting glass samples had compositions of $(Ga_{10}Ge_{15}Te_{75})_{100-x}(AgI)_x$ (x = 0, 3, 5, 8, 10, 12, 15) in the form of cylindrical rods up to 100 mm long. For brevity, the samples were designated as GGTAI-x.

2.2. Differential scanning calorimetry

The samples were investigated by means of differential scanning calorimetry (DSC) using an STA 409 PC Luxx microcalorimeter (Netzsch, Germany) in a high-purity argon flow in the temperature range of 50–450 °C at a heating rate of 10 deg/min. The measurements were carried out in aluminum pans, the mass of the samples in the form of irregularly shaped pieces was ≈30 mg. Preliminary calibration of the device using standard samples ensured a temperature measurement accuracy of ± 0.1 °C. The error in determining the glass transition temperature (T_g), the onset of crystallization (T_x), and the onset of crystal melting (T_m) was ±2 °C; the error in determining the temperature of maximum crystallization (T_p) was ±1 °C. The generally accepted criterion $\Delta T = T_x - T_g$ [18] was used as a parameter characterizing the glass stability against crystallization. According to established practice, glasses with a ΔT value > 120 °C are suitable for drawing optical fibers [19].

To increase the reliability of the DSC analysis results, as one of the key analytical methods in this study, repeated measurements were performed on additionally synthesized glass samples. Glass with the $(Ga_{10}Ge_{15}Te_{75})_{92}(AgI)_8$ composition was additionally studied at heating rates of 2.5 and 5 K/min.

2.3. Scanning electron microscopy

The stability against crystallization of the glasses was additionally studied by means of scanning electron microscopy (SEM). The analysis was performed using a JSM-IT300LV electron microscope (JEOL) with backscattered and secondary electrons. The elemental composition of the surfaces was measured by means of energy-dispersive X-ray microanalysis (EDXMA) using an attachment with an X-MaxN 20 detector (Oxford Instruments). For the study, disc-shaped samples with parallel-plane polished faces were used. The samples were pre-annealed for 1 hour in evacuated silica-glass ampoules at a temperature of T_g +120 °C, corresponding to the conditions for drawing fiber. After annealing, the samples were re-polished to remove vapor condensation products from their surfaces.

2.4. IR spectroscopy

The transparency of the glasses in the spectral range of 2–25 μm was studied using a Fourier-transform IR Tensor 27 spectrometer (Bruker, Germany) at a resolution of 4 cm^{-1}. The samples used for the measurements were 2-mm-thick disks with parallel-plane polished edges. Based on the obtained data, absorption coefficient spectra $\alpha(\lambda)$ were plotted:

$$\alpha(\lambda) = -\frac{\ln(T(\lambda))}{l}, \quad (5)$$

where $T(\lambda)$ is the transparency; l is the sample thickness (cm).

To clarify the position of the short-wavelength transparency edge of the glasses, additional measurements were carried out in the spectral region of 1–3 μm using a UV 3600 spectrophotometer (Shimadzu, Japan) at a resolution of 2 nm. The energy of direct optical transitions and the corresponding short-wavelength transparency edge were determined using the generally accepted method for chalcogenide glasses in coordinates $(\alpha h\nu)^{1/2} = f(h\nu)$, where α is the absorption coefficient, h is Planck's constant, and ν is the radiation frequency [20].

3. Results and discussion

3.1. Stability against crystallization

The DSC heating curves of the prepared samples are shown in Fig. 1a. The curves exhibit devitrification ranges typical for glasses. For samples GGTAI-0 and GGTAI-3, an exothermic peak of glass crystallization and an endothermic peak of crystal melting are observed. The curve for sample GGTAI-5 shows weak endothermic signals in the 320–340 °C range, the nature of which requires clarification (melting of a small amount of the crystalline phase or fluctuations associated, for example, with the non-stationarity of the inert

gas flow). The characteristic temperature values of the samples are given in Table 1. The glass transition temperature decreases monotonically with an increase in the silver iodide content (Fig. 1b). From the standpoint of the structural approach, this is due to a decrease in the overall connectivity of the glass network due to the "loosening" effect of iodine, and an increase in the ionic nature of chemical bonds [21, 22]. Fig. 1b (curve 2) shows the dependence of T_g on the average coordination of atoms in glass $< r >$, calculated using the equation:

$$\langle r \rangle = \sum r_i x_i \,, \quad (6)$$

where r_i is the coordination number of the i-th atom; x_i is the atomic fraction [23]. In accordance with the literature data for chalcogenide glasses, it was assumed that $r_{Ge} = 4$, $r_{Ga} = 4$, $r_{Te} = 2$, $r_{Ag} = 3$; $r_I = 1$ [24–27]. The obtained dependence fits the general trend for glassy materials of decreasing T_g with a decreasing average coordination number [28].

According to the obtained results, glasses with a silver iodide content of 5–15 mol % do not

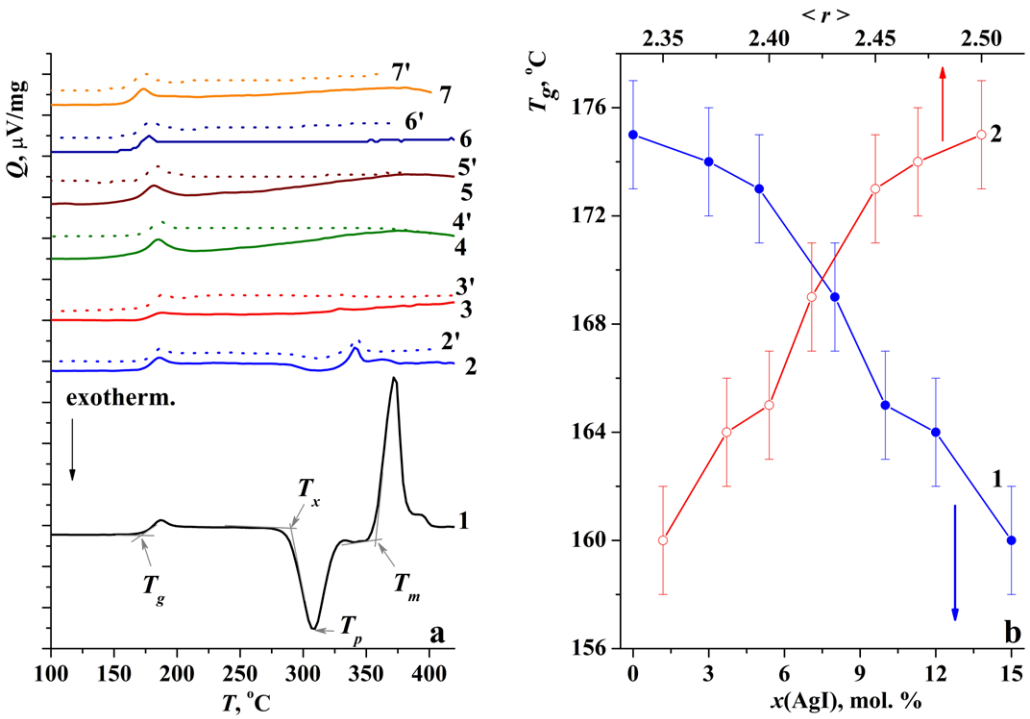

Fig. 1. The DSC heating curves of $(Ga_{10}Ge_{15}Te_{75})_{100-x}(AgI)_x$ (x = 0, 3, 5, 8, 10, 12, 15) glasses based on the results of two independent experiments (a) and the influence of silver iodide content (1b) and average coordination of atoms (2b) on their glass transition temperature

Table 1. Characteristic temperatures, energy of direct optical transitions and position of the short-wavelength transparency edge of $(Ga_{10}Ge_{15}Te_{75})_{100-x}(AgI)_x$ glasses

Sample	T_g, ± 2 °C	T_x, ± 2 °C	ΔT, ± 2 °C	T_p, ± 1 °C	T_m, ± 2 °C	E_g, ± 0.01 эВ	$\lambda_{cut.}$, ± 2 nm
GGTAI-0	175	289	114	308	357	0.59	2116
GGTAI-3	174	290	116	312	339	0.63	1981
GGTAI-5	173	–	–	–	–	0.64	1925
GGTAI-8	169	–	–	–	–	0.65	1899
GGTAI-10	165	–	–	–	–	0.66	1884
GGTAI-12	164	–	–	–	–	0.67	1840
GGTAI-15	160	–	–	–	–	0.70	1771

crystallize during DSC analysis at a heating rate of 10 K/min. This refutes the previously presented data on the crystallization stability of glasses of the $(Ga_{10}Ge_{15}Te_{75})_{100-x}(AgI)_x$ system [15]. The authors of that work reported crystallization of glasses upon heating to 259–266 °C. Moreover, the disappearance of the exothermic peak of crystallization in the studied system occurs at lower concentrations of silver iodide compared to the $(GeTe_4)_{100-x}(AgI)_x$ system [10]. This is due to the increased crystallization stability of the $Ga_{10}Ge_{15}Te_{75}$ base glass.

To further confirm the stability of the studied glasses against crystallization, Fig. 2 shows the DSC curves of the GGTAI-8 sample at lower heating rates: 5 and 2.5 K/min. The choice of the composition for the study is due to the fact that for practical applications it is desirable that crystallization stability be achieved with the minimum possible content of silver iodide. This is due to the low chemical stability of chalcogenide glasses with high iodine content. A decrease in the thermal scanning rate does not lead to the appearance of an exothermic crystallization peak, which indicates a high glass-forming ability of the sample. From the obtained data, the enthalpy of glass transition activation [29] was calculated using the equation:

$$\frac{d\ln V}{dT_g} = \frac{\Delta h^*}{R}, \quad (7)$$

where V is the heating rate, K/min; R is the universal gas constant, J/(mol·K). The obtained value was 320 ± 25 kJ/mol. This parameter does not provide direct information on the crystallization stability of glasses. However, it was found that is close in value to the enthalpy of activation of viscous flow [30], which is used to calculate relaxation processes in glasses and evaluate the kinetic criteria of glass formation.

Fig. 3 shows SEM images of the surface of samples GGTAI-3 and GGTAI-12 after annealing at a temperature of T_g + 120 °C. Low contrast due to the small size and concentration of crystals prevented the detection of clusters of crystalline inclusions on the polished surface. Clear images of the crystalline phase were captured in pores measuring 100–300 μm, formed due to partial evaporation of volatile glass components. Such pores can act as crystallization centers for the glass. All pores in sample GGTAI-3 contained a high concentration of crystals (estimated, > 30 vol. %) with an average size of 2 μm. In samples with a silver iodide content of 5–15 mol %, crystalline inclusions were captured in individual large pores, and their proportion did

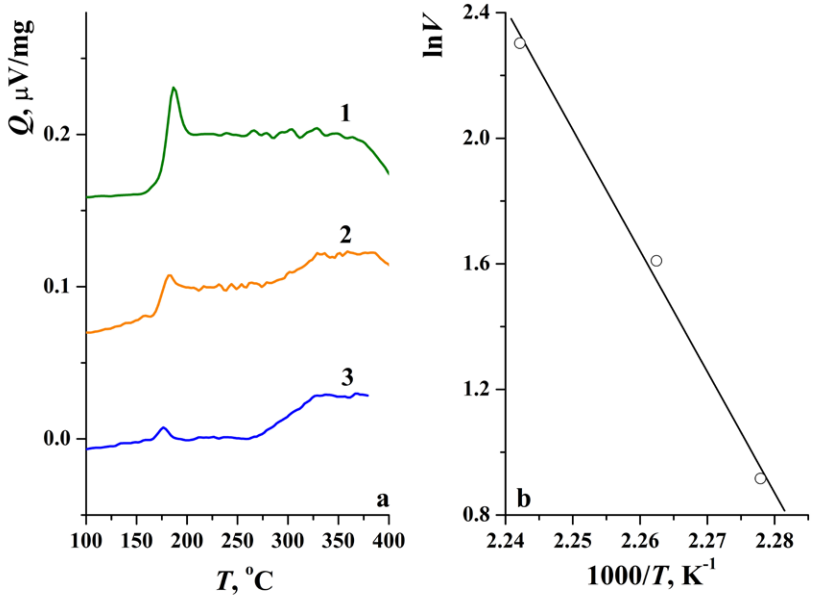

Fig. 2. DSC heating curves of the GGTAI-8 sample at heating rates of 10 K/min (1a), 5 K/min (2a) and 2.5 K/min (3a) and linearization of the ln$V$ dependence on $1/T_g$ to determine the enthalpy of glass transition activation (b)

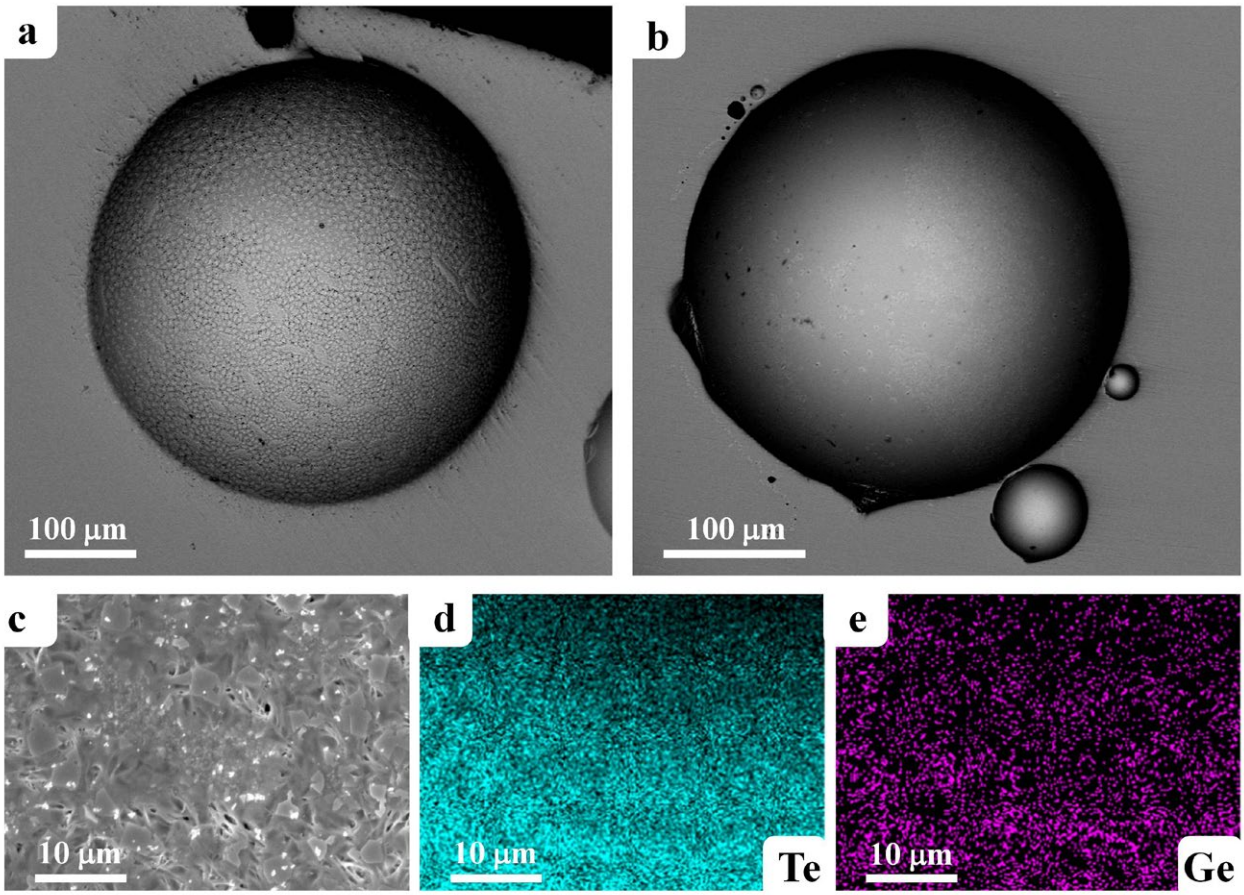

Fig. 3. Electronic images of the surface of the GGTAI-3 and GGTAI-12 samples after annealing at T_g + 120 °C for an hour; a – pore in the GGTAI-3 sample; b – pore in the GGTAI-12 sample; c – image of crystals inside the pores of the GGTAI-3 sample; d, e – corresponding this image shows the distribution maps of Te and Ge

not exceed 10 % of the pore volume. According to the element distribution maps over the surface of the samples, the forming crystalline phase corresponds to tellurium. This is consistent with known literature data on the crystallization of telluride glasses [14, 16]. The total volume fraction of crystalline inclusions in the annealed samples did not exceed 1 vol. % (the detection limit of the crystalline phase in the glass matrix for X-ray phase analysis under the used imaging conditions). In reality, when drawing fiber from a rod [4], the time the sample is kept at the maximum process temperature does not exceed 5 min. This suggests that, under actual drawing conditions, GGTAI-5–GGTAI-15 glasses will not undergo crystallization.

The observed high stability against crystallization of the $(Ga_{10}Ge_{15}Te_{75})_{100-x}(AgI)_x$ (x = 5–15 mol %) glasses may be due to several factors, including various approaches to glass formation. Some of these are listed below:

– approaching the optimal average coordination of atoms with an increase in the proportion of silver iodide, which, according to the topological Phillips criterion [23], for glasses with a three-dimensional structural network corresponds to a value of 2.4. This criterion, however, does not explain the difference between the glass-forming ability of the Ge – Te – AgI and Ga – Ge – Te – AgI systems due to the close values of the coordination numbers of germanium and gallium in chalcogenide glasses;

– complication of the glass network structure due to the formation of structural fragments of the $[MeTe_{(4-x)/2}]I_x$ type, where Me = Ge, Ga; x = 0–4 [24, 25, 31]. This explains the increase in the glass-forming ability of germanium telluride glasses with the addition of gallium, associated with the appearance of new $[GaTe_{(4-x)/2}]I_x$ structural units;

– a decrease in the liquidus temperature (or glass transition) in the $(Ga_{10}Ge_{15}Te_{75})_{100-x}(AgI)_x$

system with an increase in the proportion of AgI while maintaining a relatively high average bond energy, corresponding to the modified San-Rawson criterion [28]. This criterion is mainly fulfilled due to the formation of strong Ga–I chemical bonds during structural transformations of the type

$$[GaTe_4] + xAg–I = [GaTe_{4-x}]I_x + xAg–Te. \quad (8)$$

The corresponding bond energies have the following values (in kJ/mol): $E_{Ga–I}$ = 339; $E_{Ga–Te}$ = 265; $E_{Ag–I}$ = 252; $E_{Ag–Te}$ = 196 [32]. The formation of the silver telluride phase during the distillation of Ge–Te–AgI glasses, confirming the possible occurrence of the indicated process, was reported earlier in [33].

The presented arguments do not claim to strictly substantiate the glass-forming ability of the $(Ga_{10}Ge_{15}Te_{75})_{100-x}(AgI)_x$ system, but they indicate the naturally expected high stability of glasses against crystallization, which was confirmed experimentally in this work.

3.2. Optical transparency

The absorption spectra of the prepared glasses in the spectral range of 2–25 μm are shown in Fig. 4a. The spectra exhibit intense absorption bands in the range of 15–20 μm, corresponding to the gallium oxide impurity. This impurity is present in the initial gallium and additionally appears during the glass synthesis process due to the reduction of germanium and tellurium oxides due to the high thermodynamic stability of Ga_2O_3 ($\Delta_f G^0(298.15) = -998.339$ [34]). This explains the low (below the detection limit) intensity of the absorption bands from the impurities of the oxides of the remaining glass components. There is no generally accepted criterion in the literature for assessing the long-wavelength transparency edge of chalcogenide glasses. In this work, the absorption coefficient value at a wavelength of 23 μm was used as such a comparative characteristic, since the maximum of the intrinsic absorption band of the glass matrix, which limits the transparency of optical fibers, is located in this region. Fig. 4b shows the obtained dependence of α on the silver iodide content. An increase in the proportion of AgI in the glasses leads to a decrease in the intensity of this absorption band. As was shown in [2] from a comparison of the transmission spectra of glasses of the $(GeTe_4)_{100-x}(AgI)_x$ and $(GeTe_4)_{100-x}Ag_x$ systems, the observed broadening of the transparency window is due to the influence of iodine. In the harmonic approximation, the vibration frequency of atoms is proportional to the square root of

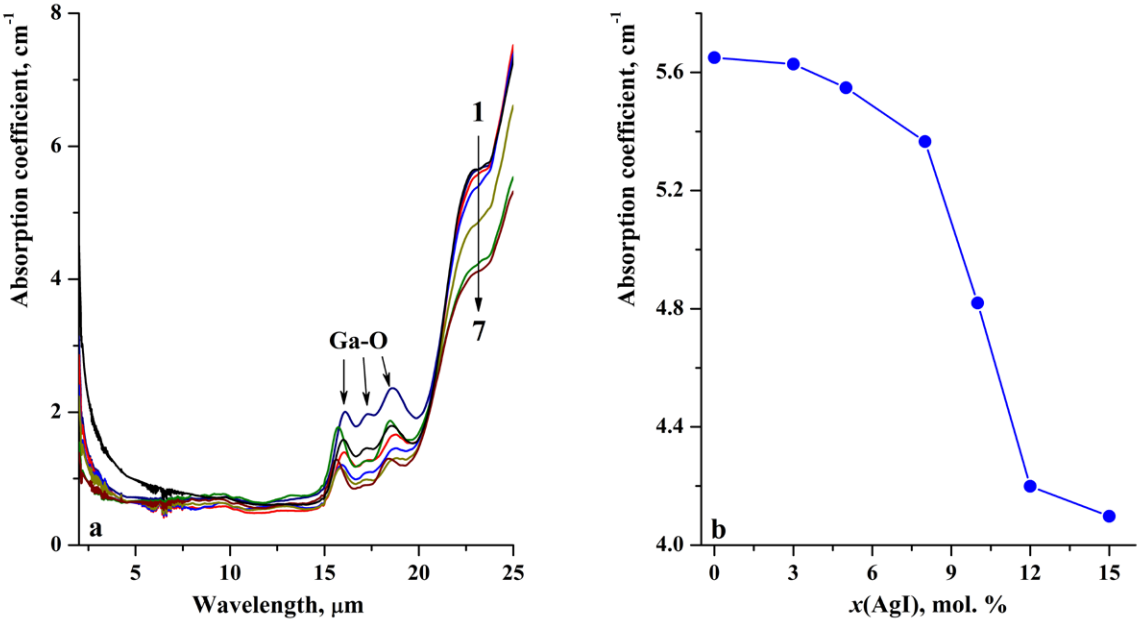

Fig. 4. Absorption spectra of the $(Ga_{10}Ge_{15}Te_{75})_{100-x}(AgI)_x$ glass system in the range of 2–25 microns (a) and the dependence of the absorption coefficient at a wavelength of 23 microns on the glass composition (b). 1a: x = 0; 2a: x = 3; 3a: x = 5; 4a: x = 8; 5a: x = 10; 6a: x = 12; 7a: x = 15. The thickness of the samples is 2 mm

the ratio of the force constant of the bond to the reduced mass [35]. Since the atomic mass of I (126.90447(3) a.m.u.) is less than that of Te (127.60(3) a.m.u.) [36], the observed effect is due to the destructive action of iodine on the structural network, i.e., a decrease in the force constant. The sharp change in absorption in the range of silver iodide content of 8–12 mol % could be caused by the structural rearrangement of the glass network from three-dimensional to layered and pseudo-chain, described, for example, in [37] for the Ge–Se–I system. This effect also manifests itself in the dependence of T_g on the composition of the glasses (Fig. 1b).

The near-IR transmission spectra of glasses, the calculated E_g values (Fig. 5), and the corresponding positions of the short-wavelength transparency edge λ_{cut} are shown in Fig. 6 and Table 1. An increase in the AgI content in glasses leads to an increase in E_g and a shift of λ_{cut} to the short-wavelength region. According to generally accepted concepts, the energy of direct optical transitions in chalcogenide glasses is determined by the band structure of the short-range order elements of the glass network [38]. Based on this, the observed changes are associated with higher E_g values for germanium and silver iodides

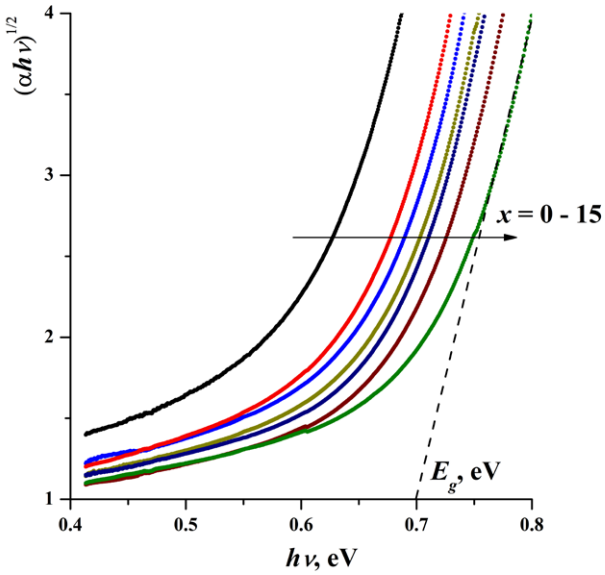

Fig. 5. Graphical determination of the direct optical transitions energy of $(Ga_{10}Ge_{15}Te_{75})_{100-x}(AgI)_x$ (x = 0, 3, 5, 8, 10, 12, 15) chalcogenide glasses in coordinates $(\alpha h\nu)^{1/2} = f(h\nu)$

compared to germanium telluride: E_g = 0.742 eV for trigonal GeTe [39], 2.8 eV for GeI_2 [40], 2.37 eV for cubic AgI [41]. In addition, the position of the short-wavelength transparency edge and its absolute value can be affected by the phase homogeneity of the glass, which increases

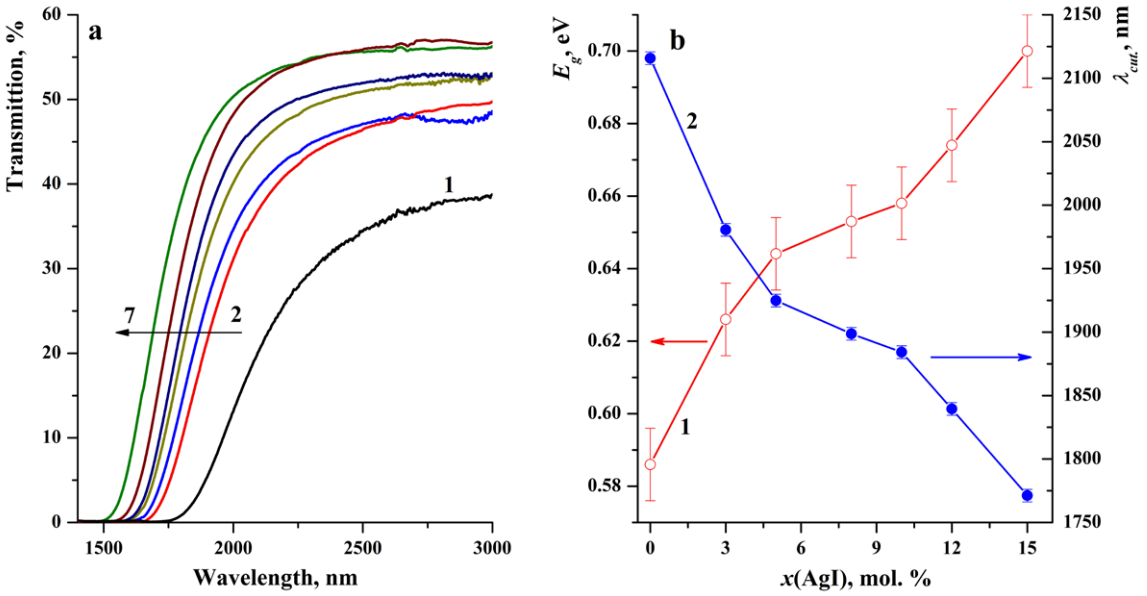

Fig. 6. Transmission spectra of the $(Ga_{10}Ge_{15}Te_{75})_{100-x}(AgI)_x$ glass system in the range of 1–3 microns (a) and the dependence of E_g (1b) and $l_{cut.}$ (2b) on the composition. 1a: x = 0; 2a: x = 3; 3a: x = 5; 4a: x = 8; 5a: x = 10; 6a: x = 12; 7a: x = 15. The thickness of the samples is 2 mm

with the addition of AgI due to the increased crystallization stability of the glasses. The most important positive result of shifting λ_{cut} to the short-wavelength region for glasses is the potentially more efficient pumping of rare earth elements in doped samples used as IR radiation sources [42]. For fiber sensor element materials, shifting the short-wavelength edge will improve the sensitivity to detecting substances absorbing in the 2–4 μm range (water, methane, etc.).

The results obtained indicate that the addition of silver iodide to $Ga_{10}Ge_{15}Te_{75}$ glass significantly improves its stability against crystallization and optical properties. This makes these materials promising competitors to Ge – Te – AgI glasses, which have been used to manufacture optical fibers with relatively low optical losses [4, 13]. Further research in this area could be aimed at optimizing the ratio of components of the base Ga – Ge – Te glass to more improve its stability against crystallization and at developing methods for producing Ga – Ge – Te – AgI glasses with extremely an low content of absorbing impurities.

4. Conclusions

Based on the results obtained in this work, the following key conclusions can be drawn:

– glasses of the $(Ga_{10}Ge_{15}Te_{75})_{100-x}(AgI)_x$ system with a silver iodide content of 5–15 mol % are highly resistant to crystallization and do not show exothermic signals during DSC analysis at a heating rate of 10 K/min;

– increasing the silver iodide content in $(Ga_{10}Ge_{15}Te_{75})_{100-x}(AgI)_x$ glasses increases their transparency in the long-wavelength region of the spectrum due to a decrease in the intensity of their intrinsic absorption bands;

– the fundamental absorption edge shifts to the short-wavelength region from 2116 ± 2 to 1771 ± 2 nm, as the proportion of AgI in these glasses increases from 0 to 15 mol %.

The obtained results makes it possible to consider glasses of the $(Ga_{10}Ge_{15}Te_{75})_{100-x}(AgI)_x$ (x = 5–15 mol %) system as one of the most promising materials for the production of fibers with low optical losses in the spectral range of 4–16 μm.

Author contributions

E. A. Tyurina – Research concept, Methodology, Investigation, Original draft. A. P. Velmuzhov – Research concept, Methodology, Investigation, Writing – review & editing. M. V. Sukhanov – Research concept, Methodology, Investigation, Writing – review & editing. A. D. Plekhovich – Methodology, Investigation, Writing – editing. D. G. Fukina – Methodology, Investigation, Writing – editing. V. S. Shiryaev – Research concept, Writing – review & editing.

Conflict of interests

The authors declare that they have no known competing financial interests or personal relationships that could have influenced the work reported in this paper.

References

1. Conseil C., Bastien J.-C., Boussard-Plédel C., ... Bureau B. Te-based chalcohalide glasses for far-infrared optical fiber. *Optical Materials Express*. 2012;2(11): 1470–1477. https://doi.org/10.1364/OME.2.001470

2. Le Coq D., Cui S., Boussard-Pledel C., ... Bureau B. Telluride glasses with far-infrared transmission up to 35 μm. *Optical Materials*. 2017;72: 809–812. https://doi.org/10.1016/j.optmat.2017.07.038

3. Gu J., Shen X., Jia G., Xia K. Optical properties of Ge-Ga-Ag-Te high refractive index chalcogenide glasses. *Optical Materials Express*. 2023;13(5): 1320–1327. https://doi.org/10.1364/OME.484948

4. Cui S., Boussard-Plédel C., Lucas J., Bureau B. Te-based glass fiber for far-infrared biochemical sensing up to 16 μm. *Optics Express*. 2014;22(18): 21253–21262. https://doi.org/10.1364/OE.22.021253

5. Shiryaev V. S, Velmuzhov A. P., Kotereva T. V., ... Karaksina E. V. Recent achievements in development of chalcogenide optical fibers for mid-IR sensing. *Fibers*. 2023;11: 54. https://doi.org/10.3390/fib11060054

6. Kotsuyama T., Matsumura H. Light transmission characteristics of telluridebased chalcogenide glass for infrared fiber application. *Journal of Applied Physics*. 1994;75: 2743. https://doi.org/10.1063/1.356210

7. Bureau B., Maurugeon S., Charpentier F., ... Zhang X.-H. Chalcogenide glass fibers for infrared sensing and space optics. *Fiber and Integrated Optics*. 2009;28: 65–80. https://doi.org/10.1080/01468030802272542

8. Zhang S., Zhang X., Barillot M., ... Parent G. Purification of $Te_{75}Ga_{10}Ge_{15}$ glass for far infrared transmitting optics for space application. *Optical Materials*. 2010;32: 1055–1059. https://doi.org/10.1016/j.optmat.2010.02.030

9. Savage J. A. Glass formation and D.S.C. data in the Ge–Te and As–Te memory glass systems. *Journal of Non-Crystalline Solids*. 1972;11(2): 121–130. https://doi.org/10.1016/0022-3093(72)90294-3

10. Shiryaev V. S., Velmuzhov A. P., Churbanov M. F., ... Plotnichenko V. G. Preparation and investigation of high purity Ge–Te–AgI glasses for optical application. *Journal of Non-Crystalline Solids*. 2013;377: 1–7. http://dx.doi.org/10.1016/j.jnoncrysol.2013.03.039

11. Wang X., Nie Q., Wang G., ... Ma H., Investigations of Ge–Te–AgI chalcogenide glass for far-infrared application. *Spectrochimica Acta Part A: Molecular and Biomolecular Spectroscopy*. 2012;86: 586–589. http://dx.doi.org/10.1016/j.saa.2011.11.018

12. Lucas P., Boussard-Pledel C., Wilhelm A., ... Bureau B. The development of advanced optical fibers for long-wave infrared transmission. *Fibers*. 2013;1: 110–118. https://doi.org/10.3390/fib1030110

13. Velmuzhov A. P., Tyurina E. A., Sukhanov M. V., ... Shiryaev V. S. First <1dB/m optical loss fiber based on germanium telluride glasses. *Optics and Laser Technology*. 2025;192: 113727. https://doi.org/10.1016/j.optlastec.2025.113727

14. Upadhyay M., Murugavel S. Correlation between crystallization, electrical switching and local atomic structure of Ge-Te glasses. *Journal of Non-Crystalline Solids*. 2013;368: 34–39. http://dx.doi.org/10.1016/j.jnoncrysol.2013.02.028

15. Cheng C., Wang X., Xu T., ... Chen. W. Optical properties of Ag- and AgI-doped Ge–Ga–Te far-infrared chalcogenide glasses. *Infrared Physics & Technology*. 2016;76: 698–703. https://doi.org/10.1016/j.infrared.2016.04.035

16. Zhu E., Wu B,, Zhao X.,... Tian P. Surface crystallization behavior and physical properties of $(GeTe_4)_{85}(AgI)_{15}$ chalcogenide glass. *Infrared Physics & Technology*. 2017;86: 135–138. https://doi.org/10.1016/j.infrared.2017.09.006

17. Velmuzhov A. P., Sukhanov M. V., Churbanov M. F., ... Kirillov Yu. P. Behavior of hydroxyl groups in quartz glass during heat treatment in the range 750–950 °C. *Inorganic Materials*. 2018;54(9): 925–930. https://doi.org/10.1134/S0020168518090169

18. Hruby A. Evaluation of glass-forming tendency by means of DTA. *Czechoslovak Journal of Physics*. 1972; 22(11): 1187–1193. https://doi.org/10.1007/BF01690134

19. Snopatin G. E., Shiryaev V. S., Plotnichenko V. G., ... Churbanov M. F. High-purity chalcogenide glasses for fiber optics. *Inorganic Materials*. 2009;45(13): 1439–1460. https://doi.org/10.1134/S0020168509130019

20. Tanaka K. Have we understood the optical absorption edge in chalcogenide glasses? *Journal of Non-Crystalline Solids*. 2016;431: 21–24. https://doi.org/10.1016/j.jnoncrysol.2015.03.006

21. Seddon A. B., Hemingway M. A. Thermal properties of chalcogenide-halide glasses in the system: Ge-S-I. *J. Thermal Analysis*. 1991;37: 2189–2203. https://doi.org/10.1007/BF01905586

22. Bartenev G. M. *Structure and mechanical properties of inorganic glasses**. Moscow: Stroyizdat Publ.; 1996. 216 p. (in Russ.)

23. Sen S., Mason J. K. Topological constraint theory for network glasses and glass-forming liquids: a rigid polytope approach. *Frontiers in Materials*. 2019; 6. https://doi.org/10.3389/fmats.2019.00213

24. Bouzid A., Pham T.-L., Chaker Z., ... Ori. G. Quantitative assessment of the structure of $Ge_{20}Te_{73}I_7$ chalcohalide glass by first-principles molecular dynamics. *Physical Review B*. 2021;103: 094204. https://doi.org/10.1103/PhysRevB.103.094204

25. Jovari P., Kaban I., Bureau B., ... Zajac D.A. Structure of Te-rich Te–Ge–X (X = I, Se, Ga) glasses. *Journal of Physics: Condensed Matter*. 2010;22: 404207. https://doi.org/10.1088/0953-8984/22/40/404207

26. Chaker Z., Ori G., Boero M., Massobrio C. First-principles study of the atomic structure of glassy $Ga_{10}Ge_{15}Te_{75}$. *Journal of Non-Crystalline Solids*. 2018;498: 338–344. https://doi.org/10.1016/j.jnoncrysol.2018.03.039

27. Salmon P. S, Liu J. The coordination environment of Ag and Cu in ternary chalcogenide glasses. *Journal of Non-Crystalline Solids*. 1996; 205–207: 172–175. https://doi.org/10.1016/S0022-3093(96)00225-6

28. Scholze H. *Glass nature, structure, and properties*. New York: Springer Verlag; 1991. 454 p.

29. Larmagnac J. P., Grenet J., Michon P. Glass transition temperature dependence on heating rate and on ageing for amorphous selenium films. *Journal of Non-Crystalline Solids*. 1981;45: 157–168. https://doi.org/10.1016/0022-3093(81)90184-8

30. Moynihan C. T., Easteal A. J., Wilder J., Tucker J. Dependence of the glass transition temperature on heating and cooling rate. *The Journal of Physical Chemistry*. 1974;78(26): 2673–2677. https://doi.org/10.1021/j100619a008

31. Sun J., Nie Q., Wang X., ... Ma H. Structural investigation of Te-based chalcogenide glasses using Raman spectroscopy. *Infrared Physics & Technology*. 2012;55: 316–319. https://doi.org/10.1016/j.infrared.2012.03.003

32. Luo Y.-R. *Comprehensive handbook of chemical bond energies*. CRC Press; 2007. 1688 p. https://doi.org/10.1201/9781420007282

33. Velmuzhov A. P., Tyurina E. A., Sukhanov M. V., ... Shiryaev V. S.. Effect of AgI and Te/Ge ratio on the properties of glasses in the Ge–Te–AgI system. *Optical Materials*. 2026;169: 117626. https://doi.org/10.1016/j.optmat.2025.117626

34. Barin I. *Thermochemical data of pure substances*. Weinheim, New York: VCH; 1995. 1885 p. https://doi.org/10.1002/9783527619825

35. Harris C. M., Piersol A. G. *Harris' shock and vibration handbook*. McGraw-Hill; 2002. 1456 p.

36. Cohen E. R., Cvitas T., Frey F. G., ..., Thor A. J. *Units and symbols in physical chemistry*. London: Royal Society of Chemistry; 2007. 235 p.

37. Wang F., Boolchand P., Jackson K. A., Micoulaut M. Chemical alloying and light-induced collapse of intermediate phases in chalcohalide glasses. *Journal of Physics: Condensed Matter*. 2007;19: 226201. https://doi.org/10.1088/0953-8984/19/22/226201

38. Holomb R., Mitsa V., Johansson P. Localized states model of GeS_2 glasses based on electronic states of Ge_nS_m clusters calculated by using TD-DFT. *Journal of Optoelectronics and Advanced Materials*. 2005;7(4): 1881–1888.

39. Palaz S., Koc H., Mamedov A.M., Ozbay E. Topological insulators: electronic band structure and spectroscopy. *IOP Conference Series: Materials Science and Engineering*. 2017;175: 012004 https://doi.org/10.1088/1757-899X/175/1/012004

40. Dhingra A., Lipatov A., Lu H., ... Dowben P.A. Surface and dynamical properties of GeI_2. *2D Materials*. 2022;9(2): 025001. https://doi.org/10.1088/2053-1583/ac4715

41. Gordienko A. B., Zhuravlev Yu. N., Poplavnoi A. S. Electronic structure of AgCl, AgBr, and AgI. *Physica Status*

Solidi (b). 1991;168(1): 49–156. https://doi.org/10.1002/pssb.2221680114

42. Koltashev V. V., Denker B. I., Galagan B. I., ... Plotnichenko V. G. 150 mW Tb3+ doped chalcogenide glass fiber laser emitting at λ > 5 μm. *Optics & Laser Technology*. 2023;161: 109233. https://doi.org/10.1016/j.optlastec.2023.109233

** Translated by author of the article*

Information about the authors

Elizaveta A. Tyurina, Cand. Sci. (Chem.), Researcher at the Laboratory of High-Purity Chalcogenide Glasses for Mid-IR Photonics, G. G. Devyatykh Institute of Chemistry of High-Purity Substances of the Russian Academy of Science (Nizhny Novgorod, Russian Federation).

https://orcid.org/0000-0002-6107-9862
tyurina.ichps@mail.ru

Aleksandr P. Velmuzhov, Cand. Sci. (Chem.), Senior Research Fellow at the Laboratory of High-Purity Chalcogenide Glasses for Mid-IR Photonics, G. G. Devyatykh Institute of Chemistry of High-Purity Substances of the Russian Academy of Science (Nizhny Novgorod, Russian Federation).

https://orcid.org/0000-0002-8739-3868
velmuzhov.ichps@mail.ru

Maxim V. Sukhanov, Cand. Sci. (Chem.), Senior Research Fellow at the Laboratory of High-Purity Chalcogenide Glasses for Mid-IR Photonics, G. G. Devyatykh Institute of Chemistry of High-Purity Substances of the Russian Academy of Science (Nizhny Novgorod, Russian Federation).

https://orcid.org/0000-0003-0525-6286
sukhanov@ihps-nnov.ru

Aleksandr D. Plekhovich, Cand. Sci. (Chem.), Senior Research Fellow at the Laboratory of High-Purity Chalcogenide Glasses for Mid-IR Photonics, G. G. Devyatykh Institute of Chemistry of High-Purity Substances of the Russian Academy of Science (Nizhny Novgorod, Russian Federation).

https://orcid.org/0000-0002-1726-7313
plekhovich@ihps-nnov.ru

Diana G. Fukina, PhD, Senior Research Fellow at the Laboratory of Inorganic Materials, Lobachevsky State University of Nizhny Novgorod (Nizhny Novgorod, Russian Federation).

https://orcid.org/0000-0001-8375-6863
dianafuk@yandex.ru

Vladimir S. Shiryaev, Dr. Sci. (Chem.), Deputy Director for Research, G. G. Devyatykh Institute of Chemistry of High-Purity Substances of the Russian Academy of Science (Nizhny Novgorod, Russian Federation).

https://orcid.org/0000-0002-1726-7313
shiryaev@ihps-nnov.ru

Received June 30, 2025; approved after reviewing December 4, 2025; accepted for publication December 15, 2025; published online April 01, 2026.

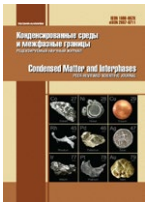

ISSN 1606-867X (Print)
ISSN 2687-0711 (Online)
Condensed Matter and Interphases
Kondensirovannye Sredy i Mezhfaznye Granitsy
https://journals.vsu.ru/kcmf/

Original articles

Research article
https://doi.org/10.17308/kcmf.2026.28/13564

MOCVD and ferromagnetic resonance of epitaxial $Lu_3Fe_5O_{12}$ films for high-frequency applications

A. A. Hafizov[1], M. N. Markelova[1]✉, Gu Ruoxuan[1], I. E. Graboy[1], V. A. Amelichev[2], D. A. Volkov[3,4], D. A. Gabrielyan[3,4], A. R. Safin[3,4], S. A. Nikitov[3], A. R. Kaul[1]

[1]Lomonosov Moscow State University,
1. Leninskie Gory, Moscow 119991, Russian Federation

[2]S-Innovations,
20-2. Nauchniy Proezd, Moscow117246, Russian Federation

[3]Kotelnikov Institute of Radio Engineering and Electronics, Russian Academy of Sciences,
11-7 Mokhovaya st., Moscow 125009, Russian Federation

[4]National Research University Moscow Power Engineering Institute,
14-1, Krasnokazarmennaya st., Moscow 111250, Russia

Abstract

Objectives: The production of thin films of rare earth iron garnets with a narrower ferrimagnetic resonance (FMR) linewidth is extremely important in the development of spintronic materials. Among rare earth iron garnets, the compound $Lu_3Fe_5O_{12}$, which has the highest saturation magnetization, is promising. The aim of this work is to study the dependence of the FMR linewidth of $Lu_3Fe_5O_{12}$ iron garnet films on the lattice mismatch between the film and the substrate, as well as on the film thickness during their production by metalorganic chemical vapor deposition (MOCVD).

Experimental: Thin films of $Lu_3Fe_5O_{12}$ garnet were obtained by MOCVD technique on isostructural single-crystal substrates of $Nd_3Ga_5O_{12}$(111), $Gd_3Ga_5O_{12}$(111), $Gd_3Ga_5O_{12}$(210), $Gd_3(AlGa_4)O_{12}$(111) and $Y_3Al_5O_{12}$(111). The films were studied by XRD, EDX, and FMR methods. The dependences of the FMR linewidth on the mismatch of the unit cell (UC) parameters of the garnet at the film–substrate interface, substrate orientation, and film thickness were studied.

Conclusions: It has been established that the minimum FMR linewidth (ΔH) of $Lu_3Fe_5O_{12}$ films is achieved on substrates with minimal mismatch at the interface. The dependence of ΔH on film thickness is shown to be extreme, with the minimum corresponding to a film thickness at which significant relaxation of epitaxial stresses has occurred, but the concentration of defects characteristic of the polycrystalline state is still low. Taking these factors into account will make it possible to obtain iron garnet films with a narrower ferromagnetic resonance linewidth, which can subsequently be used in various areas of spintronics as sensitive elements in microwave detectors.

Keywords: Thin films, Iron garnet, MOCVD, Structure, Ferrimagnetic resonance

Funding: This work was supported by a State assignment to Lomonosov Moscow State University, registration number AAAA-A21-121011590082-2.

For citation: Hafizov A. A., Markelova M. N., Gu R., Graboy I. E., Amelichev V. A., Volkov D. A., Gabrielyan D. A., Safin A. R., Nikitov S. A., Kaul A. R. MOCVD and ferromagnetic resonance of epitaxial $Lu_3Fe_5O_{12}$ films for high-frequency applications. *Condensed Matter and Interphases*. 2026;28(1): 126–136. https://doi.org/10.17308/kcmf.2026.28/13564

Для цитирования: Хафизов А. А., Маркелова М. Н., Гу Ж., Грабой И. Э., Амеличев В. А., Волков Д. А., Габриелян Д. А., Сафин А. Р., Никитов С. А., Кауль А. Р. Синтез из газовой фазы и ферримагнитный резонанс эпитаксиальных пленок $Lu_3Fe_5O_{12}$ для высокочастотных приложений. *Конденсированные среды и межфазные границы*. 2026;28(1): 126–136. https://doi.org/10.17308/kcmf.2026.28/13564

✉ Maria N. Markelova, e-mail: maria.markelova@gmail.com

1. Introduction

The ever-increasing pace of daily data production in a wide variety of human activities, the rapid expansion of accumulated knowledge, and the development of artificial intelligence highlight the fundamental problem of efficient recording and reliable storage of information. This creates significant incentives for the development of new areas of electronics – spintronics and magnonics [1–3]. Spintronic devices are characterized by high write and read speed, information recording density, energy independence, and a number of other advantages over traditional semiconductor electronic analogues [4–6], therefore they have undergone great development over the past two decades. These devices operate using materials in which the primary role is played not by the charge current, which causes Joule heating, but by the spin current, which is free of this drawback. One of the key requirements for such materials is a narrow ferromagnetic resonance (FMR) linewidth [7]. Ferrimagnetic resonance manifests itself in the selective absorption of electromagnetic field energy by a ferrimagnet at frequencies that coincide with the natural precession frequencies of the magnetic moments of the ferrimagnet's electron system in an internal effective field. Intensive research is underway to replace traditional magnetic metals or semiconductors used in spintronic devices with magnetic insulators, specifically ferrimagnetic iron garnets.

The structural type of garnet belongs to the space group *Ia*3*d*. The cubic body-centered unit cell of rare earth (RE) iron garnets consists of 8 identical octants corresponding to the formula composition $\{R\}_3[Fe]_2(Fe)_3O_{12}$, where the curly brackets { } denote the dodecahedral positions of the RE^{3+} ions, and the brackets [ ]- and ( )- correspond to the octahedral and tetrahedral positions occupied by Fe^{3+} ions. The three-sublattice structure and wide possibilities of varying the elemental composition of garnets lead to an almost unlimited variety of their magnetic properties [8].

The narrow ferromagnetic resonance linewidth in iron garnets minimizes losses during electromagnetic wave propagation. A narrower ferromagnetic resonance linewidth in the magnetic layer allows for the propagation of a spin wave or spin current over a greater distance [9], as well as the switching of magnetic moments at a higher speed and with a lower required current density [9, 10]. These arguments indicate that the FMR linewidth is the most important parameter to consider when creating a magnetic layer in spintronic devices. Therefore, producing magnetic iron garnets with a much narrower FMR linewidth than other ferrites and other magnetic insulators has recently become extremely important. For some iron garnet compositions, the width of FMR line is as small as few Oe (e.g., for epitaxial films of $Y_3Fe_5O_{12}$ on $Ga_3Ga_5O_{12}$) [11, 12], while for other compositions the line broadens. At the same time, among RE-iron garnets, there are compositions with high saturation magnetization (e.g., for $Lu_3Fe_5O_{12}$, M_s = 1815 Oe), which is also favorable for the operation of spin devices. The possibility of obtaining thin $Lu_3Fe_5O_{12}$ films with a narrow FMR line would be a significant achievement in expanding the arsenal of spintronic materials, but this requires a detailed understanding of the nature of the FMR line broadening, which is still not fully understood.

The authors of [13] obtained $Lu_3Fe_5O_{12}$ films with a thickness of less than 10 nm on GGG(111) substrates using the molecular beam epitaxy method, in which they showed that $Lu_3Fe_5O_{12}$ films have very low values of the Gilbert damping constant: $11\cdot10^{-4}$ for films with a thickness of 5.3 nm and $32\cdot10^{-4}$ for films of 2.8 nm, which is comparable with the best values of the damping constant for very thin $Y_3Fe_5O_{12}$ films. It is also worth mentioning the discovery of magnetodielectric properties (change in permittivity under the influence of an external magnetic field) in ceramic [14] and thin-film [15] samples of $Lu_3Fe_5O_{12}$. The latter work showed that in epitaxial films of $Lu_3Fe_5O_{12}$ /$Y_3Al_5O_{12}$(111) the magnetodielectric effect at room temperature reaches 0.9 % at a relatively low magnetic field of 1000 Oe and 12.5 % at 9000 Oe. These results indicate the possibility of tuning the magnetic properties of $Lu_3Fe_5O_{12}$ films using an electric field and the real prospects for the subsequent development of microwave modulators, filters, and switches based on them. Recently, Japanese scientists [16] observed the splitting of spin waves

reflected from the edge of the sample into two modes with different wavelengths using doped lutetium iron garnet $Lu_2BiFe_{3.4}Ga_{1.6}O_{12}$ films, which exhibited a much stronger Faraday rotation than $Y_3Fe_5O_{12}$ films. This result demonstrates the potential for controlling spin wave propagation in magnetic films using the modal degree of freedom of elastic waves.

The diverse potential spintronic applications of garnets, and in particular $Lu_3Fe_5O_{12}$, are only just beginning to be realized in operational high-frequency devices [17–19], and for successful development in this area, epitaxial films with a narrow FMR line are primarily needed. Microwave (MW) technology, which has long used garnet films in devices operating on surface magnetostatic waves [20], meets its needs with films obtained by liquid-phase epitaxy, based on growth from supersaturated solution-melts [21, 22]. For applications in spintronics, however, other technological approaches are required to produce thinner epitaxial films (in the submicron thickness range) that are minimally subject to chemical interaction with the melt and the substrate. In light of these requirements, vacuum methods for the epitaxy of RE-iron garnet films are being developed: magnetron deposition [15, 23], pulsed laser deposition [24–26], molecular beam epitaxy [13, 27], and MOCVD [28, 29].

Any film production method involves operational parameters that significantly influence the actual structure and resonance properties of thin films. These parameters influence the simultaneous influence of more general factors that are essential for any film production method and reflect, on the one hand, the principles of epitaxial growth and, on the other, the physics of film magnetism. Given the exceptional sensitivity of resonance properties, developing methods for producing spintronic materials necessitates a detailed study of the role of all factors and the establishment of optimal values for all parameters affecting the resonance of garnet films of specific compositions.

The aim of this study is to investigate the dependence of the FMR linewidth of lutetium iron garnet $Lu_3Fe_5O_{12}$ films on the lattice mismatch between the film and substrate, as well as on the film thickness during metal-organic chemical vapor deposition. Such studies have not been described in the literature and, therefore, represent a significant innovation.

2. Experimental

$Lu_3Fe_5O_{12}$ thin films were deposited by MOCVD on single-crystal $Nd_3Ga_5O_{12}$ (NdGG), $Ga_3Ga_5O_{12}$ (GGG), $Ga_3(AlGa_4)O_{12}$ (GAGG), and $Y_3Al_5O_{12}$ (YAG) substrates with a (111) deposition surface orientation. In some experiments, GGG substrates with a (210) orientation were also used. $Lu(thd)_3$ and $Fe(thd)_3$ dipivaloylmethanates (thd is the 2,2,6,6-tetramethylheptane-3,5-dionate anion) were used as volatile precursors.

The MOCVD setup is shown in Fig. 1. The precursor source is a microcontainer filled with a homogenized mixture of precursor powders. A thin hole is drilled in the bottom of the microcontainer, through which precursor particles can only spill out when the container is vigorously shaken. Shaking is accomplished by periodically oscillating a small magnet placed inside the container in an alternating magnetic field. As a result, microportions of the precursor mixture are periodically fed into the heated evaporator, almost instantly transforming into the vapor phase. The precursor vapors are then transported by a carrier gas (argon) through a hot line into the reactor, where oxidative thermolysis occurs on the surface of the heated substrate, forming the final metal oxide film. The feed rate was 6.8 μmol/min, and the film growth time was 5–90 min. This setup utilizes a "hot-wall reactor," heated by an external furnace, which reduces temperature gradients in the film deposition zone. To prevent the substrates from

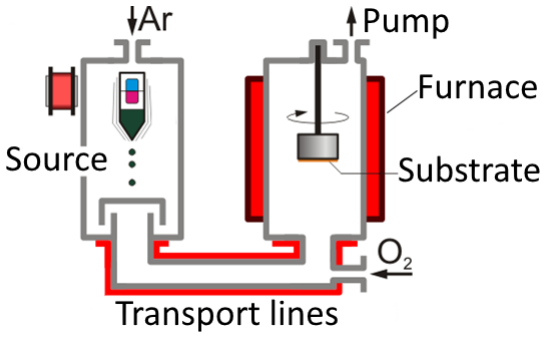

Fig. 1. Schematic diagram of a MOCVD setup with a powder feeder and a hot-wall reactor

being exposed to dusty oxide particles, partially formed when the decomposition of precursors during homogeneous nucleation occurs, an inverted substrate holder was used, to which the substrates were attached from below. In terms of mass transfer, this reactor is a reactor with "stagnant zone", formed under the substrate as a normally directed, rarefied gas flow passes over it. Precursors penetrate from the vapor to the deposition surface via molecular diffusion through a near-surface barrier gas layer, the thickness of which depends on the reactor pressure, the substrate temperature, and the velocity of the incoming gas flow. The hot line and reactor temperatures during deposition were 240 and 970 °C, the total pressure p(total) = 6 mbar, and the partial oxygen pressure pO_2 = 3 mbar. After deposition, the setup was filled with oxygen, and the films were oxidatively annealed at 970°C for 20 minutes. The Fe/Lu ratio in the resulting films was determined using EDX on a Zeiss EVO 50 SEM scanning electron microscope with an e2v Sirius SD IXRF EDMA analyzer. Film thickness was determined from cleavage on a Leo Supra 50 VP scanning electron microscope using a secondary electron detector (SE2).

The phase composition of the resulting films was determined from X-ray θ–2θ scanning data on a Rigaku SmartLab diffractometer (Cu$K\alpha$, secondary graphite radiation monochromator). θ–2θ scanning was performed in the angular range of 5–80° with a step of 0.02°, with a signal accumulation time of 1 s. The ICDD PDF database was used for phase identification. X-ray φ-scanning was used to determine the film orientation in the substrate plane and confirm epitaxial growth. The thickness of the films was determined as follows: two films were analyzed by scanning electron microscopy of a cross-section, their thickness was determined with an accuracy of +/– 5 nm, for the remaining films the thickness was calculated on the assumption that the thickness is directly proportional to the deposition time with constant parameters determining the deposition rate.

To study the ferromagnetic resonance absorption spectra, a setup (Fig. 2) assembled on the basis of a vector network analyzer (VNA), the operating principle of which is described in [17], was used. During the experiments, the real part of the parameter S_{21} was measured for the studied thin-film $Lu_3Fe_5O_{12}$ sample located on a coplanar waveguide. The parameter S_{21} characterizes the ratio of the power transmitted through the coplanar waveguide to the power acting at its input. When the ferromagnetic resonance frequency and the microwave signal frequency applied to the coplanar waveguide input coincide, the microwave signal power is absorbed, which is clearly reflected by this parameter. All obtained dependences of parameter S_{21} were described by a Lorentz function, defining the FMR linewidth.

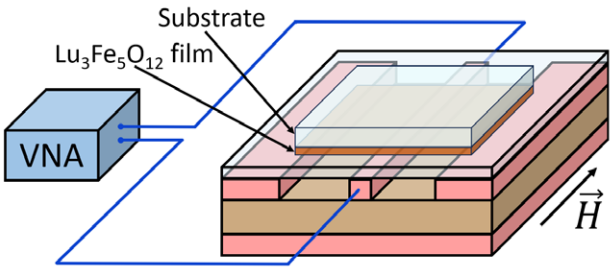

Fig. 2. Schematic diagram of the setup for measuring FMR spectra (VNA – vector network analyzer)

3. Results and discussion

To study the dependence of the FMR linewidth on the substrate type, we selected four substrates with garnet structures: NdGG(111), GGG(111), GAGG(111), and $Y_3Al_5O_{12}$(111) and deposited $Lu_3Fe_5O_{12}$ films of the same thickness (270 nm) on them. All selected substrates are isostructural with each other and with the grown $Lu_3Fe_5O_{12}$ film; however, they have different unit cell parameters (Fig. 3), resulting in different mismatches at the film/substrate interface. The parameter mismatch values (ε) for each substrate/film pair, calculated using the formula:

$$\varepsilon = \frac{a_{\text{film}} - a_{\text{substrate}}}{a_{\text{film}}} \cdot 100\,\%,$$

are 2.3 %, -0.3 %, -0.8 %, and -1.8 % for YAG(111), GAGG(111), GGG(111), and NdGG(111) films, respectively. As can be seen from the calculated values, for YAG, the substrate compresses the film in the contact plane, while for GAGG, GGG, and NdGG, the substrate stretches the film. Thus, during the growth of $Lu_3Fe_5O_{12}$ films on all of these substrates, significant elastic stresses in the film should be expected, which typically lead to

changes in many physical properties, particularly magnetic ones.

As can be seen from the X-ray θ-2θ scanning results (Fig. 4), the films on all four substrates exhibit oriented (444) growth of the $Lu_3Fe_5O_{12}$ phase, mirroring the orientation of the substrates. Considering the X-ray φ-scan results (Fig. 5), which indicate that the film orientation in the lateral plane also follows the substrate orientation, it can be concluded that garnet films on all substrates grow as a single epitaxial "cube-on-cube" pattern. However, alongside reflections from the main garnet phase, the X-ray diffraction patterns also contain peaks from iron(III) oxide and lutetium orthoferrite $LuFeO_3$, the amounts of which do not exceed fractions of a percent relative to the main phase. It is significant that these impurities form only on NdGG(111) and YAG(111) substrates, whose unit cell parameters deviate most from the unit cell parameter of $Lu_3Fe_5O_{12}$. This observation indicates the emergence of obvious difficulties in layer-by-layer epitaxial growth and the facilitation of nucleation of structurally incoherent phases with increasing mismatch of cell parameters at the interface.

By comparing the film peak shifts relative to its position in the X-ray powder diffraction spectrum (i.e., in the free-running, unstressed state), one can assess the presence or absence of an elastic-stressed state, as well as the magnitude of the elastic stress. For example, on GAGG, GGG, and NdGG substrates, a slight shift of the $Lu_3Fe_5O_{12}$ film reflection toward larger angles is observed. This indicates a decrease in the unit cell parameter perpendicular to the substrate due to film stretching by the substrate in the interface plane, while the film's unit cell volume remains unchanged (Table 1). Judging by the insignificant deviation of the film peak from the tabulated value for $Lu_3Fe_5O_{12}$ (444), one can conclude that

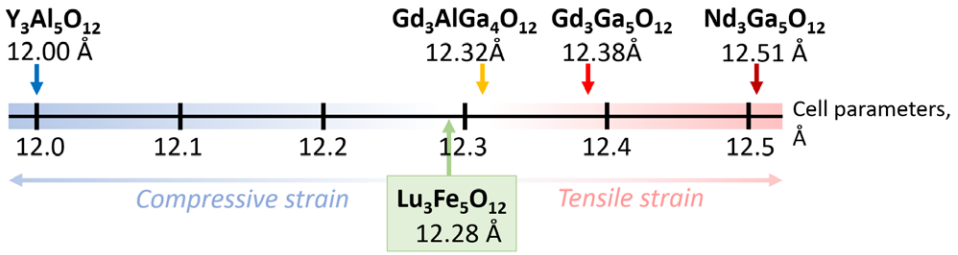

Fig. 3. Schematic illustration of the difference in the unit cell parameters of YAG(111), GAGG(111), GGG(111), and NdGG(111) garnet substrates and $Lu_3Fe_5O_{12}$ film

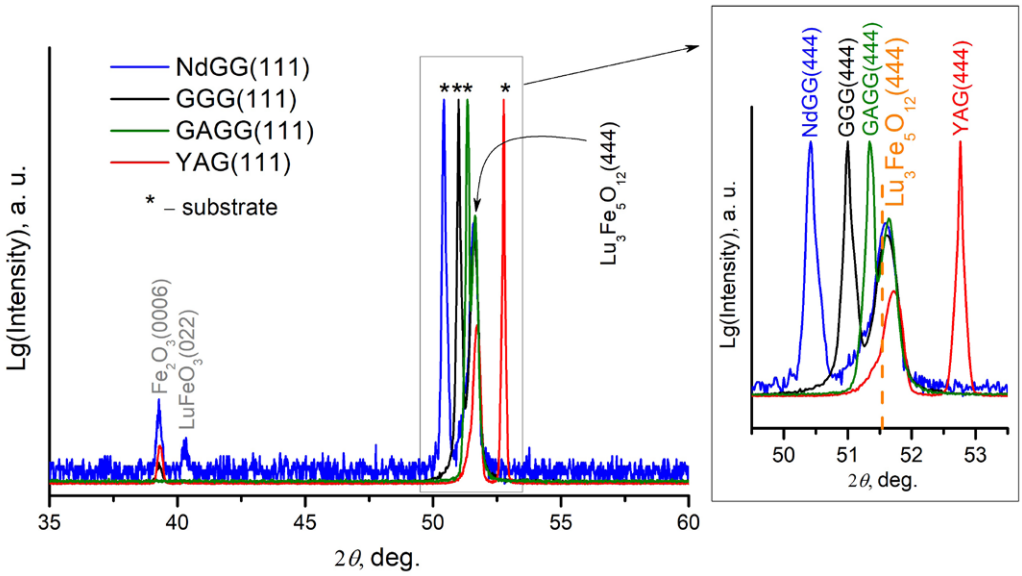

Fig. 4. X-ray diffraction patterns of $Lu_3Fe_5O_{12}$ films deposited on NdGG(111), GGG(111), GAGG(111), and YAG(111) substrates. The dashed line indicates the (444) peak position of bulk $Lu_3Fe_5O_{12}$

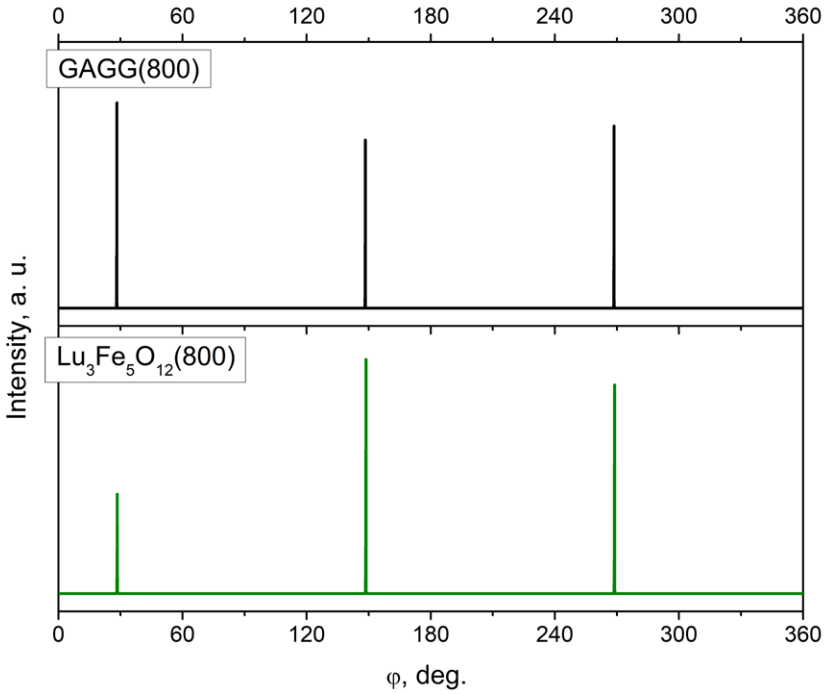

Fig. 5. X-ray φ-scans results for $Lu_3Fe_5O_{12}$ films on a GAGG(111) substrate

the films obtained on GAGG, GGG, and NdGG are in a partially relaxed state. On the YAG substrate, which has a smaller unit cell parameter than the film, a shift of the film peak toward larger angles (i.e., a decrease in the parameter along the normal) is also observed. However, judging by the ratio of the unit cell parameters, elastic stress should cause a deformation of the opposite sign: with the unit cell film volume unchanged, compression along the film/substrate interface leads to an increase in the parameter along the normal to the growth surface and a shift of the film peak toward smaller diffraction angles. The distinct behavior of the $Lu_3Fe_5O_{12}$ film on the YAG substrate suggests that the distortion of the parameters is not due to elastic stresses, but has a different origin. The most likely (but not yet proven) cause is the chemical interaction between the film and the substrate, which involves $Fe^{3+} \leftrightarrow Al^{3+}$ exchange, during which Fe^{3+} ions in octahedral and/or tetrahedral positions are partially replaced by smaller Al^{3+} ions. The possibility of such a substitution was demonstrated in [30] in a study of $Y_3Fe_5O_{12}$ films obtained on $Y_3Al_5O_{12}$ substrates using secondary ion mass spectroscopy. Analysis of the values of the full width at half maximum (FWHM) of X-ray reflections (444) of films on different substrates (Table 1) allows us to state that the most perfect and least stressed epitaxial crystallites of $Lu_3Fe_5O_{12}$ are formed on GAGG substrates.

As shown by the FMR spectral results (Fig. 6a), films on the NdGG substrate exhibit a broader FMR peak compared to films on GGG and GAGG, which is clearly related to the higher stress state of the film on NdGG. It should be noted that at a frequency of 9 GHz, the FMR spectrum of the film on the YAG substrate has a diffuse, weakly

Table 1. Values of unit cell parameters in the direction perpendicular to the substrate (out-of-plane) of $Lu_3Fe_5O_{12}$ films (for comparison, the unit cell parameter for a $Lu_3Fe_5O_{12}$ single crystal = 12.284 Å) and the full width at half maximum (FWHM) of X-ray reflections (444) of films on different substrates

Monocrystal substrate	Out-of-plane unit cell parameter $Lu_3Fe_5O_{12}$ films, Å	FWHM of (444)$Lu_3Fe_5O_{12}$ reflection, deg.
YAG(111)	12.29(1)	0.22(1)
GAGG(111)	12.26(1)	0.17(1)
GGG(111)	12.26(1)	0.22(1)
NdGG(111)	12.26(1)	0.20(1)

defined character, which can also be interpreted as a consequence of high elastic compressive stresses (and, possibly, chemical interactions at the interface) while maintaining the epitaxial inheritance of the substrate structure by the film. Plotting the dependence of the FMR line width (ΔH) (Fig. 6b) on the mismatch value at the interface reveals a clear minimum for the $Lu_3Fe_5O_{12}$ film obtained on the GAGG(111) substrate: the least deformed film on this substrate exhibits the narrowest FMR line $\Delta H = 171(+/-8)$ Oe. Thus, among the substrates we have considered, $Gd_3(AlGa_4)O_{12}$ is more suitable than others for obtaining high-quality epitaxial $Lu_3Fe_5O_{12}$ films with a minimum FMR line width due to the smallest mismatch of parameters between the film and the substrate.

In the next stage of the study, $Lu_3Fe_5O_{12}$ films with thicknesses ranging from 45 to 800 nm were deposited on the surface of single-crystal GGG-substrates with (111) and (210) orientations, with growth on substrates of both orientations being performed in a single cycle. Deposition of all films was carried out under identical conditions ($T_{deposition}$, p_{total}, pO_2, V_{growth}), with only the deposition time varied to obtain films of different thicknesses. The results of X-ray phase analysis of the films on the GGG(111) substrate are shown in Fig. 7a. As can be seen from these data, the resulting films remain epitaxial at all thicknesses. However, a decrease in intensity and an increase in reflection width with increasing film thickness indicate a gradual accumulation of epitaxial layer defects. A noticeable shift in the reflection of the $Lu_3Fe_5O_{12}$ garnet film toward the value indicated by the "powder card" indicates that elastic stresses in the film, arising at the interface with the substrate, decrease as the epitaxial layer thickness increases, which is also demonstrated by the dependence of the unit cell parameters of the $Lu_3Fe_5O_{12}$ film on thickness (Fig. 7b). This pattern is entirely consistent with the classical behavior of thin-film heteroepitaxial structures. It should also be noted that reflections from secondary phases of α-Fe_2O_3 and o-$LuFeO_3$ appear in the X-ray diffraction patterns of 800 nm-thick films. Their origin is similar: with increasing film thickness, the orienting force of epitaxy weakens, and on the surface of the thickest films, phase formation during film deposition resembles a solid-phase reaction proceeding via a diffusion mechanism, with diffusion having a two-dimensional surface character. The completeness of the formation of the $Lu_3Fe_5O_{12}$ phase by the reaction of α-Fe_2O_3 with o-$LuFeO_3$ depends on the rate of surface diffusion, which decreases sharply as the film thickness increases with increasing surface roughness.

In the thinnest film (45 nm) on GGG(111), a weak reflection of the hexagonal phase *h*-$LuFeO_3$ is noticeable. This phase is thermodynamically unstable in the autonomous state, but is easily stabilized by minimizing the interface energy on

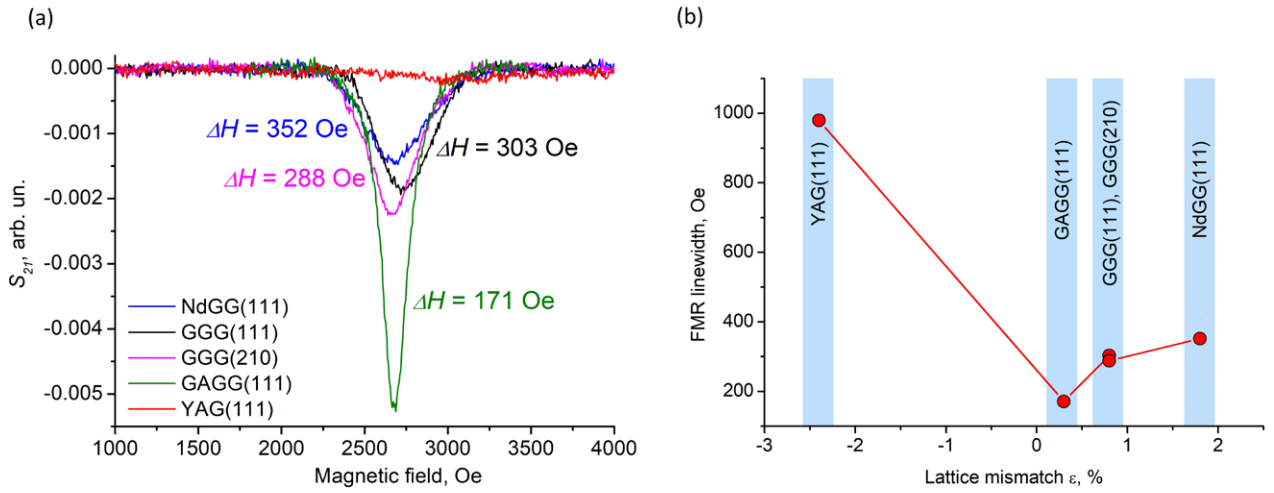

Fig. 6. (a) Comparison of FMR spectra (S_{21} – the absorption coefficient) of $Lu_3Fe_5O_{12}$(111) films on different substrates. Microwave frequency is 9 GHz. (b) Dependence of ferromagnetic resonance linewidth on the lattice mismatch of film/substrate

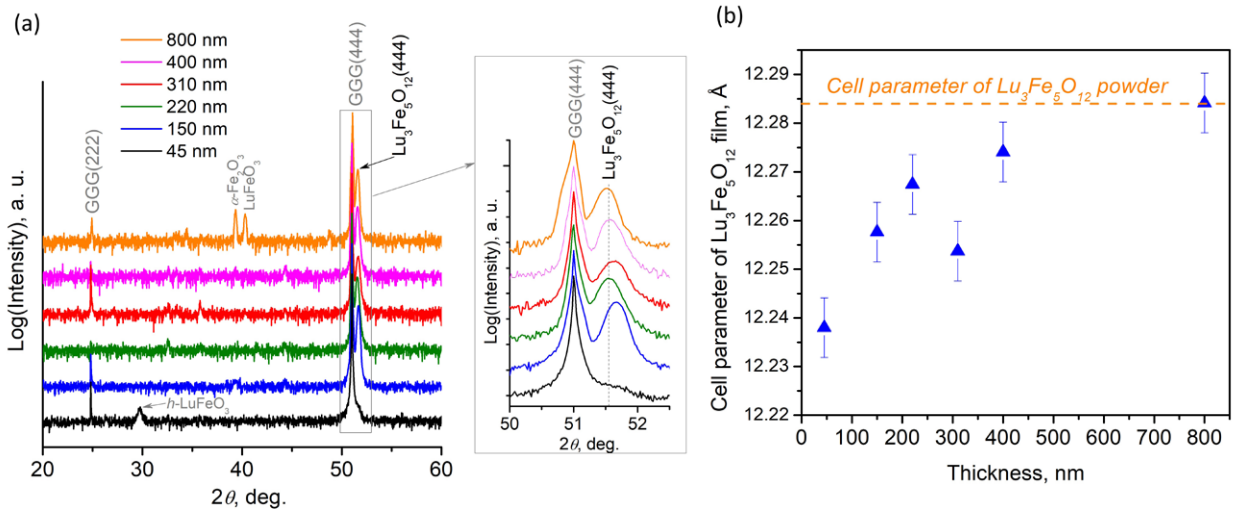

Fig. 7. (a) θ–2θ X-ray diffraction patterns of $Lu_3Fe_5O_{12}$ films of different thicknesses on a $Gd_3Ga_5O_{12}$(111) substrate. (b) Dependence of the unit cell parameters on the thickness of $Lu_3Fe_5O_{12}$ films on a $Gd_3Ga_5O_{12}$(111) substrate

surfaces with a hexagonal oxygen ion packing motif, which includes the (111) plane of garnet [31, 32]. The FMR measurement results presented in Fig. 8a and Fig. 8b demonstrate that ferromagnetic resonance is observed in all of the obtained films, with the exception of the 45 nm-thick films. Fig. 9 shows the obtained dependences of the FMR linewidth (ΔH) on the film thickness. These dependences, for films of both orientations, clearly show two distinct branches, characterizing two alternating stages of epitaxial growth. The descending branch (to the left of the minimum) at small thicknesses reflects the influence of epitaxial elastic stresses in the films arising from the difference in the UC- parameter at the boundary with the substrate, and the ascending branch (to the right of the minimum) indicates that in thicker films, due to the weakening of the orienting influence of the substrate, local disturbances of the crystalline order occur, and various extended defects accumulate (low-angle and high-angle boundaries, mosaicism, antiphase boundaries, etc.), i.e., a gradual transition to the growth of a polycrystalline layer occurs. The minimum ΔH(FMR) corresponds to films in which significant relaxation of epitaxial stresses has occurred, but the concentration of defects characteristic of the polycrystalline state is still low.

Further work toward producing $Lu_3Fe_5O_{12}$ garnet films with a narrower FMR linewidth

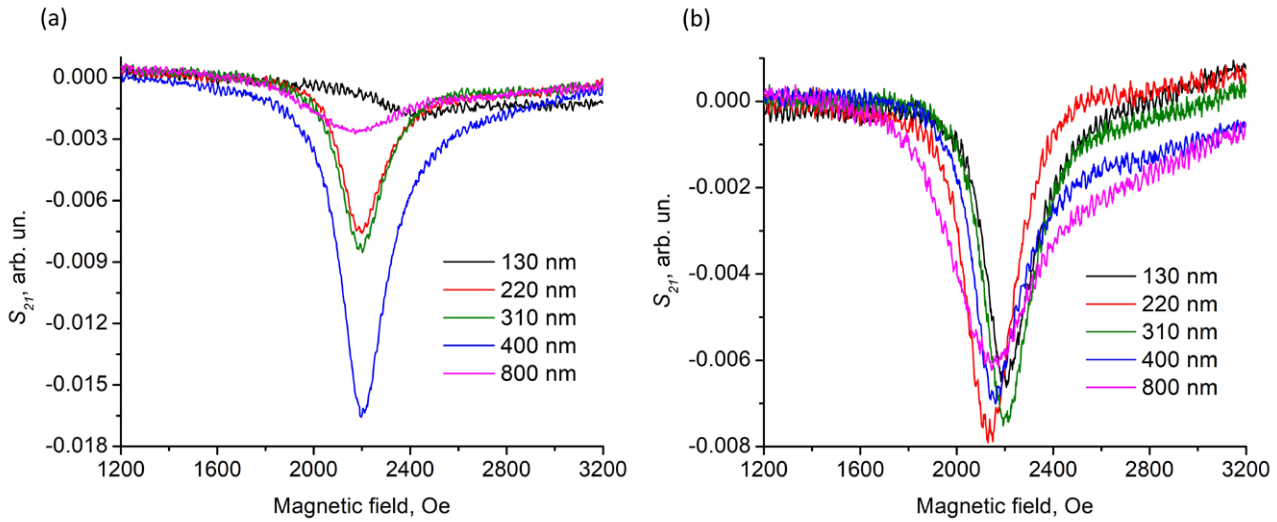

Fig. 8. FMR spectra of $Lu_3Fe_5O_{12}$ films of various thicknesses on $Gd_3Ga_5O_{12}$(111) (a) and $Gd_3Ga_5O_{12}$(210) (b) substrates. Microwave frequency is 9 GHz

requires a more detailed study of the influence of temperature and film deposition rate, taking into account the results of this paper.

4. Conclusions

$Lu_3Fe_5O_{12}$ films of varying thickness were synthesized for the first time using the MOCVD method on $Nd_3Ga_5O_{12}(111)$, $Gd_3Ga_5O_{12}(111)$, $Gd_3Ga_5O_{12}(210)$, $Gd_3(AlGa_4)O_{12}(111)$, and $Y_3Al_5O_{12}(111)$ substrates. X-ray diffraction (θ–2θ and ϕ-scanning) demonstrated the epitaxial nature of the films, and their magnetic properties were studied using ferrimagnetic resonance spectroscopy. A systematic study of the dependence of the FMR linewidth of $Lu_3Fe_5O_{12}$ on the mismatch between the unit cell parameters of the film and the substrate was performed for the first time. It was found that the minimum ΔH(FMR) of $Lu_3Fe_5O_{12}$ films is achieved on $Gd_3(AlGa_4)O_{12}$ substrates, which have a minimal mismatch between the unit cell parameters and the film. It has been shown that the dependence of ΔH(FMR) on film thickness is extreme, with the minimum corresponding to a film thickness at which significant relaxation of epitaxial stresses has occurred, but the concentration of defects characteristic of the polycrystalline state is still low. Taking these factors into account will enable the production of Lu-iron garnet films with a narrower ferromagnetic resonance linewidth, which could be used in various areas of spintronics as sensitive elements in microwave detectors.

Author contributions

A. A. Hafizov and R. Gu conducted the thin-film vapor-phase deposition experiments. M. N. Markelova developed the study concept, processed the X-ray diffraction data, and wrote the manuscript. I. E. Graboy developed the methodology and wrote the manuscript. V. A. Amelichev conducted the thin-film X-ray diffraction experiments. D. A. Volkov and D. A. Gabrielyan conducted the FMR absorption spectroscopy experiments and edited the manuscript. Safin A. R. – research concept, methodology development, text editing. Nikitov S. A. – scientific supervision, research concept, methodology development. Kaul A. R. – scientific supervision, research concept, methodology development, text editing.

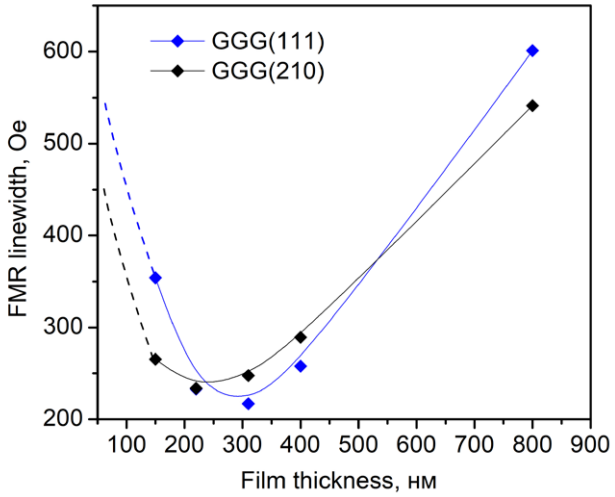

Fig. 9. Dependence of FMR linewidth on the $Lu_3Fe_5O_{12}$ film thickness on $Gd_3Ga_5O_{12}(111)$ and $Gd_3Ga_5O_{12}(210)$ substrates

Conflict of interests

The authors declare that they have no known competing financial interests or personal relationships that could have influenced the work reported in this paper.

References

1. Yang Y., Liu T., Bi L., Deng L. Recent advances in development of magnetic garnet thin films for applications in spintronics and photonics. *Journal of Alloys and Compounds*. 2021;860: 158235. https://doi.org/10.1016/j.jallcom.2020.158235

2. Borisenko V. E., Danilyuk A. L., Migas D. B. *Spintronics**. Laboratoriya znaniy Publ.; 2017. 229 p. (in Russ.)

3. Nikitov S. A., Kalyabin D. V., Lisenkov I. V… Pavlov E. S. Magnonics: a new research area in spintronics and spin wave electronics. *Physics-Uspekhi*. 2015;58: 1002–1028. https://doi.org/10.3367/UFNr.0185.201510m.1099

4. Žutić I., Fabian J., Das Sarma S. Spintronics: fundamentals and applications. *Reviews of Modern Physics*. 2004;76(2): 323–410. https://doi.org/10.1103/RevModPhys.76.323

5. Fert A. Nobel lecture: origin, development, and future of spintronics*. *Reviews of Modern Physics*. 2008;80(4): 1517–1530. https://doi.org/10.1103/RevModPhys.80.1517

6. Hirohata A., Yamada K., Nakatani Y., … Hillebrands B. Review on spintronics: principles and device applications. *Journal of Magnetism and Magnetic Materials*. 2020;509: 166711. https://doi.org/10.1016/j.jmmm.2020.166711

7. Chechenin N. G., Dzhun I. O., Babaytsev G. V., Kozin M. G., Makunin A. V., Romashkina I.L. FMR damping in thin films with exchange bias. *Magnetochemistry*. 2021;7(5): 70. https://doi.org/10.3390/magnetochemistry7050070

8. Geller S. Crystal chemistry of the garnets. *Zeitschrift für Kristallographie*; 1967;125: 1-47. https://doi.org/10.1524/zkri.1967.125.16.1

9. Liu C., Chen J., Liu T., … Wu M. Long-distance propagation of short-wavelength spin waves. *Nature Communications*. 2018;9(1): 738. https://doi.org/10.1038/s41467-018-03199-8

10. Zhu D., Zhao W. Threshold current density for perpendicular magnetization switching through spin-orbit torque. *Physical Review Applied*. 2020;13(4): 044078. https://doi.org/10.1103/PhysRevApplied.13.044078

11. Hahn C., de Loubens G., Klein O., Viret M., Naletov V. V., Ben Youssef J. Comparative measurements of inverse spin Hall effects and magnetoresistance in YIG/Pt and YIG/Ta. *Physical Review B*. 2013;87(17): 174417. https://doi.org/10.1103/PhysRevB.87.174417

12. Knauer S., Davídková K., Schmoll D., … Chumak A. V. Propagating spin-wave spectroscopy in a liquid-phase epitaxial nanometer-thick YIG film at millikelvin temperatures. *Journal of Applied Physics*. 2023;133(14): 143905. https://doi.org/10.1063/5.0137437

13. Jermain C. L., Paik H., Aradhya S. V., Buhrman R. A., Schlom D. G., Ralph D. C. Low-damping sub-10-nm thin films of lutetium iron garnet grown by molecular-beam epitaxy. *Applied Physics Letters*. 2016;109(19): 192408. https://doi.org/10.1063/1.4967695

14. Wu X., Wang X., Liu Y., … Zhu J. Study on dielectric and magnetodielectric properties of $Lu_3Fe_5O_{12}$ ceramics. *Applied Physics Letters*. 2009;95: 182903. https://doi.org/10.1063/1.3259651

15. Hou Y. Epitaxial growth and observation of the magnetodielectric effect in ferrimagnetic $Lu_3Fe_5O_{12}$ films. *Journal of Physics D: Applied Physics*. 2018;51(27): 275001. https://doi.org/10.1088/1361-6463/aac8d1

16. Hioki T., Hashimoto Y., Saitoh E. Bi-reflection of spin waves. *Communications Physics*. 2020;3: 188. https://doi.org/10.1038/s42005-020-00455-6

17. Volkov D. A., Gabrielyan D. A., Matveev A. A., … Nikitov S. A. Spin pumping from $Lu_3Fe_5O_{12}$. *JETP Letters*. 2024;119(5): 357–362. https://doi.org/10.1134/S0021364024600150

18. Dubs C., Surzhenko O. Magnetically compensated nanometer-thin Ga-substituted yttrium iron garnet (Ga:YIG) films with robust perpendicular magnetic anisotropy. *Advanced Electronic Materials*. 2025;11(15): e00232. https://doi.org/10.1002/aelm.202500232

19. Arsad A. Z., Zuhdi A. W. M., Ibrahim N. B., Hannan M. A. Recent advances in yttrium iron garnet films: methodologies, characterization, properties, applications, and bibliometric analysis for future research directions. *Applied Sciences*. 2023;13(2): 1218. https://doi.org/10.3390/app13021218

20. Yakovlev Yu. M., Gendelev S. Sh. *Iron ferrites monocrystals in radioelectonics**. "Sovetskoye Radio" Publ.; 1975. 360 p. (in Russ.)

21. Yushchuk S. I. Layered structure of epitaxial yttrium iron garnet films. *Technical Physics*. 1999;44: 1454–1456. https://doi.org/10.1134/1.1259547

22. Prokopov A. R., Vetoshko P. M., Shumilov A. G., … Belotelov V. I. Epitaxial Bi–Gd–Sc iron-garnet films for magnetophotonic applications. *Journal of Alloys and Compounds*. 2016;671: 403–407. https://doi.org/10.1016/j.jallcom.2016.02.036

23. Soumah L., Beaulieu N., Qassym L., … Anane A. Ultra-low damping insulating magnetic thin films get perpendicular. *Nature Communications*. 2018;9(1): 3355. https://doi.org/10.1038/s41467-018-05732-1

24. Yamahara H., Feng B., Seki M., … Tabata H. Flexoelectric nanodomains in rare-earth iron garnet thin films under strain gradient. *Communications Materials*. 2021;2: 95. https://doi.org/10.1038/s43246-021-00199-y

25. Khurana B., Kaczmarek A. C., Chou C.-T., … Ross C. A. Rare earth iron garnet superlattices with sub-unit-cell composition modulation. *ACS Nano*. 2024;18(52): 35269–35275. https://doi.org/10.1021/acsnano.4c11117

26. Ahamed E. I., Sarker M. S., Yamahara H., … Tabata H. Spin wave perturbation in rare-earth iron garnet thin films with epitaxial strain relaxation. *APL Materials*. 2025;13: 041114. https://doi.org/10.1063/5.0257413

27. Krichevtsov B. B., Gastev S. V., Suturin S. M., … Sokolov N. S. Magnetization reversal in YIG/GGG(111) nanoheterostructures grown by laser molecular beam epitaxy. *Science and Technology of Advanced Materials*. 2017;18(1): 351–363. https://doi.org/10.1080/14686996.2017.1316422

28. Samoilenko K. D., Volkov D. A., Gabrielyan D. A., … Nikitov S. A. Spintronic detector of linearly polarized microwave radiation based on a ferromagnet/normal metal heterostructure. *JETP Letters*, 2025;121(7): 554–561. https://doi.org/10.1134/S002136402460530X

29. Markelova M. N., Hafizov A. A., Shi X., … Kaul A. R. Chemical vapor deposition of $Tm_3Fe_5O_{12}$ epitaxial films, investigation of their structure and properties in the terahertz range. *Condensed Matter and Interphases*. 2025;27(1): 104–114. https://doi.org/10.17308/kcmf.2025.27/12488

30. Popova E., Keller N., Jomard F., … Tessier M. Exchange coupling in ultrathin epitaxial yttrium iron garnet films. *The European Physical Journal B - Condensed Matter*. 2003;31: 69–74. https://doi.org/10.1140/epjb/e2003-00010-2

31. Bossak A., Graboy I., Gorbenko O., … Zandbergen H. W. XRD and HREM studies of epitaxially stabilized hexagonal orthoferrites $RFeO_3$ (R = Eu–Lu). *Chemistry of Materials*. 2004;16(9): 1751–1755. https://doi.org/10.1021/cm0353660

32. Kaul A. R., Nygaard R. R., Ratovskiy V. Yu., Vasiliev A. L. TSF-MOCVD – a novel technique for chemical vapour deposition on oxide thin films and layered heterostructures. *Condensed Matter and Interphases*. 2021;23(3): 396–405. https://doi.org/10.17308/kcmf.2021.23/3531

* *Translated by author of the article*

Information about the authors

Abduvosit A. Hafizov, graduate student at the Higher School of Material Science, Lomonosov Moscow State University (Moscow, Russian Federation).

https://orcid.org/0009-0003-0740-8180

abduvosithafizov220@gmail.com

Maria N. Markelova, Cand. Sci. (Chem.), Research Fellow at the Department of Chemistry, Lomonosov Moscow State University (Moscow, Russian Federation).

https://orcid.org/0000-0002-1014-9437

maria.markelova@gmail.com

Ruoxuan Gu, master degree student at the Higher School of Material Science, Lomonosov Moscow State University (Moscow, Russian Federation).
https://orcid.org/0009-0006-5998-2194
grxuan969@outlook.com

Igor E. Graboy, Cand. Sci. (Chem.), Senior Research Fellow at the Department of Chemistry, Lomonosov Moscow State University (Moscow, Russian Federation).
https://orcid.org/0009-0003-7011-2200
graboi@inorg.chem.msu.ru

Vadim A. Amelichev, Cand. Sci. (Chem.), Technical Director at S-Innovations (Moscow, Russian Federation).
https://orcid.org/0000-0003-0886-9854
mailto:vadim.amelichev@gmail.com

Dmitry A. Volkov, Junior Researcher at the Kotelnikov Institute of Radio Engineering and Electronics, Russian Academy of Sciences; Assistant at Moscow Power Engineering Institute (Moscow, Russian Federation).
https://orcid.org/0009-0004-1655-8348
d.a.volkov.work@gmail.com

David A. Gabrielyan, Junior Researcher at the Kotelnikov Institute of Radio Engineering and Electronics, Russian Academy of Sciences; Assistant at Moscow Power Engineering Institute (Moscow, Russian Federation).
https://orcid.org/0000-0003-0801-0134
davidgabrielyan1997@gmail.com

Ansar R. Safin, Dr. Sci. (Phys.–Math.), Leading Researcher, Head of the Laboratory, Kotelnikov Institute of Radio Engineering and Electronics of the Russian Academy of Sciences; Professor, Moscow Power Engineering University; Professor, Moscow Institute of Physics and Technology (National Research University); Professor, National Research University Higher School of Economics (Moscow, Russian Federation).
https://orcid.org/0000-0001-6507-6573
arsafin@gmail.com

Sergey A. Nikitov, Dr. Sci. (Phys.–Math.), Acting Director, Head of Laboratory, Kotelnikov Institute of Radio Engineering and Electronics of the Russian Academy of Sciences; Head of Department, Moscow Institute of Physics and Technology (National Research University) (Moscow, Russian Federation); Head of Laboratory, N. G. Chernyshevsky Saratov National Research State University (Saratov, Russian Federation); Academician, Russian Academy of Sciences (Moscow, Russian Federation).
https://orcid.org/0000-0002-2413-7218
nikitov@cplire.ru

Andrey R. Kaul, Dr. Sci. (Chem.), Full Professor at the Chair of Inorganic Chemistry, Lomonosov Moscow State University, Moscow, Russian Federationю
https://orcid.org/0000-0002-3582-3467
arkaul@mail.ru

Received November 19, 2025; approved after reviewing December 1, 2025; accepted for publication December 15, 2025; published online April 01, 2026.

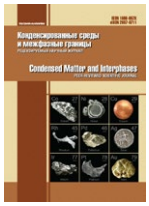

ISSN 1606-867X (Print)
ISSN 2687-0711 (Online)
Condensed Matter and Interphases
Kondensirovannye Sredy i Mezhfaznye Granitsy
https://journals.vsu.ru/kcmf/

Short communication

Short communication
https://doi.org/10.17308/kcmf.2026.28/13565

Lead-free smart materials based on alkali metal niobates: phase formation, crystal structure, macroscopic responses

S. I. Dudkina[1], D. I. Zorin[1], E. V. Glazunova[1,2], L. A. Shilkina[1], I. N. Andryushina[1]✉, K. P. Andryushin[1,2], I. A. Verbenko[1], L. A. Reznichenko[1]

[1]Physics Research Institute of Southern Federal University, 194, Stachki ave., Rostov-on-Don 344090, Russian Federation

[2]Kh. I. Ibragimov Integrated Research Institute of the Russian Academy of Sciences, 21a, V. Aliyev Ave. (Staropromyslovoe Shosse), Grozny 364020, Chechen Republic, Russian Federation

Abstract

Objectives: In the global practice of researching various materials for piezoelectric devices, one of the first places is occupied by functional (smart) materials based on lead-containing compositions. However, the transition to environmentally friendly products, necessitated by the formation of new Russian and European legislative frameworks, has forced the search for other materials science solutions by eliminating lead from the elemental base of materials. An alternative to known compositions are solid solutions based on alkali metal niobates from morphotropic heterophase regions of the corresponding binary and ternary systems, characterized by extreme properties near the interphase boundaries. However, they have not found wide application in practice due to difficulties in phase formation during synthesis and the formation of a dense ceramic framework during sintering.

Experimental: In this work, using mechanical activation and hot pressing procedures, which were not previously used in such environments, it was possible to obtain lead-free, non-toxic ferroelectric piezoelectric ceramics with improved macroscopic responses due to the transformation of the phase coexistence regions.

Conclusions: As a result of the research, multi-frequency materials have been developed and created, including those with an elevated Curie temperature, piezoelectric sensitivity, thermal stability, and pyroelectric effect for various piezoelectric applications.

Keywords: Lead-free piezoceramics, Alkali metal niobates, Solid solutions, Interphase boundaries, Mechanical activation, Hot pressing

***Funding*:** The study was carried out with financial support from the Ministry of Science and Higher Education Russian Federation (State assignment in the field of scientific activity), within the framework of scientific project No. FENW-2026-0022

***For citation*:** Dudkina S. I., Zorin D. I., Glazunova E. V., Shilkina L. A., Andryushina I. N., Andryushin K. P., Verbenko I. A., Reznichenko L. A. Lead-free smart materials based on alkali metal niobates: phase formation, crystal structure, macroscopic responses. *Condensed Matter and Interphases*. 2026;28(1): 137–142. https://doi.org/10.17308/kcmf.2026.28/13565

Для цитирования: Дудкина С. И., Зорин Д. И., Глазунова Е. В., Шилкина Л. А., Андрюшина И. Н., Андрюшин К. П., Вербенко И. А., Резниченко Л. А. Бессвинцовые интеллектуальные материалы на основе ниобатов щелочных металлов: фазообразование, кристаллическая структура, макроотклики. *Конденсированные среды и межфазные границы*. 2026;28(1): 137–142. https://doi.org/10.17308/kcmf.2026.28/13565

✉ Inna N. Andryushina, e-mail: futur6@mail.ru

1. Introduction

Recently, in the practice of using various materials in real sectors of the global economy, functional materials, primarily smart materials (SMs), "capable of actively counteracting external factors and adapting to them after assessing the nature of the external impact and their own condition," have come to the forefront. [1]. Among them, those whose operation is based on the piezoelectric effect, the conversion of mechanical force into an electrical signal and vice versa, are in high demand. Their main disadvantage is the presence of lead in the compositions, an element belonging to the first hazard class [2, 3]. The transition to environmentally friendly products that has now begun is due to the formation of a new Russian [4] and European [5, 6] legislative frameworks, which has forced us to look for other materials science solutions by excluding lead from the elemental base of SMs. An analysis of bibliographic information and patent literature [7–17] showed that the undisputed alternative to global brands of materials are SMs based on alkali metal niobates (AMN) from morphotropic heterophase regions of the corresponding binary and ternary systems, characterized by extreme properties near the interphase boundaries: rhombic-rhombohedral in the (Na,Li)NbO_3 system and rhombic-rhombic of different multiplicity, characteristic of different configurations of rotations of oxygen octahedra, in systems based on (Na, K)NbO_3 [18]. However, they have not yet found wide application in practice. This is largely due to the impossibility of obtaining them by traditional methods, which, in turn, is associated with the complexity of their crystalline structure; the presence of extensive polymorphism, which destabilizes the structure of materials; the ease of violation of the stoichiometry of a given composition due to the increased volatility of alkaline cations; polarization electrolysis; strong dependence of properties on the thermodynamic history (preparation conditions) [19].

This study, driven by current trends in the greenification of electronic components, aims to demonstrate the potential for improving the properties of SMs with reduced mass capacity and dimensions for use in devices where weight is critical; an extended frequency range, enabling the use of SMs in digital information processing systems; a high operating temperature limit for the creation of contact thermal sensors; increased thermal stability and, consequently, improved reliability and resistance to environmental factors.

2. Experimental

The objects of the study were sodium, potassium, and lithium niobates and solid solutions (SS) based on them, including those modified with various elements. The objects were obtained by one/two-stage solid-phase synthesis followed by sintering using conventional ceramic technology (CCT) or hot pressing (HP) with the simultaneous application of temperature and pressure to the powder press blank. Process procedures for obtaining objects are shown in the table: temperatures T_1, T_2 and isothermal holding time τ_1, τ_2 first and second synthesis respectively, sintering temperature, T_{si}, and the holding time during sintering, τ_{si}. In all cases, mechanical activation (MA) procedures were used for 10 min at the stages of preparing the initial precursors or preparing the batches. Mechanical activation (mechanical impact on objects by crushing them) was carried out in an AGO-2 high-energy grinding planetary ball mill manufactured by Novits (Novosibirsk). Grinding was carried out in an ethyl alcohol environment; the drum rotation frequency was 1050 rpm. Hydrocarbonates, carbonates and oxides of the corresponding elements of at least analytical grade (pure for analysis) were used as raw materials. Hot press sintering was carried out in a UGP-1 (disks with dimensions Ø10×1 mm^2) under pressure, R, equal to 200 kg/cm^2, developed and designed at the Research Institute of Physics [20]. The selection of the HP modes was made based on shrinkage curves and adjusted in accordance with the data from microstructural analysis. Polarization of the samples was carried out in a polyethylenesiloxane fluid PES-5 at 413 K for (15–20) min in a field of strength of (5–6) kV/mm.

X-ray diffraction studies were carried out by powder diffraction using a DRON-3 diffractometer (filtered Co$K\alpha$-radiation, Bragg-Brentano focusing scheme). The study involved crushed ceramic objects, which made it possible to exclude the influence of surface effects, stresses, and textures that arise during the ceramic

Table. Elemental compositions, production conditions, and electrophysical characteristics of the objects under study are the basis of the materials being developed

No.	Elemental composition, Wt.%	Production conditions (T_1, T_2, T_{si}) K $\tau_1 = \tau_2 = 5$ hours $\tau_{si} = 1.5$ hours	Electrophysical characteristics (with MA and HP; without MA and HP*)			
			$\varepsilon^T_{33}/\varepsilon_0$	K_p	$\lvert d_{31}\rvert$, pC/N	Q_M
low-frequency materials						
1	Na_2O = 8.75–9.72; K_2O = 5.32–5.37; Nb_2O_5 = 75.05–75.76; CdO = 9.15–10.88	HP T_1 = 1220 K; T_2 = 1240 K; T_{si} =1240 K;	1360–2020 (1280–1930)*	0.32–0.33 (0.30–0.31)*	67–70 (62–64)*	1000–1090 (960–1040)*
mid-frequency materials						
2	Na_2O = 8.49–8.67; K_2O = 11.00–11.25; Li_2O = 0.49–0.65; NiO = 0.82–0.83; Nb_2O_5 = 60.68–61.98; Ta_2O_5 = 11.20–11.44; Sb_2O_5 = 5.35–7.15	HP T_1=1223 K; T_{si}=1393 K;	1095–1097 (1040–1045)*	0.42–0.43 (0.415–0.42)*	80–84 (72–76)*	45–49 (55–60)*
high-frequency materials						
3	Na_2O = 16.20–16.68; Li_2O = 1.12–1.15; Nb_2O_5 =8 1.25–81.98; SrO = 0.19–1.43	HP T_1 = 1143 K; T_2 = 1193 K; T_{si} = 1433 K;	110–125 (114–135)*	0.136–0.225 (0.125–0.193)*	7.1–11.3 (7.0–11.0)*	904–1338 (855–1060)*
4	Na_2O = 8.56–8.75; K_2O = 12.75–13.04; Nb_2O_5 = 77.28–77.35; CuO = 1.16–1.17	HP T_1=1223 K; T_{si} =1373 K;	240–355 (290–370)*	0.20–0.32 (0.18–0.29)*	20.0–30.0 (19.0–27.0)*	215–500 (205–400)*
high-temperature materials						
5	Li_2O = 21.15–21.65; Nb_2O_5 = 76.11–77.89; NiO = 0.22–1.32; TiO_2 = 1.24–1.41	HP T_1= 1050 K; T_{si} =1240 K;	48–51 $T_к$ > 1273 K (50–52)*	0.015–0.020 (0.010–0.012)*	0.37–0.51 (0.30–0.35)*	60–70 (50–57)*
highly sensitive materials						
6	Na_2O = 8.69–8.91; K_2O = 13.20–13.53; Nb_2O_5 = 74.51–76.37; CdO = 3.60–3.61	HP T_1=1043 K; T_2= 1093 K; T_{si} =1233 K;	510–610 (540–650)*	0.27–0.34 (0.25–0.32)*	28–32 $\lvert g_{31}\rvert$ = 5.9–6.2 mV·m/N (26–29)* ($\lvert g_{31}\rvert$=5.0–5.4 mV·m/N)*	115–123 (115–125)*
thermostable materials						
7	Na_2O = 8.54–8.67; K_2O = 11.06–11.22; Li_2O = 0.32–0.33; Sb_2O_5 = 3.44–3.49; Ta_2O_5 = 11.28–11.44; Nb_2O_5 = 61.05–61.95; NiO = 1.94–2.87; B_2O_3 = 0.97–1.44	HP T_1= 1223 K; T_{si} =1273 K;	1194–1200 ($\Delta\varepsilon^T_{33}/\varepsilon_0$ = 2–3 %) (1140–1150)* ($\Delta\varepsilon^T_{33}/\varepsilon_0$ = 4–5 %)*	0.30–0.32 (ΔK_p=5–6 %) (0.28–0.30)* (ΔK_p = 6–7 %)*	59–62 ($\Delta\lvert d_{31}\rvert$=5–6 %) (53–58)* ($\Delta\lvert d_{31}\rvert$ =6–7 %)*	80–82 (ΔQ_M = 3 %) (72–76)* (ΔQ_M = 4 %)*
pyroelectric materials						
8	Na_2O = 18.38–18.73; Nb_2O_5 = 78.79–80.32; TiO_2 = 0.49–1.46; CoO = 0.46–1.37	HP T_1=1070 K; T_2= 1120 K; T_{si} = 1380 K	180–220 $\gamma = (1.44–1.5)\cdot10^{-4}$ C/m² ·K (205–240)* ($\gamma = (1.3–1.4)\cdot10^{-4}$ C/m² ·K)*	0.16–0.168 (0.145–0.150)*	11–12 (10–11)*	340–390 (280–320)*
9	Na_2O = 16.21–18.73; Nb_2O_5 = 69.52–80.32; TiO_2 = 0.49–7.37; NiO = 0.46–6.90	HP T_1 = 1070 K; T_2 = 1120 K; T_{si} = 1380 K	170-250 $\gamma = (1.6–1.7)\cdot10^{-4}$ C/m² ·K (195–230)* ($\gamma = (1.5–1.6)\cdot10^{-4}$ C/m² ·K)*	0.13-0.16 (0.12–0.14)*	9-10 (8–9)*	320-380 (250–310*

manufacturing process. The calculation of structural parameters was carried out according to the methodology presented in the work [20]. The errors in measuring the structural parameters had the following values: linear $\Delta a = \Delta b = \Delta c = \pm(0.002–0.004)$ Å; angular $\Delta\alpha(\beta) = 0.05^{o}$; volume $\Delta V = \pm 0.05 Å^3$.

X-ray density was calculated using the formula: $\rho_{xray} = MZ / (N_A V)$, where M is the molecular weight, Z is the number of formula units per unit cell, N_A – Avogadro's number, V – volume of the unit cell. The experimental density, ρ_{exp}, of the samples was determined by hydrostatic weighing in octane. Relative density, ρ_{rel}, was calculated using the formula $(\rho_{exp}/\rho_{xray})\cdot 100$ %.

To certify the electrophysical properties of the investigated SSs, measurements of their dielectric, piezoelectric and electroelastic parameters were carried out at room temperature in accordance with [21]. In this case, the relative permittivity of polarized samples was determined, $\varepsilon^{T}_{33}/\varepsilon_0$, piezomodule, $|d_{31}|$, the coefficient of electromechanical coupling of the planar oscillation mode, K_p, mechanical quality factor, Q_M, including specific parameters of the developed materials (Curie temperature, T_C, piezo sensitivity, $|g_{31}|$, pyroelectric coefficient, γ, thermal stability – $\Delta\varepsilon^{T}_{33}/\varepsilon_0$, ΔK_p, $\Delta|d_{31}|$, ΔQ_M).

3. Results and discussion

The Table shows the optimized elemental compositions of the studied objects: the basis of the developed materials, the technological conditions for their production, and the main electrophysical characteristics.

As can be seen from the table, the use of MA and HP operations during the two main stages (synthesis and sintering) of ceramic production led to a significant improvement in the macro properties of the objects. The reason for the observed phenomenon may be the transformation of their internal structure (crystalline, granular) as a result of the influence of external factors. Thus, the grinding of batches during MA led to the acceleration of diffusion phenomena during the synthesis process, and sintering of synthesized powders under pressure led to the activation of mass transfer during recrystallization. This ensured a decrease in the temperatures of synthesis and sintering and, as a consequence, a reduction in the extent of morphotropic heterophase regions in the corresponding SS systems and a "shift" of the selected objects into single-phase regions.

Fig. 1 shows X-ray diffraction patterns of some of the materials presented for illustration purposes. X-ray diffraction analysis has shown

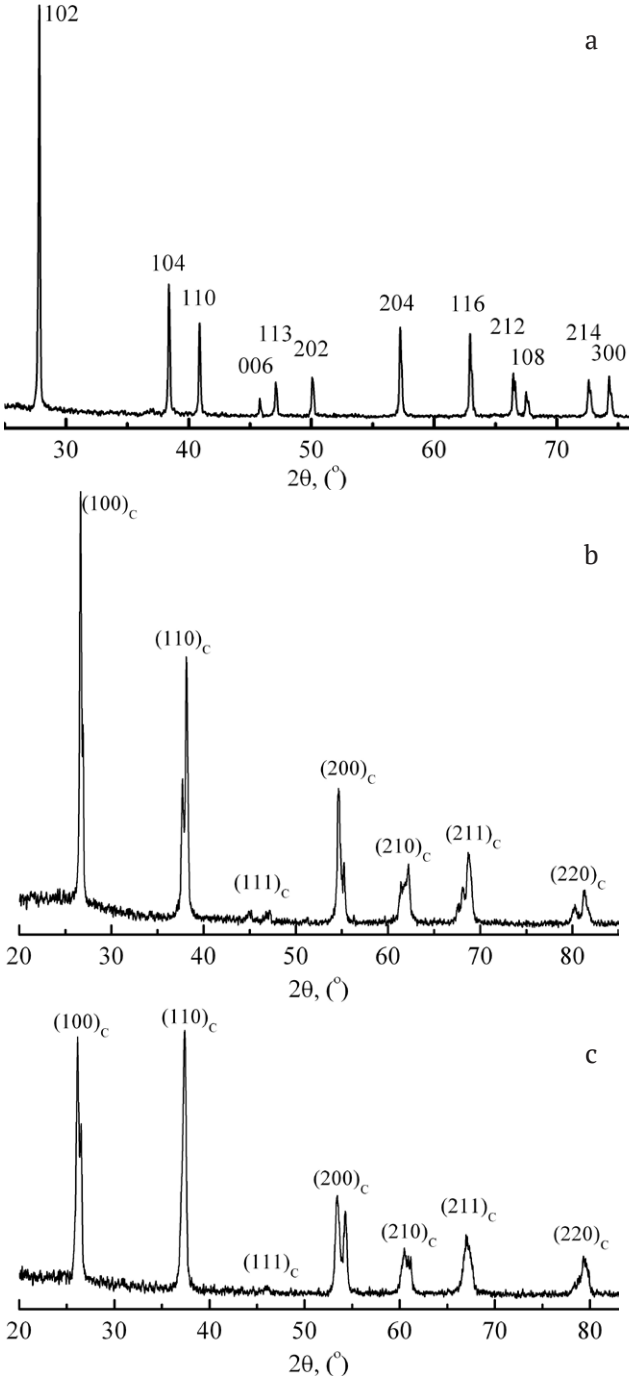

Fig. 1. X-ray diffraction patterns of materials: high-temperature (ilmenite-type structure) – a; high-frequency (perovskite-type structure) – b; high-sensitivity (perovskite-type structure) – c

that the resulting ceramic compositions are pure and have a density higher than 95 % of the theoretical value, which is typical for the technologies used [22]. The X-ray diffraction patterns show that all materials are well structured without impurity phases. This implementation of more favorable conditions for diffusion and recrystallization processes ensures the formation of a more perfect microstructure of ceramics [23] and, as a consequence, improving their dielectric and piezoelectric properties.

The specific gravity of all the developed materials is about 4 g/cm^3, which is half as much as in the known Pb-containing analogues. This allows, as mentioned above, to use these materials in devices in which weight characteristics are decisive.

The obtained low-frequency materials can be used in low-frequency receiving devices – hydrophones, microphones, seismic receivers. Medium-frequency materials can be used in radio-electronic devices operating in reception mode, including in transducers of ultrasonic (US) transmitters.

High-frequency materials can be used for ultrasonic delay lines on bulk and surface waves and medical diagnostic devices. Highly sensitive materials can be useful, for example, in devices for measuring mechanical impacts (pressure). High-temperature materials can be used to create reusable generator-type piezoelectric sensors for monitoring equipment (nuclear reactors, nuclear missile systems) subject to extreme thermal effects. Thermally stable materials will find application in the creation of knock sensors for internal combustion engines. Pyroelectric materials will be useful for creating highly efficient thermoelements in radiation pyrometry devices based on pyroelectric phenomena.

4. Conclusions

Thus, the analysis of the above information showed that it is possible to improve the properties of ferroelectric ceramic materials, free of toxicity and lead, with low specific gravity by using mechanical activation during synthesis followed by hot press sintering for applications in devices where weight characteristics are decisive, as well as in multi-frequency systems as thermocouples and in other electronic devices.

Author contributions

The authors contributed equally to this article.

Conflict of interests

The authors declare that they have no known competing financial interests or personal relationships that could have influenced the work reported in this paper.

References

1. Mikhailin Yu. A. *Intelligent Materials. Polymer Materials. Products. Equipment. Technologies**. 2004; 8 (63): 6–8. (in Russ.)

2. *List of Pollutants Subject to State Regulation in the Field of Environmental Protection**. Approved by Decree of the Government of the Russian Federation of July 8, 2015, No. 1316-R. (in Russ.)

3. *On Amendments to the Federal Law "On Environmental Protection" and Certain Legislative Acts of the Russian Federation**. Federal Law of July 21, 2014, No. 219-FZ. (in Russ.)

4. *Strategy for the Scientific and Technological Development of the Russian Federation**. Approved by Criminal Code of the President of the Russian Federation of December 1, 2016, No. 642. (in Russ.)

5. Directive 2002/95/EU of the European Parliament and of the Council of 27 January 2003 on the restriction of the use of certain hazardous substances in electronic equipment. *Official Journal of the European Union L. 37*. 2003;46: 19–23.

6. Directive 2011/65/EU of the European Parliament and of the Council of 8 June 2011 on the restriction of the use of certain hazardous substances in electrical and electronic equipment. *Official Journal of the European Union. L. 174*. 2011;54: 88–110.

7. Saito Y., Takao H., Tani T., Tatsuhiko N., Kazumasa T., Takahiko H., Toshiatsu N., … Masaya N. Lead-free piezoceramics. *Nature*. 2004;432: 84–87. https://doi.org/10.1038/nature03028

8. Zhang S., Lee H. J., Ma C., Tan X. Sintering effect on microstructure and properties of (K,Na)NbO_3 ceramics. *Journal of the American Ceramic Society*. 2011;94: 3659–3665. https://doi.org/10.1111/j.1551-2916.2011.04833.x

9. Liu L. J., Huang Y. M., Li Y. H., … Thi M. P. Orthorhombic to tetragonal structural phase transition in $Na_{0.5}K_{0.5}NbO_3$-based ceramics. *Materials Letters*. 2012;68: 300–302. https://doi.org/10.1016/j.matlet.2011.10.103

10. Bomlai P. Sintering, microstructure and electrical properties of MnO_2 and CuO doped $[Na_{0.515}K_{0.485}]_{0.94}Li_{0.06}(Nb_{0.99}Ta_{0.01})O_3$ ceramics. *Advanced Materials Research*. 2013;770: 258. https://doi.org/10.4028/www.scientific.net/AMR.770.258

11. Koruza J., Bell A. J., Frömling T., Webber K. G., Wang K., Rödel J. Requirements for the transfer of lead-free piezoceramics into application. *Journal of Materiomics*. 2018;4: 13–26. https://doi.org/10.1016/j.jmat.2018.02.001

12. Zhang Y., Li M., Yang S., Zhai J. Low-temperature sintering of KNN-based lead free ceramics. *Solid State Communications*. 2021;324: 114133. https://doi.org/10.1016/j.ssc.2020.114133

13. Zhao Y., Liu J., Yan D. Improved piezoelectric and strain performance of $Na_2B_4O_7$-doped (Li,K,Na)NbO_3 lead-free piezoceramics. *Journal of Materials Science*. 2019;54: 1126–1135. https://doi.org/10.1007/s10853-018-2906-z

14. Yu Z., Chen X., Su Y., … Liu P. Hot-press sintering $K_{0.5}Na_{0.5}NbO_3$–0.5 mol % Al_2O_3 ceramics with enhanced ferroelectric and piezoelectric properties. *Journal of Materials Science*. 2019;54: 13457–13466. https://doi.org/10.1007/s10853-019-03850-9

15. Ponomarev S. G., Smirnov A. V., Reznichenko A. V., … Solov'ev I. S. Vibrocompaction of lead-free piezoceramic material based on solid solutions of potassium and sodium niobates. *Glass and Ceramics*. 2019;(9): 31–36. https://doi.org/10.1007/s10717-020-00197-5

16. Shi W., Du J., Zhai Y., … Fu P. Intrinsic and extrinsic dielectric contributions to the electrical properties in $CaZrO_3$-doped KNN-based electrical/optical multifunctional ceramics. *Journal of Materials Science*. 2020;55: 5741–5749. https://doi.org/10.1007/s10853-020-04444-6

17. Lu Y., Zhang J., Zhou K., He L. Capacitive energy storage performance of lead-free sodium niobate-based antiferroelectric ceramics. *Journal of Materials Science*. 2023;58: 11886–11893. https://doi.org/10.1007/s10853-023-08769-w

18. Reznichenko L. A., Shilkina L. A., Razumovskaya O. N., Dudkina S. I., Gagarina E. S., Borodin A. V. Dielectric and piezoelectric properties of $NaNbO_3$-based solid solutions. *Inorganic Materials*. 2003;39(2): 139–151. https://doi.org/10.1023/a:1022194512814

19. Verbenko I. A., Reznichenko L. A. Lead-free ferroelectric ceramics based on alkali metal niobates: History, Technology, and Prospects. *Physics of Lead-Free Piezoactive and Related Materials. (Analysis of the Current State and Development Prospects): Proceedings of the Second International Youth Symposium, September 6–7, 2013, Rostov-on-Don – Tuapse*. Rostov-on-Don: Publishing House of the SKNC HSE SFedU APSN; 2013. Issue 2, Vol. 1. pp. 52–64. (in Russ.)

20. Fesenko E. G. *The perovskite family and ferroelectricity**. Moscow: Atomizdat Publ.; 1972. 248 p. (in Russ.)

21. *IEEE Standard on Piezoelectricity ANSI/IEEE Std. 176-1987*. New-York: IEEE; 1988. https://doi.org/10.1109/IEEESTD.1988.79638

22. Okazaki K. *Ceramic engineering for dielectrics*. Tokyo: Gakken Sha Publishing Co. Ltd; 1969. 332 p.

23. Dantsiger A. Ya., Razumovskaya O. N., Reznichenko L. A., … Rybyanets A. N. *Multicomponent systems of ferroelectric complex oxides: physics, crystal chemistry, and technology. Aspects of piezoelectric materials design**. Vol. 1, 2. Rostov-on-Don: MP "Kniga" Publ.; 2001-2002. 800 p. (in Russ.)

* *Translated by author of the article*

Information about the authors

Svetlana I. Dudkina, Senior Researcher, Department of Intelligent Materials and Nanotechnology, Physics Research Institute, Southern Federal University (Rostov-on-Don, Russian Federation).
https://orcid.org/0000-0003-3525-6973
s.i.dudkina@yandex.ru

Denis I. Zorin, postgraduate student, Research Assistant, Department of Intelligent Materials and Nanotechnology, Physics Research Institute, Southern Federal University (Rostov-on-Don, Russian Federation).
dezorin@sfedu.ru

Ekaterina V. Glazunova, Cand. Sci. (Chem.), Researcher, Department of Intelligent Materials and Nanotechnology, Physics Research Institute, Southern Federal University (Rostov-on-Don, Russian Federation).
https://orcid.org/0000-0002-2596-2471
kate93g@mail.ru

Lidiya A. Shilkina, Senior Researcher, Department of Intelligent Materials and Nanotechnology, Physics Research Institute, Southern Federal University (Rostov-on-Don, Russian Federation).
https://orcid.org/0000-0002-8048-3617
lid-shilkina@yandex.ru

Inna N. Andryushina, Cand. Sci. (Chem.), Senior Researcher, Department of Intelligent Materials and Nanotechnologies, Physics Research Institute, Southern Federal University (Rostov-on-Don, Russian Federation).
https://orcid.org/0000-0001-8058-4381
futur6@mail.ru

Konstantin P. Andryushin, Dr. Sci. (Phys.–Math.), Leading Researcher, Department of Intelligent Materials and Nanotechnology, Physics Research Institute, Southern Federal University (Rostov-on-Don, Russian Federation).
https://orcid.org/0000-0003-0147-8359
e-mail: kpandryushin@gmail.com

Ilya A. Verbenko, Dr. Sci. (Phys.–Math.), Director of the Physics Research Institute, Southern Federal University (Rostov-on-Don, Russian Federation).
https://orcid.org/0000-0001-6229-9691
iaverbenko@sfedu.ru

Larisa A. Reznichenko, Dr. Sci. (Phys.–Math.), Professor, Head of the Department of Intelligent Materials and Nanotechnology, Physics Research Institute, Southern Federal University (Rostov-on-Don, Russian Federation).
https://orcid.org/0000-0003-4591-1601
lareznichenko@sfedu.ru

Received January 15, 2026; accepted after reviewing February 9, 2026; accepted for publication February 16, 2026; published online April 01, 2026.

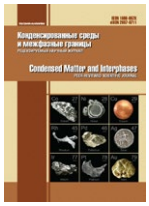

ISSN 1606-867X (Print)
ISSN 2687-0711 (Online)
Condensed Matter and Interphases
Kondensirovannye Sredy i Mezhfaznye Granitsy
https://journals.vsu.ru/kcmf/

Short communication

Short communication
https://doi.org/10.17308/kcmf.2026.28/13566

Electronic structure and spatial architecture of chemically deposited high-phosphorus nickel coatings for application in advanced microelectronics technologies

V. V. Pobedinsky[1,2], N. S. Buylov[1,2]✉, E. A. Ilina[1], D. L. Goloshchapov[1], E. S. Kersnovsky[1], I. V. Polshin[1], A. I. Chukavin[3], K. V. Zolnikov[4], P. P. Kutsko[2], P. L. Parmon[2], I. V. Semeykin[2], I. V. Koniaev[2], P. V. Seredin[1]

[1]*Voronezh State University,*
1, Universitetskaya pl., Voronezh 394018, Russian Federation

[2]*Research Institute of Electronic Technology,*
5, Staryh Bolshevikov st., Voronezh 394033, Russian Federation

[3]*Udmurt Federal Research Center Ural Branch of the Russian Academy of Sciences,*
34, T. Baramzina st., Izhevsk 426067, Russian Federation

[4]*Voronezh State University of Forestry and Technologies named after G. F. Morozov,*
8, Timiryazeva st., Voronezh 394087, Russian Federation

Abstract

Objectives: This article examines the suitability of chemically deposited high-phosphorus nickel-phosphorus coatings as barrier layers for Through-Silicon Via (TSV) technology. Energy-dispersive X-ray microanalysis revealed that the phosphorus content in the coating is 10.2 wt. % (17.8 at. %). This high phosphorus concentration ensures the coating remains in an amorphous state, which is a critical prerequisite for effective barrier performance.

Experimental: Using X-ray photoelectron spectroscopy and soft X-ray spectroscopy, it was determined that the spherical globular formations comprising the coating have a core–shell structure. It was also demonstrated that the phosphorus concentration in the shell is higher than in the core.

Conclusions: The results obtained are of significant interest for advancing modern semiconductor manufacturing technologies, particularly in the area of heterogeneous 3D integration.

Keywords: Electroless nickel plating, High-phosphorus nickel coatings, Barrier layer, TSV technology, Heterogeneous 3D integration

Funding: This work was supported by a grant from the Ministry of Science and Higher Education of the Russian Federation (Project No. FZGU-2026-0009).

Acknowledgements: The research was conducted using equipment from the Gallium Nitride and Silicon Electronics Laboratory at Voronezh State University and the Research Institute of Electronic Engineering. X-ray photoelectron spectra were obtained at the Center for Physical and Physico-Chemical Methods of Analysis, Study of Properties and Characteristics of Surfaces, Nanostructures, Materials, and Products at the Udmurt Federal Research Center of the Ural Branch of the Russian Academy of Sciences.

For citation: Pobedinsky V. V., Buylov N. S., Ilina E. A., Goloshchapov D. L., Kersnovsky E. S., Polshin I. V., Chukavin A. I., Zolnikov K. V., Kutsko P. P., Parmon P. L., Semeykin I. V., Koniaev I. V., Seredin P. V. Electronic structure and spatial architecture of chemically deposited high-phosphorus nickel coatings for application in advanced microelectronics technologies. *Condensed Matter and Interphases*. 2026;28(1): 143–147. https://doi.org/10.17308/kcmf.2026.28/13566

✉ Nikita S. Buylov, e-mail: buylov@phys.vsu.ru

Для цитирования: Побединский В. В., Буйлов Н. С., Ильина Е. А., Голощапов Д. Л., Керсновский Е. С., Польшин И. В., Чукавин А. И., Зольников К. В., Куцько П. П., Пармон П. Л., Семейкин И. В., Коняев И. В., Середин П. В. Электронное строение и пространственная структура химически осажденных высокофосфористых покрытий никеля для применения в передовых технологиях микроэлектроники. *Конденсированные среды и межфазные границы*. 2026;28(1): 143–147. https://doi.org/10.17308/kcmf.2026.28/13566

1. Introduction

Heterogeneous 3D integration technology is widely regarded as the most promising approach for advancing silicon microelectronics. The primary advantages of this technology include a significant increase in electronic device performance, a simultaneous reduction in heat generation, and a substantial decrease in chip footprint on printed circuit boards [1, 2].

The manufacturing of microelectronic devices using 3D technology involves the formation of through-silicon via (TSV) interconnects within a silicon wafer. Typically, TSVs are filled with copper through electroplating, which requires the deposition of adhesion, barrier, and seed layers onto their sidewalls [3–7].

The uniformity and continuity of the barrier and seed layers significantly affect not only the quality of copper filling in TSV holes but also the performance characteristics of the finished semiconductor devices. Traditionally, barrier and seed layers are deposited by physical vapor deposition (PVD) [8]. However, as the aspect ratio (AR > 5) of TSV holes increases, obtaining conformal coatings becomes challenging [9]. An alternative approach for depositing a continuous barrier/seed layer is the chemical deposition of metals, particularly nickel [10–12]. In addition to the continuity of the barrier layer, a critical quality criterion is the amorphous nature of the resulting coating [13]. Chemically deposited nickel coatings with medium to high phosphorus content satisfy these requirements [14, 15], making them highly promising for application in advanced heterogeneous 3D integration technology.

In this study, high-phosphorus nickel coatings were deposited onto silicon substrates via electroless plating. We evaluated the spatial structure of the spherical grains comprising the nickel coating using techniques sensitive to variations in the electronic structure at different analysis depths.

2. Materials and methods

Electroless nickel coatings were deposited on a pre-oxidized, (100)-oriented monocrystalline silicon substrate.

The electroless nickel plating bath composition consisted of 0.08 mol/L nickel chloride ($NiCl_2 \cdot 6H_2O$), 0.28 mol/L sodium hypophosphite ($NaH_2PO_2 \cdot H_2O$) as the reducing agent, 0.2 mol/L aminoacetic acid (NH_2CH_2COOH) as the complexing agent, and 0.12 mol/L sodium acetate (CH_3COONa) as the buffering additive. The solution pH was maintained at 5.5 by adding a 10% aqueous NaOH solution. The electroless nickel coating was deposited for 3 minutes at 80 °C.

The surface morphology and elemental composition of the obtained coating were analyzed using a Quattro-S scanning electron microscope equipped with an EDAX Octane Elect Plus EDS system for energy-dispersive X-ray microanalysis. X-ray photoelectron spectra (XPS) of Ni 2p and P 2p were acquired using a SPECS spectrometer (Germany). The spectra were excited by Mg Kα radiation (E = 1253.6 eV). Surface profiling of the samples was performed by sputtering with argon ions (Ar^+) at an energy of 3 keV and an ion current density of 10 μA/cm^2 for 2 minutes. X-ray emission P $L_{2,3}$ spectra were obtained using an RSM-500 X-ray spectrometer monochromator at various analysis depths ranging from 10 to 120 nm.

3. Results and discussion

Fig. 1a presents a micrograph of the surface of the nickel coating deposited on a silicon substrate. Scanning electron microscopy (SEM) reveals globular, spherical formations on the coating surface. The most common globule size is approximately 200 nm; however, larger formations measuring 400–500 nm are also observed. Energy-dispersive X-ray spectroscopy (EDX) analysis indicates that the phosphorus content in the coating is C_p = 10.2 wt. % (17.8 at. %), classifying it as a high-phosphorus coating.

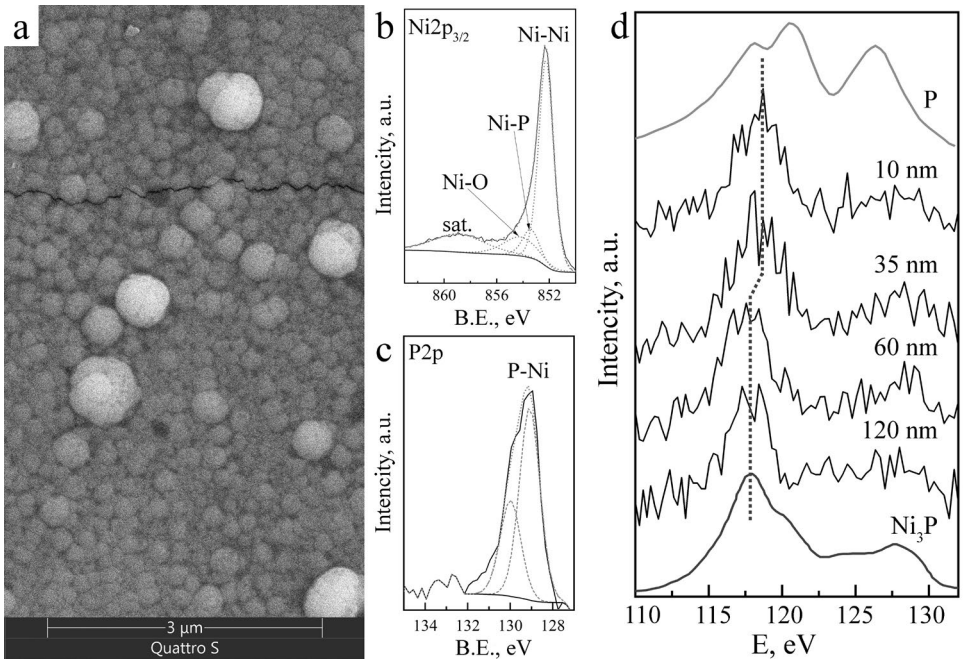

Fig. 1. Results of studies of chemically deposited nickel coating using the following methods: a – scanning electron microscopy, b, c – X-ray photoelectron spectroscopy and d – ultra-soft X-ray emission spectroscopy

X-ray photoelectron spectra of nickel ($Ni2p_{3/2}$) and phosphorus (P 2p) are presented in Figs. 1b and 1c, respectively. According to the XPS data (Fig. 1b), nickel in the coating exists in metallic (Ni–Ni, 852.2 eV) [16, 17], oxide (Ni–O, 854.2 eV) [18], and phosphide (Ni–P, 853.1 eV) [19] states. The P 2p spectrum (Fig. 1c) exhibits a single peak at 129.1 eV ($2p_{3/2}$), corresponding to the formation of nickel phosphide. Thus, the XPS data indicate that all phosphorus in the coating is bonded to nickel. Using the relative sensitivity factor method [20], the phosphorus concentration in the surface layers of the coating was calculated to be C_p = 23.2 at. %. This phosphorus concentration, determined from XPS spectral analysis, exceeds the previously reported value obtained by EDX (17.8 at. %), suggesting a non-uniform distribution of phosphorus atoms between the surface and the bulk of the nickel globular formations.

Fig. 1d presents the results of a layer-by-layer analysis of the nickel coating using ultra-soft X-ray emission spectroscopy (USXES). According to the USXES data, all phosphorus in the coating is chemically bound to nickel. Furthermore, the experimental P $L_{2,3}$ spectra for phosphorus at analysis depths of 120 nm and 60 nm closely match the shape of the reference spectrum for the Ni_3P phase. At shallower depths of 10 nm and 35 nm, a shift of the main spectral maximum toward higher energies is observed. This shift is attributed to an increased concentration of phosphorus in the surface layers of the coating globules.

Fig. 2 presents a schematic representation of the structure of the spherical nickel-coated globules. Based on the average size of the globules (approximately 200 nm) and the results of the

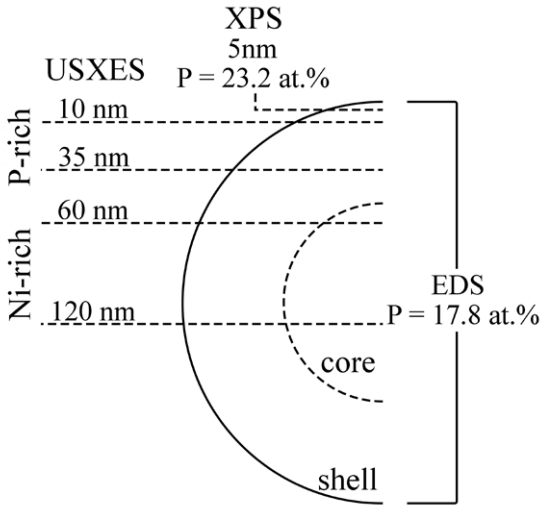

Fig. 2. Schematic representation of nickel coating globules

layer-by-layer spectral analysis of the nickel coating, it is evident that the surface layers of the nickel globules are enriched with phosphorus atoms. The phosphorus content decreases with increasing analysis depth. Therefore, the structure of the globular formations comprising the nickel coating can be described using a core-shell model, in which the core is enriched with nickel atoms and the shell is enriched with phosphorus atoms.

4. Conclusion

This study demonstrates the potential of electrolessly deposited nickel coatings as barrier layers in through-silicon via (TSV) technology. The phosphorus content in the nickel coating deposited on an oxidized silicon substrate is C_P = 10.2 wt. % (17.8 at. %), classifying it as a high-phosphorus coating.

Using X-ray photoelectron spectroscopy and ultra-soft X-ray emission spectroscopy, both capable of layer-by-layer analysis up to a depth of 120 nm, it was demonstrated that the spherical globular formations comprising the nickel coating can be described by a core-shell model. In this model, the shell contains a higher concentration of phosphorus atoms than the core.

The results obtained are significant for establishing a scientific and technical foundation in advanced semiconductor manufacturing technologies, particularly in the field of heterogeneous 3D integration.

Author contributions

The authors contributed equally to this article.

Conflict of interests

The authors declare that they have no known competing financial interests or personal relationships that could have influenced the work reported in this paper.

References

1. Huang M., Wang T., Hou F., Su P., Sun C., Luan H. A 3D TSV-MEMS based heterogeneous Integration technology for RF application. In: *2021 22nd International Conference on Electronic Packaging Technology (ICEPT)*. Xiamen, China: IEEE; 2021; 1–4. https://doi.org/10.1109/icept52650.2021.9567915

2. Green D. S., Dohrman C. L., Demmin J., Zheng Y., Chang T.-H. A revolution on the horizon from DARPA: heterogeneous integration for revolutionary microwave/millimeter-wave circuits at DARPA: progress and future directions. *IEEE Microwave Magazine*. 2017;18(2): 44–59. https://doi.org/10.1109/MMM.2016.2635811

3. Kim Y., Park A.-Y., Kao C.-L., Su M., Black B., Park S. Prediction of deformation during manufacturing processes of silicon interposer package with TSVs. *Microelectronics Reliability*. 2016;65: 234–242. https://doi.org/10.1016/j.microrel.2016.07.153

4. Murugesan M., Mori K., Bea J. C., Koyanagi M., Fukushima T. High aspect ratio through-silicon-via formation by using low-cost electroless-Ni as barrier and seed layers for 3D-LSI integration and packaging applications. *Japanese Journal of Applied Physics*. 2020;59(SG): SGGC02. https://doi.org/10.35848/1347-4065/ab75b8

5. Kim Y., Jin S., Park K., Lee J., Lim J.-H., Yoo B. Effect of pulse current and pre-annealing on thermal extrusion of Cu in through-silicon via (TSV). *Frontiers in Chemistry*. 2020;8: 771. https://doi.org/10.3389/fchem.2020.00771

6. Zhao Z., Liu Z., Chen L., Sun Q., Liu H., Sun Y. FEA study on the TSV copper filling influenced by the additives and electroplating process. *Microelectronic Engineering*. 2023;275: 111981. https://doi.org/10.1016/j.mee.2023.111981

7. Zhang Z., Ding Y., Xiao L., ... Xie H. Enabling continuous Cu seed layer for deep through-silicon-vias with high aspect ratio by sequential sputtering and electroless plating. *IEEE Electron Device Letters*. 2021;42(10): 1520–1523. https://doi.org/10.1109/LED.2021.3105667

8. Mariappan M., Mori K., Koyanagi M., Fukushima T. A TSV-last approach for 3D-IC integration and packaging using WNi platable barrier layer In: *2021 IEEE 71st Electronic Components and Technology Conference (ECTC)*.San Diego, CA, USA: IEEE; 2021: 315–320. https://doi.org/10.1109/ectc32696.2021.00060

9. Armini S. Cu electrodeposition on resistive substrates in alkaline chemistry: effect of current density and wafer RPM. *Journal of The Electrochemical Society*. 2011;158(6): D390. https://doi.org/10.1149/1.3576121

10. Buylov N. S., Sotskaya N. V., Kozaderov O. A., ... Seredin P.V. Fabrication and Characterization of thin metal films deposited by electroless plating with organic additives for electrical circuits applications. *Micromachines*. 2023;14(6): 1151. https://doi.org/10.3390/mi14061151

11. Shimizu T., Shingubara S., Matsui K., ... Motoyoshi M. Low cost TSV fabrication technologies using anisotropic Si wet etching and conformal electroless plating of barrier and seed metals In: *2021 IEEE International Interconnect Technology Conference (IITC)*.Kyoto, Japan: IEEE; 2021: 1–3. https://doi.org/10.1109/iitc51362.2021.9537363

12. Shingubara S., Matsudaira T., Shimizu T. (Invited) Film properties of various electroless plated Co alloy films formed on SiO_2/Si substrate and its interdiffusion properties against Cu. *ECS Meeting Abstracts*. 2020;MA2020-01(20): 1219–1219. https://doi.org/10.1149/MA2020-01201219mtgabs

13. Murugesan M., Mori K., Kojima T., ... Koyanagi M. Nano Ni/Cu-TSVs with an improved reliability for 3D-IC integration application In: *2020 31st Annual SEMI Advanced Semiconductor Manufacturing Conference (ASMC)*.Saratoga Springs, NY, USA: IEEE; 2020: 1–5. https://doi.org/10.1109/asmc49169.2020.9185397

14. Fayyad E. M., Abdullah A. M., Hassan M. K., Mohamed A. M., Jarjoura G., Farhat Z. Recent advances in elec-

troless-plated Ni-P and its composites for erosion and corrosion applications: a review. *Emergent Materials*. 2018;1(1–2): 3–24. https://doi.org/10.1007/s42247-018-0010-4

15. Guo Z., Keong K. G., Sha W. Crystallisation and phase transformation behaviour of electroless nickel phosphorus platings during continuous heating. *Journal of Alloys and Compounds*. 2003;358(1–2): 112–119. https://doi.org/10.1016/S0925-8388(03)00069-0

16. Hengne A. M., Samal A. K., Enakonda L. R., ... Basset J.-M. Ni–Sn-supported ZrO_2 catalysts modified by indium for selective CO_2 hydrogenation to methanol. *ACS Omega*. 2018;3(4): 3688–3701. https://doi.org/10.1021/acsomega.8b00211

17. Hu X., Tian X., Lin Y.-W., Wang Z. Nickel foam and stainless steel mesh as electrocatalysts for hydrogen evolution reaction, oxygen evolution reaction and overall water splitting in alkaline media. *RSC Advances*. 2019;9(54): 31563–31571. https://doi.org/10.1039/C9RA07258F

18. Ramkumar R., Dhakal G., Shim J.-J., Kim W. K. NiO/Ni nanowafer aerogel electrodes for high performance supercapacitors. *Nanomaterials*. 2022;12(21): 3813. https://doi.org/10.3390/nano12213813

19. Xu W., Zhu L., Sun Z., ... Sun H. P-Induced permeation of nickel into WO_3 octahedra to form a synergistic catalyst for urea oxidation**. *ChemSusChem*. 2022;15(24): e202201584. https://doi.org/10.1002/cssc.202201584

20. *Handbook of X-ray photoelectron spectroscopy: a reference book of standard spectra for identification and interpretation of XPS data*. Update Moulder J. F., Chastain J.(eds.). Eden Prairie, Minn: Perkin-Elmer Corporation; 1992. 261 p.

Information about the authors

Vitaly V. Pobedinsky, Cand. Sci. (Eng.), Advisor to the General Director, Research Institute of Electronic Technology (Voronezh, Russian Federation).
pobedinsky@niiet.ru

Buylov Nikita Sergeevich, Cand. Sci. (Phys.–Math.), Educator, Department of Solid State Physics and Nanostructures, Voronezh State University (Voronezh, Russian Federation).
https://orcid.org/0000-0003-1793-4400
buylov@phys.vsu.ru

Evgenia A. Ilina, Junior Researcher, Laboratory of organic additives for the processes of chemical and electrochemical deposition of metals and alloys used in the electronics industry, Voronezh State University (Voronezh, Russian Federation).
https://orcid.org/0009-0004-4825-5894
zhenya.ali@yandex.ru

Dmitry L. Goloshchapov, Cand. Sci. (Phys.–Math.), Assistant Professor, Department of Solid State Physics and Nanostructures, Voronezh State University (Voronezh, Russian Federation).
https://orcid.org/0000-0002-1400-2870
goloshchapov@phys.vsu.ru

Eugeny S. Kersnovsky, graduate student, Technician, Department of Solid State Physics and Nanostructures, Voronezh State University, (Voronezh, Russian Federation).
https://orcid.org/0009-0006-8215-6077
kersnovsky@phys.vsu.ru

Ivan V. Polshin, magistrate, Laboratory Assistant, Department of Solid State Physics and Nanostructures, Voronezh State University, (Voronezh, Russian Federation).
https://orcid.org/0009-0008-7639-6538
polshin@phys.vsu.ru

Andrey I. Chukavin, Cand. Sci. (Phys.–Math.), Senior Researcher, Udmurt Federal Research Center of the Ural Branch of the Russian Academy of Sciences (Izhevsk, Russian Federation).
https://orcid.org/0000-0002-9590-9238
chukavin@udman.ru

Konstantin V. Zolnikov, Cand. Sci. (Eng.), Associate Professor, Head of the Department, Basic Department of Technical and Software Support for Computing and Information Systems, Voronezh State Forestry Engineering University named after G. F. Morozov (Voronezh, Russian Federation).
https://orcid.org/0009-0000-4539-7556
kvzolnikoff@yandex.ru

Pavel P. Kutsko, Cand. Sci. (Eng.), General Director, Research Institute of Electronic Technology (Voronezh, Russian Federation).
kutsko@niiet.ru

Pavel L. Parmon, Director of Quality, Research Institute of Electronic Technology (Voronezh, Russian Federation.
p.parmon @niiet.ru

Igor V. Semeykin, Cand. Sci. (Eng.), Technical Director, Research Institute of Electronic Technology (Voronezh, Russian Federation).
sig@niiet.ru

Koniaev Ivan Vasilevich, Cand. Sci. (Eng.), Lead Engineer, Research Institute of Electronic Technology (Voronezh, Russian Federation).
konyaev@niiet.ru

Seredin Pavel Vladimirovich, Dr. Sci. (Phys.–Math.), Full Professor, Chair of department, Department of Solid State Physics and Nanostructures, Voronezh State University (Voronezh, Russian Federation).
https://orcid.org/0000-0002-6724-0063
paul@phys.vsu.ru

Received February 02, 2026; accepted after reviewing February 24, 2026; accepted for publication February 25, 2026; published online April 01, 2026.

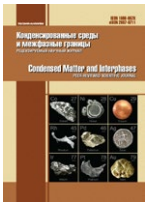

ISSN 1606-867X (Print)
ISSN 2687-0711 (Online)
Condensed Matter and Interphases
Kondensirovannye Sredy i Mezhfaznye Granitsy
https://journals.vsu.ru/kcmf/

Short communication

Short communication
https://doi.org/10.17308/kcmf.2026.28/13560

Detection of acetone by a sensor based on clinoptilolite

E. A. Popov[1]✉, D. S. Potanina[1], E. V. Bogatikov[1]

[1]Voronezh State University,
1, Universitetskaya pl., Voronezh 394018, Russian Federation

Abstract

Objectives: The active development of bioreactors used in a wide range of biotechnological, medical, agricultural, and environmental applications requires improvements in their components, including gas-sensitive sensors for various metabolites. Particular preference is given to sensors that are capable of recognizing the composition of complex gas mixtures without the use of bulky and expensive structures.

Experimental: Zeolite-based sensors are a promising technology. The ion conductivity relaxation curves of zeolites under the application of step voltage pulses are considered. The power dependence of the ion conductivity current over time is shown with parameters depending on the sorption of acetone vapors.

Conclusions: The results obtained demonstrate the possibility of using gas-sensitive sensors based on clinoptilolite for the detection of acetone, which is important for their use in microbioreactors.

Keywords: Clinoptilolite, Zeolite, Acetone, Gas-sensitive sensor, Microbioreactor, Ionic conductivity

For citation: Popov E. A., Potanina D. S., Bogatikov E. V. Detection of acetone by a clinoptilolite-based sensor. *Condensed Matter and Interphases*. 2026;28(1): 000-000. https://doi.org/10.17308/kcmf.2026.28/13560

Для цитирования: Попов Е. А., Потанина Д. С., Богатиков Е. В. Детектирование ацетона сенсором на основе клиноптилолита. *Конденсированные среды и межфазные границы*. 2026;28(1): 000-000. https://doi.org/10.17308/kcmf.2026.28/13560

✉ Popov Evgenij Anatolyevich, e-mail: crystal.guy@yandex.ru

1. Introduction

Currently, there is active development of microbioreactor components that control and optimize the growth conditions of microorganisms, cells, and tissues. An important component of microbioreactors [1–4] are gas-sensitive sensors that allow the registration of microbial waste products [5, 6]. A distinctive feature of such sensors is their single-use nature, as well as increased requirements for miniaturization and cost.

Sensors based on natural zeolites meet these requirements [7–13]. The presence of a system of channels with a diameter of up to 1 nm in the crystal lattice provides sorption processes that affect the electrophysical properties of zeolites. The prevalence of zeolites in nature ensures their low cost. Of particular interest is the possibility of using a single sensor to detect a mixture of gases. This is especially important for microbioreactors, in which space is extremely limited in replaceable units with growth chambers, where it is difficult to place multisensors with a large number of sensitive elements. The most promising zeolite appears to be the most common natural zeolite, clinoptilolite, which has fairly large channels with a size of ~0.8 nm.

Impedance spectroscopy is most often used to record the response of zeolite-based sensors [14–17]. However, it is impossible to record a number of long-term processes associated with ion drift in zeolite channels [18]. The solution is to record the response to a step voltage function. Previously, it was shown that it is possible to isolate the response to ammonia vapor sorption against the background of water vapor sorption [19]. When using sensors in microbioreactors, it is also important to detect metabolites such as acetone or ethyl alcohol. They are more difficult to detect because they have large molecules that participate weakly in ion transport in zeolite channels.

The aim of this work was to find the response parameters of clinoptilolite-based sensors that enable the detection of acetone vapors for use in microbioreactors.

2. Experimental

A system of opposing pin electrodes (40×20 mm, electrode pitch 2 mm) with a layer of clinoptilolite was used as a sensor. The gas-sensitive layer was formed by precipitation from an aqueous suspension of zeolite without the use of additional binders (since the sensors in microbioreactors are disposable and do not require mechanical strength and durability).

The experimental design corresponded to that used previously in [19] for detecting ammonia vapor. To observe the ion conductivity relaxation process, a series of stepped pulses of constant voltage with variable polarity was applied to the electrodes. The pulse duration was 30 s, and the applied voltage amplitude was 5 V. To measure the current flowing through the zeolite layer, the voltage drop across a measuring resistor connected in series with the sensor was measured. The voltage drop across the resistor was first amplified by a precision instrument amplifier and then digitized using a 24-bit sigma-delta ADC with a sampling frequency of 20 Hz, which allowed for hardware-based suppression of the 50 Hz mains interference. The obtained data was smoothed using a 5-point moving average and transmitted to a computer. As a result, the noise amplitude in the obtained data did not exceed 0.1 nA.

The sensor was placed in a desiccator, the humidity inside which was set by a saturated salt solution (NaCl – to obtain a relative humidity of 75 % and KCl to obtain a relative humidity of 84 %). The relative humidity and temperature were additionally controlled by sensors with an accuracy of 1 % and 1 °C, respectively. Before being placed in the desiccator, the sensor was heated to a temperature of ~80 °C for desorption. The efficiency of desorption was monitored by measuring ion conductivity. After placing the sensor in the desiccator, it was kept at a constant temperature (20 °C or 25 °C) for 24 hours to achieve equilibrium. At the beginning of the experiment, the results were recorded for 1 hour without adding acetone vapors, after which a solution of acetone was fed into the desiccator, providing a vapor concentration of ~1000 ppm (which corresponds to the threshold of acetone perception by the human sense of smell) or ~50000 ppm (which roughly corresponds to the average lethal concentration of acetone for animals). The results were recorded for ~4 hours.

3. Results and discussion

An example of measuring ion conductivity current when applying pulses of variable polarity is shown in Fig. 1a. According to the results presented, the experiment can be divided into four stages (marked in Fig. 1a with Roman numerals I-IV). In the first stage, before the introduction of the acetone solution into the desiccator, the amplitude of the response to step pulses is constant. In the second stage, after the introduction of acetone, the amplitude of the response begins to decrease. In the third stage, the amplitude of the response begins to increase again, and in the fourth stage of the experiment, it reaches saturation (at this point, the amplitude exceeds the initial amplitude corresponding to the absence of acetone vapors).

Fig. 1b shows a fragment of the time series corresponding to the second stage of the experiment, and Fig. 1c shows a fragment of the relaxation of ionic conductivity in double logarithmic coordinates. The classical Curie-von Schweidler power law [18] is observed, with a change in the exponent at a certain point in time, which is typical for zeolites, in which the main contribution is made by ion conductivity in the crystal lattice channel system [18, 20].

The values of the degree indicators obtained in the experiment are shown in the table. The values of indicator n1 correspond to the initial stage of conductivity relaxation (~2.5 s from the moment of a step change in the applied voltage), while indicator n2 corresponds to the final stage of relaxation (time interval ~20÷30 s). As can be seen, the introduction of a high concentration of acetone vapors is accompanied by a decrease in the n1 index during all stages of the experiment. In contrast, the n2 index first decreases in value and then increases. At the same time, the ratio of n2/n1 always increases from the moment acetone is introduced. This behavior persists both when the temperature of the experiment is changed and when the relative humidity is changed.

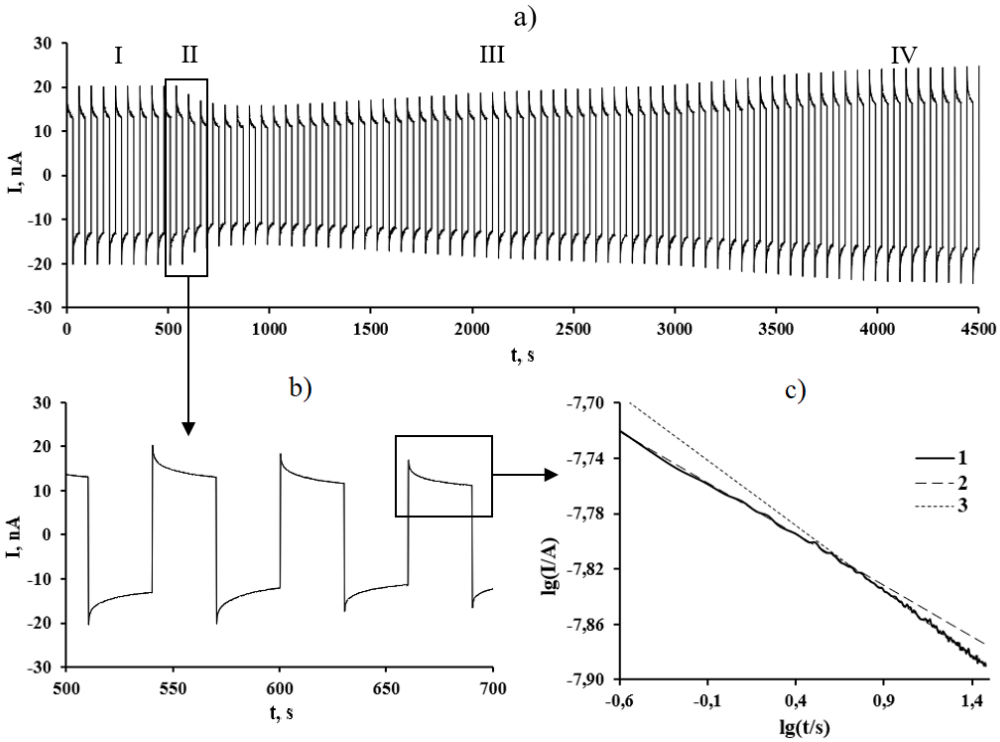

Fig. 1. Response of a clinoptilolite-based sensor to step voltage pulses in the absence of acetone vapors (I) and in the presence of acetone vapors (II–IV): a) time dependence of ion conductivity current; b) time dependence of ion conductivity current at the moment of acetone vapor introduction; c) power-law relaxation of ion conductivity: *1* – experimental curve in double logarithmic coordinates; *2* – approximating power-law dependence for the interval $t < 2.5$ s; *3* – approximating power-law dependence for the interval $20 < t < 30$ s

Table. Values of exponents for ion conductivity relaxation curves of clinoptilolite

Acetone vapor content, ppm	*T*, °C	%RH	Experiment stage	n1	n2	n2/n1
~50000	25	75	I	0.081	0.108	1.33
			II	0.070	0.095	1.36
			III	0.073	0.104	1.42
			IV	0.072	0.102	1.42
		84	I	0.088	0.124	1.41
			II	0.076	0.113	1.49
			III	0.075	0.114	1.52
			IV	0.075	0.125	1.67
	20	75	I	0.085	0.102	1.20
			II	0.073	0.088	1.21
			III	0.074	0.094	1.27
			IV	0.076	0.100	1.32
~1000	25	75	I	0.075	0.098	1.31
			II	0.076	0.101	1.33
			III	0.080	0.118	1.48
			IV	0.078	0.120	1.54

At low acetone concentrations, the ratio n2/n1 continues to increase with the introduction of acetone, but this is caused not by a decrease in the n1 index, but by an increase in the n2 index.

Compared to the significant change in degree indicators obtained earlier during ammonia vapor sorption [19], the change in degree indicators during acetone sorption is significantly less. This is due to the fact that ammonia molecules, firstly, have a significantly smaller diameter and, therefore, greater mobility in the pores of zeolite compared to acetone. Second, ammonium ions formed in the zeolite pores are directly involved in ionic conductivity. In the case of acetone, the effect on conductivity appears to be indirect (a change in the mobility of water and metal ions in the zeolite pores, as well as a change in the number of water molecules in the pores).

4. Conclusion

The detected change in the power indices of the clinoptilolite conductivity relaxation curve in the presence of acetone vapors allows us to consider zeolite-based sensors as being promising components of microbioreactors. It has been shown that the ratio of exponents during different stages of ion conductivity relaxation can be used as an important parameter for acetone detection.

Author contributions

All authors have made an equivalent contribution to the preparation of the publication.

Conflict of interest

The authors declare that they have no known competing financial interests or personal relationships that could have influenced the work reported in this paper.

References

1. Kim K. R., Yeo W.-H. Advances in sensor developments for cell culture monitoring. *BMEMat*. 2023;1(4): e12047. https://doi.org/10.1002/bmm2.12047

2. Jansen R., Morschett H., Hasenklever D., Moch M., Wiechert W., Oldiges M. Microbioreactor-assisted cultivation workflows for time-efficient phenotyping of protein producing Aspergillus niger in batch and fed-batch mode. *Biotechnology Progress*. 2021;37: e3144. https://doi.org/10.1002/btpr.3144

3. Fink M., Cserjan-Puschmann M., Reinisch D., Striedner G. High-throughput microbioreactor provides a capable tool for early stage bioprocess development. *Scientific Reports*. 2021;11: 2056. https://doi.org/10.1038/s41598-021-81633-6

4. Podunavac I., Knežić T, Djisalov M., … Radonic V. Mammalian cell-growth monitoring based on an impedimetric sensor and image processing within a microfluidic platform. *Sensors*. 2023;23(7):3748. https://doi.org/10.3390/s23073748

5. Viebrock K., Rabl D., Meinen S., … Krull R. Microsensor in microbioreactors: full bioprocess characterization in a novel capillary-wave microbioreactor. *Biosensors*. 2022;12(7): 512–530. https://doi.org/10.3390/bios12070512

6. Helwig A., Hackner A., Müller G., Zappa D., Sberveglieri G. Self-test procedures for gas sensors embedded in microreactor systems. *Sensors*. 2018;18(2): 453–468. https://doi.org/10.3390/s18020453

7. Park J., Tabata H. Gas sensor array using a hybrid structure based on zeolite and oxide semiconductors for multiple bio-gas detection. *ACS Omega*. 2021;6(33): 21284–21293. https://doi.org/10.1021/acsomega.1c01435

8. Stosic D., Zholobenko V. Application of zeolite-based materials for chemical sensing of VOCs. *Sensors*. 2025;25(5): 1634–1658. https://doi.org/10.3390/s25051634

9. Yamada Y., Hiyama S., Toyooka T., ... Tabata H. Ultratrace measurement of acetone from skin using zeolite: toward development of a wearable monitor of fat metabolism. *Analytical Chemistry*. 2015;87(15): 7588–7594. https://doi.org/10.1021/acs.analchem.5b00296

10. Kucherenko I. S., Soldatkin O. O., Dzyadevych S. V., Soldatkin A. P. Application of zeolites and zeolitic imidazolate frameworks in the biosensor development. *Biomaterials Advances*. 2022;143: 213180. https://doi.org/10.1016/j.bioadv.2022.213180

11. Bacakova L., Vandrovcova M., Kopova I., Jirka I. Applications of zeolites in biotechnology and medicine. *Biomaterials Science*. 2018;6(5): 974–989. http://dx.doi.org/10.1039/C8BM00028J

12. Wang W., Zhang Q., Lv R., Wu D., Zhang S. Enhancing formaldehyde selectivity of SnO_2 gas sensors with the ZSM-5 modified layers. *Sensors*. 2021;21(12): 3947–962. https://doi.org/10.3390/s21123947

13. Simonov V. N., Fomkin A. A., Shkolin A. V., Menshchikov I. E. Acetone-neutral adsorption sensor for measuring the humidity of exhaled air in the diagnosis of diabetes mellitus. *Protection of Metals and Physical Chemistry of Surfaces*. 2023;59(4): 456–460. https://doi.org/10.31857/S004418562370050X

14. Reiß S., Hagen G., Moos R. Zeolite-based impedimetric gas sensor device in low-cost technology for hydrocarbon gas detection. *Sensors*. 2008;8(12): 7904–7916. https://doi.org/10.3390/s8127904

15. Zheng Y., Li X., Dutta P. K. Exploitation of unique properties of zeolites in the development of gas sensors. *Sensors*. 2012;12(4): 5170–5194. https://doi.org/10.3390/s120405170

16. Pullano S. A., Falcone F., Critello D. C., Bianco M. G., Menniti M., Fiorillo A. S. An affordable fabrication of a zeolite-based capacitor for gas sensing. *Sensors*. 2020;20(7): 2143. https://doi.org/10.3390/s20072143

17. Wu Q., Zheng Y., Jian J., Wang J. Gas sensing performance of ion-exchanged Y zeolites as an impedimetric ammonia sensor. *Ionics*. 2017;23: 751–758. https://doi.org/10.1007/s11581-016-1849-0

18. Jonscher A. K., Haidar A. R. The time-domain response of humid zeolites. *Journal of the Chemical Society, Faraday Transactions 1: Physical Chemistry in Condensed Phases*. 1986;82(12): 3553–3560. https://doi.org/10.1039/F19868203553

19. Kutsova D. S., Bogatikov E. V., Smirnova K. G., Glushkov G. I. Analysis of the composition of a complex gas mixture using a zeolite-based sensor. *Nano-and Microsystems Technology*. 2016;18(9): 589–592. (in Russ.). Available at: https://www.elibrary.ru/item.asp?id=26711244

20. Weisman V. L., Markov V. N., Nikolaeva L. V., Pankova S. V., Solovyov V .G. Conductivity of zeolite single crystals. *Physics of the Solid State*. 1993;35(5): 1390–1393. (in Russ.). Available at: https://journals.ioffe.ru/articles/14932

Information about the authors

Eugenij A. Popov, graduate student, Department of Semiconductor Physics and Microelectronics, Voronezh State University (Voronezh, Russian Federation).

https://orcid.org/0009-0007-5323-7238

crystal.guy@yandex.ru

Daria S. Potanina, graduate student, Department of Semiconductor Physics and Microelectronics, Voronezh State University (Voronezh, Russian Federation).

https://orcid.org/0009-0009-0453-0977

potanina.ds@gmail.com

Eugenij V. Bogatikov, Cand. Sci. (Phys.–Math.), Associate Professor, Department of Semiconductor Physics and Microelectronics, Voronezh State University (Voronezh, Russian Federation).

https://orcid.org/0009-0006-5349-1466

evbogatikov@yandex.ru

Received January September 15, 2025; approved after reviewing October 30, 2025; accepted for publication November 14, 2025; published online April 01, 2026.

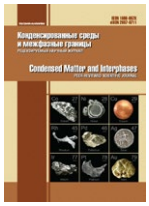

ISSN 1606-867X (Print)
ISSN 2687-0711 (Online)
Condensed Matter and Interphases
Kondensirovannye Sredy i Mezhfaznye Granitsy
https://journals.vsu.ru/kcmf/

Short communication

Short communication
https://doi.org/10.17308/kcmf.2026.28/13601

E. coli cells as a source of biohybrid material: electron microscopy and microanalysis study

S. Yu. Turishchev[1]✉, E. A. Belikov[1], E. V. Parinova[1], D. Z. Kureshi[1], O. A. Chuvenkova[1], V. Sivakov[2], S. S. Antipov[1]

[1]*Voronezh State University,*
1 Universitetskaya pl., Voronezh 394018, Russian Federation

[2]*Leibniz Institute of Photonic Technology,*
9, Albert-Einstein-Str., Jena 07745, Germany

Abstract

Objectives: The work relates to the research of *E.coli* cells formed under conditions of superproduction of the bacterioferritin protein Dps. These protein molecules are capable of forming biohybrid structures by accumulating inorganic nanoparticles of the iron-oxygen system with identical properties, including sizes within the nanometer range, in their internal cavities. Current methods of obtaining bacterioferritin Dps protein molecules rely on destroying their source: *E.coli* cells. A key issue for study and subsequent application is establishing whether it is possible to obtain these protein molecules without destroying *E.coli* cells in order to form biohybrid structures.

Experimental: E.coli cells were grown under conditions of superproduction of bacterioferritin Dps protein molecules, then deposited on a molybdenum foil substrate for electron microscopy and energy-dispersive microanalysis studies. Based on the resulting data on morphology data and elemental composition, the possibility of forming protein molecules without destroying the cells was investigated in order to create biohybrid structures based on them.

Conclusions: It has been established that under conditions of protein superproduction, *E.coli* cells produce bacterioferritin Dps molecules, with a significant amount of this protein possibly being released into the extracellular space. The morphology of *E.coli* cells themselves does not change under conditions of superproduction and protein emission. When Mohr's salt was added to the culture fluid, the released protein contains a significant amount of iron atoms, which may result from bacterioferritin Dps molecules forming biohybrid structures. These results demonstrate a simple, affordable method of forming biohybrid structures containing iron-oxygen nanoparticles for use in technologies, including the targeted delivery of nanoparticles and the functionalization of accessible surfaces.

Keywords: *E.coli* cells, Dps protein molecules, Protein superproduction, Biohybrid material, Scanning electron microscopy, Energy-dispersive microanalysis, Morphology and composition

Funding: The study was funded by the Russian Science Foundation, research project No. 25-12-00413, https://rscf.ru/project/25-12-00413/. VS acknowledges the German Research Foundation (DFG) for financial support under project no. SI1893/18-1 (2018-2019).

For citation: Turishchev S. Yu., Belikov E. A., Parinova E. V., Kureshi D. Z., Chuvenkova O. A., Sivakov V., Antipov S. S. *E.coli* cells as a source of biohybrid material: electron microscopy and microanalysis study. *Condensed Matter and Interphases*. 2026;28(1): 153–158. https://doi.org/10.17308/kcmf.2026.28/13601

Для цитирования: Турищев С. Ю., Беликов Е. А., Паринова Е. В., Куреши Д. З., Чувенкова О. А., Сиваков В., Антипов С. С. Клетки *E.coli* как источник биогибридного материала: исследование методами электронной микроскопии и микроанализа. *Конденсированные среды и межфазные границы*. 2026;28(1): 153–158. https://doi.org/10.17308/kcmf.2026.28/13601

✉ Sergey Yu. Turishchev, e-mail: tsu@phys.vsu.ru

1. Introduction

Nature-like materials and structures are a promising object of modern scientific research and development of technological approaches in terms of low cost or efficiency and flexibility in their practical use [1–5]. A bright example of this class of objects are protein molecules, for example, bacterioferritin Dps (DNA-binding Protein from Starved cells) of *Escherichia coli* (*E. coli*) bacteria, which is a representative of bacterial ferritins [1, 4]. These natural objects are known for their ability to form inorganic iron-oxygen (Fe–O) nanoparticles of a given composition and size inside the voids of molecules [1, 4, 6–8]. Moreover, the result of the formation of a biohybrid material is the fact that each of the particles is initially, by its natural origin, packaged in an organic container, the protein molecule itself. Such objects can be stored for a long, practically unlimited time without changing their macro- and microscopic properties. Finally, considering that the storage of a molecular culture or biohybrid material takes place in a liquid medium, it is convenient to deliver such objects in a targeted manner within the framework of the technology used [9]. The source of bacterioferritin Dps molecules are *E.coli* cells. The traditional way to obtain protein here is to isolate it upon complete destruction of the source cells, followed by a sequence of complex, often costly biophysical and biochemical procedures for purification, filtration and stabilization of the molecular culture [1–2, 7, 10]. Subsequently, after the cells are destroyed and the molecular culture of bacterioferritin Dps is isolated, interaction with the decomposition products of the Mohr salt $Fe(NH_4)_2(SO_4)_2 \cdot 6H_2O$ occurs to form a biohybrid material as a source of divalent iron (Fe^{2+}) in a culture solution. The natural function of Dps molecules is to deposit or accumulate iron oxide Fe^{2+}, which is toxic to biological culture, into a nanoparticle predominantly consisting of iron Fe^{3+} bound to oxygen [4, 8]. Note that the dimensions of the outer walls of the protein molecule, according to the data obtained earlier, do not exceed ten nanometers, while the sizes of nanoparticles formed inside the molecules can be several nanometers [4, 6, 7]. One Dps protein molecule can act as a single "setup" for the controlled production of a biohybrid structure with an inorganic nanoparticle of specified properties, including sizes up to units of nanometers. An attractive development of approaches for obtaining a molecular culture or biohybrid objects based on it is an attempt to use *E.coli* cells to isolate protein without destroying them i.e. repeatedly. Then a cell, an object much more massive than a molecule, can be considered to be a kind of "factory" for the production of hybrid structures.

Note that with such a modification of the cell culture, which leads to the release of protein in sufficient quantities [11] and without cell destruction, the key issue is the influence of the source of iron atoms, for example, Mohr salt, necessary for the formation of biohybrid nanostructures, on the properties, primarily the morphology of (modified) *E.coli* cells. Attempts to use cells for the repeated production of molecules can lead to a disruption in the shape of such a natural source of biohybrid material. Therefore, an important and necessary task is to study the morphology and elemental composition of a modified cell culture.

Scanning electron microscopy (SEM) is one of the most in-demand methods for a variety of objects diagnostics, including nanoscale structures and biomaterials. The method's capabilities make it possible to study the morphological features of various origins objects, including natural ones, with high lateral resolution [3, 9, 12–14]. One of the most useful additions to the scanning electron microscopy method is the possibility of conducting energy-dispersive X-ray microanalysis of an object being studied in an electron microscope. The use of this method, within the framework of a single experiment with the study of morphology, by means of scanning electron microscopy, allows us to obtain information about the presence of an element in the composition of a microscopic area of the studied object. The present work is dedicated to the research of modified *E.coli* cells as a multiple source of molecular material or biohybrid structures using SEM and microanalysis methods.

2. Experimental

To achieve protein superproduction conditions, *E. coli* BL21*(DE3) cells pre-grown

to an optical density of 0.4 (λ = 600 nm), were washed with a buffer solution containing 0.1M Tris-HCl (pH 8.0) from nutrient residues and exposed to $CaCl_2$, according to the procedure described in [15] to form perforations in the cell membrane. Then, a pre-prepared aqueous solution of circular pGEM*dps* plasmid DNA (pDNA) molecules containing a full-size copy of the *dps* gene were added to the cell suspension. Based on the saturating concentration of pDNA during transformation equal to 10 μg/ml, 0.5 μl of their solution was added to the cells, followed by half an hour incubation on ice, then exposed to heat at 42 °C for 2 minutes. The tubes were then placed in an ice bath for 2 minutes, after which the cells were transferred to 750 μl of a SOC solution containing trypton (20 g/l), yeast extract (5.5 g/L), NaCl (10 mM), KCl (2.5 mM), $MnCl_2$/$MgSO_4$ (10 mM), glucose (20 mM) and incubated for 1 hour, at 37 °C in a thermostat with constant stirring at 180 rpm. After that, the cell suspension was centrifuged, and the resulting precipitate with a volume of about 50 μl was sown onto Petri dishes with LB-agar (pH 7.4) containing trypton (10 g/l), yeast extract (5 g/l), NaCl (10 g/l), bactoagar (15 g/l) and ampicillin (20 μg/ml). The growth of the obtained cells was carried out at 37 °C in the presence of ampicillin (20 μg/ml) for 16 hours in the presence of 0.02 mM IPTG. The presence of the recombinant Dps protein was controlled by electrophoresis in 12.5% denaturing polyacrylamide gel using the modified Davis method. Next, the cells were harvested by centrifugation at 10,000 rpm, washed twice from the medium with a cold buffer containing 0.1M Tris-HCl (pH 8.0), and used for research. A freshly prepared solution of Mohr salt was used as an iron source, which was added to the protein solution until an iron ion concentration of 0.25 mM was reached and incubated for 15 minutes, after which the same portion of Mohr salt was added and incubation was repeated. The resulting sample was used in studies. Obtained samples of cell culture were deposited to pre-purified molybdenum foil by layering.

A Carl Zeiss ULTRA 55 scanning electron microscope equipped with an energy dispersive microanalysis unit was used. The mode of secondary electrons registration with low values of accelerating voltages up to 5 kV was used, which is necessary for studying biostructures. The Image J software package was used to estimate the areas occupied by the cells and to estimate the spread of their shape. An energy dispersion (X-ray) spectrum was obtained from a surface area of ~ 15×20 μm for which the element distribution was mapped.

3. Results and discussion

Fig. 1 shows a surface morphology obtained by the SEM method for the cellular array formed on the molybdenum foil. Data on the shape and size of cells and their arrays (accumulations) are shown in Fig. 1a, information on the shape and size of a single cell is given in Fig. 1b, and section "c" of the same figure represents the result of estimating the size of cells in the surface area of Fig. 1a, made according to the cell areas. It should be noted that the size of *E.coli* cells grown under protein superproduction conditions is about three micrometers long and one micrometer wide, which corresponds to the selected cell type [12]. They are generally oval in shape with clear boundaries, the observation of which suggests that the height of the cell is comparable to its width, including after vacuuming of the formed cell array in the electron microscope chamber. It should also be noted that, as a result of layering, it is possible to form a sufficiently dense layer of cells distributed over the surface of the foil in "islands" one cell high, incompletely covering the bearing surface of molybdenum. The conditions of protein superproduction during the formation of a cell array do not lead to significant cell morphology disorders. Some of the cells, however, are smaller (~ 1×1 μm) or larger (~ 5×1 μm) than indicated above (Fig. 1c). This is the result of ongoing cell division at the time of layering on the substrate. In addition to the forming cell arrays and uncovered sections of molybdenum foil, there are a number of elements indicated in Fig. 1a with a white dotted line. The size of these elements is comparable to the size of a cell, they have random contours, uneven morphology and are adjacent directly to individual cells or are located within the cell array. Such elements are not observed on the surface of cell arrays themselves and are not located on individual areas of the substrate surface that are not coated with *E. coli*. At the same time, there are

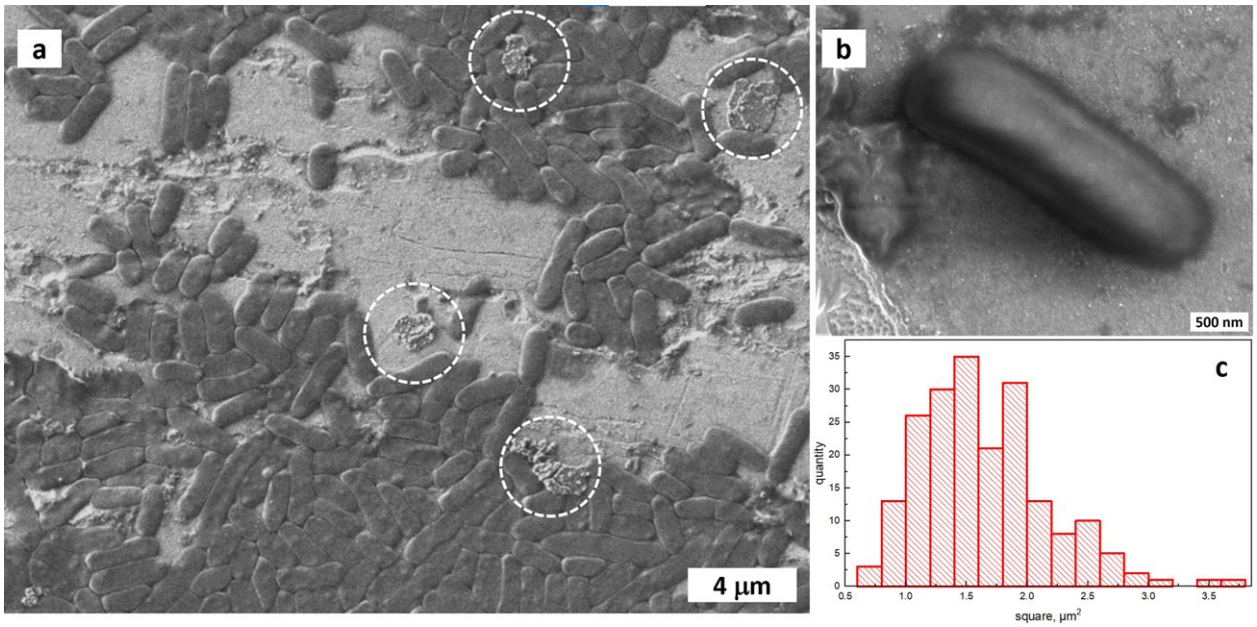

Fig. 1. Scanning electron microscopy of the *E.coli* cells on a molybdenum foil substrate. a: cells array with white dotted lines showing areas of protein release; b: single *E. coli* cell image; c: distribution of cells by their surface areas

no noticeable variations of the shape and size of cells adjacent to these morphological elements. It should be noted that the modified *E. coli* cells were formed under conditions of the superproduction of bacterioferritin Dps protein molecules, placed after layering on the substrate surface in a scanning electron microscope chamber, and then evacuated. Thus, the origin of these arrays may be related to the release of excess protein into the extracellular media, including during the transition of vacuum conditions.

Fig. 2 contains the results of the elemental composition microanalysis for a surface area covered with a cells array. Fig. 2a shows an electron microscopic image of a surface area from which a mapping of iron and nitrogen atoms distribution was obtained (Fig. 2b) and spectral information was recorded (Fig. 2c) containing a signal from all sorts of atoms of the studied sample area measuring about 15×20 microns. The choice of Fe and N atoms to obtain a map of the elements distribution is caused by the fact that nitrogen atoms are contained in *E. coli* cells only and are not located on the surface of the foil.

At the same time, iron atoms, as a result of the dissolution of the Mohr salt in the culture media, can be found both in the cells themselves and around them. The molecules of the bacterioferritin

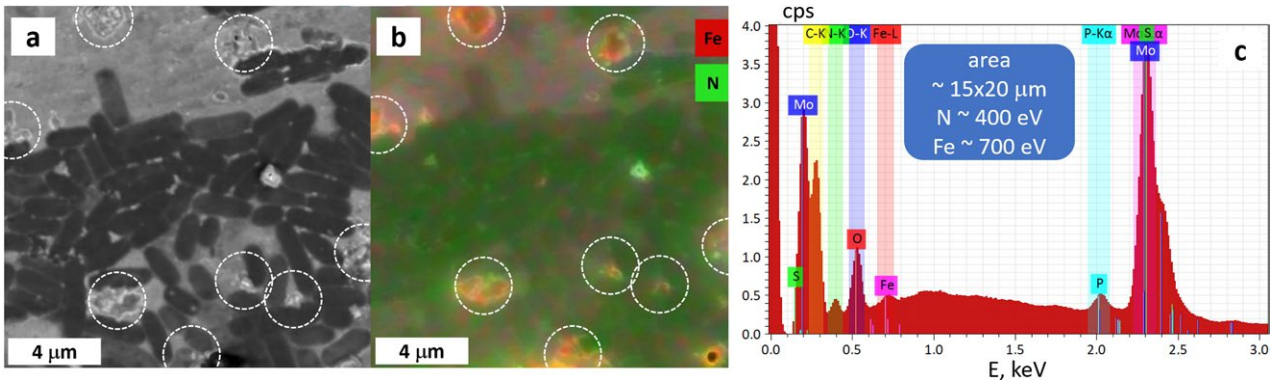

Fig.2. Energy-dispersive microanalysis of the surface area with *E. coli* cells array on a molybdenum foil substrate. a: SEM image with white dotted lines showing areas of protein release; b: distribution mapping for atoms of iron (red) and nitrogen (green); c: energy-dispersive X-ray spectrum

Dps protein are able to accumulate inside their cavities the result of dissolution of the Mohr salt, forming a nanoparticle of the iron-oxygen system consisting of iron atoms ions in different charge states of Fe^{2+} and Fe^{3+} [4, 8]. We assumed the release of bacterioferritin Dps protein molecules into the extracellular space as a result of studying the SEM data (see Fig. 1a) for *E.coli* cells formed under conditions of this protein superproduction. The signal from the iron atoms is confirmed by the spectral information obtained from the observed microarray of the surface (Fig. 2b, peak at 700 eV). The mapping data (Fig. 2b) show that the signal from the iron atoms contributes most to the areas indicated by the dotted white line in Figs 1a, 2a and 2b. We associate these sites with the "release" of the Dps protein by modified *E.coli* cells into the extracellular space.

4. Conclusions

Thus, based on the results of the morphological and elemental composition studies, the following can be stated. During superproduction and growth of *E. coli* cells, bacterioferritin Dps molecules are produced in sufficient quantities to allow this protein to be released into the extracellular space without altering the shape or size of *E. coli* cells. The released protein contains a significant number of iron atoms, which may result from bacterioferritin Dps molecules forming biohybrid structures without destroying their source, i.e. *E. coli* cells. This approach to forming biohybrid materials using protein molecules of cellular origin is promising for producing iron-oxygen nanoparticles with specific properties, including those intended for long-term storage or use in technologies such as targeted nanoparticle delivery and surface functionalization.

Contribution of the authors

The authors contributed equally to this article.

Conflict of interests

The authors declare that they have no known competing financial interests or personal relationships that could have influenced the work reported in this paper.

References

1. Nikandrov V. V. Inorganic semiconductors in biological and biochemical systems: biosynthesis, properties, and photochemical activity. *Advances in biological chemistry*. 2000;40: 357–396.

2. Behrens S. S. Synthesis of inorganic nanomaterials mediated by protein assemblies. *Journal of Materials Chemistry*. 2008;18: 3788–3798. https://doi.org/10.1039/B806551A

3. *Biological and Bio-inspired Nanomaterials. Properties and Assembly Mechanisms*. Sarah Perrett, Alexander K. Buell, Tuomas P. J. Knowles (eds.). Springer, Singapore; 2019. 440 p. https://doi.org/10.1007/978-981-13-9791-2.

4. Parinova E. V., Antipov S. S., Belikov E. A., ... Turishchev S. Yu. TEM and XPS studies of bio-nanohybrid material based on bacterial ferritin-like protein Dps. *Condensed Matter and Interphases*. 2022;24(2): 265–272. https://doi.org/10.17308/kcmf.2022.24/9267

5. Nazarovskaia D. A., Turishchev S. Yu., Titova S. S., Shatov A. A., Tyurin-Kuzmin P. A., Osminkina L. A. Photoluminescent properties of porous silicon nanoparticles: synthesis, characterization, and cellular imaging. *Condensed Matter and Interphases*. 2025;27(3): 422–432. https://doi.org/10.17308/kcmf.2025.27/13181

6. Antipov S. S., Pichkur E. B., Praslova N. V., ... Turishchev S. Yu. High resolution cryogenic transmission electron microscopy study of Escherichia coli Dps protein: first direct observation in quasinative state. *Results in Physics*. 2018;11: 926–928. https://doi.org/10.1016/j.rinp.2018.10.059

7. Antipov S., Turishchev S., Purtov Yu., ... Ozoline O. The Oligomeric Form of the Escherichia coli Dps Protein Depends on the Availability of Iron Ions. *Molecules*. 2017;22(11):1904. https://doi.org/10.3390/molecules22111904

8. Turishchev S. Yu., Antipov S. S., Novolokina N. V., ... Domashevskaya E. P. A soft X-ray synchrotron study of the charge state of iron ions in the ferrihydrite core of the ferritin Dps protein in Escherichia coli. *Biophysics*. 2016;61(5): 705–710. https://doi.org/10.1134/S0006350916050286

9. Parinova E. V., Antipov S. S., Sivakov V., ... Turishchev S. Yu. Photoluminescent properties of porous silicon nanoparticles: synthesis, characterization, and cellular imaging. *Condensed Matter and Interphases*. 2023;25(2): 207–214. https://doi.org/10.17308/kcmf.2023.25/11102

10. Antipov S. S., Tutukina M. N., Preobrazhenskaya E. V., ... Ozoline O. N. The nucleoid protein Dps binds genomic DNA of Escherichia coli in a non-random manner. *PLOS ONE*. 2017;12(8): 1–27. https://doi.org/10.1371/journal.pone.0182800

11. Hudson A. J., Andrews S. C., Hawkins C., ... Gues J. R. Overproduction, purification and characterization of the Escherichia coli ferritin. *European journal of biochemistry*. 1993;218(3): 985–995. https://doi.org/10.1111/j.1432-1033.1993.tb18457.x

12.Turishchev S.Yu., Marchenko D., Sivakov V., ... Antipov S.S. On the possibility of PhotoEmission Electron Microscopy for E. coli advanced studies. *Results in Physics*. 2020;16: 102821-1-3. https://doi.org/10.1016/j.rinp.2019.102821

13. Alvear-Daza J. J., García-Barco A., Osorio-Vargas P., Gutierrez-Zapata H. M., Sanabria J., Rengifo-Herrera J. A. Resistance and induction of viable but non culturable states (VBNC) during inactivation of E. coli and Klebsiella pneumoniae by addition of H2O2 to natural well water under

simulated solar irradiation. *Water Research*. 2021;188(116499): 1–11. https://doi.org/10.1016/j.watres.2020.116499

14. He Q., Liu D., Guo M., … Guo M. Antibacterial mechanism of ultrasound against Escherichia coli: Alterations in membrane microstructures and properties. *Ultrasonics Sonochemistry*. 2021;73(105509): 1–12. ttps://doi.org/10.1016/j.ultsonch.2021.105509

15. Sambrook J. *Molecular cloning: a laboratory manual* J. Sambrook, E. F. Fritsch, T. Maniatis (eds.). Cold Spring Harbor Laboratory Press; 1989. 1546 p.

Information about the authors

Turishchev Sergey Yu., Dr. Sci. (Phys.-Math.), Associate Professor, Head of the General Physics and Physical Materials Science Department, Voronezh State University (Voronezh, Russia).
https://orcid.org/0000-0003-3320-1979
tsu@phys.vsu.ru

Belikov Evgenii A., post graduate student of the General Physics and Physical Materials Science Department, Voronezh State University (Voronezh, Russia).
bp4nth3r@mail.ru

Parinova Elena V., PhD in Physics and Mathematics, Assistant Professor of the General Physics and Physical Materials Science Department, Voronezh State University (Voronezh, Russia).
https://orcid.org/0000-0003-2817-3547.
parinova@phys.vsu.ru

Kureshi Daniel Z., student of the General Physics and Physical Materials Science Department, Voronezh State University (Voronezh, Russia).
kureshi@phys.vsu.ru

Olga A. Chuvenkova, Cand. Sci. (Phys.-Math.), Senior Researcher, Joint Scientific and Educational Laboratory "Atomic and Electronic Structure of Functional Materials" of Voronezh State University and the National Research Center "Kurchatov Institute", Voronezh State University (Voronezh, Russian Federation).
https://orcid.org/0000-0001-5701-6909
chuvenkova@phys.vsu.ru

Sivakov Vladimir, PhD, Group Leader, Leibniz Institute of Photonic Technology (Jena, Germany).
https://orcid.org/0000-0002-3272-501X
vladimir.sivakov@leibniz-ipht.de

Antipov Sergey S., Dr.Sci. (Biology), Professor, Biophysics and Biotechnology Department, Voronezh State University, Voronezh State University (Voronezh, Russian Federation).
ss.antipov@gmail.com

Received 11.08.2025; approved after reviewing 25.08.2025; accepted for publication 05.09.2025; published online 01.04.2026.

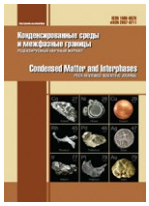

ISSN 1606-867X (Print)
ISSN 2687-0711 (Online)
Condensed Matter and Interphases
Kondensirovannye Sredy i Mezhfaznye Granitsy
https://journals.vsu.ru/kcmf/

Anniversary

Anniversary of Professor Aleksandr V. Vvedenskii's anniversary

On April 2, 2026, Aleksandr Viktorovich Vvedenskii, Doctor of Chemical Sciences, Honorary Worker of Higher Professional Education of the Russian Federation, Professor of the Department of Physical Chemistry at the Chemical Faculty of Voronezh State University, turns 80 years old.

Aleksandr Viktorovich's whole life is closely connected with physical chemistry and the problems of electrochemistry, both fundamental and applied. After graduating from the Physics Department of Voronezh State University (VSU) in 1968, he worked his way up from assistant and junior researcher to professor and head of the department. In 1979, he defended his PhD thesis "Mechanism and kinetics of interaction of copper with dilute chloride solutions and desalinated water", specialty 02.00.04 — "Physical Chemistry", and then in 1994 his doctoral thesis in the same specialty on the topic "Thermodynamics and kinetics of selective dissolution of binary solid solutions", in which he made a significant contribution to the construction of a general theory of alloy dissolution with an analytical description of kinetic patterns. It presented, for the first time, a fairly complete and consistent physico-chemical model of anodic dissolution of a homogeneous alloy. In 1996, Aleksandr Viktorovich was awarded the academic title of professor, and in 1998 he became a member of the International Society of Electrochemistry (ISE). For twenty years, from 2000 to 2019, A. V. Vvedenskii headed the Department of Physical Chemistry at VSU. His outstanding organizational skills and ebullient energy made it possible to create all the necessary conditions for successful scientific and educational work at the department and strengthen cooperation with Russian Academy of Sciences (RAS) institutions and other Russian and foreign universities. Currently, Aleksandr Viktorovich heads a joint laboratory with the Institute of Physical Chemistry and Electrochemistry of the RAS "Coupled processes in Electrochemistry and Metal Corrosion".

Close interaction and collaboration with his teacher, Professor Igor Kirillovich Marshakov, a leading Russian specialist in corrosion, greatly influenced the scientific style and character of A. V. Vvedenskii as a scientist and teacher. Aleksandr Viktorovich is distinguished by his integrity and dedication, and his responsible and creative approach to solving a wide range of scientific and pedagogical problems. Offering new scientific ideas, he takes an active part in their

implementation, setting relevant tasks within the scientific areas of the department and forming original ways to solve them.

The authority of Professor A. V. Vvedenskii in the field of physical chemistry and electrochemistry is widely recognized. His research interests include the kinetics of multistage electrode processes; effects of structural vacancy disequilibrium and chemical composition in the electrochemistry of solid metal solutions and the adsorption of media components; structure of charged interphase boundaries; electrocatalytic reactions on alloys; selective anodic dissolution of alloys complicated by the formation of insoluble compounds; transient methods of electrochemical research; photoelectrochemistry; quantum chemical modeling of adsorption processes. The results of his research are presented in several monographs, as well as in more than 700 scientific papers. They have been discussed at numerous international and All-Russian conferences and symposiums, and have repeatedly received grant support from various Russian and international foundations.

Throughout the 56 years of his scientific and teaching activities, Aleksandr Viktorovich has paid great attention to the training of specialists in the field of physical chemistry and electrochemistry. During various periods of his work at the department, A. V. Vvedenskii has given lectures at a high professional level on the courses "Physical Chemistry", "Fundamentals of Electrochemistry", "Kinetics of electrochemical processes", "Physico-chemistry of adsorption processes", and "Actual problems of physical chemistry". He is an active supporter of the implementation of scientific and applied research results in the educational process. Professor A. V. Vvedenskii was the supervisor, consultant, and mentor of more than 20 graduate students and applicants who became candidates and doctors of sciences. Currently, he heads the leading scientific and pedagogical school of the VSU "Electrochemistry and Corrosion of Metals and Alloys".

For many years, Aleksandr Viktorovich has been Chairman of the Dissertation Council 24.2.288.04 (formerly – D212.038.08) in chemical sciences, a member of the editorial board of the Russian scientific journal “Condensed Media and Interphase Boundaries”, the editorial board of the scientific journal “Bulletin of Perm University. Series: Chemistry", Dissertation Council 24.2.408.02 (previously – D 212.260.06, Tambov), and the Scientific Council on Physical Chemistry of the Russian Academy of Sciences.

Aleksandr Viktorovich's dedication to his beloved work, his heightened sense of responsibility, exactingness, correctness, and tact are highly appreciated by students, graduate students, and colleagues.

Dear Aleksandr Viktorovich, we wish you good health, new creative ideas and success in solving complex electrochemical problems. Have a long and happy life!

Students, colleagues, and friends,
Editorial Board of Condensed Matter and Interphases

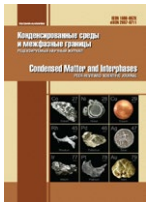

ISSN 1606-867X (Print)
ISSN 2687-0711 (Online)
Condensed Matter and Interphases
Kondensirovannye Sredy i Mezhfaznye Granitsy
https://journals.vsu.ru/kcmf/

Guide for Authors – 2026

Manuscripts should be submitted as single **Microsoft Word 2003** files.

Preferred font 12 pt Times New Roman (please, do not use any other fonts, except for Symbol), 1.5 spaced lines, 1.25 cm first-line indent. Decimal values (e.g. 0.1; 0.9; 2.3) should be written using a decimal point.

Review/Research article/Short communication
https://doi.org/10.17308/kcmf.2025.27/000

Modelling of interdiffusion and phase formation in thin-film two-layer systems of polycrystalline oxides of titanium and cobalt

(All proper nouns should be capitalized; titles and subtitles should be left-aligned)

N. N. Afonin[1]✉, V.A. Logacheva[2]

[1]Voronezh State Pedagogical University,
86 ul. Lenina, Voronezh 394043, Russian Federation
(Official name and address of the organisation)
[2]Voronezh State University,
1 Universitetskaya pl., Voronezh 394018, Russian Federation

Abstract

The abstract should be 200-250 words and include the following sections.

Purpose: States the problem considered in the article, its importance, and the purpose of the research.

Experimental: Provides information about the objects being studied and the methods used.

Conclusions: Provides a brief description of the principal results, major conclusions, and their scientific and practical relevance.

Keywords: Please, provide 5-10 keywords for the principal concepts, results, and terms used in the article.

Funding: The study was funded by the Russian Science Foundation, research project No.

Acknowledgments: The DTATGA, XRD and SEM studies were performed on the equipment of the Engineering Center of Saint Petersburg State Institute of Technology.

For citation: Afonin N. N., Logacheva V. A. Modelling of interdiffusion and phase formation in the thin-film two-layer system of polycrystalline oxides of titanium and cobalt. *Condensed Matter and Interphases.* 2025;27(1): 000-000. https://doi.org/10.17308/kcmf.2025.27/000

✉ Nikolay N. Afonin, e-mail: nafonin@vspu.ac

ARTICLE STRUCTURE (IMRAD)

1. Introduction

The introduction (1–2 pages) states the problem under consideration, its relevance, and the most important tasks that need to be resolved. Describe the scientific problems which have not yet been solved and which you sought to solve in your research. The introduction should contain a short critical review of previously published works in this field and their comparative analysis. It is recommended that the analysis is based on 20–30 studies (no more than 20% of references to the author's own works, at least 50% of the references should be to articles published within the previous 5 years). **The purpose** of the article is indicated by the problem statement.

The Vancouver reference style is used in the journal: bibliographic references in the text of the article are indicated by numbers in square brackets; in the references section, the references are numbered in the order they are mentioned in the text.

Example of references in-text citations:

Single crystals of difluorides of alkaline earth elements are widely used as photonics materials [1–3] as well as matrices for doping with rare-earth ions [4,10].

References should primarily be made to original articles published in scientific journals indexed by global citation databases. References should indicate the names of all authors, the title of the article, the name of the journal, year of publication, volume (issue), number, pages, and DOI (Digital Object Identifier https://search.crossref.org/). If a DOI is lacking, a link to the online source of the article must be indicated. References to dissertation abstracts are acceptable if the texts are available online. It is vital that our readers can find any of the articles or other sources listed in the reference section as fast as possible. Links to unpublished literature sources or sources not available online are unacceptable.

2. Experimental

The experimental section (2-3 pages) provides the details of the experiment, the methods, and the equipment used. The object of the study and the stages of the experiment are described in detail and the choice of research methods is explained.

3. Results and discussion

Results and discussion (6-8 pages) should be brief, but detailed enough for the readers to assess the conclusions made. It should also explain the choice of the data being analysed. Measurement units on graphs and diagrams should be separated with a coma. **Formulae should be typed using Microsoft Office Equation 3 or Math Type** and aligned on the left side. Latin letters should be in italics. Do not use italics for Greek letters, numbers, chemical symbols, and similarity criteria.

All subheadings should be in italics.

Example:

1.1. *X-ray diffraction analysis*

Example of figure captions in the text of the article: Fig. 1, curve *1*, Fig. 2b.

A complete list of figures should be provided at the end of the paper after the information about the authors.

Figures and tables should not be included in the text of the article. They should be placed on a separate page. Figures should also be **submitted as separate** *tif, *jpg, *cdr, or *ai. files. **All figures should have a minimum resolution of 300 dpi.** Name each figure file with the name of the first author and the number of the figure.

4. Conclusions

Conclusions (1 paragraph) should briefly state the main conclusions of the research. Do not repeat the text of the article. The obtained results are to be considered with respect to the purpose of the research. This section includes the conclusions, a summary of the results, and recommendations. It states the practical value of the research and outlines further research problems in the corresponding field.

Contribution of the authors

At the end of the Conclusions the authors should include notes that explain the actual contribution of each co-author to the work.

Example 1:

Nikolay N. Afonin – Scientific management, Research concept, Methodology development, Writing – original draft, Final conclusions.

Vera A. Logachova – Investigation, Writing – review & editing.

Example 2:

The authors contributed equally to this article.

Conflict of interests

The authors declare that they have no known competing financial interests or personal relationships that could have influenced the work reported in this paper.

References

(The references are to be formatted according to the Vancouver Style. The reference list should only include articles published in peer-reviewed journals)

Examples:

Journal article

1. Bahadur A., Hussain W., Iqbal S., Ullah F., Shoaib M., Liu G., Feng K. A morphology controlled surface sulfurized $CoMn_2O_4$ microspike electroncatalyst for water splitting with excellent OER rate for binder-free electrocatalytic oxygen evolution. *Journal of Materials Chemistry A*. 2021;20(9): 12255–12264. https://doi.org/10.1039/D0TA09430G

2. Alexandrov A. A., Mayakova M. N., Voronov V. V., Pominova D. V., Kuznetsov S. V., Baranchikov A. E., Ivanov V. K., Fedorov P. P. Synthesis upconversion luminophores based on calcium fluoride. *Condensed Matter and Interphases.* 2020;22(1): 3–10. https://doi.org/10.17308/kcmf.2020.22/2524

3. Kopeychenko E. I., Mittova I. Y., Perov N. S., Alekhina Y. A., Nguyen A. T., Mittova V. O., Pham V. Synthesis, composition and magnetic properties of cadmium-doped lanthanum ferrite nanopowders. *Inorganic Materials.* 2021;57(4): 367–371. https://doi.org/10.1134/S0020168521040075

Book: print

4. Nakamoto K. *Infrared and Raman spectra of inorganic and coordination compounds*. New York: John Wiley; 1986. 479 p.

5. Fedorov P. P., Osiko V. V. Crystal growth of fluorides. In: *Bulk Crystal Growth of Electronic. Optical and Optoelectronic Materials.* P. Capper (ed.). Wiley Series in Materials for Electronic and Optoelectronic Applications. John Wiley & Son. Ltd.; 2005. pp. 339-356. https://doi.org/10.1002/9780470012086.ch11

6. *Nanostructured oxide materials in modern micro-, nano- and optoelectronics*. V. A. Moshnikov, O. A. Aleksandrova (eds.). Saint Petersburg: Izd-vo SPbGETU "LETI" Publ., 2017. 266 p. (in Russ.)

Conference proceeding: individual paper

7. Afonin N. N., Logacheva V. A., Khoviv A. M. Synthesis and properties of functional nanocrystalline thin-film systems based on complex iron and titanium oxides. In: *Amorphous and microcrystalline semiconductors: Proc. 9th Int. Conf., 7–10 July 2014.* St. Petersburg: Polytechnic University Publ.; 2014. p. 356–357. (In Russ.)

Website

8. NIST Standard Reference Database 71. *NIST Electron Inelastic-Mean-Free-Path Database: Version 1.2.* Available at: www.nist.gov/srd/nist-standard-reference-database-71

Patent

9. Chekanov V. V., Kandaurova N. V., Rakhmanina Yu. A., Chekanov V. S. *Ultrasound indicator 2*. Patent RF, no. 2446384, 2012. Publ. 27.03.2012, bull. no. 9. (In Russ.)

Information about the authors

This section should include the full last and first name(s) of the author(s), their academic degree, academic title, affiliation, position, city, country. ORCID (register for an ORCID here https://orcid.org/register) and e-mail.

Nikolay N. Afonin, Dr. Sci. (Chem.), Research Fellow, Professor at the Department of Science and Technology Studies, Voronezh State Pedagogical University (Voronezh, Russian Federation).
https://orcid.org/0000-0002-9163-744X
nafonin@vspu.ac.ru

Vera A. Logachova, Cand. Sci. (Chem.), Research Fellow at the Department of General and Inorganic Chemistry, Voronezh State University (Voronezh, Russian Federation).
https://orcid.org/0000-0002-2296-8069
kcmf@main.vsu.ru

Tien Dai Nguyen, PhD in Advanced Materials Science and Engineering, Lecturer/ Research at Institute of Theoretical and Applied Research (ITAR), Duy Tan University (DTU), Hanoi, Vietnam.
https://orcid.org/0000-0002-9420-210X
nguyentiendai@duytan.edu.vn

Valery V. Voronov, Cand. Sci. (Phys.–Math.), Head of the Laboratory, Prokhorov General Physics Institute of the Russian Academy of Science (Moscow, Russian Federation).
https://orcid.org/0000-0001-5029-8560
voronov@lst.gpi.ru

Received __.__.2025; approved after reviewing __.__.2025; accepted for publication __.__.2025; published online __.__.2025.

A complete list of figures should be provided at the end of the paper after the information about the authors.

Example:

Fig. 1. Dependences of the parameters *a* and *c* of the tetragonal lattice of nanocrystalline PdO films on the oxidation temperature T_{ox}: *1* – single-phase PdO films, *2* – heterophase PdO + Pd films; *3* – data of the ASTM standard [22, 23]

Table 1. The values of relative electronegativity (ENE) of some chemical elements [30] and the proportion of the ionic component of the chemical bond in binary compounds of the AB composition formed by these elements

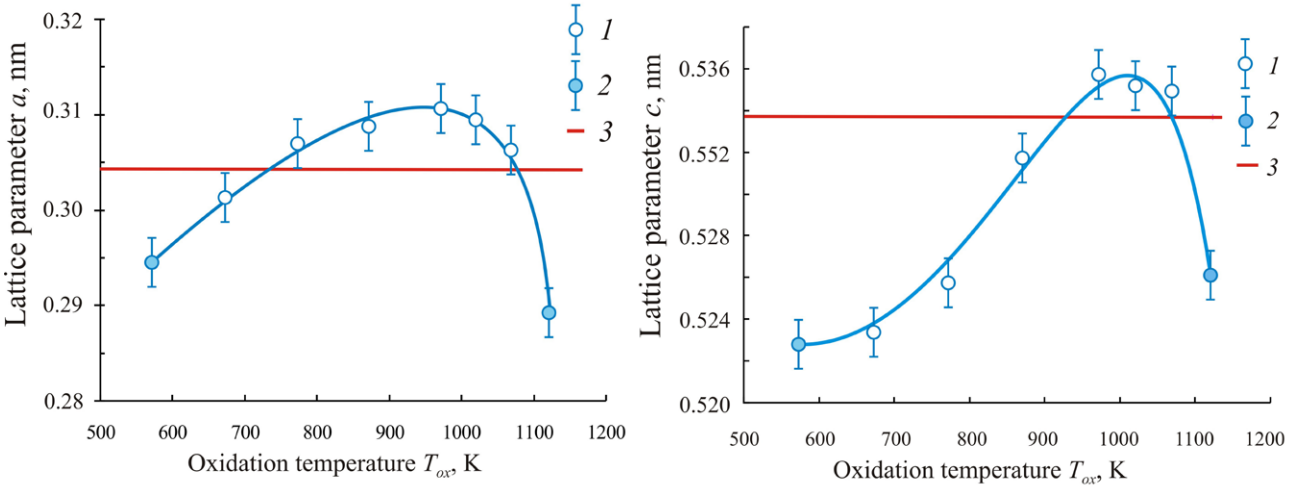

a *b*

Fig. 1. Dependences of the parameters *a* and *c* of the tetragonal lattice of nanocrystalline PdO films on the oxidation temperature T_{ox}: *1* – single-phase PdO films; *2* – heterophase PdO + Pd films; *3* – data of the ASTM standard [22, 23]

Table 1. Values of the ionic radii of palladium Pd^{2+} and oxygen O^{2-} [30–32]

Ion	Coordination number CN	Coordination polyhedron	Values of ionic radii R_{ion}, nm
Pd^{2+}	4	Square (rectangular)	0.078 [30]; 0.086 [31]; 0.078 [32]
O^{2-}	4	Tetragonal tetrahedron	0.132 [30]; 0.140 [31]; 0.124* [31]; 0.132 [32]

*The values of ionic radius were obtained on the basis of quantum mechanical calculations.

ACCOMPANYING DOCUMENTS

(The following documents should be submitted as PDF files)

1. Covering letter (with authorisation for open access publication)
2. License agreement *(signed by all authors)* https://journals.vsu.ru/kcmf/Licensingcontract
3. Manuscript.

EDITING AND PROOFREADING

When the layout is ready it is sent back to the authors for proofreading. The article should be sent back to the publisher within a maximum of three days. The authors may only correct printing mistakes.